coatings

Special Issue Reprint

Green Asphalt Materials

Surface Engineering and Applications

Edited by
Qian Chen, Xiaolong Sun, Tao Wang and Guoqiang Sun

mdpi.com/journal/coatings

MDPI

Green Asphalt Materials—Surface Engineering and Applications

Green Asphalt Materials—Surface Engineering and Applications

Guest Editors

Qian Chen
Xiaolong Sun
Tao Wang
Guoqiang Sun

MDPI

Basel • Beijing • Wuhan • Barcelona • Belgrade • Novi Sad • Cluj • Manchester

Guest Editors

Qian Chen
School of Highway
Chang'an University
Xi'an
China

Xiaolong Sun
School of Civil and
Transportation Engineering
Guangdong University
of Technology
Guangzhou
China

Tao Wang
School of Civil Engineering
Beijing Jiaotong University
Beijing
China

Guoqiang Sun
Department of Road & Urban
Railway Engineering
Beijing University
of Technology
Beijing
China

Editorial Office
MDPI AG
Grosspeteranlage 5
4052 Basel, Switzerland

This is a reprint of the Special Issue, published open access by the journal *Coatings* (ISSN 2079-6412), freely accessible at: https://www.mdpi.com/journal/coatings/special_issues/SC65Y4RH68.

For citation purposes, cite each article independently as indicated on the article page online and as indicated below:

Lastname, A.A.; Lastname, B.B. Article Title. *Journal Name* **Year**, *Volume Number*, Page Range.

ISBN 978-3-7258-7526-9 (Hbk)
ISBN 978-3-7258-7527-6 (PDF)
https://doi.org/10.3390/books978-3-7258-7527-6

Contents

About the Editors

Qian Chen

Qian Chen is Associate Professor, Master's Supervisor, School of Highway, Chang'an University. He was selected for the Shaanxi Association for Science and Technology Youth Talent Support Program and the Young Key Talents Program of Chang'an Scholars. He is the key member of the Key Scientific and Technological Innovation Teams in Shaanxi Province. He is mainly dedicated to the development and application of new materials and technologies for green functional pavement. He has won the first and second prizes of four provincial and ministerial scientific research awards. He has published more than 50 SCI/EI academic papers.

Xiaolong Sun

Xiaolong Sun is Associate Professor, Science and Technology Talent of the China Highway Construction Industry Association, Outstanding Science and Technology Faculty in Civil Engineering and Architecture in Guangdong province, Guangdong Science and Technology Commissioner, Guangdong intellectual property expert, visiting scholar at Texas State University, Austin, USA. Published over 30 academic papers and granted over 20 patents. Received scientific and technological awards such as the Guangdong Provincial Technology Invention Award, China Highway Society Science and Technology Award, China Municipal Engineering Association Science and Technology Award, Guangdong Civil Engineering and Architecture Society Science and Technology Award, and Guangdong Mechanical Society Technology Invention Award.

Tao Wang

Tao Wang is Associate Professor. Interests: Self-healing asphalt materials; high-viscosity modified asphalt material; bio-asphalt material; phase change asphalt material; recycled asphalt pavement; conductive ultra-thin wearing course; asphalt aging and anti-aging.

Guoqiang Sun

Guoqiang Sun is Professor at Beijing University of Technology. He is mainly engaged in teaching and research in the field of smart low-carbon pavement. He teaches several undergraduate/graduate courses such as "Asphalt and Asphalt Mixtures", "Road Construction Material" and "Pavement Maintenance and Management Technology". He has presided over 10 projects at various levels. He has published more than 60 publications, and applied for and has been authorized more than 10 patents. He has served as a Young Editorial Board member of several Chinese and English journals and as the reviewers of more than 20 journals/conferences.

coatings

Article

Long-Term Performance Analysis of Epoxy Resin Ultra-Thin Wearing Course Overlay on Cement Concrete Pavement

Xiaoguang Zheng [1], Yajie Chen [1], Wanwan Xu [1], Zhen Zhang [1], Guoqiang Sun [2] and Tao Wang [3,*]

[1] Shanghai Municipal Engineering Design Institute (Group) Co., Ltd., Shanghai 200092, China; zhengxiaoguang@smedi.com (X.Z.); chenyajie@smedi.com (Y.C.); xuwanwan@smedi.com (W.X.); zhangzhen8@smedi.com (Z.Z.)
[2] Beijing Key Laboratory of Traffic Engineering, Beijing University of Technology, Beijing 100124, China; gqsun@bjut.edu.cn
[3] School of Civil Engineering, Beijing Jiaotong University, Beijing 100044, China
* Correspondence: wangtao1@bjtu.edu.cn

Abstract: The overall rigidity of the cement concrete pavement is high, but there are defects such as easy cracking and insufficient anti-slip performance. The epoxy resin ultra-thin wearing course overlay can effectively solve these issues. However, there is still a lack of knowledge about the long-term performance of epoxy resin ultra-thin wearing course overlay on cement concrete pavement. Therefore, this article analyzed the interlayer adhesion and durability of epoxy resin ultra-thin wearing course overlay through the Hamburg rutting test and a series of shear tests under damp heat, thermal oxygen aging, and ultraviolet (UV) aging conditions. Shear test results indicated that the shear performance of epoxy resin overlay grew with the increase in epoxy resin content and was severely affected by high temperature, and the optimal content was set as 3.4 kg/m^2. The Hamburg rutting test results showed that the epoxy resin overlay exhibited satisfactory high-temperature performance and water resistance. For the damp heat effect, it was revealed that damp heat led to more significant shear strength loss compared with the overlay specimens without damp heat. The water immersion caused the shear strength decline due to the water damage to the overlay interface. As for the thermal oxygen aging effect, it was reflected that the short-term thermal oxygen aging had a minor impact on the shear performance of the epoxy resin overlay. However, with the increase in thermal oxygen aging duration, the shear strength of the epoxy resin overlay significantly decreased due to the aging of epoxy resin binders. Regarding the UV aging impact, it was also found that the shear performance of the epoxy resin overlay rapidly decreased as the UV aging duration grew whether at 20 °C or 60 °C. Moreover, UV aging led to a more significant impact on the shear performance of the epoxy resin overlay than thermal oxygen aging.

Keywords: road engineering; ultra-thin wearing course overlay; epoxy resin; long-term performance; aging; shear performance

1. Introduction

The resin ultra-thin wearing course overlay is a critical coating technology that can effectively solve early pavement damage such as cracks, peeling, and potholes in cement concrete pavement; meanwhile, it can also improve driving comfort and anti-slip performance [1–5]. Sprinkel [6] conducted a long-term tracking investigation on a road surface paved with the resin wearing course and found that it had excellent anti-slip performance and long service life. Hong [7] proposed a new type of tunnel pavement, i.e., polyurethane ultra-thin wearing course, which exhibited satisfactory mechanical properties and wear resistance, and had nearly no harmful emissions due to its room-temperature construction. Compared with traditional asphalt mixtures, the resin ultra-thin wearing course was proved to have excellent mechanical properties, slip resistance, sound absorption, flame retardancy, and other functional properties, as well as good environmental performance.

The resin ultra-thin wearing course is mainly composed of aggregates and resin-based binders. Aggregates are used to enhance the friction coefficient of road surfaces and play a role in anti-slip. Wear-resistant and anti-slip materials such as ceramic particles and quartz sand can be selected. Deng et al. studied the performance and nano adhesion behavior of the overlay using experimental and molecular dynamics simulation methods [8,9] and found that using diamond sand with a particle size of 2–3 mm as the ultra-thin overlay aggregate exhibited more favorable wear and skid resistance than ceramic particles. The resin binders play a bonding role and are often selected from resin materials such as polyurethane or epoxy resin, which have good bonding performance, stability, and wear resistance. Compared with an asphalt binder, most of these resins exhibit thermosetting behavior as the temperature rises, and the molecular networks created during hardening are refined to form other networks. In contrast, asphalt binders tend to soften at high temperatures. As a result, these binders perform better, especially in high temperatures where the use of an asphalt binder can cause the binder to bleed out. Wu et al. confirmed that using an epoxy resin ultra-thin wearing course overlay can significantly improve the poor anti-slip performance of steel bridge decks, and the ultra-thin wearing course has good high-temperature resistance and mechanical properties [10]. After 7 months of use, the overall condition of the road surface was good, with a structural depth of over 1.4 mm, and the bond strength was still stable at 3.71 MPa. The experimental results from Stenko et al. [11] showed that the compressive strength of the epoxy resin ultra-thin wearing course material was about 40 MPa and the bending strength was about 13 MPa. Horn et al. [12] compared different types of resin concrete and established that the performance of epoxy resin concrete was superior to that of methyl acrylic acid resin concrete in all aspects. Attanayake et al. [13] found that regardless of the concrete age at the time of overlay application, the bond strength of an epoxy overlay under elevated temperatures was less than 1.7 MPa. The primary failure type was a bond failure at the concrete/overlay interface. Freeseman et al. [14] proposed that the accelerated freezing and thawing exposure greatly affects the bond strength of epoxy overlays.

The epoxy resin has certain chemical activity and can be ring-opened, cured, and cross-linked by compounds containing active hydrogen to form a network structure [15], Therefore, the epoxy resin ultra-thin wearing course overlay can play a role in anti-slip and extending the service life of the road surface [16,17]. However, the long-term performance of epoxy resin ultra-thin wearing course overlay is affected by rain, high temperatures, and strong ultraviolet radiation during service, and its durability varies with different environmental influences. Therefore, the long-term durability of the epoxy resin ultra-thin overlay layer is closely related to the impact of aging. Epoxy resin is prone to aging during use, manifested in surface yellowing, loss of gloss, cracking, and overall mechanical properties degradation [18]. Epoxy resin aging is mainly divided into three types: thermal oxygen aging, humid heat aging, and ultraviolet aging. Among them, when the epoxy resin is thermally excited in an oxygen-containing environment, the molecular chain will absorb the oxygen in the environment and generate hydroperoxide, which will lead to instability of hydroperoxide, rearrangement reaction of polymer main chain, and chain breaking or cross-linking, which will degrade the performance of polymer materials and lead to thermal–oxidative aging [19]. Yu conducted a 30-day thermal aging of an epoxy resin matrix at 130~160 °C to study the effect of thermal oxygen aging on epoxy resin [20]. The FTIR results indicated that during the thermal aging process, the epoxy resin sample undergoes oxidation and molecular rearrangement. The bending test results indicated that the thermal aging significantly reduced the fracture strain, while the bending strength was only slightly affected and the modulus increased. When epoxy resin materials underwent high humidity or rainwater environments during service, they will experience significant damp heat [21,22], resulting in a performance degradation and an inability to meet usage requirements. Wang et al. conducted an in-depth study on the effects of humidity and time on the structure and mechanical properties of phenolic epoxy resin during the wet heat aging process [23]. The results indicated that the moisture absorption rate increased

linearly with the square root of aging time and follows Fick's second law. There were two main types of reactions during wet heat aging: the first type was the post-curing process, which led to a higher crosslinking density and reduced internal stress; another was the plasticization and degradation of epoxy resin caused by the entry of moisture. The unsaturated bonds or polar groups such as benzene rings and ether bonds contained in epoxy resin, as well as impurities introduced during the polymerization stage and processing, were prone to absorbing ultraviolet radiation and causing photooxidation reactions in epoxy resin [24]. Affected by aging, the bonding and shear properties of epoxy resin decrease. Therefore, the firmness of the bonding between the epoxy resin ultra-thin overlay layer and cement concrete pavement is one of the key issues that needs to be solved when adding the epoxy resin ultra-thin overlay layer to cement concrete pavement.

Overall, it was noted that there is still a lack of knowledge about the long-term performance of epoxy resin ultra-thin wearing courses. Firstly, the optimum dosage and high temperature resistance of epoxy resin ultra-thin wear layer covering were evaluated by oblique shear test and Hamburg rutting test. Secondly, the effects of different aging conditions, including damp heat, thermal oxygen aging, and ultraviolet aging, on the shear resistance of epoxy resin ultra-thin wearing course overlay were investigated by means of oblique shear tests. This study was expected to provide an experimental theoretical basis for the engineering feasibility of the epoxy resin ultra-thin wearing course overlay on cement concrete pavement.

2. Materials and Experiment Methods

2.1. Materials

The performance of the epoxy resin was the key to ensuring the quality and longevity of the epoxy resin ultra-thin wearing course. The epoxy resin materials were divided into two components, A and B, and were blended in proportion to the application. Two kinds of commercial epoxy resin materials were shown in Figure 1, i.e., RS epoxy resin and RA epoxy resin, were selected. The main performance indicators after the blending reaction are shown in Table 1.

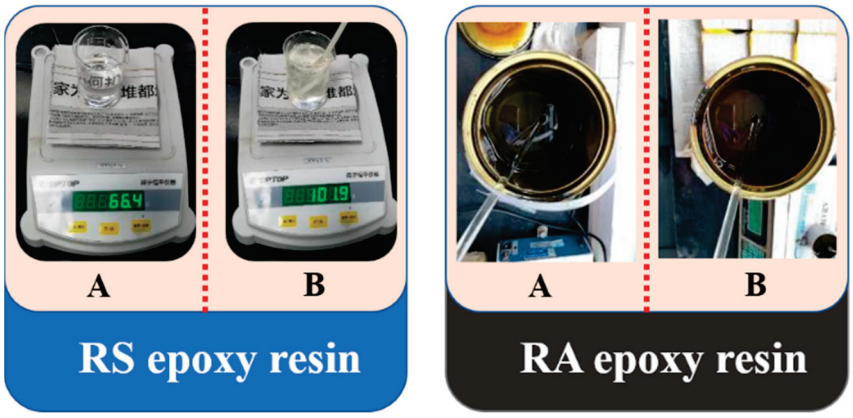

Figure 1. Two kinds of commercial epoxy resin materials.

Table 1. Performance indicators of epoxy resins used in this study.

Index	Unit	RS Epoxy Resin	RA Epoxy Resin
Solids content	%	99.7	99.7
Tensile strength (25 °C)	MPa	20.3	10.6
Elongation at break (25 °C)	%	45.0	30.5
Tensile strength (25 °C)	Mpa	7.6	18.0
Tensile strength (60 °C)	Mpa	4.8	4.8

2.2. Preparation

The cement concrete panel was made of C40 strength grade concrete. In order to simulate the actual situation of cement concrete pavement with epoxy resin ultra-thin overlay, composite rutting specimens were formed by using special rutting plate test molds. Firstly, according to the requirements of the "Test Procedure for Cement and Cement Concrete in Highway Engineering" [25], $30 \times 30 \times 7$ cm^3 cement concrete specimens were prepared by vibratory compact forming method using asphalt mixture rutting plate. The cement concrete panel was then cleaned and dried naturally, placed under standard curing conditions, and cured for 28 d to reach the design strength; the cured cement concrete panel was put into a $30 \times 30 \times 7$ cm^3 mold, the epoxy resin components A and B were mixed and stirred nicely, and the designed amount of resin was evenly applied using a brush. After the resin was applied, the gravel was spread in time according to the design requirements after the first layer of resin was cured and stabilized, the unadhered aggregate was swept away and the second layer of resin material was applied, the gravel was spread in time after the resin was cured and stabilized, the unadhered aggregate was swept away, and the specimen was cured for 3 days at room temperature. The automatic rock cutting machine was used to cut the cured composite rutting slab into composite specimens of $8 \times 8 \times 7$ cm^3, which were subjected to the 45° oblique shear test and pull-out test, with three parallel specimens in each group. The forming process is shown in Figure 2.

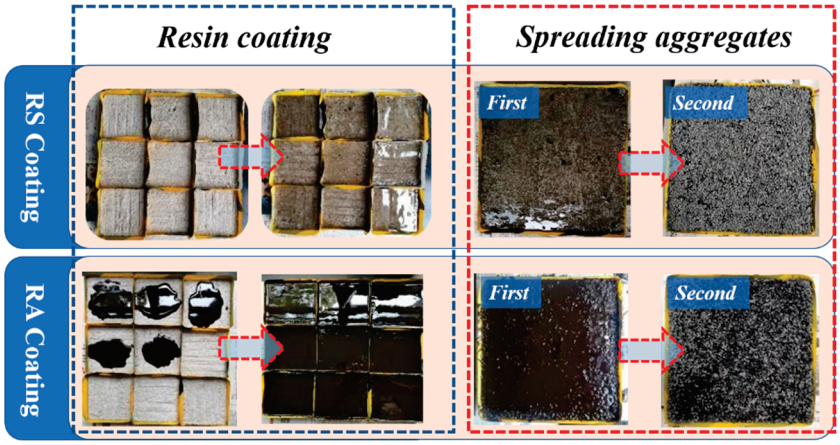

Figure 2. Preparation process of test samples.

2.3. Test Methods

2.3.1. Shear Test

The sample group was fixed to conduct the shear test using the 45° oblique shear fixture and oblique shear instrument [26,27]. Evaluation of shear resistance was carried out in an electro-hydraulic servo mechanical test system with a measurement accuracy of 1 N for the pressure measuring unit, 0.1 mm for the displacement sensor, and 0.1 °C for the ambient room temperature sensor. The shear stress and shear strain were calculated according to Equation (1). The tests started with the preparation of thin layers on cement concrete panels at room temperature with different resin dosages selected and tested for shear resistance, the main test procedure is shown in Figure 3 below. The load was then applied at a rate of 1.0 N/s until shear damage occurred to the specimen. The value of the applied load at the time of damage was recorded and the shear strength of the shear surface was calculated.

$$\tau = \frac{P \times \sin \alpha}{S} \quad (1)$$

P—load (N); S—shear area of the specimen (mm^2); τ—shear strength (MPa); α—angle between shear surface and horizontal surface, which, in this test, was 45 degrees.

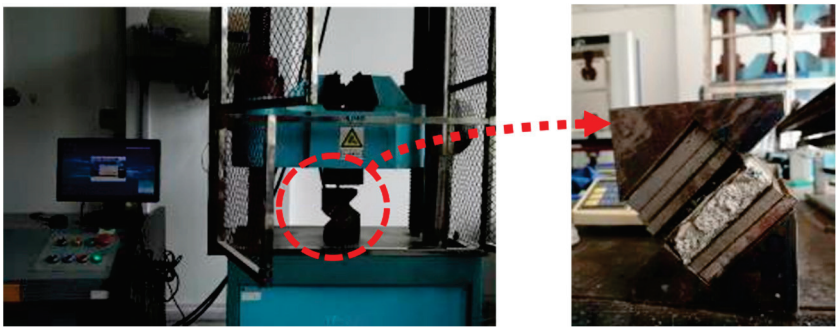

Figure 3. Shear test.

2.3.2. Hamburg Rutting Test

The high-temperature performance and water resistance of epoxy resin ultra-thin overlay under the combined action of water and heat was evaluated by conducting Hamburg rutting test according to the AASHTO T324 specification [28]. The test piece was placed in a water bath of the Hamburg rut testing machine, maintained in a 60 °C water bath for 30 min, and the test was then conducted under a pressure of 0.7 MPa. When the steel wheel passed 20,000 cycles or reached the maximum allowable rut depth, the instrument automatically stopped the test.

2.3.3. Durability Tests

(1) Damp heat impact test

Summer high temperatures and rainfall were vital factors affecting road paving. To evaluate the impact of high temperature and rainfall on epoxy resin ultra-thin wearing course overlay, the test was carried out by submerging thin resin pavement specimens in a water bath at 60 °C for 48 h and examining the shear resistance of the pavement under damp heat conditions by means of a shear test.

(2) Thermal oxygen aging impact test

High-temperature thermal oxygen aging was one of the important factors affecting the performance of resin materials. Resin materials exposed to long-term, high-temperature air were prone to oxidation, degradation, cross-linking, or creep damage, resulting in a decrease in bonding strength. The epoxy resin ultra-thin wearing course specimens were aged for 7, 14, and 28 days in a 60 °C oven, and their shear resistance after aging was tested.

(3) Ultraviolet (UV) aging impact test

China has a vast territory, and most areas are affected by strong solar radiation. The problem of UV aging of the road pavement cannot be ignored. Therefore, the epoxy resin ultra-thin wearing course specimens were aged for 7, 14, and 28 days, respectively, at 60 °C, 70%, and 1000 W/m^2 of radiant intensity. The daily working time of the equipment was 20 h. The conversion between indoor ultraviolet radiation time and outdoor strong sunlight radiation time is shown in Table 2.

Table 2. Conversion between UV aging time and outdoor aging time.

Aging Mode	**Aging Time**		
Indoor simulation	7 days	14 days	28 days
Outdoor aging	6 months	12 months	24 months

3. Results and Discussion

3.1. Determination of the Optimal Dosage of Epoxy Resin Overlay

The failure load and shear strength of the RS epoxy resin ultra-thin wearing course overlay with different content is shown in Figure 4. Shear test was used to test the ability

of epoxy resin ultra-thin wearing course overlay to resist shear stress generated by vertical and horizontal forces under driving loads. In order to determine the optimal dosage of the RS ultra-thin wearing course overlay, shear tests were used to evaluate the shear resistance performance of the RS ultra-thin wearing course overlay with different ratios. In this experiment, the ratio of A and B in RS was 1:2. The used RS was applied in the first layer and second layer. For example, the RS content of 1.8 (0.6 + 1.2) kg/m^2 meant that the first layer used 0.6 kg/m^2 RS and the second layer used 1.2 kg/m^2 RS. Correspondingly, the aggregate dosage was set as 13.0 (5.4 + 7.6) kg/m^2. It can be found that with the increase in RS content, its failure load and shear strength increase significantly. It indicated that with the increase in RS dosage, the shear resistance of the epoxy resin ultra-thin wearing course was greatly improved. However, with the increase in RS content, the increase percent of shear strength and failure load gradually decreased. Compared with the addition of 1.8 kg/m^2, the shear strength increased by 129% with the addition of 3.4 kg/m^2. During the test, the surface of the epoxy resin overlay specimen with 3.4 kg/m^2 resin did not deform, and only a minor amount of aggregate fell off. It was because the epoxy resin greatly improved the bonding among aggregates as its dosage increased. This indicated that the epoxy resin overlay structure had good deformation resistance and certain wear resistance; therefore, only aggregates with poor surface adhesion fell off. Thus, based on the comprehensive shear strength and the shedding during the test, the optimal dosage of the RS resin overlay was determined as 3.4 kg/m^2. To compare with the RS ultra-thin wearing course overlay, the dosage of the RA resin pavement was also determined to be 3.4 kg/m^2.

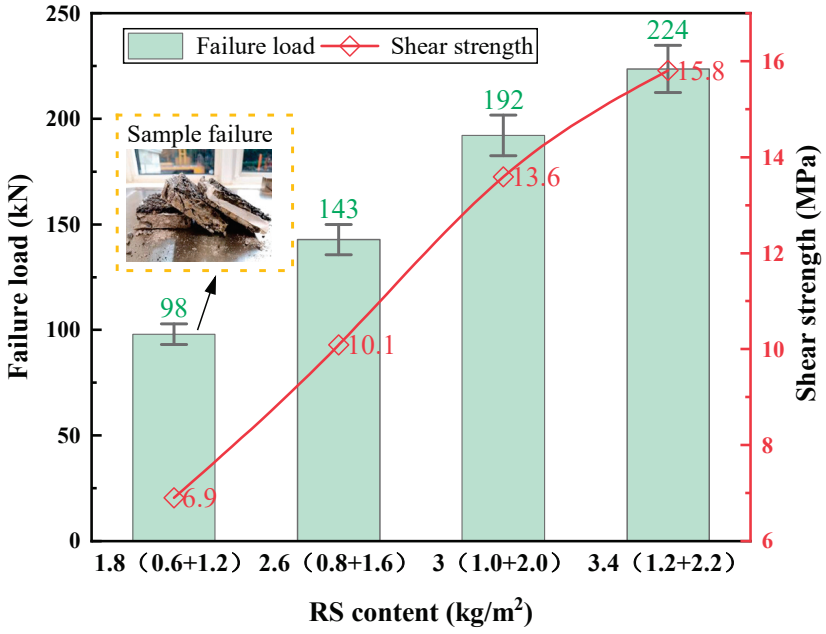

Figure 4. Failure load and shear strength of RS epoxy resin overlay with different content.

3.2. High-Temperature Shear Performance of Epoxy Resin Overlay

(1) High-temperature shear test results

To investigate the effect of high temperature on the shear resistance of epoxy resin overlay bonding, the epoxy resin overlay specimens were placed in an oven at 60 °C and 70 °C for 6 h before conducting shear tests. The results are shown in Figure 5. Obviously, the shear strength of the RS epoxy resin overlay was highest at room temperature (20 °C), indicating that the shear resistance of the RS epoxy resin overlay at room temperature was excellent. With the increase in temperature, the shear strength of the RS and RA epoxy resin overlays both decreased significantly, indicating that the shear performance of epoxy resin overlay was severely affected by high temperature. When the temperature reached 60 °C, the shear strength of RS was reduced by 53.2%; when the temperature reached

70 °C, the shear strength dropped by 98.0%. Compared with the shear strength at 20 °C of the RA epoxy resin overlay, its shear strength at 60 °C was reduced by 46.5%; when the temperature reached 70 °C, its shear strength decreased by 93.3%. Nonetheless, the shear strength of the RS epoxy resin overlay was obviously higher than that of the RA epoxy resin overlay at 20 °C and 60 °C, while it was lower at 70 °C. In fact, the RA epoxy resin overlay showed slightly higher high-temperature resistance than the RS epoxy resin overlay due to the smaller decrease percent with test temperature. Overall, the results indicated that the high-temperature performance of epoxy resin overlay was poor. Although the shear resistance of epoxy resin overlay decayed quickly with temperature, it was still higher than the performance of traditional asphalt bonding materials (0–0.2 MPa). The shear failure was generally between the resin and cement board surface, indicating that, at this time, a strong bonding force had not yet formed between the thin layer of this type of resin and the cement board. The reason for this phenomenon was that the high temperature reduced the bond between the epoxy resin overlay and the cement concrete interface, resulting in the epoxy resin overlay spalling from the cement concrete surface more easily at high temperatures [13].

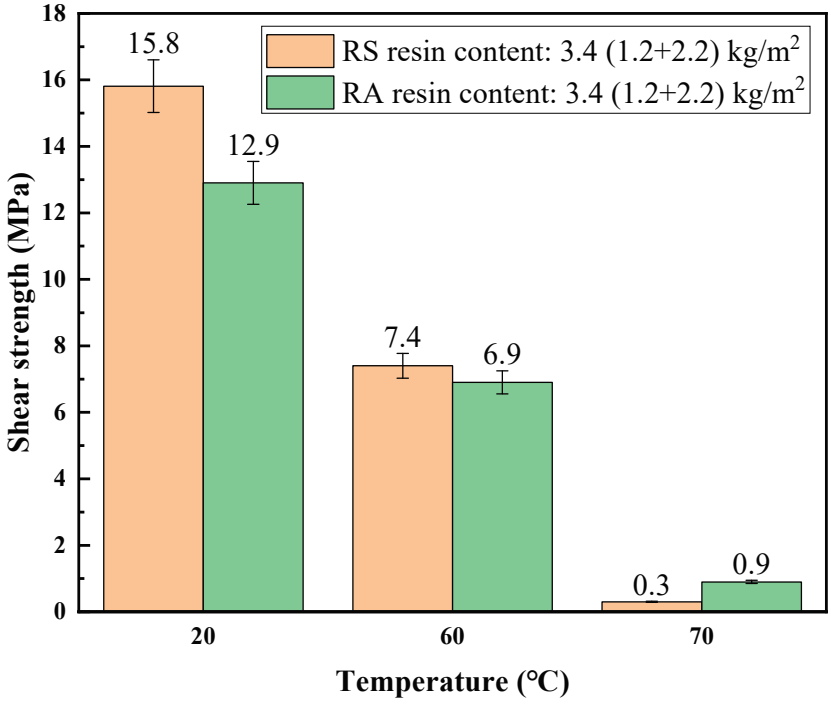

Figure 5. Effect of high temperature on shear resistance of epoxy resin overlay.

(2) Hamburg rutting test results

The Hamburg rut test results are shown in Figures 6 and 7, and Table 3. The Hamburg rut test was conducted under high temperature and water bath conditions by applying repeated steel wheel loads to the specimen [29]. The test termination condition was controlled by two indicators: rolling frequency and rut depth, with a maximum rolling frequency of 20,000 cycles and a maximum rut depth of 20 mm [30]. When the rolling depth reached 20 mm, the test was terminated; if the number of rolling passes reaches 20,000 cycles and the rut depth still does not reach 20 mm, the test will also be terminated. The test piece terminated due to the maximum number of rolling cycles had better high-temperature performance and water damage resistance than the test piece terminated due to the maximum rut depth. If the number of rolling tests reached 20,000 cycles, the smaller the rut depth, the better its high-temperature and water resistance performance; if the number of passes did not reach 20,000 cycles, the higher the number of passes, the better its high-temperature and water resistance performance. Through the results

of the Hamburg rut test, it was found that after 20,000 cycles of the Hamburg rut test, the RS ultra-thin wearing course had a maximum rut depth of 1.73 mm at 60 °C and 0.7 MPa. At the same time, when the number of rolling cycles was 15,000–20,000 cycles, the rolling depth fluctuated significantly, indicating that the RS ultra-thin wearing course had better deformation resistance; the maximum rut depth of RA ultra-thin wearing course at 60 °C and 0.7 MPa was 2.14 mm. Throughout the entire test process, the rolling depth fluctuated greatly with the increase in rolling times, indicating the deformation resistance of the RA epoxy resin overlay. After the experiment, it was found that both types of epoxy resin paving specimens exhibited obvious peeling and particle shedding on the surface, indicating that the coupling of high temperature and water can lead to a decrease in the adhesion ability of the surface, resulting in peeling. The two types of epoxy resin ultra-thin wearing course had a rolling frequency of 20,000 cycles and a lower rolling depth, indicating that epoxy resin overlay had excellent high-temperature performance and water damage resistance; however, further research is needed on its anti-peeling performance. At the same time, the RS epoxy resin overlay had better high-temperature performance and water resistance than the RA epoxy resin overlay.

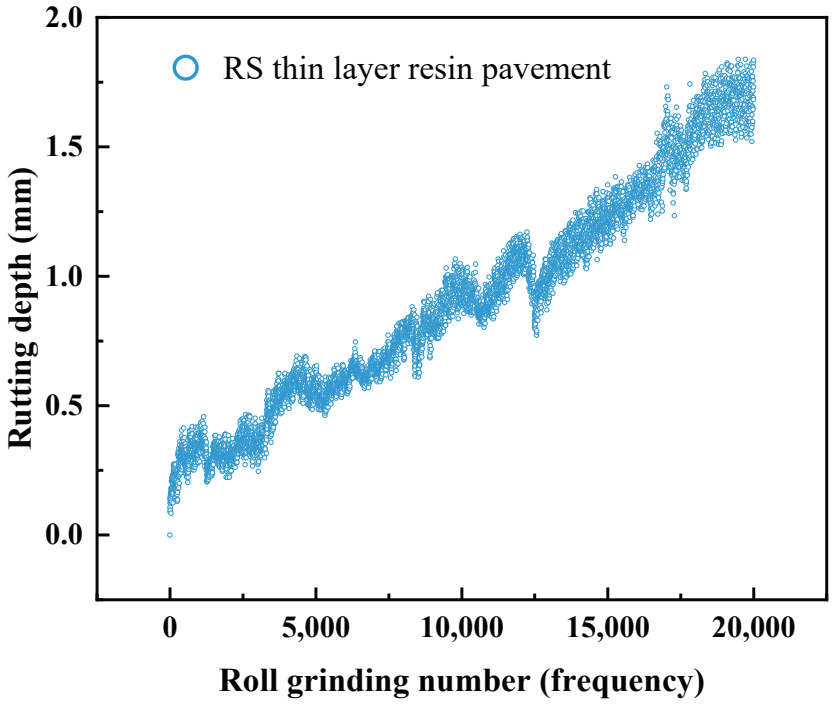

Figure 6. Results of Hamburg rutting test for RS epoxy resin overlay.

Table 3. Hamburg rutting test results.

Materials	Temperature (°C)	Stress (MPa)	Rolling Times (Freq)	Rutting Depth (mm)
RA RS	60	0.7	20,000	1.731 2.142

3.3. Durability Performance Evaluation of Epoxy Resin Overlay

3.3.1. Effect of Damp Heat on Shear Resistance of Epoxy Resin Overlay

The effect of damp heat on the shear strength of epoxy resin overlay is shown in Figure 8. To simulate the effect of summer rainwater on the ultra-thin wear layer, the resin overlay was immersed in a water bath at 60 °C for 48 h; then, we conducted shear performance tests at temperatures of 20 °C and 60 °C. Compared with the shear strength results in the air bath (see Figure 5), it was found that the shear strength of both epoxy resin overlays after water immersion was reduced, especially at 60 °C, indicating that the

water immersion caused the shear strength decline due to the water damage to the overlay interface. As for the couple impacts of damp heat, the shear strength at 60 °C of the RS epoxy resin overlay dropped by 73.4% compared with the shear strength at 20 °C, and the shear strength at 60 °C of the RA epoxy resin overlay decreased by 74.6%. Obviously, the damp heat led to more significant shear strength loss than the overlay specimens without damp heat. Moreover, the RS epoxy resin overlay showed similar damp heat resistance to the RS epoxy resin overlay according to the close decrease percent.

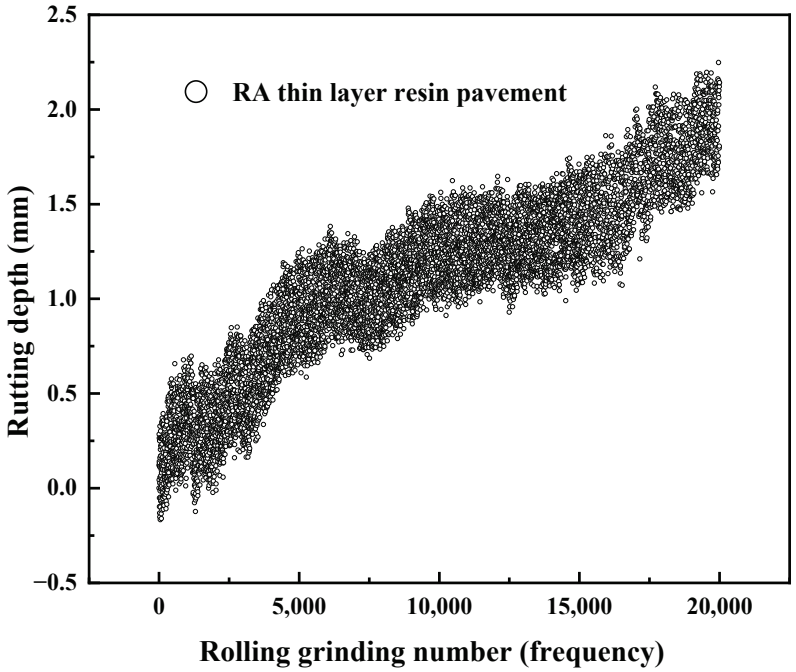

Figure 7. Results of Hamburg rutting test for RA epoxy resin overlay.

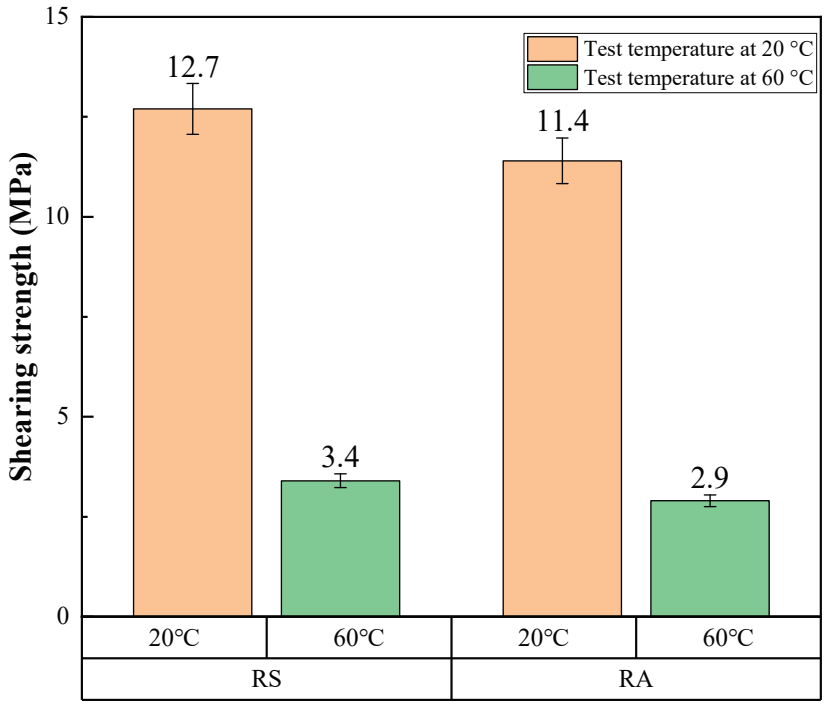

Figure 8. Effect of damp heat on shear strength of epoxy resin overlay.

3.3.2. Effect of Thermal Oxygen Aging on Shear Resistance of Epoxy Resin Overlay

The effect of thermal oxygen aging on the RS epoxy resin overlay is shown in Figure 9. High-temperature thermal and oxygen aging was one of the most important factors in the aging of resin material properties. Resin materials exposed to long periods of high-temperature air were susceptible to oxidation, degradation, cross-linking, or creep damage, resulting in a reduction in bond strength. The test was carried out on resin thin-layer specimens aged at 60 °C in an oven for 7, 14, and 28 days and tested for shear resistance after aging. The results showed that the shear strength of the RS resin laminate decreased significantly as the aging time increased, with an 8.3%, 25.7%, and 62% reduction in the shear strength of the specimens after 7, 14, and 28 days of aging, respectively, compared to the unaged test. This indicates that aging over a short period of time does not have a significant impact on shear resistance. However, aging over a long period of time had a serious impact on the shear resistance based on the significant reduction in the bonding properties of the epoxy resin, which can be attributed to the long-term aging induced structural damage of the resin material. The effect of thermo-oxidative aging on the epoxy resin overlay mainly occurred on the surface. With the increase of aging time, the effect of thermo-oxidative aging was gradually strengthened, and the macroscopic manifestation was the reduction in bonding performance and aggregate spalling. After aging, the different shear resistance test temperatures also had a significant effect on the shear strength of the RS resin paving. The aging shear resistance was tested at 20 °C and 60 °C to evaluate the shear strength decay at room temperature and high summer temperatures, respectively. At 60 °C, the shear strength decreased by 16.2%, 34.1%, and 71.4%, respectively, with increasing aging time. It can be found that aging has a more significant effect on high-temperature shear performance. Results indicated that the resin material a had further reaction at the initial stage of high temperature, so short-term aging has a lesser effect on the shear performance; however, the time aging and high temperature have more effect on the shear performance of this epoxy resin ultra-thin wearing course overlay. With the continuous increase in aging duration and aging temperature conditions, the adhesion will decompose due to oxidation and its shear strength will gradually decrease, with the decreasing trend gradually increasing, which seriously reduces the bonding performance of the epoxy resin overlay.

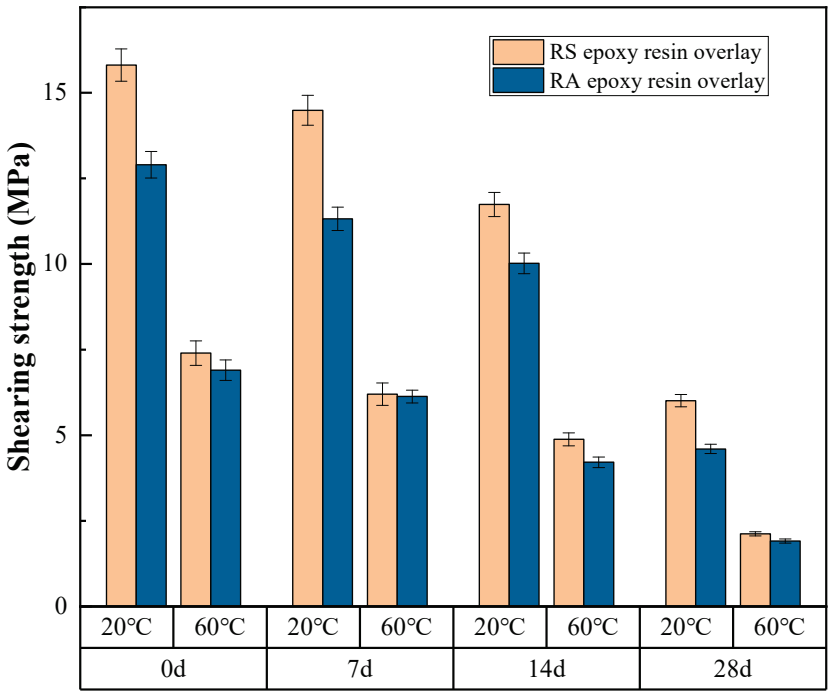

Figure 9. Effect of thermal oxygen aging on the shear strength of epoxy resin overlay.

The shear strength of the RA epoxy resin overlay decreased substantially as the aging time increased, with the shear strength of the specimens decreasing by 12.2%, 22.3%, and 64.3% after 7, 14, and 28 days of aging, respectively, relative to the unaged test. This indicates that aging had a greater effect on shear resistance in a shorter period of time; however, the severity of the effect on shear resistance increased over a longer period of time, mainly due to the significant reduction in bonding properties of the epoxy resin as a result of aging. After aging, the shear strength of RA resin paving was significantly affected by thermal oxygen aging at high temperatures. The shear strength decreased by 11.1%, 39.0%, and 72.3%, respectively, as the aging time increased in the test environment of 60 °C. The effect of aging on the high-temperature shear performance of the RA thin-layer resin overlay was even more significant, severely reducing the bonding performance of the overlay. Additionally, the RS epoxy resin overlay had superior thermal oxygen aging resistance to the RA epoxy resin overlay.

3.3.3. Effect of UV Aging on the Shear Resistance of Epoxy Resin Overlay

The effect of UV aging on the shear resistance of RS resin overlay is shown in Figure 10. Ultraviolet light is one of the main natural factors that causes the aging of resinous thin-layered paving. UV light degrades epoxy resins because the aromatic structure of epoxy resins is susceptible to UV light absorption and oxidation. As a polymeric material, the bond between the resin and the aggregate is easily weakened by UV light, which causes the aggregate to fall off and affect the durability of the resin paving. The shear strength of the RS resin overlay decreased by 25.1%, 36.1%, and 81.9% at 20 °C after 7, 14, and 28 days, respectively. The interlayer shear resistance of the RS resin overlay showed a significant decrease with the increase in UV aging time, and the bonding performance decayed significantly. UV aging had a significant effect on the bonding shear resistance of the epoxy resin ultra-thin wearing course overlay. In order to simulate the simultaneous effect of high temperature and UV aging in summer, the shear resistance of the RS thin-layer resin overlay samples treated with different UV aging times was tested at 60 °C. After 7, 14, and 28 days of UV aging, their shear strength at 60 °C was reduced by 13.8%, 37.3%, and 86.8%, respectively. The results show that the combination of extreme temperature and UV aging leads to a significant reduction in the shear strength of the RS epoxy resin overlay, especially at 28 days. Compared with thermal-oxidative aging, the shear resistance decreased more significantly after UV aging, and the effect of UV aging on the shear resistance of the RS resin overlay was also significant. As the UV aging time increases, the surface of the epoxy resin continues to become rough and is accompanied by the emergence of wrinkles, surface layer peeling, hole generation, and other phenomena. This resulted in a decrease in the bonding ability between the epoxy resin and the aggregate, and between the epoxy resin and the cement concrete interface.

The shear strength of RA resin overlay decreased by 6.12%, 30.1%, and 69.6% at 20 °C after 7, 14, and 28 days, respectively. The shear resistance of the RA resin overlay showed a significant decrease with the increase in UV aging time, and the bonding performance decayed significantly. In order to simulate the effects of high temperatures and UV aging in summer, the shear resistance of the RA thin-layer resin overlay samples treated with different UV aging times was tested at 60 °C. After 7, 14, and 28 days of UV aging, their shear strength at 60 °C was reduced by 8.7%, 54.5%, and 90.9%, respectively. The results show that the coupled effects of high temperature and UV aging caused a significant reduction in the interlayer shear resistance of the RA epoxy resin overlay. Moreover, the results from the decrease percent further confirmed that the RS epoxy resin overlay had superior UV aging resistance to the RA epoxy resin overlay.

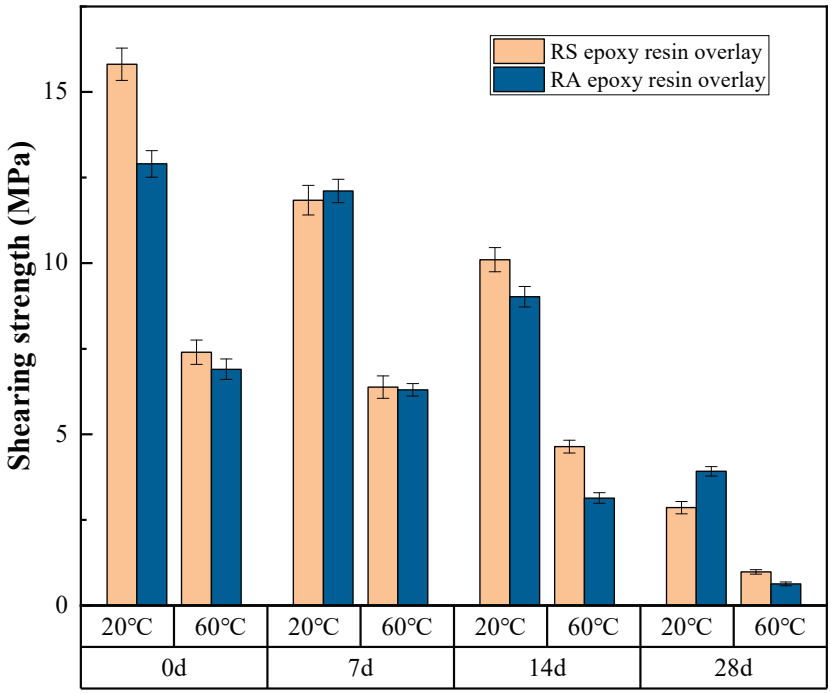

Figure 10. Effect of UV aging on shear strength of epoxy resin overlay.

4. Conclusions

(1) Through shear tests, it was found that the shear strength of epoxy resin overlay grew with the increase in epoxy resin content, and the optimal content was set as 3.4 kg/m^2. The Hamburg rutting test results showed that the epoxy resin overlay exhibited satisfactory high-temperature performance and water resistance, and the RS epoxy resin overlay had better high-temperature performance and water resistance than the RA epoxy resin overlay. Moreover, the shear performance of the epoxy resin overlay was severely affected by high temperature.

(2) Compared with the overlay specimens without damp heat, the damp heat led to more significant shear strength loss. The shear strength of both epoxy resin overlays after water immersion was reduced, especially at 60 °C, indicating that the water immersion caused the shear strength decline due to the water damage to the overlay interface. Moreover, the RS epoxy resin overlay showed similar damp heat resistance to the RS epoxy resin overlay.

(3) As for the thermal oxygen aging effect, it was reflected that the short-term thermal oxygen aging had a minor impact on the shear performance of the epoxy resin overlay. However, with the increase in thermal oxygen aging duration, the shear strength of epoxy resin overlay significantly decreased, especially at 60 °C, due to the aging of epoxy resin binders. The shear strength at 60 °C of the RS and RA epoxy resin overlays decreased by 71.4% and 72.2%, respectively, after 28 days of aging. Additionally, the RS epoxy resin overlay had superior thermal oxygen aging resistance to the RA epoxy resin overlay.

(4) Regarding the UV aging impact, it was also found that the shear performance of epoxy resin overlay rapidly decreased as the UV aging duration grew, whether at 20 °C or 60 °C. After 28 days of UV aging, the shear strength of the RS and RA epoxy resin overlays decreased by 86.8% and 90.1%, respectively. Moreover, the UV aging led to a more significant impact on the shear performance of the epoxy resin overlay than thermal oxygen aging, and the RS epoxy resin overlay had superior UV aging resistance to RA epoxy resin overlay.

Overall, the epoxy resin ultra-thin wearing course overlay has excellent high-temperature performance and durability and can be used as a long-term, high-performance pavement

structure. In the future, in-depth research can be conducted on the anti-peeling performance of the epoxy resin ultra-thin wearing course overlay under different aging and temperature conditions in order to provide the design and construction of the epoxy resin ultra-thin wearing course overlay and compose a reference for cement concrete pavement engineering.

Author Contributions: Conceptualization, X.Z. and Y.C.; methodology, X.Z.; software, W.X.; validation, Z.Z., G.S. and X.Z.; formal analysis, Z.Z.; investigation, X.Z.; resources, Y.C.; data curation, Z.Z.; writing—original draft preparation, X.Z.; writing—review and editing, T.W.; visualization, Z.Z.; supervision, T.W.; project administration, T.W.; funding acquisition, X.Z. All authors have read and agreed to the published version of the manuscript.

Funding: The work described in this paper was supported by the Excellent Technical Leader Program of Shanghai Science and Technology Innovation Action Plan (21XD1434200); Shanghai Science and Technology Innovation Action Plan (21DZ1203300); and Scientific Research Project of Chengdu Xingcheng Investment Group Co., Ltd. (DXZX-20044).

Institutional Review Board Statement: Not applicable.

Informed Consent Statement: Not applicable.

Data Availability Statement: Not applicable.

Conflicts of Interest: The authors declare no conflict of interest.

References

1. Chan, S.; Lane, B.; Kazmierowski, T.; Lee, W. Pavement preservation: A solution for sustainability. *Transp. Res. Rec.* **2011**, *2235*, 36–42. [CrossRef]
2. Mahmoud, A.; Coleri, E.; Batti, J.; Covey, D. Development of a Field Torque Test to Evaluate In-Situ Tack Coat Performance. *Constr. Build. Mater.* **2017**, *135*, 377–385. [CrossRef]
3. Phares, B.M.; Dahlberg, J.M. *Polymer Concrete Overlay Evaluation: Tech Transfer (No. InTrans Project 13-463)*; Iowa State University, Institute for Transportation: Ames, IA, USA, 2016.
4. Editorial Department of China Journal of Highway and Transport. Review on China's Pavement Engineering Research·2020. *China J. Highw. Transp.* **2020**, *10*, 1–66. (In Chinese)
5. Fowler, D.W.; Whitney, D.W. *Long-Term Performance of Polymer Concrete for Bridge Decks. Nchrp Synthesis of Highway Practice*; National Academies Press: Washington, DC, USA, 2012.
6. Sprinkel, M. *Twenty-Five Year Experience with Polymer Concrete Bridge Deck Overlays*; Virginia Research Council: Charlottesville, VA, USA, 2003.
7. Hong, B.; Lu, G.; Gao, J.; Dong, S.; Wang, D. Green tunnel pavement: Polyurethane ultra-thin friction course and its performance characterization. *J. Clean. Prod.* **2020**, *289*, 125131. [CrossRef]
8. Deng, M.; Cao, X.; He, Z.; Wei, K.; Tang, B. Experimental and Molecular Dynamics Simulation Investigation on Filler Reinforcement for Property Enhancement of PU Composites. *Mech. Adv. Mater. Struct.* **2022**, *30*, 2780–2792. [CrossRef]
9. Deng, M.; Ding, Y.; He, Z.; Shan, B.; Cao, X.; Tang, B. Investigation on Performances and Nano-Adhesion Behavior of Ultra-Thin Wearing Course Using Polyurethane as Binder. *Constr. Build. Mater.* **2021**, *278*, 122349. [CrossRef]
10. Wu, D.; Han, Y.; Jin, X. Research on Key Technology of Anti-sliding Treatment of Resin Thin Layer of Bascule Bridge Steel Panel. In Proceedings of the 8th International Conference on Civil Engineering, Singapore, 11–14 March 2021; pp. 495–507.
11. Stenko, M.S.; Chawalwala, A.J. Thin Polysulfide Epoxy Bridge Deck Overlays. *Trans. Res. Rec.* **2001**, *1749*, 64–67. [CrossRef]
12. Horn, M.; Stewart, C.F. (Eds.) *Field Evaluation of Concrete Polymerization as a Bridge Deck Seal*; Final Report, No. CA-DOT-ST4174-1-74-4; Transportation Research Board: Washington, DC, USA, 1974.
13. Attanayake, U.; Mazumder, A.F. Performance-Based Approach for Deciding the Age of New Concrete for Thin Epoxy Overlay Application. *Transp. Res. Rec.* **2021**, *2675*, 1055–1068. [CrossRef]
14. Freeseman, K.; Wang, K.; Tan, Y. Bond Strength and Chloride Resistance of Epoxy and Concrete Overlays on Bridge Decks. *Int. J. Pavement Eng.* **2022**, *23*, 916–921. [CrossRef]
15. Kayan, A. Recent Studies on Single Site Metal Alkoxide Complexes as Catalysts for Ring Opening Polymerization of Cyclic Compounds. *Catal. Surv. Asia* **2020**, *24*, 87–103. [CrossRef]
16. Cong, P.L.; Chen, S.F.; Yu, J.Y.; Chen, H.X. Compatibility and Mechanical Properties of Epoxy Resin Modified Asphalt Binders. *Inter. J. Pav. Res. Technol.* **2011**, *4*, 118–123. (In Chinese)
17. Parvizi, A.; Garrett, K.W.; Bailey, J.E. Constrained Cracking in Glass Fibre-Reinforced Epoxy Cross-Ply Laminates. *J. Mater. Sci.* **1978**, *13*, 195–201. [CrossRef]
18. Liu, S.X.; Xu, Z.Q.; Zhao, F.C.; Jiang, A.F.; Li, H.; Yang, H.M.; Chen, J.H. Research progress on aging and anti-aging of epoxy resin materials. *Equip. Environ. Eng.* **2023**, *1*, 127–134. (In Chinese)

19. Zhang, D.J.; Liu, G.; Bao, J.W.; Tang, B.M.; Zhong, X.Y.; Chen, B.X. Environmental aging performance and mechanism of T700 carbon fiber reinforced epoxy resin matrix composites. *Acta Mater. Compos. Sin.* **2016**, *7*, 1390–1399. (In Chinese)
20. Yu, B.; Jiang, Z.; Yang, J. Long-Term Moisture Effects on the Interfacial Shear Strength between Surface Treated Carbon Fiber and Epoxy Matrix. *Compos. Part Appl. Sci. Manuf.* **2015**, *78*, 311–317. [CrossRef]
21. Niu, Y.F.; Yan, Y.; Yao, J.W. Hygrothermal Aging Mechanism of Carbon Fiber/Epoxy Resin Composites Based on Quantitative Characterization of Interface Structure. *Polym. Test.* **2021**, *94*, 107019. [CrossRef]
22. Zheng, Q.; Morgan, R.J. Synergistic Thermal-Moisture Damage Mechanisms of Epoxies and Their Carbon Fiber Composites. *J. Compos. Mater.* **1993**, *27*, 1465–1478. [CrossRef]
23. Wang, M.; Xu, X.; Ji, J.; Yang, Y.; Shen, J.; Ye, M. The Hygrothermal Aging Process and Mechanism of the Novolac Epoxy Resin. *Compos. Part B Eng.* **2016**, *107*, 1–8. [CrossRef]
24. Zhai, Z.; Feng, L.; Li, G.; Liu, Z.; Chang, X. The Anti-Ultraviolet Light (UV) Aging Property of Aluminium Particles/Epoxy Composite. *Prog. Org. Coat.* **2016**, *101*, 305–308. [CrossRef]
25. *JTG 3420-2020*; Testing Methods of Cement and Concrete for Highway Engineering. Research Institute of Highway Ministry of Transport: Beijing, China, 2020.
26. Wu, Y.H.; Xiao, P.; Wu, B.W.; Lou, K.; Shen, Q.C. Interlaminar Shear Resistance Test of Ultra-thin Wearing Layer Overlay Pavement. *China Sci.* **2022**, *7*, 739–745+758. (In Chinese)
27. Mohammad, L.N.; Bae, A.; Elseifi, M.A.; Button, J.; Patel, N. Effects of Pavement Surface Type and Sample Preparation Method on Tack Coat Interface Shear Strength. *Trans. Res. Rec.* **2010**, *2180*, 93–101. [CrossRef]
28. *AASHTO T 324-2019*; Standard Method of Test for Hamburg Wheel-Track Testing of Compacted Asphalt Mixtures. US-AASHTO: Washington, DC, USA, 2019.
29. Yang, L.Y.; Tan, Y.Q.; Dong, Y.M.; Li, E.G. Rutting Resistance Property of Warm Recycled Asphalt Mixture. *Appl. Mech. Mater.* **2012**, *204–208*, 3749–3753. [CrossRef]
30. Wang, W.-H.; Huang, C.-W. Establishing Indicators and an Analytic Method for Moisture Susceptibility and Rutting Resistance Evaluation Using a Hamburg Wheel Tracking Test. *Materials* **2020**, *13*, 3269. [CrossRef]

coatings

Article

Enhancing the Efficiency of Ice-Resistant Materials in Asphalt Road Surfaces: A Comprehensive Performance Analysis

Xijuan Zhao [1], Yemao Zhang [2,*] and Mulian Zheng [3]

[1] Institute of Industrial Economy and Innovation Management, Nanjing Institute of Technology, Nanjing 211167, China; njdjzxj@126.com
[2] School of Civil Engineering and Architecture, Nanjing Institute of Technology, Nanjing 211167, China
[3] Department of Highway and Railway Engineering, School of Highway, Chang'an University, Xi'an 710064, China; zhengml@chd.edu.cn
* Correspondence: zhangyemao158@163.com

Abstract: This study addresses the critical issue of traffic safety in winter, particularly focusing on the challenges posed by ice and snow on roads. Traditional methods of snow and ice removal are often labor-intensive, inefficient, and environmentally harmful. The objective is to develop a more effective solution for asphalt pavement deicing. Inspired by the anti-icing coating technology used in high-voltage conductors, this research develops an ice-suppressing material designed to reduce the adhesion between snow, ice, and pavement surfaces. The material's performance is evaluated in terms of deicing efficiency, durability, adhesive properties, and its impact on pavement performance. Test results demonstrate that the developed ice-suppressing material significantly reduces the adhesion between the ice layer and the pavement, facilitating easier removal. This study concludes that the developed ice-suppressing material significantly enhances deicing efficiency on asphalt pavements. It exhibits strong hydrophobic properties, as evidenced by increased water droplet contact angles on coated surfaces (99.5° to 83.3°) compared to clean glass slides (39.2° to 29°). This hydrophobicity effectively reduces ice adhesion, decreasing tensile and shear strength of the ice layer by 38.2% and 63.6%, respectively. Additionally, the material demonstrates superior ice-melting capabilities in sub-zero temperatures, with coated ice cubes showing a higher mass reduction rate than uncoated ones. Importantly, its slow-release nature ensures sustained deicing performance over multiple cycles, maintaining effectiveness after seven test cycles. This study introduces an innovative ice-suppressing material that not only improves the efficiency and environmental impact of deicing methods but also contributes to enhancing road safety in winter conditions. The material's novel composition and sustained effectiveness present a significant advancement in the field of winter road maintenance.

Keywords: ice-suppressing materials; mix design; deicing performance; durable performance

1. Introduction

Snow and ice on road pavements are common in most regions of China during winter. These conditions significantly reduce the road surface's adhesion coefficient and skid resistance, leading to decreased vehicle speed, extended travel times, increased fuel consumption, and even traffic accidents [1]. Furthermore, traffic issues caused by icy road conditions are a global concern [2]. Consequently, snow and ice melting have become integral components of winter road maintenance, carrying substantial economic and societal benefits [3]. Consequently, many nations prioritize the treatment of road snow and ice and have conducted extensive research. The literature has explored various solutions, including manual and mechanical removal, snow melting agent application, heated pavement systems, conductive concrete, freezing inhibition pavement technology, and ice-suppressing and coating technologies [4,5].

Ice-suppressing materials, which can lower the freezing point through embedded melting agents or isolate the ice layer from the road surface using hydrophobic materials, have

emerged as effective solutions. These materials are applied to asphalt pavements through manual brushing or mechanical spraying [6]. When rain or snow falls, the ice-melting- and snow-removing materials on the carrier are released to melt snow and ice. Simultaneously, hydrophobic materials within the ice-suppressing material isolate the ice layer from the pavement, effectively reducing adhesion and facilitating easy removal. Compared to traditional deicing methods, ice-suppressing and coating technologies offer several advantages, including active ice and snow melting, excellent environmental performance, efficient and long-lasting deicing, and preventive capabilities [7].

Hydrophobic ice-suppressing technology originally found its application in the treatment of icing on high-voltage transmission lines [1]. This involved the application of a superhydrophobic nano-deicing coating material on the conductors, effectively reducing ice formation on the transmission lines. In the field of road science and technology, efforts have been made to develop anti-icing and thin-ice removal coatings using hydrophobic deicing technology for high-voltage transmission lines [8].

Ma et al. conducted a study on the anti-icing performance of asphalt pavement using hydrophobic surface and thin-ice removal pavement coating technology. They developed a coating technology with hydrophobic properties, inspired by the deicing mechanism employed for high-voltage conductors [9,10]. This technology involves the creation of a hydrophobic film on the asphalt pavement surface, which isolates the ice layer. However, this approach does not rely on self-melting capabilities. While some preliminary test sections were conducted, there is a lack of comprehensive documentation of the construction process, technology, and specialized construction machinery and equipment.

The concept of an environmentally friendly asphalt pavement snow and ice-melting coating technology was initially proposed by Yang [11]. This eco-friendly technology offers hydrophobic properties that reduce adhesion between the ice layer and the pavement. It also provides slow-release snow melting and deicing capabilities. Although the coating's performance has been studied, there is a lack of construction technical indicators, requirements, and specific construction tools and machinery tailored to the coating's features [12].

Several scholars have examined ice-suppressing materials and explored construction technologies based on the principles of ice and snow melting and ice suppression [4,13]. An anti-freeze ice-suppressing material for asphalt pavement was developed by adding a suitable amount of slow-release anti-icing agent (Mafilon) to emulsified asphalt. Tests were conducted to evaluate deicing effectiveness and conductivity at various Mafilon contents, including an experiment to determine the optimal spraying thickness of the ice-suppressing material. Siegmund Werner et al. used porous adsorption materials to absorb self-melting snow additives, achieving long-term snow melting through slow-release mechanisms [14]. Kaemereit Wilhelm et al. successfully prepared 0.5~1 mm granular self-melting snow additive material by utilizing cement as a carrier material through cement solidification [15]. The V-260 snow melting agent developed by Verglimit Company in Switzerland consists of calcium chloride-coated hydrophobic material and is widely used today [16].

In Japanese self-snow melting technology, porous zeolite is used as an absorbent to adsorb salt, which is then added to asphalt mixtures in powder form to replace fine aggregate or mineral powder. This approach achieves snow melting and ice removal through salt release [17–19]. China first introduced imported self-snow melting technology and materials around 2000. In recent years, many domestic road researchers have embarked on the study of self-snow melting technology [20]. Zhou et al. adopted Japanese snow melting technology to research and develop self-snow melting additives [21].

Ma et al. have researched and developed the granular snow melting admixture Iceguard, known for its slow-release- and non-corrosive properties. It is considered safe and environmentally friendly for the metal components of bridges and road structures [5]. Shan et al. conducted studies measuring pavement wettability after applying a hydrophobic coating, changes in stone absorption rates, and the length and density of cracks in the ice layer following the impact of a steel ball [22]. Zheng et al. conducted an analysis and

evaluation of the deicing coating's performance from various perspectives, including anti-ice and snow performance, durability of the coating materials, and impact on pavement skid resistance [23]. Wu et al. developed a regression model for long-term snow melting performance and provided a calculation formula for determining the precipitation amount of additives on self-melting asphalt pavement in different regions of the country [24]. The long-term snow melting performance of asphalt mixtures with Iceguard was evaluated through comparisons with foreign products and testing roads, complemented by rapid dissolution tests to determine Iceguard's service life [25,26].

Through research and the application of ice-suppressing materials both in China and abroad, it becomes evident that current ice-suppressing material technologies are in their initial and exploratory stages. A comprehensive set of technical evaluation indicators and quality control standards for ice-suppressing materials has yet to be established, and ongoing project applications remain in the testing phase [27,28].

The ice-suppressing material developed in this study exhibits several key characteristics: active deicing, no adverse impact on roads, bridges, ancillary facilities, and vegetation, preventive pavement maintenance, and continuous winter deicing. This presents a novel approach to road deicing. The composition design method for the ice-suppressing material is proposed, and considering the material's unique characteristics, a performance evaluation methodology is introduced. This evaluation serves as a theoretical foundation for the widespread adoption of asphalt pavement ice-suppressing materials.

2. Materials and Methods

2.1. Deicing Performance Test Methods of Ice-Suppressing Materials

One crucial functional aspect of ice-suppressing materials is their deicing effectiveness. Anti-freezing/anti-icing tests, hydrophobic property assessments, adhesion property examinations, and ice-melting property tests are employed to assess the deicing performance of these materials.

2.1.1. Anti-Icing Test Method

This paper utilizes the kinetic energy generated by the free fall of a steel ball to simulate the force required for ice removal from the road surface equivalently. The magnitude of the adhesion force between the ice and the road surface is determined by the cracking of the ice layer, as illustrated in Figure 1, depicting the test principle.

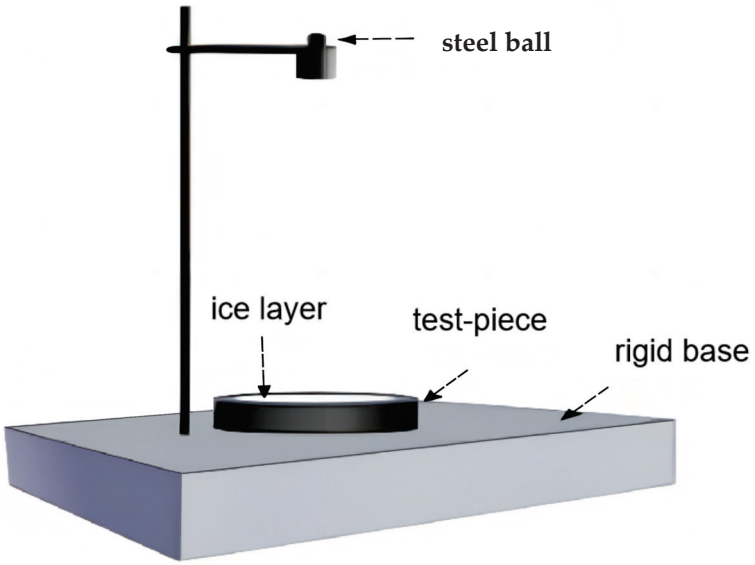

Figure 1. Principle diagram of falling ball impact test.

A qualitative method was used to observe the cracking and breaking condition of the ice surface to evaluate the anti-icing effect as shown in Table 1.

Table 1. Anti-icing effect evaluation method.

Anti-Icing Effect	Ice Surface Condition
Excellent	Significant breakage and peeling on the ice surface
Good	Small amount of breakage and cracks on the ice surface
Medium	Only a few cracks on the ice surface
Bad	The only marks on the ice surface are from the impact of the steel ball

To enhance the precision of assessing the anti-icing effect of the ice-suppressing material, the breakage rate index is introduced by drawing on the pavement structure layer damage evaluation index. The calculation formula for the breakage rate is depicted in Equation (1) [29].

$$B_R = \frac{B_A + \lambda L}{A} \quad (1)$$

where

B_R—breakage rate, expressed in percentage, %.
B_A—Total area of crushing and cracking, cm^2.
L—extended single crack length, cm.
λ—Influence factor for converting single cracks to area, generally taken as 0.3.
A—Total area of the test, cm^2.

2.1.2. Hydrophobic Performance Test Method

The hydrophobic performance of ice-suppressing materials plays a crucial role in the deicing effectiveness of asphalt pavement. Therefore, evaluating the hydrophobic performance after application is essential. Hydrophobic performance is typically assessed by measuring the contact angle (θ). It is generally considered that when $\theta > 90^\circ$, the material is hydrophobic, while $\theta < 90^\circ$ indicates hydrophilic properties. A larger contact angle (θ) signifies superior hydrophobic performance. Currently, methods for measuring the contact angle include angle measurement, height measurement, force measurement, droplet image analysis, and transmission methods, among others [29].

With advancements in image processing technology, the droplet image analysis method offers higher accuracy and simplifies the measurement process. In this study, the contact angle is calculated using the droplet image analysis fitting method [30]. The following steps are involved:

Droplet edge acquisition methods can be categorized into automatic image processing and manual image processing. Each method has its own advantages and disadvantages. Automatic image processing offers fast acquisition but requires further research to enhance its resistance to interference. Manual processing, on the other hand, exhibits strong interference resistance but involves a significant workload. The contact angle can be calculated using methods such as the tangent method, circle fitting method, ellipse fitting method, Young–Laplace method, and polynomial fitting method.

Based on the aforementioned theory and methodology, the contact angle is determined by creating ice-suppressing material samples. A high-resolution digital camera is used to capture droplet morphology, and Image-Pro Plus or CAD image processing software (version 2.8) is employed for analysis. The specific steps are outlined as follows:

Preparation of ice-suppressing material samples.

Application of the prepared material sample onto glass slides or microscope slides, followed by curing at room temperature.

Spraying droplets onto the surface of the glass slides coated with the cured deicing material.

Recording and photographing the process of droplet morphology change using a high-resolution digital camera positioned perpendicular to the slide's plane.

The contact angle is then plotted and calculated using image processing software.

2.1.3. Adhesion Performance Test Method

The force per unit area required to bond the bonding material is referred to as bond strength. Common methods for measuring bond strength include the three-point bending test, shear strength test, and tensile strength test. The primary purpose of the tensile and shear tests is to quantitatively assess the adhesion between the ice-suppressing material sprayed on the specimens and the ice cubes. To clearly reveal the deicing capability of the coated ice-suppressing material test specimens, comparative tests were conducted between the spraying group and the control group.

Two cylindrical specimens of asphalt mixture were prepared, securely fixed, and filled with water in the middle. Subsequently, they were placed in a freezer and frozen under conditions simulating real-world scenarios. The test temperature was set at −30 °C, and the freezing duration was 12 h. Afterward, the test specimens were removed from the freezer, and both tensile and shear tests were immediately conducted using a 100 KN universal testing machine. The principles of the tensile and shear tests are illustrated in Figures 2 and 3, respectively.

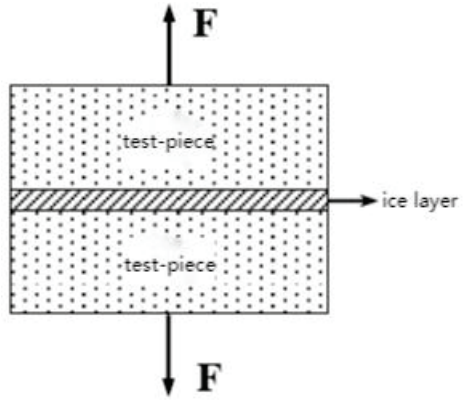

Figure 2. Tensile test schematic.

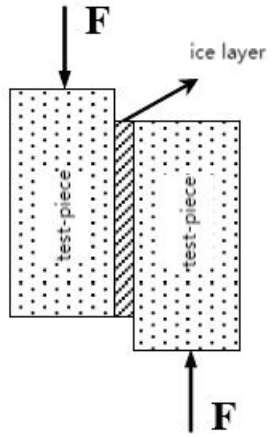

Figure 3. Shear test schematic.

2.2. Design of the Composition of the Ice-Suppressing Material

To enhance the deicing capabilities of the pavement without compromising its skid resistance, a systematic experimental study was undertaken to formulate an ice-suppressing material characterized by long-lasting- and slow-release properties. The ultimate composition of the ice-suppressing material comprises three key components: film-forming component A, adhesive component B, and ice suppression component C.

2.2.1. Modified Ice Suppression Component C Composition Design

In accordance with the design of the ice suppression function within the ice-suppressing material, component C should incorporate the freezing point inhibitor C1, which necessitates a porous adsorption carrier C2 for adsorption. Therefore, the ice-suppressing material includes the porous adsorption carrier C2. To prevent the ice-suppressing material from altering the road surface's color, a small amount of carbon black component C3 is added to enhance the color of the ice-suppressing material powder. The ice suppression component powder is adjusted using a modified coupling agent C4 to enhance its dispersibility [31].

The adsorption capacity of the porous adsorption carrier material C2 for the freezing point inhibitor C1 can be quantitatively expressed by the mass change before and after adsorption, referred to as the adsorption rate. The specific test procedure is as follows: weigh the porous adsorption carrier material C2 with a mass of m_0 (accurate to 0.01 g) after drying. Subsequently, immerse it in a pre-prepared saturated solution of the ice point inhibitor C1 and remove it after 24 h. Weigh the mass m1 after drying in a low-temperature drying oven at 110 °C, and calculate the adsorption rate of the porous adsorption carrier material using the Formula (2).

$$S_a = \frac{m_1 - m_0}{m_0} \tag{2}$$

where

m_1 is the mass of the material after immersion.
m_0 is the mass of the material before immersion.
S_a is the adsorption rate of the porous adsorption carrier material.

The optimal ratio of freezing point inhibitor C1 to porous adsorption carrier C2 can be determined using the adsorption rate test method described above. The test results are presented in Table 2.

Table 2. Adsorption performance test results.

Time (h)	Mass of the Material before Immersion m_0 (g)	Mass of the Material after Immersion m_1 (g)	Adsorption Rate (%)
2	100	122.21	22.21
4	100	134.31	34.31
6	100	144.33	44.33
8	100	149.42	49.42
10	100	152.17	52.17
12	100	153.32	53.32
14	100	154.02	54.02
16	100	154.33	54.33
18	100	154.45	54.45
20	100	154.45	54.45
22	100	154.45	54.45
24	100	154.45	54.45

It can be observed from Table 2 that the adsorption rate of the porous adsorption carrier increases over time, and the rate of increase becomes gradual. After 18 h, the adsorption rate of the porous adsorption carrier material reaches a plateau and stabilizes, indicating that the porous adsorption carrier has reached saturation. Consequently, it can be concluded that the mass ratio of the porous adsorption carrier C2 to the freezing point inhibitor C1 is C2:C1 = 100:54. The proportions of carbon black C3 and modified silane coupling agent C4 in the composite freezing point inhibitor C1 and porous adsorption carrier C2 can be determined based on practical experience and adsorption performance tests, as presented in Table 3.

Table 3. Modified ice suppression component C composition ratio.

Ingredients	Proportion of Each Component (%)
Complex freezing point inhibitor C1	54
Porous adsorption carrier C2	100
Carbon black C3	2.5
Modified silane coupling agent C4	1.6

2.2.2. Composition Design of Film-Forming Component A

In accordance with the hydrophobic function design of the ice-suppressing material, the composition of the film-forming component A should include the hydrophobic road bonding material, silicone-rubber lotion A1, along with various additives and fillers. These include a reinforcing agent A2, filler A3, film-forming agent A4, plasticizer A5, catalyst A6, leveling agent A7, defoamer A8, diluent water A9, and anti-skid material quartz sand A10. The additives serve to promote the plastic flow and elastic deformation of silicone rubber lotion, enhancing its bonding performance and facilitating effective film-forming. Fillers play a role in reinforcing silicone rubber and improving its tensile strength.

The ratio of silicone rubber lotion A1 to diluent water was analyzed through hydrophobic and adhesive tests. Multiple portions of organic silicone rubber lotion with a mass of 100 g and a solid content ranging from 20% to 60% were weighed. The organic silicone rubber lotion was then mixed with diluent water A9 in proportions ranging from 20 g to 300 g, respectively. Subsequently, hydrophobic property tests and adhesion property tests were conducted. The contact angle was measured using the height method, while tensile and shear forces were measured using a UTM machine. The results of these tests are presented in Table 4.

Table 4. Hydrophobic and adhesion test results.

Silicone Rubber Emulsion (g)	Diluent (g)	Contact Angle (°)	Hydrophobic Grade	Tensile Force (N)	Shear Force (N)
100	20	90.2	HC1	1644	10,506
100	60	96.3	HC1	1478	8056
100	100	102	HC1	1354	6537
100	140	108.5	HC1	1259	5245
100	180	112.1	HC1	1215	4165
100	220	109.3	HC1	1242	5148
100	260	107.4	HC1	1340	6449
100	300	98.2	HC1	1537	8730

According to the results of the hydrophobic and adhesion tests presented in Table 4, it is observed that the contact angle in the hydrophobic test initially increases and then decreases with an increase in the quality of the diluent. Conversely, the tensile force and shear force in the adhesion test exhibit a decreasing trend followed by an increase as the quality of the diluent increases. These trends suggest that as the quality of the diluent gradually increases, the hydrophobicity of the ice-suppressing material first increases and then decreases, while the adhesion property decreases initially and then increases. The optimal performance is achieved when the contact angle is at its maximum, and the tensile force and shear force are at their minimum, which occurs when the mass of the diluent is 180 g. At this point, the ice-suppressing material exhibits the best anti-icing performance. Simultaneously, the ideal ratio of silicone rubber lotion A1 to diluent A9 is A1:A9 = 100:180. Based on practical experience, hydrophobic property tests, and adhesive property tests, as summarized in Table 5, it is possible to determine the optimal ratio of each component in the film-forming component.

Table 5. Composition ratio of film-forming component A.

Ingredients	Proportion of Each Component (%)
Silicone rubber emulsion A1 with a solid content of 20%~60%	100.0
Reinforcing agent A2	4.0
Packing A3	3.0
Film-forming agent A4	4.0
Plasticizer A5	4.2
Catalyst A6	1.7
Levelling agent A7	3.0
Defoamer A8	0.3
Diluent A9	180.0
Anti-slip quartz sand A10	3.0

2.2.3. Adhesive Component B Composition Design

The role of the adhesive component is to accelerate the reaction speed between the components of the ice-suppressing material and speed up the time of opening traffic. The adhesive component is composed of cross-linking agent B1 and coupling agent B2. Based on actual experience, the proportion of the components of the cross-linking agent and coupling agent is usually taken as shown in Table 6.

Table 6. Composition ratio of gluing component B.

Ingredients	Proportion of Each Component (%)
Cross-linking agent B1	29
Coupling agent B2	71

2.2.4. Ice-Suppressing Material A, B, C Composition Ratio

(1) Determination of the mass ratio of component B

Prepare components A and C according to the optimum composition of each component determined in advance for components A and C. The preparation principle involves dispersing component C evenly into component A to prevent agglomeration. The A:C mass ratio is 100:2. Component C should be slowly poured into component A to create the mixture of components A and C according to this specified ratio. Then, various quantities of component B are added to the previously prepared mixture of components A and C to create the ice-suppressing material. Under conditions where the spraying temperature is 5 °C, and the spraying rate of the ice-suppressing material is 0.5 kg/m^2, Marshall test specimens are fabricated according to the anti-icing test method.

The three components of the ice-suppressing material will undergo a curing reaction after mixing. The curing time of the ice-suppressing material includes two phases: the curing time in the spraying equipment and the interval of time from when the ice-suppressing material is sprayed on the road to when it completely solidifies. The curing time of the ice-suppressing material in the spraying equipment is referred to as the pre-curing time, while the time from when the ice-suppressing material is sprayed onto the road surface until it completely solidifies is termed the post-curing time. The post-curing time of the Marshall test specimens was measured, and the "falling ball impact test" was conducted. The test results are presented in Table 7.

Table 7. Falling ball impact test results.

(A + C) Component Mass (g)	Mass of Component B (g)	Post-Curing Time (h)	Breakage Rate (%)
100	0.5	7.2	17.9
100	1.0	5.3	17.8
100	1.5	3.8	17.7
100	2.0	3.1	17.6
100	2.5	2.5	15.5
100	3.0	1.7	12.4
100	3.5	0.6	9.9
100	4.0	0.2	6.2

Table 7 reveals that the post-curing time of the test specimen gradually decreases with an increase in the mass of component B, and the damage rate of the test specimen decreases as well. When component B is less than 2 g, the damage rate decreases slowly, but when component B exceeds 2 g, the damage rate decreases significantly. This suggests that when component B exceeds 2 g, the deicing performance is noticeably reduced. Taking into account both the deicing performance of the ice-suppressing material and its impact on traffic due to post-curing time, the mass of component B should be 2 g, and the mass ratio of (A + C):B should be 100:2.

(2) Determination of the mass ratio of component A and C

Under the condition of a mass ratio of (A + C):B = 100:2, different proportions of components A and C were used to formulate the ice-suppressing material. The results of the "falling ball impact test" and bonding performance test, conducted in accordance with the anti-icing test method, are presented in Table 8. From the results in Table 8, it is evident that as the mass of component C gradually increases, the breakage rate also increases progressively. The rate of increase levels off when component C exceeds 3 g. Additionally, the tensile force and bonding force gradually decrease with an increase in the mass of component C, and the rate of reduction levels off as well. Therefore, it is recommended that the mass ratio of component A and C be set at 97:3 to fully address the deicing performance of the ice-suppressing material.

Table 8. Falling ball impact test and bonding performance test.

Mass of Component A (g)	Mass of Component C (g)	Mass of Component B (g)	Breakage Rate (%)	Tensile Force (N)	Shear Force (N)
99.5	0.5	2.0	5.8	1753	10,513
99.0	1.0	2.0	9.8	1629	9238
98.5	1.5	2.0	12.9	1537	8295
98.0	2.0	2.0	15.4	1454	7450
97.5	2.5	2.0	17.4	1379	6697
97.0	3.0	2.0	18.2	1304	6148
96.5	3.5	2.0	18.4	1237	5685
96.0	4.0	2.0	18.6	1181	5282
95.5	4.5	2.0	18.7	1151	4906
95.0	5.0	2.0	18.7	1129	4549
94.5	5.5	2.0	18.7	1110	4275
94.0	6.0	2.0	18.7	1095	4034

In summary, the mass ratio of components A, B, and C is determined as follows: m_A:m_B:m_C = 97:2:3.

3. Results and Discussion

3.1. Analysis of Anti-Icing Test Results

Two sets of Marshall specimens and rutting plate specimens were prepared using AC-13 grade asphalt mixture with an asphalt-aggregate ratio of 5.0%. One set of Marshall

specimens and rutting plate specimens were subjected to a spraying treatment with an ice-suppressing material at a rate of 0.5 kg/m^2, while the other set of Marshall specimens and rutting plate specimens were left untreated. The testing procedures followed the anti-icing test protocol, including the falling ball impact test. Figures 4 and 5 illustrate the Marshall specimens after the falling ball impact test and the gravity knockdown test, respectively. Figure 6 depicts the rutting plate specimens following the falling ball test.

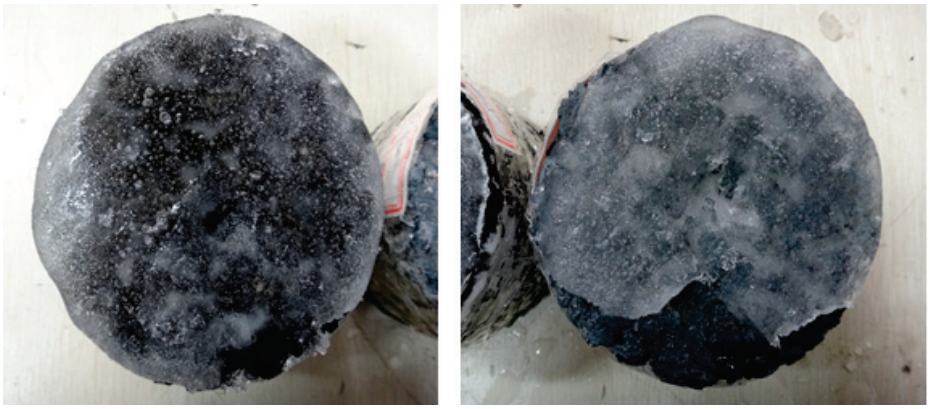

Unsprayed Sprayed

Figure 4. Marshall specimens after falling ball impact test.

Sprayed group specimen Unsprayed group specimen

Figure 5. Marshall specimens after gravity knockdown test.

Without spraying group specimen Sprayed group specimen

Figure 6. Rutting plate specimens after falling ball impact.

From Figure 4, it can be deduced that the surface of the Marshall specimen in the contrast group (left) displays only steel ball impact marks and pits. In contrast, the surface of the Marshall specimen in the spraying group (right) exhibits clear fracture boundaries, and there is no residual ice adhesion in the fractured areas. This qualitative assessment

suggests that the ice-suppressing substance has a superior anti-icing effect. The calculated ice broken area is 12.72 cm^2, determined through indoor measurements of the Marshall specimen in the spraying group, resulting in a calculated breakage rate of 16.2%.

Figure 5 demonstrates that the ice layer on the surface of the sprayed Marshall specimen can be completely removed by gravity, leaving no residual dark ice on the specimen's surface. Conversely, the Marshall specimen in the contrast group (unsprayed) exhibits substantial dark ice, indicating a higher adhesion between the ice layer and the specimen in the contrast group compared to the spraying group.

Regarding the falling ball impact test of the rutting plate specimen shown in Figure 6, it can be inferred that the ice layer on the rutting plate specimen in the contrast group partially detaches in a small area after impact, with most of the ice layer remaining attached to the specimen. In contrast, the rutting plate specimen sprayed with the ice-suppressing material experiences a significant detachment of the ice layer over a large area, with no dark ice remaining on the rutting plate after the fall. This suggests that the ice-suppressing material effectively isolates the ice layer from the specimen, and the ice layer on the specimen treated with the ice-suppressing material is easily removed.

3.2. Analysis of Hydrophobic Performance Test Results

In accordance with the test procedure of the droplet image analysis method, water droplets were placed on the surfaces of both uncoated glass slides and glass slides coated with the ice-suppressing material. Photographs were taken at various time intervals (5 s, 30 s, 2 min, 4 min, 6 min, 8 min, 10 min, 12 min, 14 min, 16 min, 18 min, 20 min). The comparison of static contact angles from the test results is presented in Figure 7. In each image, the droplets on the left side are on regular glass slides (contrast group), and those on the right side are on slides coated with the ice-suppressing material (spraying group). The change in droplet contact angles over time is illustrated in Figure 8.

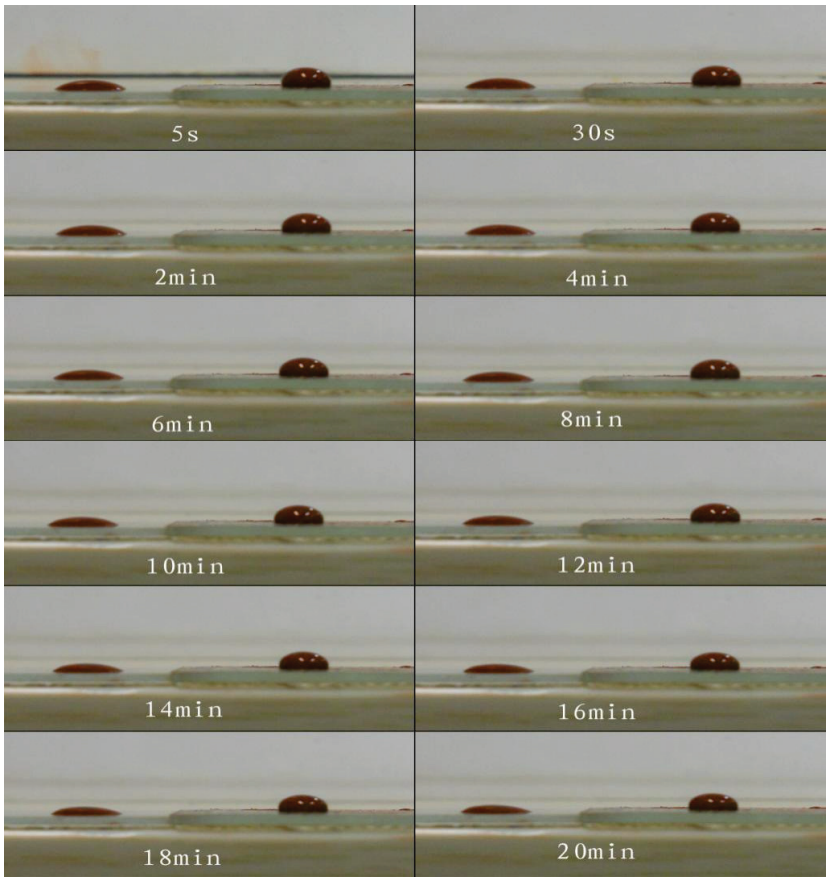

Figure 7. Real-time image of liquid drop contact angle.

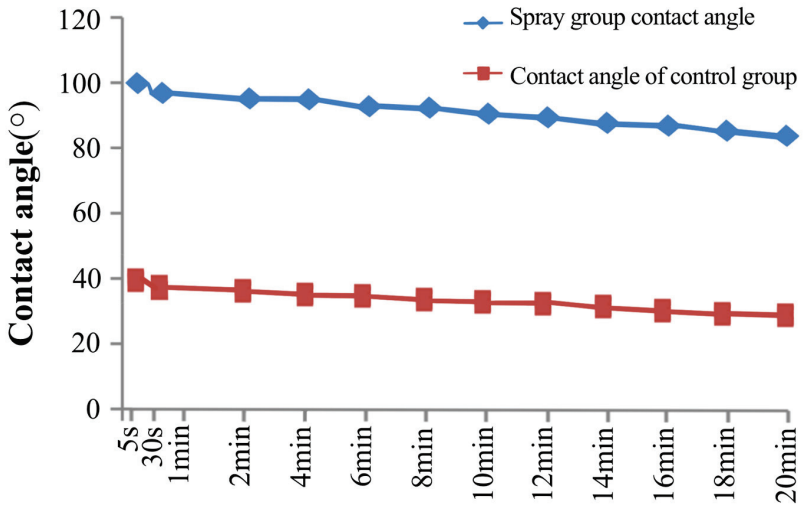

Figure 8. Plot of droplet contact angle over time.

Figure 8 demonstrates the temporal evolution of droplet contact angles. The contact angle gradually decreases as time progresses, primarily due to water droplet evaporation and the gradual spreading of droplets on the slide's surface. To minimize errors and obtain more accurate contact angle measurements, it is advisable to measure the contact angle as quickly as possible.

For droplets on slides coated with the ice-suppressing material, the contact angle was 99.5° at 5 s and gradually decreased to 83.3° at 20 min. In contrast, the contact angle for droplets on clean slides ranged from 39.2° to 29° over the same time period. A comparison of the data leads to the conclusion that the ice-suppressing material exhibits excellent hydrophobic properties and significantly reduces the adhesion between the ice layer and the road surface.

3.3. Analysis of Adhesion Performance Test Results

In accordance with the test methods and procedures for assessing adhesion performance, asphalt mixture specimens that were sprayed with ice-suppressing material and contrast asphalt mixture specimens that remained unsprayed were subjected to both tensile and shear tests. The interfaces between the ice layer and the specimens after the tensile and shear tests are visually depicted in Figures 9 and 10, while the results of these tests are presented in Figure 11.

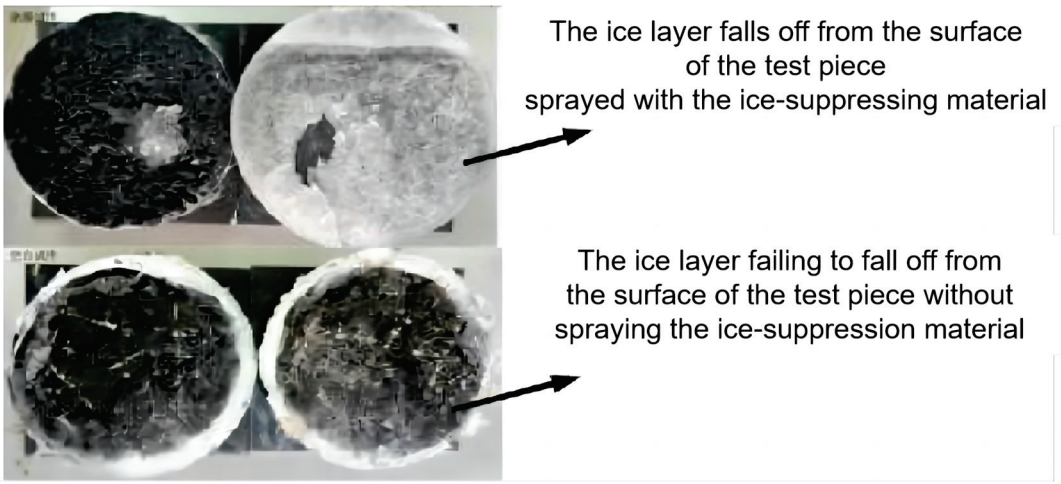

Figure 9. Ice–sample interface after tensile test damage.

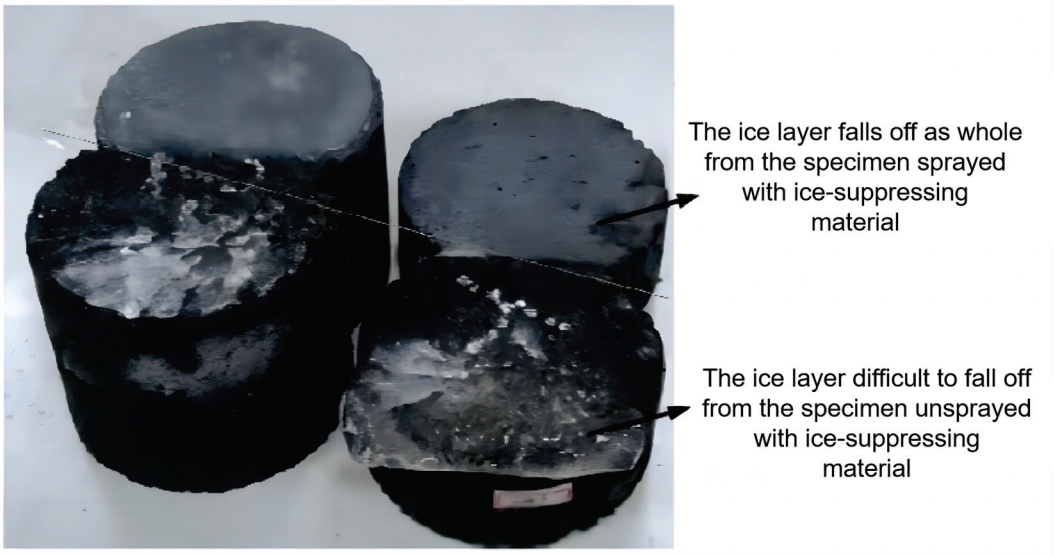

Figure 10. Ice–sample interface after shear test damage.

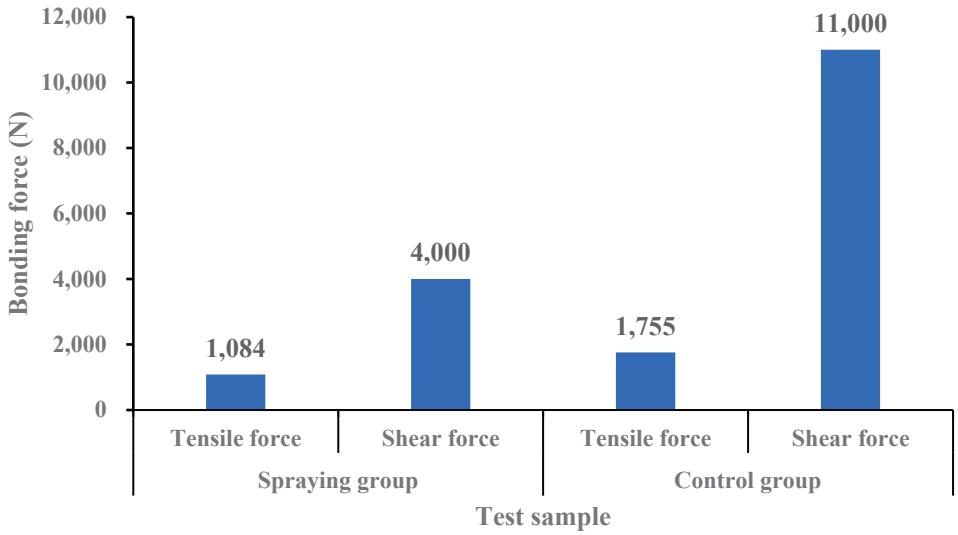

Figure 11. Test results of adhesion performance of specimens in spraying group and unsprayed contrast group.

The tensile test results presented in Figure 11 indicate that, in the case of the sprayed group specimen, the ice layer becomes detached from the specimen when the tensile force reaches 1084 N. Additionally, there is virtually no dark ice remaining on the specimen's surface, and the cross-section appears flat. This phenomenon is attributed to the chemical action of the freezing point inhibitor, which results in the interface's strength becoming weaker than that of the ice, leading to fracture at the interface.

In contrast, for the unsprayed contrast group specimen, the ice layer becomes detached from the specimen when the tensile force reaches 1755 N. In this case, the two specimens break from the middle of the ice layer, leaving a substantial amount of dark ice on the specimen's surface. The cross-section between the test piece and the ice layer exhibits a conical shape. The tensile force between the ice layer and the surface of the test piece, after being treated with the ice-suppressing material, is reduced by 38.2% compared to the untreated specimen. This lower tensile force indicates a weaker adhesive force between the ice-suppressing material test piece and the ice layer, making it easier to remove the ice layer.

The shear test results reveal that, when subjected to shear force, the sprayed group specimens detach from the ice layer when the shear force reaches 4000 N. Similar to the tensile test, there is minimal dark ice remaining on the specimen's surface, and the cross-section appears flat. In contrast, the unsprayed contrast group specimens detach from the ice layer under shear force reaching 11,000 N. In this case, the two specimens break from the middle of the ice layer, leaving a substantial amount of dark ice on the specimen's surface. The cross-section between the test piece and the ice layer exhibits a conical shape, similar to the results of the tensile test. After applying the ice-suppressing material, the shear force between the ice layer and the specimen's surface is reduced by 63.6%. A lower shear force is advantageous for crushing the ice layer under the wheel's pressure.

3.4. Ice-Melting Performance Test and Result Analysis

The effectiveness of the ice-suppressing material in melting ice is a crucial factor that influences the separation of the ice layer from the asphalt pavement. The ice-suppressing material works by melting the lower surface of the ice layer, leading to the separation of the ice layer from the asphalt pavement. To simulate the ice-melting performance of the ice-suppressing material on the ice layer, the following test method and procedure were employed.

Marshall test specimens were prepared for both the spraying group and the unsprayed contrast group. Each group had a total ice mass of 60 g, and the test was conducted at −30 °C, with the temperature increasing by 2 °C every hour. To minimize the temperature-induced changes in ice mass, the maximum temperature was limited to 0 °C. The results of the ice-melting performance test are presented in Table 9 and Figure 12.

Table 9. Ice-melting performance test results.

Temperature (°C)	Sprayed Group Ice Mass (g)	Unsprayed Group Ice Mass (g)
−30	60	60
−25	57	59
−20	51	57
−15	43	52
−10	32	45
−5	19	35
0	4	23

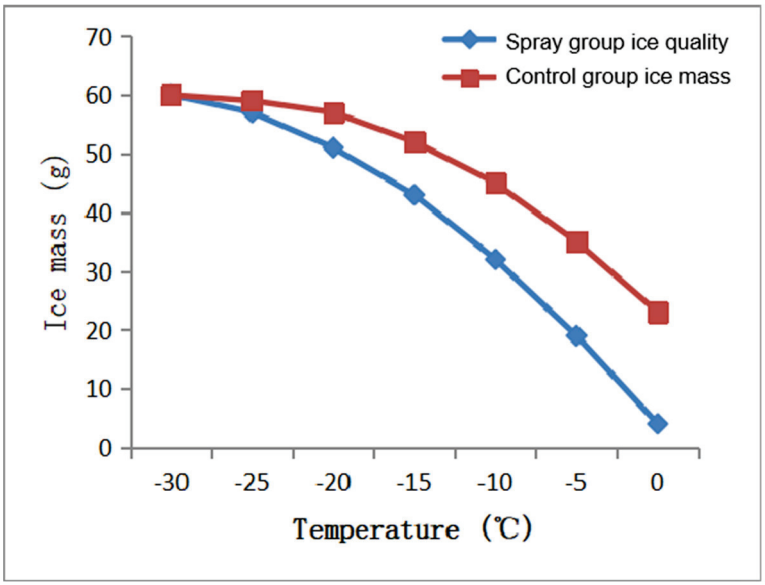

Figure 12. Ice-melting performance test results graph.

Figure 12 illustrates the relationship between temperature and the mass reduction in ice cubes. As the temperature increases, the mass of the ice cubes gradually decreases, and the rate of mass reduction steadily increases. Notably, at the same temperature, the mass reduction rate of the unsprayed group's ice cubes is significantly lower than that of the sprayed group's ice cubes. This observation, after accounting for the influence of temperature rise on the change in ice cube mass, suggests that the ice-suppressing material exhibits excellent ice-melting performance.

4. Conclusions

In consideration of the characteristics of the ice-suppressing material, a test method for evaluating its deicing performance was proposed, focusing on key technologies related to the material and the selection principles for its key component materials. Through the evaluation of the deicing performance method, the composition proportions of each component in the ice-suppressing material were determined. A comprehensive study and analysis of its performance was conducted, with a particular focus on its deicing capabilities and durability. The primary conclusions drawn from this research are as follows:

(1) In consideration of the characteristics of the ice-suppressing material, an evaluation method for assessing its deicing performance was proposed. The material's hydrophobicity was assessed by measuring the contact angle using the droplet image analysis method. Tensile and shear tests were employed to evaluate the material's adhesion to the ice layer.

(2) According to the characteristics of the ice-suppressing material, the proposed evaluation method for the deicing performance is used to design the components of the ice-suppressing material. Through analysis, the mass ratio of component A, component B, and component C is m_A:m_B:m_C = 97:2:3.

(3) The ice-suppressing material demonstrates an effective isolation effect between the ice layer and the test specimen, leading to easy detachment of the ice layer from the test specimen when the material is applied.

(4) The contact angle of water droplets on glass slides coated with the ice-suppressing material (θ) exhibits a variation ranging from 99.5° to 83.3°, while the contact angle of water droplets on clean glass slides ranges from 39.2° to 29°. A larger contact angle indicates stronger hydrophobicity, thereby signifying enhanced hydrophobic properties of the ice-suppressing material.

(5) The tensile strength of the ice layer and the coated ice-suppressing material specimen has decreased by 38.2%, and the shear strength has reduced by 63.6% compared to the uncoated ice-suppressing material specimen. This reduction suggests that the ice-suppressing material effectively diminishes the adhesion between the ice layer and the specimen, facilitating easier detachment of the ice layer.

(6) Under external conditions with temperatures below 0 °C, the mass reduction rate of ice cubes in the uncoated group is significantly lower than that of ice cubes in the coated group. After accounting for the influence of temperature on the change in ice cube mass, this observation confirms the excellent ice-melting performance of the ice-suppressing material.

Author Contributions: Conceptualization, Y.Z.; methodology, Y.Z.; software, Y.Z.; validation, M.Z.; formal analysis, M.Z.; investigation, X.Z.; resources, M.Z.; data curation, X.Z.; writing—original draft preparation, X.Z.; writing—review and editing, X.Z.; visualization, X.Z.; supervision, X.Z.; project administration, M.Z.; funding acquisition, M.Z. All authors have read and agreed to the published version of the manuscript.

Funding: This research was funded by and the project was supported by the introduction of talents and scientific research start-up Fund of Nanjing Institute of Technology, grant number No. YKJ201834 and the project was supported by the Open Research Fund of NJIT Institute of Industrial Economy and Innovation Management (No. JGKA202204).

Institutional Review Board Statement: Not applicable.

Informed Consent Statement: Not applicable.

Data Availability Statement: No new data was created.

Conflicts of Interest: The authors declare no conflicts of interest.

References

1. Shen, F.; Wei, G.; Pang, R.; Liu, F.; Fang, S. Performance Evaluation of a Hydrophobically Modified Anti-Slide and Anti-icing Coating. *IOP Conf. Ser. Mater. Sci. Eng.* **2019**, *688*, 033004. [CrossRef]
2. Wang, T.; Dra, Y.A.S.S.; Cai, X.; Cheng, Z.; Zhang, D.; Lin, Y.; Yu, H. Advanced cold patching materials (CPMs) for asphalt pavement pothole rehabilitation: State of the art. *J. Clean. Prod.* **2022**, *366*, 133001. [CrossRef]
3. Pytka, J. Determination of snow stresses under vehicle loads. *Cold Reg. Sci. Technol.* **2010**, *60*, 137–145. [CrossRef]
4. Xu, S.; Zhou, Z.; Feng, L.; Cui, N.; Xie, N. Durability of pavement materials with exposure to various anti-icing strategies. *Processes* **2021**, *9*, 291. [CrossRef]
5. Ma, T.; Geng, L.; Ding, X.; Zhang, D.; Huang, X. Experimental study of deicing asphalt mixture with anti-icing additives. *Constr. Build. Mater.* **2016**, *127*, 653–662. [CrossRef]
6. Huang, K.; Liu, J.; Wang, J.; Shi, X. Characterization and Mechanism of a New Superhydrophobic Deicing Coating Used for Road Pavement. *Crystals* **2021**, *11*, 1304. [CrossRef]
7. Pei, Z.; Yi, J.; Li, Y.; Cheng, P.; Zhu, Y.; Feng, D. Material design and performance analysis of the anti-ice and antiskid wear layer on pavement. *Constr. Build. Mater.* **2021**, *282*, 122734. [CrossRef]
8. Yang, M. Research on Application Technology of Self Melting Ice Fine Surface Treatment. In *Hydraulic and Civil Engineering Technology VI: Proceedings of the 6th International Technical Conference on Frontiers of HCET 2021*; IOS Press: Amsterdam, The Netherlands, 2021; p. 348.
9. Jiang, X.; Gabrielson, J.; Titi, H.; Huang, B.; Bai, Y.; Polaczyk, P.; Hu, W.; Zhang, M.; Xiao, R. Field investigation and numerical analysis of an inverted pavement system in Tennessee, USA. *Transp. Geotech.* **2022**, *35*, 100759. [CrossRef]
10. Ma, R.; Sun, H.; Tian, Z. Study on preparation and performance of slow-release pavement snow melting salt. In *Frontier Research: Road and Traffic Engineering*; CRC Press: Boca Raton, FL, USA, 2022; pp. 383–388.
11. Yang, Y.; Chen, G.; Yang, Y.; Yue, L.; Xu, J. Advances in Salt-Storage Materials, Road and Anti-Freezing Performances of Salt-Storage Asphalt Mixture: A Review. *Coatings* **2022**, *12*, 1323. [CrossRef]
12. Wang, T.; Wei, X.; Zhang, D.; Shi, H.; Cheng, Z. Evaluation for Low Temperature Performance of SBS Modified Asphalt by Dynamic Shear Rheometer Method. *Buildings* **2021**, *11*, 408. [CrossRef]
13. Yu, W.; Yi, X.; Guo, M.; Chen, L. State of the art and practice of pavement anti-icing and de-icing techniques. *Sci. Cold Arid Reg.* **2014**, *6*, 14–21.
14. Yu, H.; He, Z.; Qian, G.; Gong, X.; Qu, X. Research on the anti-icing properties of silicone modified polyurea coatings (SMPC) for asphalt pavement. *Constr. Build. Mater.* **2020**, *242*, 117793. [CrossRef]
15. Chen, Y.; Tan, Y.; She, H.; Zhang, M.; Jiang, X.; Guo, P.; Li, Y.; Zhang, Y. Characteristics of slow-release ice and snow melting micro-surfacing materials. *Int. J. Pavement Eng.* **2022**, *24*, 2120986. [CrossRef]
16. Zhong, K.; Sun, M.; Chang, R. Performance evaluation of high-elastic/salt-storage asphalt mixture modified with Mafilon and rubber particles. *Constr. Build. Mater.* **2018**, *193*, 153–161. [CrossRef]
17. Zheng, M.; Zhou, J.; Wu, S.; Yuan, H.; Meng, J. Evaluation of long-term performance of anti-icing asphalt pavement. *Constr. Build. Mater.* **2015**, *84*, 277–283. [CrossRef]
18. Jiang, X.; Zhu, H.; Yan, Z.; Zhang, F.; Ye, F.; Li, P.; Zhang, X.; Dai, Z.; Bai, Y.; Huang, B. A state-of-art review on development and progress of backfill grouting materials for shield tunneling. *Dev. Built Environ.* **2023**, *16*, 100250. [CrossRef]
19. Chen, J.; Ma, X.; Wang, H.; Xie, P.; Huang, W. Experimental study on anti-icing and deicing performance of polyurethane concrete as road surface layer. *Constr. Build. Mater.* **2018**, *161*, 598–605. [CrossRef]
20. Zhou, L.; Ding, L.; Yi, X. A review of snow melting and de-icing technologies for trains. *Proc. Inst. Mech. Eng. Part F J. Rail Rapid Transit* **2022**, *236*, 877–886. [CrossRef]
21. Shan, L.; Li, Z.; Tian, D.; Tan, Y. Effect of anti-icing additives on the stability of emulsified asphalt binders. *Constr. Build. Mater.* **2021**, *275*, 121951. [CrossRef]
22. Zhang, H.; Guo, R. Investigation of Long-Term Performance and Deicing Longevity Prediction of Self-Ice-Melting Asphalt Pavement. *Materials* **2022**, *15*, 6026. [CrossRef]
23. Zheng, M.; Wu, S.; Wang, C.; Li, Y.; Ma, Z.; Peng, L. A study on evaluation and application of snowmelt performance of anti-icing asphalt pavement. *Appl. Sci.* **2017**, *7*, 583. [CrossRef]
24. Peng, C.; Yu, J.Y.; Dai, J.; Zhao, Z.J.; Fu, J.Y.; Zhao, M.L.; Wang, W. Synthesis and property of a green melting-snow additive for asphalt pavement. *Appl. Mech. Mater.* **2014**, *694*, 85–89. [CrossRef]
25. Wang, T.; Weng, Y.; Cai, X.; Li, J.; Xiao, F.; Sun, G.; Zhang, F. Statistical modeling of low-temperature properties and FTIR spectra of crumb rubber modified asphalts considering SARA fractions. *J. Clean. Prod.* **2022**, *374*, 134016. [CrossRef]
26. Peng, C.; Yu, J.; Zhao, Z.; Dai, J.; Fu, J.; Zhao, M.; Wang, W. Synthesis and properties of a clean and sustainable deicing additive for asphalt mixture. *PLoS ONE* **2015**, *10*, e0115721. [CrossRef] [PubMed]

27. Wu, S.; Zheng, M.; Chen, W.; Bi, S.; Wang, C.; Li, Y. Salt-dissolved regularity of the self-ice-melting pavement under rainfall. *Constr. Build. Mater.* **2019**, *204*, 371–383. [CrossRef]
28. Wang, W.; Yu, J.Y.; Yi, Y.; Chen, X. Effect of De-Icing Additives on Aging Properties of Bitumen. *Mater. Sci. Forum* **2016**, *847*, 418–424. [CrossRef]
29. Wang, Z.; Zhang, T.; Shao, M.; Ai, T.; Zhao, P. Investigation on snow-melting performance of asphalt mixtures incorporating with salt-storage aggregates. *Constr. Build. Mater.* **2017**, *142*, 187–198. [CrossRef]
30. Akbari, R.; Antonini, C. Contact angle measurements: From existing methods to an open-source tool. *Adv. Colloid Interface Sci.* **2021**, *294*, 102470. [CrossRef]
31. Zhang, Y.; Zhao, X.; Zheng, M. Analysis of Engineering Performance and Environmental Impact of Asphalt Pavement Debonding and Ice Suppression Materials. *Buildings* **2023**, *13*, 689. [CrossRef]

coatings

Article

Study on Rheological Properties and Modification Mechanism of Budun Rock Asphalt/Nano-Silica Composite Modified Asphalt

Chaojie Li [1,2,3], Zhenxia Li [3], Tengteng Guo [3], Yuanzhao Chen [3,4,*], Shangwei Jing [3], Jing Wang [3] and Lihui Jin [3]

1 Henan Transportation Research Institute Co., Ltd., Zhengzhou 450006, China; lcj13676936229@163.com
2 Xi'an Changda Highway Engineering Inspection Center Co., Ltd., Xi'an 710064, China
3 School of Civil Engineering and Communication, North China University of Water Resources and Electric Power, Zhengzhou 450045, China; zhenxiali2009@ncwu.edu.cn (Z.L.); guotth@ncwu.edu.cn (T.G.); 13782889126@163.com (S.J.); wj@ncwu.edu.cn (J.W.); lihuijin2023@163.com (L.J.)
4 Henan Province Engineering Technology Research Center of Environment Friendly and High-Performance Pavement Materials, Zhengzhou 450045, China
* Correspondence: cyz740513@ncwu.edu.cn

Abstract: To enhance the high and low-temperature performance of asphalt materials and extend the service life of asphalt pavement, two types of external admixtures, Butonite rock asphalt, and nano-silica are added to the asphalt. By conducting dynamic shear rheological tests and bending creep stiffness tests, the high and low-temperature rheological properties of Budun rock asphalt/nano-silica composite-modified asphalt were evaluated. The distribution of Budun rock asphalt and nano-silica in asphalt was studied using scanning electron microscopy and infrared spectroscopy tests, revealing the synergistic modification mechanism of Budun rock asphalt and nano-silica. The results show that the optimal dosage of Butonite rock asphalt and nano-silica composite-modified asphalt is 25% and 5%, respectively. At this dosage, the rutting factor G*/sinδ of composite-modified asphalt at 82 °C Compared with the matrix asphalt, the frequency main curve of Budun rock asphalt/nano-silica composite-modified asphalt is higher than that of the matrix asphalt and nano-silica-modified asphalt by 4 kPa. The creep modulus S at −18 °C decreases by 117.2 MPa, indicating that the high-temperature performance, low-temperature performance, and temperature sensitivity of Budun rock asphalt/nano-silica composite-modified asphalt are significantly improved compared to the matrix asphalt; The distribution of nano-silica particles in Budun rock asphalt/nano-silica composite-modified asphalt is uniform, and together with Budun rock asphalt, it forms a stable three-dimensional network skeleton structure; Budun rock asphalt/nano-silica composite-modified asphalt has generated new functional groups, and the blending process is mainly based on physical reactions, supplemented by weak chemical reactions.

Keywords: Budun rock asphalt; nano-silica; composite modified asphalt; rheological properties; modification mechanism

1. Introduction

Nowadays, China's highways have developed relatively well, and various types of roads have emerged in an endless stream. In particular, asphalt pavement has the characteristics of low noise, stable and comfortable driving, and good mechanical properties. Asphalt pavement has become the most prevalent type of road surface; however, with its widespread use, the load on the pavement is also steadily increasing. Especially for highways and heavy-duty traffic roads, it is easy to have quality problems such as rutting, cracks, and water damage, which also tests the performance of pavement materials [1]. Ordinary asphalt obviously cannot meet the needs of the increasing load of the highway, so modified asphalt came into being. There is a wide range of choices for the incorporation

of materials in modified asphalt, and numerous studies have been conducted in this field. The incorporation of each modifier can enhance the specific characteristics of asphalt to some degree [2,3]. The incorporation of nanomaterials can significantly improve the comprehensive characteristics of asphalt [4]. Nano-silica has the characteristics of abundant reserves, high chemical purity, easy production, and low price. Its extensive utilization extends to various domains, encompassing antibacterial materials, plastic coatings, optics, electronic assembly materials, and other fields [5]. At present, the application of nano-silica-modified asphalt can significantly improve the high and low-temperature properties of asphalt and anti-ultraviolet properties [6–8]. Buton rock asphalt (BRA) is a kind of material with abundant reserves and can greatly improve the high-temperature performance of asphalt mixture [9,10]. Utilizing both nano-silica and Buton rock asphalt as modifiers can more effectively harness their individual enhancing properties. This approach holds considerable importance for the field of pavement engineering, particularly in regions with high temperatures and roads subjected to heavy traffic loads. The use of these two materials to modify asphalt is aimed at improving its performance, prolonging road service life, and alleviating the pressure of petroleum energy shortage and environmental pollution, in line with the global concept of green, environmental protection, and sustainable development.

Many scholars have conducted related research on Buton rock asphalt-modified asphalt mortar. Zhang, Z [11] determined the basic properties of BRA-modified asphalt with 10%, 15%, 20%, 25%, and 30% BRA blending ratios. Research has revealed that as the proportion of Buton rock asphalt (BRA) in the mix is elevated, the high-temperature capabilities of the modified asphalt improve, whereas its performance at lower temperatures tends to diminish, with durability remaining relatively unchanged. Zhihai, Z [12] and Li, R.X et al. [13] determined the basic properties, viscosity, and high and low-temperature rheological properties of various quantities of Buton rock-modified asphalt. The research findings showed that the incorporation of Buton rock asphalt (BRA) resulted in reduced asphalt penetration, elevated softening point, increased viscosity, increased high-temperature PG grade, increased rutting factor, and a slight reduction in the low-temperature performance of asphalt. Muhammad, K et al. [14] used the UTM25 testing machine to conduct dynamic creep tests on unmodified asphalt and BRA-modified asphalt with 10%, 20%, and 30% BRA blending ratios. The enhanced performance of BRA-modified asphalt was observed, and an additional benefit was noted: an increase in BRA content led to a reduction in the overall permanent strain of the asphalt. Bo, S [15] conducted conventional performance tests and rheological performance tests on the high viscosity elastic restored asphalt with different modifier content, and the research showed that the rutting factor of the modified asphalt with Butunite was significantly improved, that is, Butunite enhanced the high-temperature stability and shear resistance of the asphalt. Yuanfeng, W et al. [16] conducted the high-temperature performance of Buton rock-modified asphalt by conventional test, dynamic shear rheological test, and viscosity test. As the Buton rock asphalt content increased, there was a noticeable enhancement in the high-temperature performance of the modified asphalt, as observed by researchers. In addition to directly incorporating BRA into asphalt, Ming, W et al. [17] extracted the ash in BRA to prepare ash mortar, studied the rheological properties through dynamic rheological properties test, and observed the microscopic by the means of infrared spectroscopy and scanning electron microscope. Compared with mineral powder mortar, they found that BRA ash mortar had better high-temperature rheological properties, and the high-temperature grade was 76 °C. At the same time, BRA can increase the adsorption capacity of the filler to the asphalt. In their research, Chuanming, Z et al. [18] prepared BRA-modified asphalt mortar by substituting mineral powder with BRA at levels of 50%, 75%, and 100%, maintaining a powder-to-binder ratio of 1:2. The three indicators, namely asphalt properties, cloth viscosity, and DSR test results, collectively indicated an enhancement in both the high-temperature performance and temperature sensitivity of asphalt mortar, accompanied by an increase in viscosity. Fourier out-of-line spectroscopy and scanning electron microscopy tests found that there was a physical combination between BRA and asphalt mortar, and the mortar interface was improved. Mingchen, L et al. [19] prepared modified

asphalt mortar according to different high ash rock asphalt substitution ratios according to the powder-binder ratio of 1:2 and designed a BRAC-16 asphalt mixture. The mixture satisfies the requirements for road application in cold regions, boasting exceptional performance in high and low temperatures, as well as remarkable water stability. Under a powder-binder ratio of 1:2, Yong, Y et al. [20] formulated an AC-25 asphalt mixture with varying replacement ratios of high ash rock asphalt. The mixture's water stability and high-temperature performance were both significantly enhanced. The modification mechanism was examined using scanning electron microscopy (SEM) and fluorescence microscopy. The analysis revealed that high ash rock asphalt exerted a modifying effect on the asphalt mortar interface.

Currently, scholars have conducted studies on asphalt modification with single nano-silica. Shafabakhsh, G et al. [6] examined the impact of nano-SiO_2 on asphalt cracking at temperatures of -5 °C, -15 °C, and -25 °C, employing the semi-circular bending test (SCB) with mixed mode I/II loading. The results show that nano-SiO_2 increases the maximum stress intensity factor (SIF) in asphalt. When the content of SiO_2 is 1.2%, the critical stress intensity molecules of the cracked sample are significantly improved, and the low-temperature performance of asphalt is enhanced. Gholam, A.S. et al. [21] used direct shear rheometer and multi-stress creep recovery to conduct rheological tests on nano-SiO_2-modified asphalt. The results revealed that, at 40 °C, the fatigue life of 1.2% nano-SiO_2-modified asphalt increased by 50% compared to the matrix asphalt. Additionally, the rutting resistance showed a 100% increase, signifying that the inclusion of nano-SiO_2 effectively enhanced the rheological properties of the asphalt. Lu, S et al. [22] investigated the rheological properties and road performance of nano-SiO_2-modified asphalt with different contents by DSR, BBR, and road performance tests. The findings indicate that nano-SiO_2 can significantly enhance the high-temperature flow characteristics of asphalt, with a more pronounced effect observed at lower frequencies. Wenxia, Z [23] The effect of nano-SiO_2 on the low-temperature crack resistance, fatigue performance, and rutting resistance of modified asphalt mixture with 0.5%~6.0% nano-SiO_2 was obtained by differential scanning calorimetry and thermal gravimetric analysis. Lu, S et al. [24] conducted a road performance test on nano-SiO_2-modified asphalt mixture, revealing that nano-SiO_2 significantly improved the high-temperature stability and water stability of the asphalt mixture. Yang, Y.S [25] studied the viscosity of nano-SiO_2-modified asphalt emulsion. The results indicated a decline in both penetration and ductility of the modified asphalt emulsion, with a simultaneous rise in viscosity corresponding to the increase in nano-SiO_2 content. Mehmet, S et al. [26] prepared 0.1%, 0.3%, and 0.5% nano-SiO_2-modified asphalt, measured the rutting resistance and fatigue properties of asphalt, and observed the distribution of nanoparticles by scanning electron microscopy. The investigation revealed that at a SiO_2 content of 0.3%, the asphalt's performance exhibited more pronounced improvement, with agglomeration degrees of less than 4 μm and uniform distribution. He, H. et al. [27] considered that the agglomeration of nanoparticles (NPs) in nano-SiO_2-modified asphalt was serious, so the solvent SiO_2 nanofluids (NFs) were incorporated into the asphalt for modification. The investigation into the thermal stability of the asphalt employed various techniques such as scanning electron microscopy, Fourier transform infrared spectroscopy, thermogravimetric analysis, and dynamic shear rheology. The results suggest a consistent dispersion of nanofluids throughout the asphalt system. The incorporation of SiO_2 (NFs) notably improves the resistance of the asphalt mixture to low-temperature cracking and fatigue, with only a minimal adverse effect on high-temperature stability. Chuang, Y et al. [28]. first chemically modified the matrix asphalt, and then added SiO_2 grafted with polyethylenimide to prepare high-performance modified asphalt. The test found that the prepared modified asphalt had better dispersion, chemical reaction and physical reaction with asphalt, and high temperature and anti-aging properties were improved. Yanqing, T [29] used oil-wet nano-SiO_2 to observe the microstructure of oil-wet nano-SiO_2 and asphalt by SEM and to study the influence of oil-wet nano-SiO_2 and matrix asphalt on temperature sensitivity and rheological properties. The findings indicate that the modified asphalt demonstrates superior aging resistance and rheological properties. Henglong, Z et al. [30] discovered enhanced compatibility between asphalt and surface-modified

nano-SiO_2 through physical properties testing of asphalt and high-temperature storage stability testing under ultraviolet aging conditions. Meanwhile, Long, Z. et al. [31,32] unveiled the compatibility principle between nano-SiO_2 and asphalt using molecular dynamics (MD). The compatibility of nano-SiO_2 with saturates surpasses that with asphaltenes. The incorporation of nano-SiO_2 restrains the volatilization of saturates within asphalt, facilitating increased diffusion of saturates. This accelerated diffusion rate of distinctive structural molecules within the asphalt fosters self-healing and augments asphalt durability. Rezaei, S et al. [33] measured the high-temperature performance of nano-SiO_2/SBS composite-modified asphalt, which showed that the high-temperature performance of asphalt was significantly improved. Abed, A.H. et al. [34] conducted FTIR analysis of 3% and 5% nano-SiO_2/SBS composite-modified asphalt and found that the composite-modified asphalt had better oxidation resistance than the matrix asphalt. Mostafa, S. et al. [35] analyzed the road performance of SMA-type nano-SiO_2/TiO_2 composite-modified asphalt mixture, and the results showed that the mechanical properties of SMA asphalt mixture could be improved by adding nano-SiO_2. Shafabakhsh, G. H. et al. [36] prepared composite modified steel slag asphalt mixture mixed with nano-SiO_2 and nano-TiO_2. By studying the rheology of modified asphalt, it was found that the addition of nano-SiO_2 and TiO_2 increased the toughness and viscosity of asphalt by 30% and 109%, respectively, and the permeability grade of asphalt decreased.

Taking into account the research status, it has been demonstrated that incorporating Buton rock asphalt into asphalt enhances its high-temperature performance and temperature sensitivity. The impact is more pronounced with an increased blending ratio of Buton rock asphalt, and it has a less significant effect on the low-temperature performance of asphalt. Additionally, the inclusion of nano-silica in asphalt proves effective in improving its performance across high and low temperatures, water stability, and rheological properties, albeit with an associated increase in asphalt viscosity. Drawing upon the research conducted by scholars both domestically and internationally regarding Buton rock-modified asphalt and nano-silica-modified asphalt, it is noteworthy that Buton rock asphalt exhibits a substantial capability to enhance the high-temperature performance and fatigue resistance of asphalt. Nevertheless, its influence on the low-temperature performance of asphalt is relatively subdued. Nano-silica exhibits a notable capability to improve the low-temperature performance of asphalt. However, its effectiveness in enhancing high-temperature performance does not match the demonstrated efficacy of Buton rock asphalt. The modification effect of a single modifier on asphalt is not as good as that of the composite modifier. Hence, this study opts for Buton rock asphalt and nano-silica as modifiers to formulate a composite-modified asphalt. It comprehensively examines high-temperature rheological properties, low-temperature performance, and the modification mechanism. The aim is to achieve a composite-modified asphalt exhibiting exceptional high and low-temperature performance.

2. Raw Materials

2.1. Asphalt

The 70# matrix asphalt was used for experiments, and its technical indicators were tested according to specifications. The test results are shown in Table 1.

Table 1. Basic performance index of asphalt.

Item	Unit	Result	Specification
needle penetration (25 °C, 100 g, 5 s)	0.1 mm	60.7	60~80
ductility (5 °C, 5 cm/min)	cm	11.3	≥0
softening point	°C	46.9	≥46
penetration index PI		−0.49	−1.5~+1.0
equivalent softening point	°C	50.66	actual measurement
equivalent brittle point	°C	−14.87	actual measurement
Rotating film residue (163 °C, 85 min)			
rate of quality-led loss	%	0.41	−0.8~+0.8
ductility (5 °C)	cm	7.8	≥6
penetration ratio (25 °C)	%	70.9	≥61

2.2. Buton Rock Asphalt

The experiment selected Indonesian high ash rock asphalt (BRA) produced by Indonesia Budun Rock Asphalt Co., Ltd. (BAI) (Nicaea, India) and sold by Anhui Zhongyin Natural Rock Asphalt Technology Co., Ltd. (Anhui, China) Budun rock is composed of 27.2% asphaltene and 72.8% limestone minerals. The main technical indicators are shown in Table 2 and meet the requirements of the specification [37].

Table 2. Technical indicators of Butun rock asphalt.

Item	Unit	Result	Specification
mass fraction of asphalt	%	27.2	≥25
density	g/cm^3	1.77	1.60~1.80
water content	%	0.96	≤2
loss on heating	%	0.62	≤2
maximum particle size	mm	1.18	-
solubility	%	24.3	≥18

2.3. Nano-Silica

Nano-silica (nano-SiO_2) is an inorganic chemical material, also known as white carbon black. It is non-toxic, odorless, and pollution-free. It is a spherical microstructure and insoluble in organic solvents. The nano-SiO_2 of Hubei Huifu Nanomaterial Co., Ltd. (HL-200 type) was used in the test. In this study, a 5% silane coupling agent KH-550 is chosen to initially modify the surface of nano-silica, ensuring excellent compatibility with asphalt. The microscopic test images of silica before and after surface modification are shown in Figure 1. Microscopic scanning electron microscopy was used to observe the dispersion state of surface-modified nano SiO_2 particles, and it was found that the agglomeration phenomenon of surface-modified nano SiO_2 was significantly reduced. Silane coupling agent KH-550 was employed to modify the surface of nano SiO_2, effectively reducing the surface energy of nanomaterials. This process aimed to facilitate better integration and even dispersion of nano SiO_2 within the asphalt. The principal technical parameters are illustrated in Table 3. The utilized nano-silica adheres to the specification's stipulations [38].

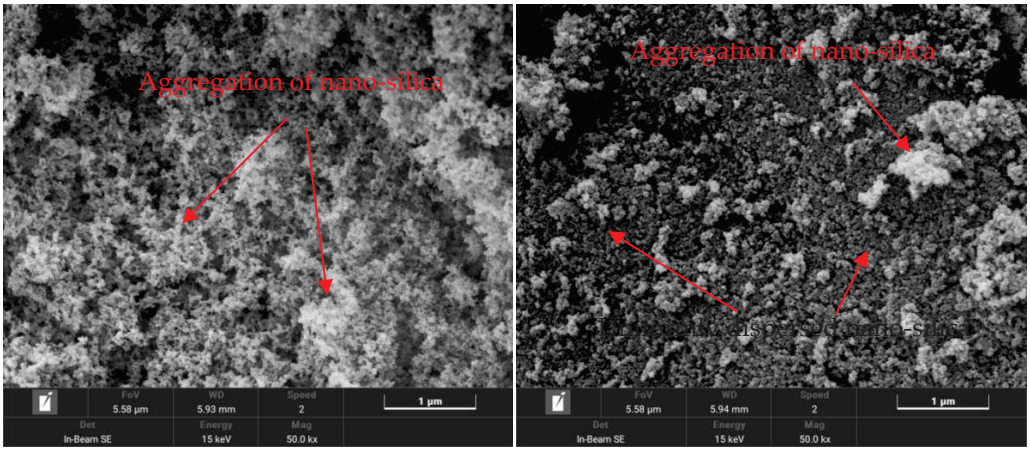

(**a**) (**b**)

Figure 1. Electron microscopy images of nano-silica before and after treatment were magnified by 50,000 times. (**a**) Untreated nano-silica magnified by 50,000 times; (**b**) Surface-modified nano-silica magnified by 50,000 times.

Table 3. Technical indicators of nano-SiO_2.

Item	Unit	Result	Specification
appearance		white powder	white powder
purity	%	99.84	≥99.8
mean diameter	nm	20	-
specific surface area	m^2/g	217	200 ± 20
Suspension pH value		4.15	3.9~4.5
105 °C volatiles	%	0.46	≤2.0
ignition loss	%	0.47	≤2.0
tap density	g/L	52	40~60
45 μm sieve residue	mg/kg	30	≤250

By observing the dispersion state of nano SiO_2 particles before and after treatment through microscopic scanning electron microscopy, it can be seen from Figure 1a that untreated nano SiO_2 exhibits severe agglomeration, which is due to the extremely small particle size, large specific surface area, and high surface energy of nano SiO_2 itself. When untreated nano SiO_2 is added to asphalt, it is easy to cause adverse modification phenomena such as nano-material agglomeration, difficulty in addition, and separation after addition. As shown in Figure 1b, the agglomeration phenomenon of surface-modified nano SiO_2 is significantly reduced. The use of silane coupling agent KH-550 for surface modification of nano SiO_2 eliminates the surface energy of the nano-material, allowing nano SiO_2 to better integrate and uniformly disperse in asphalt. It can be seen that the agglomeration phenomenon of surface-modified nano SiO_2 is significantly reduced. The use of silane coupling agent KH-550 for surface modification of nano SiO_2 eliminates the surface energy of the nano-material, allowing nano SiO_2 to better blend and uniformly disperse in asphalt.

3. Experimental Scheme

3.1. Preparation of Buton Rock Asphalt/Nano-Silica Composite-Modified Asphalt

After reading a large number of relevant literature and previous systematic experimental tests, it was found that after adding SiO_2 to the matrix asphalt, the penetration of the modified asphalt decreased, the ductility increased, the softening point increased, the penetration index increased, the equivalent softening point increased, and the equivalent brittle point decreased, and the "inflection point" appeared at the dosage of 5%, indicating that the modification effect of SiO_2 was the best at this concentration. After more than 5%, the performance of modified asphalt will decrease. The content of Budun rock asphalt should not be too high. The high-temperature performance of composite-modified asphalt is the best at a 25% content, while the low-temperature performance can be met. Therefore, 20%, 25%, and 30% are selected for composite modification. The preparation process of Budun rock asphalt/nano-silica composite-modified asphalt is as follows:

(1) Heat the base asphalt to a molten state and maintain it at 160 °C, pour nano SiO_2 into the base asphalt, and mix it with a glass rod. After pouring all, manually mix for 30 min.
(2) Cut at a speed of 5500 r/min for 20 min at high speed, pour the designed amount of Burton rock asphalt into the asphalt, and cut at high speed for 30 min at a speed of 5500 r/min.
(3) Place the sheared composite-modified asphalt in a 170 °C oven to swell for 20 min, then mix it appropriately with a glass rod to remove any bubbles in the composite-modified asphalt, thus completing the preparation of the composite-modified asphalt.

3.2. Dynamic Shear High-Temperature Rheological Test

In contrast to traditional performance measures like penetration, ductility, and softening point, the dynamic mechanical performance index reflects the viscoelastic alterations of asphalt during real-world usage. As a representative viscoelastic material, asphalt's viscoelasticity is temperature-dependent, with its dynamic mechanical attributes encompass-

ing alterations in viscosity and elasticity. It is imperative to assess the dynamic mechanical property variations of asphalt across the designated temperature spectrum.

The instrument used in the shear rheological test in this paper is the DHR-1 dynamic shear rheometer manufactured by TA Instruments in the United States. Based on recommendations and requirements from experience and standards [38], determine the Buton rock asphalt/nano-silica composite-modified asphalt DSR temperature scanning test, with a temperature range of 46~82 °C, interval 6 °C (46 °C, 52 °C, 58 °C, 64 °C, 70 °C, 76 °C, 82 °C) scanning, test process control 10 rad/s loading frequency, and 10% strain level. The sample dimensions are 25 mm in diameter and 2 mm in thickness. By means of the DSR temperature scanning test, the variation pattern of the complex shear modulus G* and phase angle δ is derived as the temperature is incrementally raised based on the designated intervals. Rutting factor G*/sinδ represents high-temperature rutting resistance, and the higher the value, the better the high-temperature rutting resistance. The rutting factor G*/sinδ is calculated, facilitating the development of a relationship curve depicting the correlation between the rutting factor and temperature. This analysis serves to assess the asphalt's temperature stability. Through the DSR frequency scanning test, five different temperature environments were selected to evaluate the frequency changes of five kinds of asphalt, and the main curve was drawn to further expand the temperature range for analysis. The multi-stress creep recovery test involves calculating the average strain recovery rate (R) and the irreversible creep compliance (Jnr) based on 20 creep cycles.

3.3. Low Temperature Bending Creep Stiffness Test

With the aim of examining whether the low-temperature performance of Buton rock asphalt/nano-silica composite-modified asphalt surpasses that of matrix asphalt, a low-temperature bending creep stiffness (BBR) test was conducted. The instrument used in this paper is the ATS low-temperature bending beam rheometer of the United States. Based on recommendations and requirements from experience and standards [38], it is determined that the BBR test of Buton rock asphalt/nano-silica composite-modified asphalt is carried out at −12 °C, −18 °C, and −24 °C. Through the BBR test, the stiffness modulus S and the rate of creep stiffness change m were derived, enabling an analysis of the low-temperature crack resistance of the composite-modified asphalt.

3.4. Fourier Infrared Spectroscopy Test

The instrument used in the Fourier transform infrared spectroscopy experiment is the NicolletiS10 Fourier transform infrared spectrometer. Infrared spectroscopy experiments were conducted on matrix asphalt and Budun rock asphalt/nano-silica composite-modified asphalt with a scanning range of 7800–375 cm^{-1}, a resolution of 0.4 cm^{-1}, and 64 scanning times.

3.5. Scanning Electron Microscope

The scanning electron microscope experiment was conducted using the JSM-7500F field emission scanning electron microscope. Microscopic observations were conducted on the matrix asphalt and Budun rock asphalt/nano-silica composite-modified asphalt. Firstly, the sample was fixed on the stage with conductive adhesive, and then vacuum gold spraying was performed. After completion, the observation was waited for.

4. Results and Analysis

4.1. Dynamic Shear Test (DSR)

(1) Temperature scanning

DSR tests were carried out on five groups of samples, including matrix asphalt, nano-SiO_2-modified asphalt with 5% content, and Buton rock asphalt-modified asphalt with 5% nano-SiO_2 composite content of 20%, 25%, and 30%, respectively. The complex shear modulus-temperature curve, phase angle-temperature curve, and rutting factor–temperature curve are illustrated in Figures 2–4, respectively.

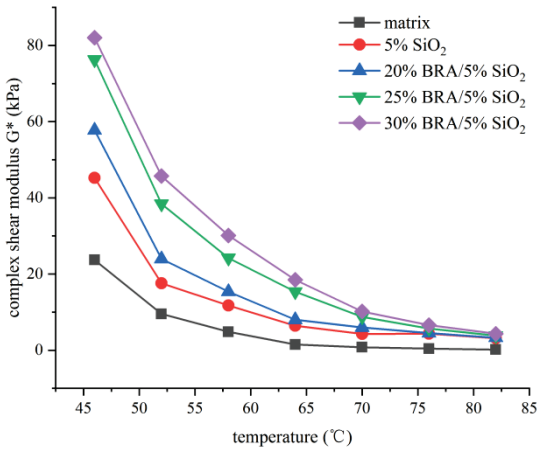

Figure 2. Complex modulus test results.

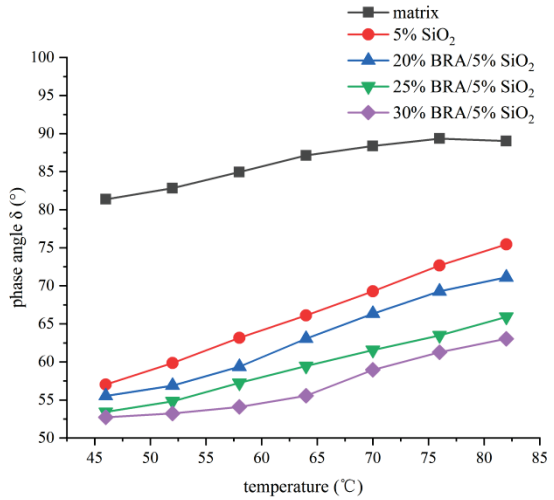

Figure 3. Phase Angle test results.

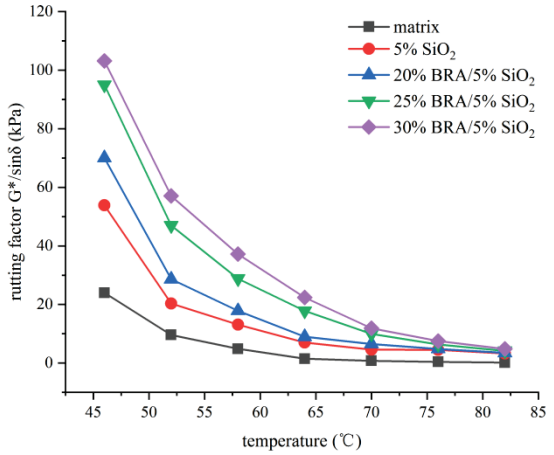

Figure 4. Rutting factor–temperature curve.

Analysis results can be obtained:

The G* trend for nano-SiO_2-modified asphalt and BRA/nano-SiO_2 composite-modified asphalt shows a decline as temperature increases. At the same temperatures, the G* of BRA/nano-SiO_2 composite-modified asphalt is notably higher than that of matrix asphalt. The shear resistance of BRA/nano-SiO_2 composite-modified asphalt surpasses that of both

matrix asphalt and nano-SiO_2-modified asphalt. Furthermore, the G* of the composite-modified asphalt increases proportionally with the augmentation of Buton rock asphalt content. The G* of the composite-modified asphalt reaches its peak at the same temperature when the Buton rock asphalt content is 30% and the nano-SiO_2 content is 5%. At this time, the shear resistance is the best. Compared with 25% BRA/5% SiO_2 composite-modified asphalt, the G* by 5.79 kPa at 46 °C, 7.3 kPa at 52 °C, 5.9 kPa at 58 °C, 3.14 kPa at 64 °C, 1.43 kPa at 70 °C, 0.91 kPa at 76 °C, and 0.5 kPa at 82 °C. The findings reveal a consistent enhancement in shear resistance for Buton rock asphalt/nano-silica composite-modified asphalt as the content of Buton rock asphalt increases.

The phase angle of nano-SiO_2-modified asphalt and BRA/nano-SiO_2 composite-modified asphalt gradually increases with rising temperature. At equivalent temperatures, the phase angle of composite-modified asphalt is smaller compared to nano-SiO_2-modified asphalt. This suggests that the addition of Buton rock asphalt has a tendency to decrease the phase angle of the asphalt. At lower temperatures, the phase angle differences among various dosages of composite-modified asphalt are relatively minimal, but these differences become more pronounced as the temperature increases. The composite-modified asphalt exhibits its smallest phase angle when the Buton rock asphalt content is 30% and the nano-SiO_2 content is 5%. The incorporation of Buton rock asphalt and nano-silica increases the viscous component/elastic component in the asphalt and contributes to the deformation recovery of the asphalt.

As the temperature rises, the rutting factor G*/sinδ of the matrix asphalt is 0.77 kPa at 70 °C, and the rutting factor of the original asphalt is required to be ≥1.0 kPa in the specification. Compared with 5% nano-SiO_2-modified asphalt, 20%, 25%, and 30% composite-modified asphalt with 5% nano-SiO_2, the rutting factors G*/sinδ at 82 °C are 3.23 kPa, 3.46 kPa, 4.17 kPa, and 4.84 kPa, respectively, which are greater than the specification requirements. This significantly improves the asphalt's resistance to rutting and enhances its high-temperature performance.

Based on the aforementioned analysis, it is evident that the integration of Buton rock asphalt and nano-silica enhances the shear resistance of asphalt, and significantly improves the rutting resistance and high-temperature performance.

(2) Frequency scanning

The complex modulus of matrix asphalt, 5% nano-SiO_2-modified asphalt, 20%, 25%, and 30% Buton rock asphalt composite 5% nano-SiO_2 composite-modified asphalt was studied at 40 °C, 52 °C, 64 °C, 76 °C, and 88 °C, respectively. The law of change with frequency (0.1–100 rad/s). In the test, the strain level was controlled to 1%, and the complex modulus–angular frequency diagram was drawn as shown in Figure 5.

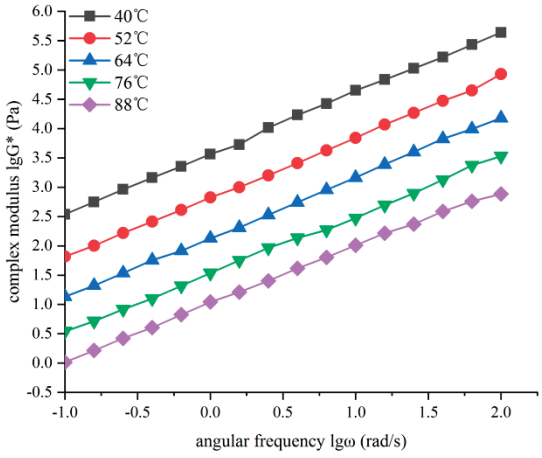

(**a**) asphalt

Figure 5. *Cont.*

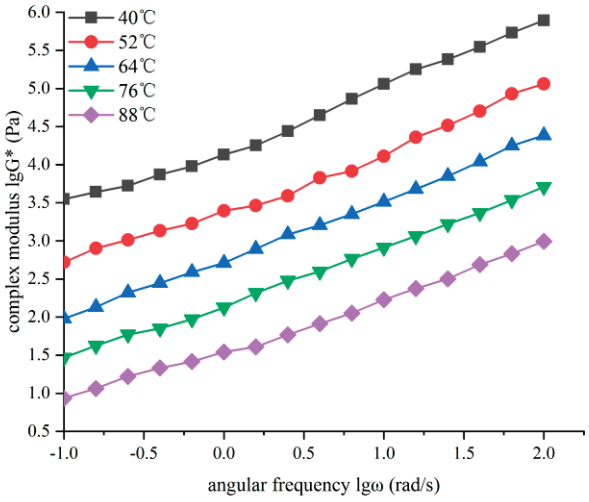

(**b**) 5% nano-SiO_2-modified asphalt.

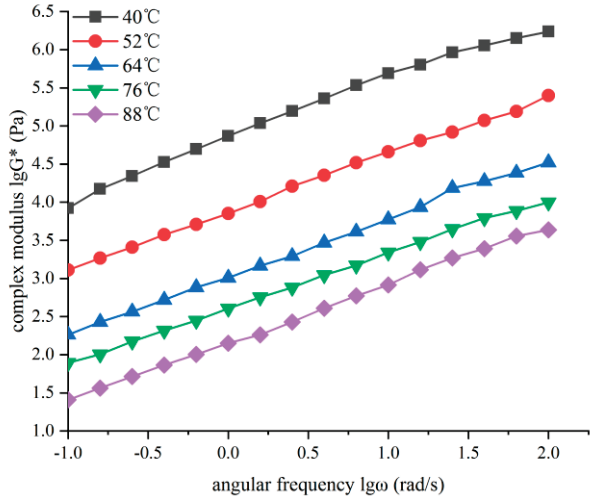

(**c**) 20% BRA/5% nano-SiO_2 composite-modified asphalt.

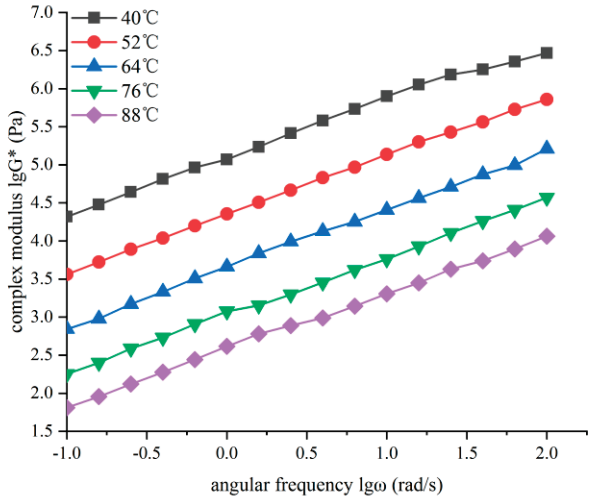

(**d**) 25% BRA/5% nano-SiO_2 composite-modified asphalt.

Figure 5. *Cont.*

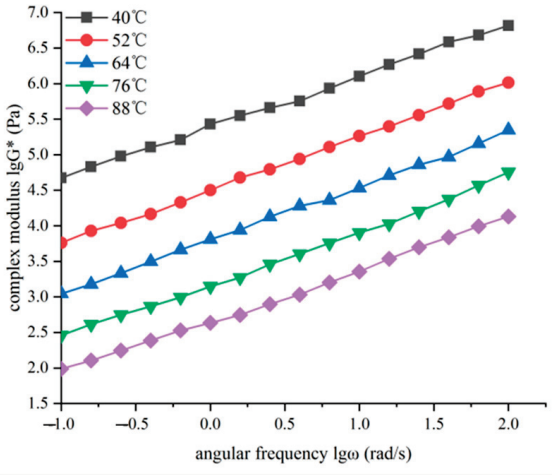

(**e**) 30% BRA/5% nano-SiO_2 composite-modified asphalt.

Figure 5. Five kinds of asphalt complex modulus change curves.

Analysis results can be obtained: Upon examining Figure 5, it becomes evident that at a constant temperature, the complex modulus of the five asphalt varieties rises in tandem with an increase in angular frequency. This observation signifies that during the practical utilization of asphalt pavement, the vibration duration at a specific asphalt point diminishes as vehicle load speed increases. When the frequency of vehicle load increases, the number of vibrations also increases. The escalation in the frequency of vibrations within specific timeframes results in reduced strain within the asphalt, thereby contributing to a reduction in pavement deformation. At the temperatures of 40 °C, 52 °C, 64 °C, 76 °C, and 88 °C, the slope depicting the alteration in asphalt's complex modulus remains relatively consistent. Furthermore, at identical angular frequencies, the complex modulus of asphalt diminishes with escalating temperatures. This shows that when the temperature increases, the asphalt softens, and the asphalt is a typical viscoelastic material, in which the viscous material increases, the elastic material content decreases, and the external performance is more viscous. In the practical context of asphalt pavement, it can be observed that as asphalt temperature increases, its resistance to deformation diminishes, consequently leading to a decline in high-temperature performance.

Compared with the complex modulus G* value of different BRA content in the single-doped nano-SiO_2-modified asphalt group, at the same frequency and temperature, with the increase of BRA content, the complex modulus value gradually increases, and at the angular frequency of 0.5 rad/s, at 40 °C, the complex modulus value of the composite-modified asphalt with 30% BRA content is 46.65% higher than that of the matrix asphalt, 30.80% higher than that of the single-doped nano-SiO_2-modified asphalt, and 9.21% higher than that of the composite asphalt with 20% BRA; it is 3.83% higher than that of composite asphalt with 25% BRA. When the temperature reaches 88 °C, the complex modulus value of composite-modified asphalt with 30% BRA content is more than 20% higher than that of single-doped nano-SiO_2-modified asphalt, indicating that BRA plays a more prominent role in improving the high-temperature stability of modified asphalt than single-doped SiO_2 modified asphalt.

(3) Main curve analysis of frequency scanning results

By calculating displacement factors from fitting curves of five asphalt varieties at different temperatures, the primary curve is formed using the time–temperature equivalence principle. This construction aims to broaden the frequency range of the analysis.

(1) Determination of displacement factor

Initially, the frequency scanning outcomes of the matrix asphalt are subjected to curve equation fitting, and the resultant findings are presented in Table 4.

Table 4. Matrix asphalt double logarithm fitting curve equation table.

Testing Temperature (°C)	Curve-Fitting Equation	R^2
40	lgG* = 0.92802 lgω + 3.57715	0.99941
52	lgG* = 0.92439 lgω + 2.82507	0.99437
64	lgG* = 0.88651 lgω + 2.12896	0.99782
76	lgG* = 0.87613 lgω + 1.53576	0.99924
88	lgG* = 0.87822 lgω + 0.98216	0.99291

In this paper, G* = 1 kPa, that is, lgG* = 3, is substituted into the fitting curve equation of Table 4, and the value of lgω is obtained. Taking 40 °C as the reference temperature, the displacement factor is obtained. The findings are displayed in Table 5.

Table 5. Summary of matrix asphalt displacement factors.

Testing Temperature (°C)	lgω (G* = 1 kP, rad/s)	Shift Factors
40	−0.6219	0
52	0.1892	−0.8111
64	0.9825	−1.6044
76	1.6713	−2.2932
88	2.2976	−2.9195

Likewise, curve fitting equations and displacement factors for nano-SiO_2-modified asphalt and Buton rock asphalt/nano-silica composite-modified asphalt were computed individually. The outcomes are detailed in Tables 6 and 7.

Table 6. Summary of double logarithm fitting curve of modified asphalt.

Types of Modified Asphalt	Testing Temperature (°C)	Curve-Fitting Equation	R^2
5% nano-SiO_2-modified asphalt	40	lgG* = 0.78164 lgω + 4.13153	0.99475
	52	lgG* = 0.75020 lgω + 3.39531	0.99631
	64	lgG* = 0.80127 lgω + 2.71575	0.99243
	76	lgG* = 0.74692 lgω + 2.13072	0.99672
	88	lgG* = 0.78625 lgω + 1.54194	0.99901
20% BRA/5% nano-SiO_2 composite-modified asphalt	40	lgG* = 0.80582 lgω + 4.46725	0.99836
	52	lgG* = 0.76273 lgω + 3.96839	0.99277
	64	lgG* = 0.75282 lgω + 3.33177	0.99131
	76	lgG* = 0.67665 lgω + 3.03513	0.99677
	88	lgG* = 0.74308 lgω + 2.15429	0.99390
25% BRA/5% nano-SiO_2 composite-modified asphalt	40	lgG* = 0.68216 lgω + 5.06413	0.99269
	52	lgG* = 0.76603 lgω + 4.55691	0.99164
	64	lgG* = 0.82397 lgω + 3.86129	0.99365
	76	lgG* = 0.81728 lgω + 3.17803	0.99243
	88	lgG* = 0.75088 lgω + 2.51576	0.99678
30% BRA/5% nano-SiO_2 composite-modified asphalt	40	lgG* = 0.71391 lgω + 5.43853	0.99263
	52	lgG* = 0.75119 lgω + 4.80385	0.99962
	64	lgG* = 0.80121 lgω + 4.12576	0.99850
	76	lgG* = 0.76467 lgω + 3.36815	0.99271
	88	lgG* = 0.69195 lgω + 2.73792	0.99372

Table 7. Summary of displacement factors of modified asphalt.

Types of Modified Asphalt	Testing Temperature (°C)	lgω (G* = 1 kP, rad/s)	Shift Factors
5% nano-SiO_2-modified asphalt	40	−1.4476	0
	52	−0.5269	−0.9207
	64	0.3547	−1.8024
	76	1.1638	−2.6115
	88	1.8544	−3.3021
20% BRA/5% nano-SiO_2 composite-modified asphalt	40	−1.8208	0
	52	−1.2696	−0.5512
	64	−0.4407	−1.3801
	76	−0.0519	−1.7689
	88	1.1381	−2.9589
25% BRA/5% nano-SiO_2 composite-modified asphalt	40	−3.0259	0
	52	−2.0324	−0.9934
	64	−1.0453	−1.9806
	76	−0.2178	−2.8080
	88	0.6449	−3.6708
30% BRA/5% nano-SiO_2 composite-modified asphalt	40	−3.4157	0
	52	−2.4013	−1.0144
	64	−1.4051	−2.0107
	76	−0.4814	−2.9343
	88	0.3788	−3.7945

(2) Principal curve analysis

Based on the computed displacement factors for various asphalt types, the five asphalts are shifted to the left to derive the complex modulus master curve at the reference temperature of 40 °C, depicted in Figure 6.

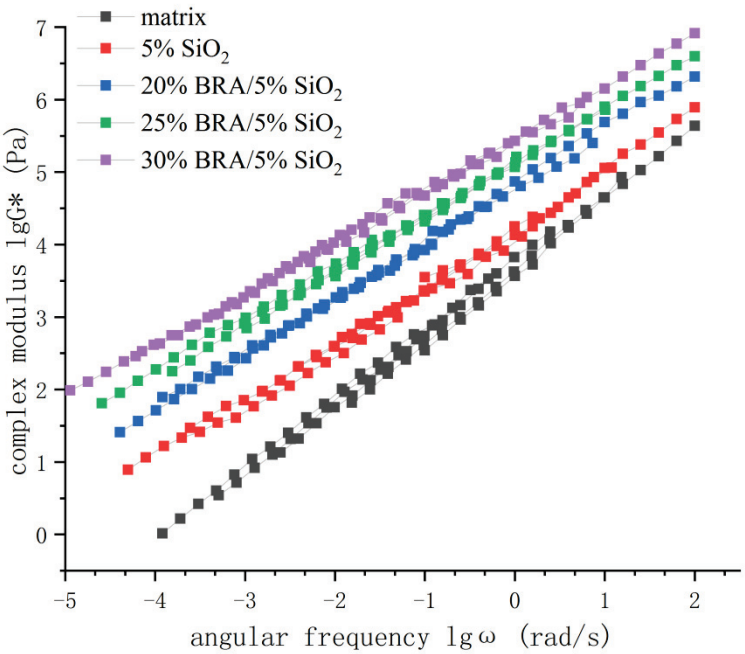

Figure 6. Summary of the master curve of complex modulus of five kinds of asphalt.

Observing Figure 6, we can get:

The matrix asphalt exhibits a notably low complex modulus under conditions of elevated temperature and low frequency, implying inadequate resistance to high-temperature

deformation. For equivalent angular frequencies, the modified asphalt showcases a higher complex modulus than the matrix asphalt, signifying the effective enhancement of asphalt's high-temperature performance through the incorporation of Buton rock asphalt and nano-silica. In comparison to modified asphalt with varying compositions, the complex modulus of Buton rock asphalt/nano-silica composite-modified asphalt surpasses that of nano-silica-modified asphalt. Furthermore, an augmentation in the content of Buton rock asphalt corresponds to an increment in the complex modulus of the composite-modified asphalt. This observation underscores that the inclusion of Buton rock asphalt leads to a heightened enhancement in the high-temperature shear resistance of the asphalt. Moreover, the amplification in the content of Buton rock asphalt accentuates this improvement effect.

Under conditions of low temperature and high frequency, the complex modulus of all five asphalt types rises with an escalation in angular frequency. Notably, the complex modulus of these five asphalt varieties demonstrates a tendency to approach one another, suggesting a certain degree of similarity. The relationship between the complex modulus of the five kinds of asphalt is 30% BRA/5% nano-SiO_2 composite-modified asphalt > 25% BRA/5% nano-SiO_2 composite-modified asphalt > 20% BRA/5% nano-SiO_2 composite-modified asphalt > 5% nano-SiO_2-modified asphalt > matrix asphalt. This observation indicates that, even in low-temperature and high-frequency conditions, the incorporation of Buton rock asphalt and nano-silica remains efficacious in significantly improving the high-temperature performance of the asphalt. As a result, the asphalt demonstrates commendable resistance to deformation.

(3) Multiple stress creep recovery test (MSCR)

The test results of four types of modified asphalt are shown in Figure 7.

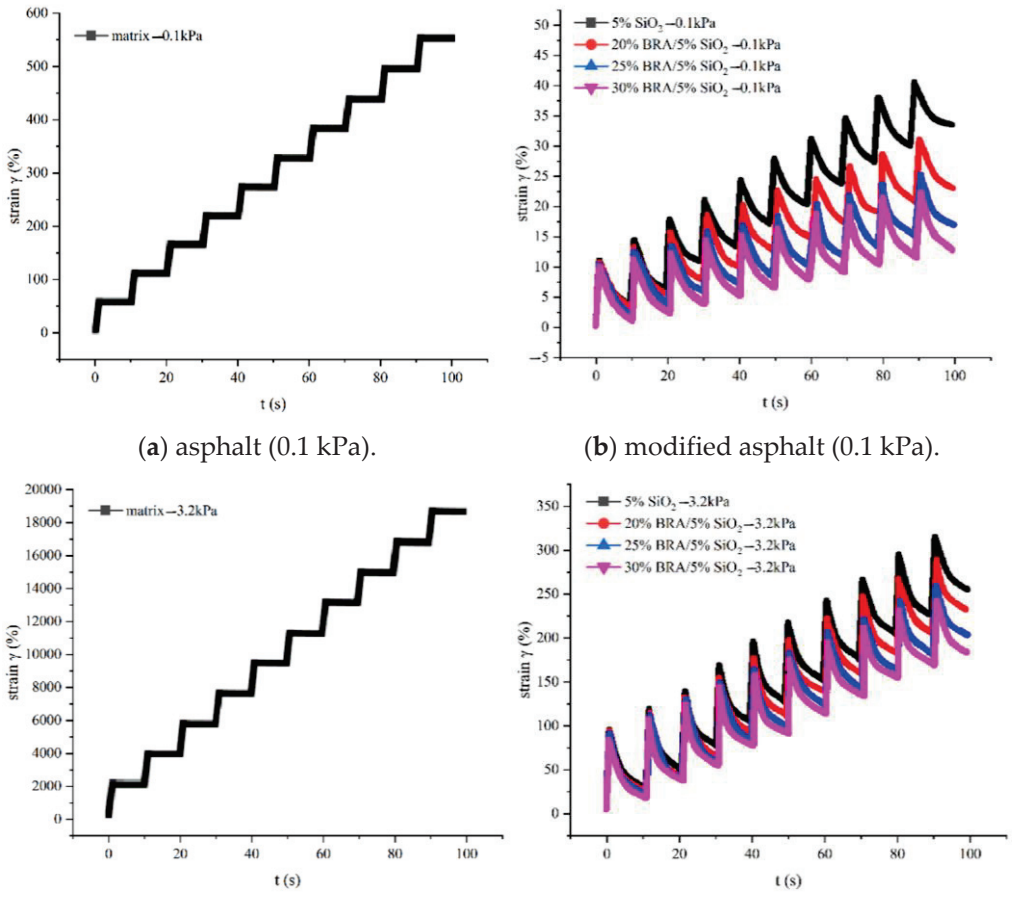

(**a**) asphalt (0.1 kPa). (**b**) modified asphalt (0.1 kPa).

(**c**) asphalt (3.2 kPa). (**d**) modified asphalt (3.2 kPa).

Figure 7. Multi-stress creep recovery test results.

Analyzing Figure 7a,c, it is evident that at the temperature of 64 °C, the strain–time curve of the matrix asphalt exhibits a right angle during each creep cycle at stress levels of 0.1 kPa and 3.2 kPa. This pattern suggests that the matrix asphalt has almost no unloading recovery strain and accumulates a considerable irrecoverable strain, surpassing that of the modified asphalt by a significant margin. From Figure 7b,d, it can be seen that under the two stress levels of 0.1 kPa and 3.2 kPa, the cumulative strain of nano-silica-modified asphalt is greater than the cumulative strain of Buton rock asphalt/nano-silica composite-modified asphalt with different Buton rock asphalt content. With the increase in the content of Buton rock asphalt, a noticeable reduction in the cumulative strain of the composite-modified asphalt becomes evident. This trend indicates that the inclusion of Buton rock asphalt contributes to an enhanced high-temperature deformation resistance of the composite-modified asphalt. Moreover, as the Buton rock asphalt content continues to rise, this enhancement effect becomes increasingly pronounced.

To provide a more comprehensive representation of asphalt's creep recovery performance, R and Jnr of the five asphalt types are individually calculated at stress levels of 0.1 kPa and 3.2 kPa. These outcomes are visually depicted in Figure 8.

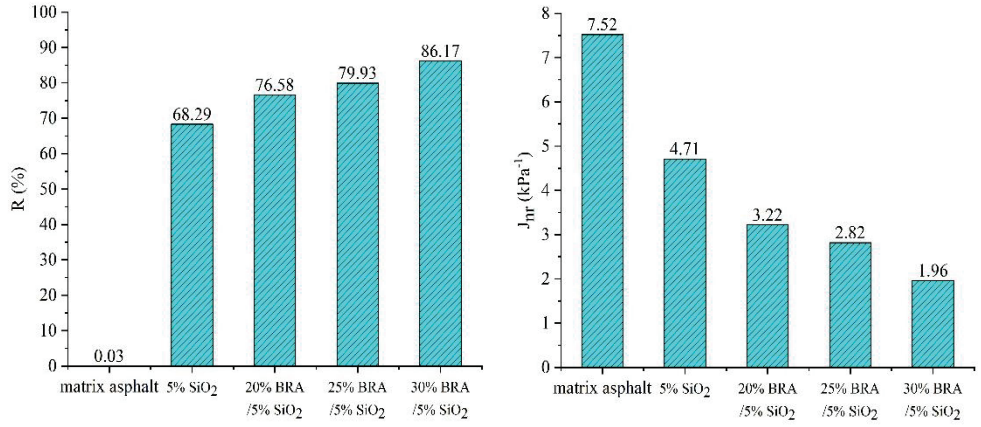

(**a**) 0.1 kPa.

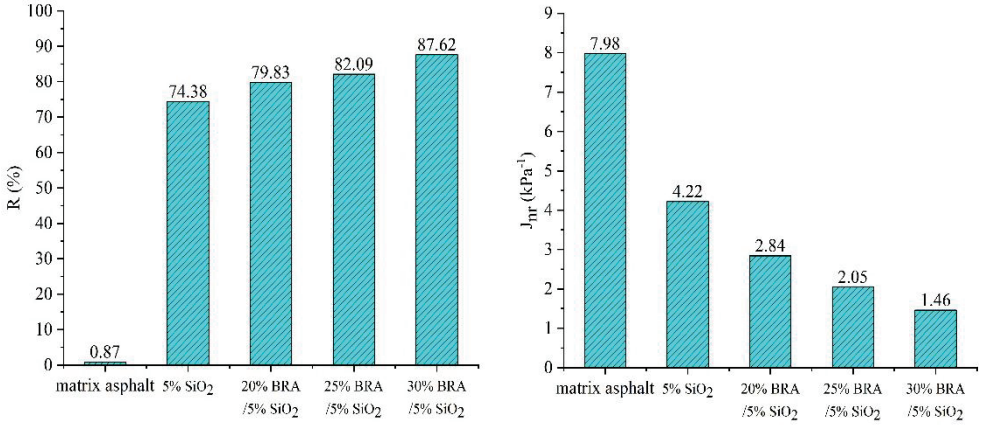

(**b**) 3.2. kPa.

Figure 8. Average creep recovery rate R and non-recoverable creep compliance Jnr of the five kinds of asphalt.

Figure 8 reveals that the strain recovery rates R (0.1) and R (3.2) for the matrix asphalt are nearly 0, indicating a notably low proportion of the elastic component within the matrix asphalt. The unrecoverable creep compliance Jnr0.1 and Jnr3.2 of the matrix asphalt are 7.52 kPa^{-1} and 7.98 kPa^{-1}, respectively. The non-recovery strain of deformation in the matrix asphalt is higher than that of the modified asphalt, and the recovery ability from deformation is extremely poor. Under the two stress levels of 0.1 kPa and 3.2 kPa, the

strain recovery rate R of modified asphalt is as follows: 30% Buton rock asphalt/5% nano-silica composite-modified asphalt > 25% Buton rock asphalt/5% nano-silica composite-modified asphalt > 20% Buton rock asphalt/5% nano-silica composite-modified asphalt > 5% nano-silica-modified asphalt > matrix asphalt. With Buton rock asphalt content at 30% and nano-silica content at 5%, the R (0.1) and R (3.2) values of the composite-modified asphalt are 26.2% and 17.8% higher, respectively, than those of the nano-silica-modified asphalt. The irrecoverable creep compliance Jnr of the modified asphalt is as follows: 30% Buton rock asphalt/5% nano-silica composite-modified asphalt < 25% Buton rock asphalt/5% nano-silica composite-modified asphalt < 20% Buton rock asphalt/5% nano-silica composite-modified asphalt < 5% nano-silica-modified asphalt < matrix asphalt. At a Buton rock asphalt content of 30% and a nano-silica content of 5%, the Jnr0.1 and Jnr3.2 of the composite-modified asphalt reach the minimum values of 1.96 kPa^{-1} and 1.46 kPa^{-1}, which are 58.3% and 65.3% lower than those of nano-silica-modified asphalt. The fluctuations observed in the two indices of R and Jnr highlight the exceptional creep recovery capability of the Buton rock asphalt/nano-silica composite-modified asphalt. Notably, as the content of Buton rock asphalt increases, the creep recovery ability further improves, underscoring the outstanding high-temperature rutting resistance exhibited by the asphalt pavement.

4.2. Bending Creep Stiffness (BBR) Test

When asphalt is used in areas below 10 °C, it is easy to become brittle due to low temperatures [39]. Under the dual impact of low temperature and external loads, shrinkage cracks appear, affecting asphalt pavement's lifespan. Hence, asphalt requires robust low-temperature crack resistance to counter this.

To assess the low-temperature crack resistance of asphalt, SHRP intends to evaluate it using the stiffness modulus (S value) and the creep rate (m value) derived from the Bending Beam Rheometer (BBR) test [40]. The stiffness modulus S value signifies the capacity to withstand load-induced deformation under varying temperatures and loads. A smaller S value indicates better flexibility of the asphalt at low temperatures. Simultaneously, the creep rate (m value) illustrates the rate of change in the stiffness modulus (S value) with temperature variations. A higher m value implies reduced susceptibility to low-temperature stress, thereby minimizing the risk of low-temperature cracking.

According to the test procedure [38], BBR tests were carried out on five groups of asphalt samples, including matrix asphalt, 5% nano-SiO_2-modified asphalt, 20%, 25%, and 30% composite-modified asphalt with 5% nano-SiO_2. The test temperature is −12 °C, −18 °C, and −24 °C. To ensure favorable low-temperature crack resistance of the asphalt, the Superpave specification mandates that $S \leq 300$ MPa and $m \geq 0.3$ at 60 s. The creep stiffness modulus S-temperature curve and the creep rate m-temperature curve are depicted in Figures 9 and 10, respectively.

Test outcomes reveal that, under three distinct low-temperature conditions, the creep stiffness modulus of nano-SiO_2-modified asphalt and BRA/nano-SiO_2 composite-modified asphalt is inferior to that of matrix asphalt. When 5% nano-SiO_2 is added alone, the decrease is the largest. When 5% nano-SiO_2 is added alone, the decrease is the largest. The creep stiffness modulus S at −12 °C, −18 °C, and −24 °C decreased by 52.9 MPa, 179.5 MPa, and 445.9 MPa, respectively. The creep stiffness modulus at −24 °C was 286.7 MPa, which was less than the 300 MPa required by the specification. The creep stiffness modulus (S) signifies the flexibility of asphalt at low temperatures. The inclusion of Buton rock asphalt in composite-modified asphalt increases the creep stiffness modulus, thereby improving stress relaxation and low-temperature crack resistance, aided by nano-SiO_2. It is crucial to acknowledge that the introduction of Buton rock asphalt does lead to a certain reduction in the low-temperature crack resistance of the asphalt.

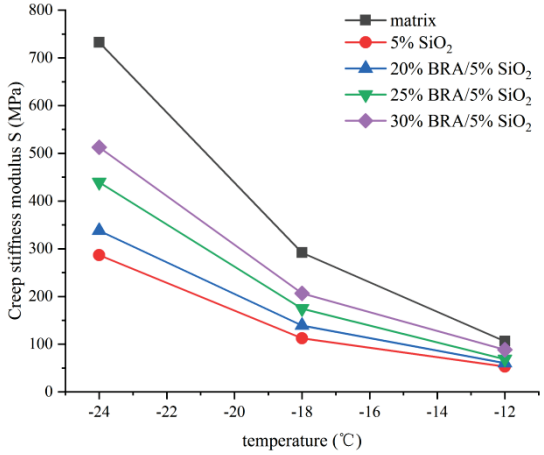

Figure 9. Creep stiffness modulus–temperature curve.

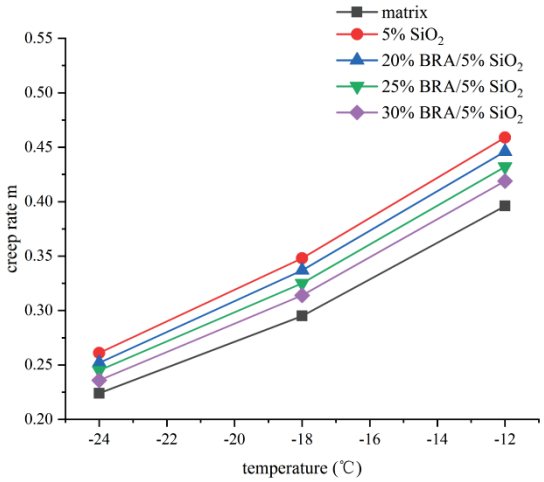

Figure 10. Creep rate–temperature curve.

The creep rate m of nano-SiO_2-modified asphalt and BRA/nano-SiO_2 composite-modified asphalt decreases with the decrease of temperature. Both nano-SiO_2-modified asphalt and BRA/nano-SiO_2 composite-modified asphalt exhibit higher creep rates than matrix asphalt at the same low temperature. At −18 °C, the creep rate m of 5% nano-SiO_2-modified asphalt, 20%, 25%, 30% nano-SiO_2-modified asphalt, and 5% nano-SiO_2-modified asphalt is 18.0%, 14.2%, 10.2%, 6.4% higher than that of matrix asphalt. The creep rate m represents the probability of low-temperature stress. The incorporation of nano-SiO_2 makes it difficult for asphalt to produce temperature stress at low temperatures. The incorporation of Buton rock asphalt makes it easier to produce temperature stress in asphalt, subsequently influencing the asphalt's resistance to low-temperature cracking.

Analyzing the creep stiffness modulus S and creep rate m reveals that the introduction of nano-SiO_2 enhances asphalt's low-temperature crack resistance, while the inclusion of Buton rock asphalt impacts the asphalt's low-temperature crack resistance. Taking all factors into account, when the composite-modified asphalt contains 25% Buton rock asphalt and 5% nano-silica, the resulting mixture exhibits excellent high-temperature performance and a certain degree of improved low-temperature performance.

4.3. Morphology Characterization Analysis of Composite-Modified Asphalt

The microscopic test image of matrix asphalt magnified by 15,000 times is shown in Figure 11.

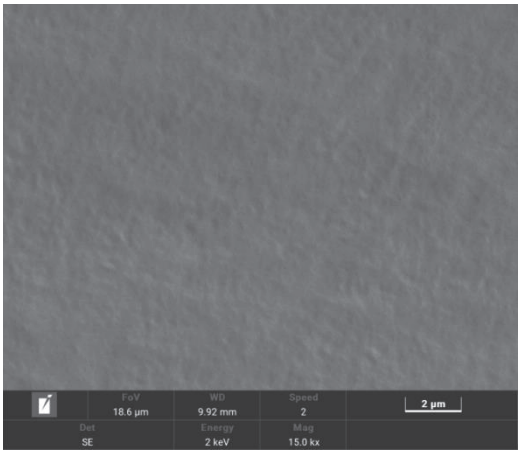

Figure 11. Electron microscopy of base asphalt.

As depicted in Figure 11, the matrix asphalt is magnified by a factor of 15,000, and no particle impurities are observed in the asphalt, which shows the characteristics of smooth and pure as a whole. This shows that the 70# road petroleum asphalt used in the test is pure and reliable, which is convenient to compare with the microstructure of Buton rock asphalt/nano-silica composite-modified asphalt.

The microscopic test image of Buton rock asphalt/nano-silica composite-modified asphalt is enlarged by 15,000 times, as shown in Figure 12.

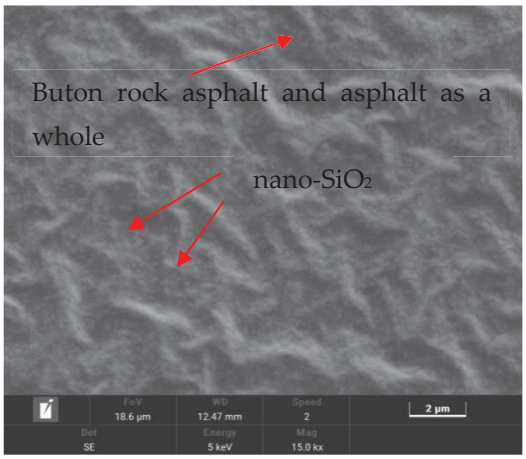

Figure 12. Electron microscopy of nano-SiO_2/BRA compound-modified asphalt.

From Figure 12, it can be seen that the Buton rock asphalt/nano-silica composite-modified asphalt is magnified by 15,000 times, the white dot material is nano-SiO_2, the white continuous phase is a structural whole composed of nano-SiO_2 and asphalt, and the black block area is Buton rock asphalt and asphalt as a whole [29]. Observations indicate the uniform distribution of nano-SiO_2 within the asphalt, attributed to the high-speed shearing process. Nano-SiO_2 belongs to the nano-size range, nano-SiO_2, and asphalt are fully integrated together, and a large part of nano-SiO_2 is wrapped by asphalt. There is no interface layering in the composite-modified asphalt, which indicates that the bonding between the substances is good. This phenomenon arises from the minute dimensions and expansive specific surface area of nano-SiO_2 particles. The activity of the existing particles has a high adsorption on the substances it contacts. The observation reveals a uniform dispersion of the medium, giving rise to a stable network structure through co-adsorption. Additionally, a polymerization effect occurs within the asphalt. This specially formed structure plays a pivotal role in transmitting and dissipating stress when the modified asphalt undergoes external and temperature-related stresses. The existence of nano-SiO_2

can produce stress concentration, micro-cracks appear around, and absorb the stress and energy of asphalt so that the asphalt shows good high and low-temperature performance and temperature sensitivity.

Due to its special "double-sided" structure, Budun rock asphalt melts at high temperatures, and its internal ash particles have been completely wrapped in asphalt, which contacts with nanoparticles and asphalt molecules, combines and interleaves. This overall structure has good support and stability. The ash particles inside this structure interlace each other to strengthen the rigidity of asphalt. The formation of the structure promotes the excellent combination and connection of nano-SiO_2 and asphalt molecules. The continuous phase formation impedes asphalt flow at high temperatures and prevents asphalt shrinkage deformation at low temperatures. The skeleton structure composed of nano and ash particles enhances the anti-bearing capacity of asphalt, leading to improved shear resistance and high/low-temperature performance in composite-modified asphalt.

4.4. Infrared Spectrum Test Analysis of Modified Asphalt

In this paper, the infrared spectrum (IR) test is carried out with a scanning range of 4000–400 cm^{-1}, a resolution of 0.4 cm^{-1}, and 64 scanning times. The infrared spectra of 5% silane coupling agent KH-550 modified nano-silica and untreated nano-silica are shown in Figure 13.

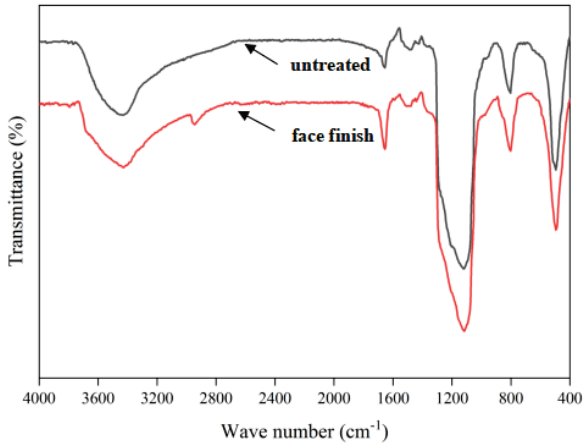

Figure 13. Infrared spectra of nano-silica before and after surface modification.

Figure 13 depict the infrared spectra of both untreated nano-SiO_2 and surface-modified nano-SiO_2. The wide absorption peak at about 3427.6 cm^{-1} in the infrared spectrum is the Si-OH stretching vibration peak of water hydroxyl (-OH) adsorbed on the surface of nano-SiO_2, and about 1653.9 cm^{-1} is the bending vibration peak of water hydroxyl Si-OH adsorbed on the surface of nano-SiO_2. The antisymmetric stretching vibration peak of Si-O-Si appears at about 1118.5 cm^{-1}, the symmetric stretching vibration peak of Si-O-Si appears at about 802.8 cm^{-1}, and the bending vibration peak of Si-O-Si appears at about 496.3 cm^{-1}. These three peaks are the characteristic absorption peaks of nano-SiO_2.

As observed in Figure 13, the absorption spectrum curves of untreated nano-SiO_2 and surface-modified nano-SiO_2 are fundamentally similar. Compared with the untreated nano-SiO_2, the surface-modified nano-SiO_2 has a weaker absorption peak at 3427.6 cm^{-1} than the untreated nano-SiO_2, which represents that the surface adsorption of nano-SiO_2 modified by silane coupling agent KH-550. The amount of water and the number of Si-OH groups decreased; a new peak at 2945.1 cm^{-1} appeared on the surface-modified nano-SiO_2, which represented the antisymmetric stretching vibration peak of methyl (-CH_3) and methylene (-CH_2) of silane coupling agent KH-550. Consequently, based on the infrared spectrum analysis, it is deduced that the chemical bond of the silane coupling agent KH-550 is indeed bonded with the surface of nano-SiO_2, and the reaction appears to be thorough

and adequate. The surface of nano-SiO_2 is 'grafted' successfully, and the nano-SiO_2 changes from inorganic to organic, which is easier to fuse with asphalt.

The infrared spectrum (IR) test of the composite-modified asphalt was also carried out with a scanning range of 4000–400 cm^{-1}, a resolution of 0.4 cm^{-1}, and a scanning number of 64 times. In order to facilitate the comparative analysis, the infrared spectra of the composite-modified asphalt and the matrix asphalt are drawn together. Figure 14 displays the infrared spectra of the composite-modified asphalt with 25% content of Buton rock asphalt and 5% content of nano-silica, alongside the infrared spectrum of the matrix asphalt.

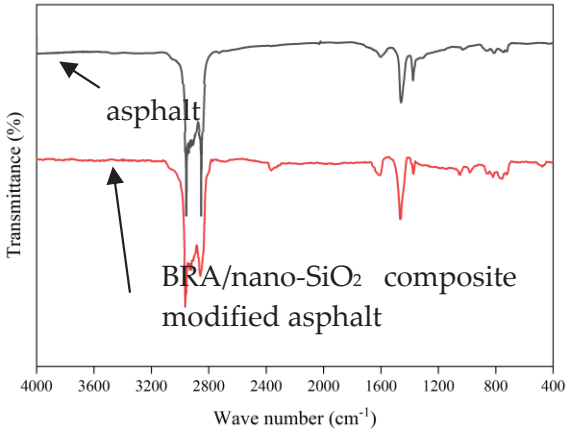

Figure 14. Infrared spectra of two kinds of modified asphalt.

As evident in Figure 14, the absorption peak of Buton rock asphalt/nano-silica composite-modified asphalt and matrix asphalt at approximately 2960.26 cm^{-1} corresponds to the antisymmetric stretching vibration peak of methyl (-CH_3) and methylene (-CH_2), indicating the stretching vibration of the C-H bond on the benzene ring. The absorption peak at about 1608.34 cm^{-1} represents the vibration peak of the benzene ring skeleton. The absorption peaks at 1463.71 cm^{-1} and 1376.85 cm^{-1} denote the antisymmetric and symmetric bending vibrations of methyl (-CH_3) or methylene (-CH_2), representing the saturated hydrocarbon structure in asphalt molecules. The absorption peak around 1049.09 cm^{-1} is the symmetrical stretching vibration peak of S = 0, which represents the sulfur functional group of sulfoxide structure in asphaltene. Multiple absorption peaks in the range of 690–870 cm^{-1} are aromatic C-H out-of-plane bending vibrations, representing aromatic compounds in asphalt.

Compared with the matrix asphalt, the absorption peak of the composite-modified asphalt is roughly all the nano-SiO_2. The new absorption peak at 979.66 cm^{-1} represents the Si-O-CH_2 bond of the silane coupling agent KH-550, indicating that the coupling agent KH-550 group is still on the nano-SiO_2 molecule after the composite-modified asphalt is prepared by high-speed shearing. Buton rock asphalt has no chemical reaction with asphalt, and the material is mainly physical blending.

5. Conclusions

(1) Incorporating Buton rock asphalt and nano-silica significantly enhances the complex shear modulus G* of the composite-modified asphalt while reducing the phase angle δ. The rutting factor G*/sinδ also experiences a substantial increase. When compared to the matrix asphalt, the composite-modified asphalt containing 30% Buton rock asphalt and 5% nano-silica exhibits a remarkable enhancement: a 9.41 kPa rise in complex shear modulus G* at 70 °C, a 29.42° decrease in phase angle δ, and an 11.11 kPa increase in rutting factor G*/sinδ. The frequency scanning master curve is at a high level at 64 °C. The matrix asphalt almost completely loses its creep recovery ability at 0.1 kPa and 3.2 kPa stress levels. Both nano-silica-modified asphalt and Buton rock asphalt/nano-silica

composite-modified asphalt exhibit superior high-temperature deformation resistance compared to the matrix asphalt.

Furthermore, the high-temperature performance of the composite-modified asphalt exhibits a continuous enhancement with the increasing content of Buton rock asphalt. Specifically, when the content of Buton rock asphalt is at 30% and the content of nano-SiO_2 is at 5%, the rutting resistance of the composite-modified asphalt reaches its peak strength. The incorporation of both Buton rock asphalt and nano-SiO_2 contributes significantly to the improvement of the asphalt's high-temperature performance.

(2) Across different low temperatures, both nano-silica-modified asphalt and Buton rock asphalt/nano-silica composite-modified asphalt showed a reduction in the creep stiffness modulus (S) compared to matrix asphalt. The inclusion of nano-silica contributes to enhanced stress relaxation performance of asphalt at low temperatures, resulting in a significant improvement in low-temperature crack resistance. Additionally, the creep rate (m) of nano-silica-modified asphalt was higher than that of matrix asphalt. In contrast to the matrix asphalt, the creep stiffness modulus S of 5% nano-silica-modified asphalt decreased by 61.5% at −18 °C, and the creep rate m increased by 18.0% at −18 °C, suggesting the introduction of nano-silica. At lower temperatures, asphalt is less prone to produce temperature stress, resulting in an improved resistance to low-temperature cracking. In comparison to the matrix asphalt, the creep stiffness modulus (S) at −18 °C decreased by 40.2%, and the creep rate (m) at −18 °C increased by 10.2% with the incorporation of Buton rock asphalt. The presence of Buton rock asphalt renders the asphalt more susceptible to temperature stress, thereby influencing its low-temperature performance.

(3) Nano-silica is uniformly dispersed throughout the asphalt. After surface modification, nano-silica is easy to combine with asphalt. Due to the existence of natural asphalt in the composition, buton rock asphalt and matrix asphalt together constitute the whole asphalt system. The overall structure has a good supporting effect and stability. Buton rock asphalt/nano-silica composite-modified asphalt shows superior bearing capacity and high and low-temperature performance.

(4) The antisymmetric stretching vibration peaks of methyl (-CH_3) and methylene (-CH_2) appeared in about 2960.26 cm^{-1} of Butun rock asphalt/nano-silica composite-modified asphalt and matrix asphalt, and the infrared spectra of the two kinds of asphalt were roughly the same. The appearance of the Si-O-CH_2 bond of silane coupling agent KH-550 represents the KH-550 group in asphalt. In general, the absorption spectra and curves of Buton rock asphalt/nano-silica composite-modified asphalt and matrix asphalt are not much different, indicating that nano-SiO_2 has a chemical reaction in asphalt, but this reaction is not strong. Buton rock asphalt has no chemical reaction with asphalt, and the material is mainly physical blending.

Author Contributions: Writing—original draft preparation, C.L., Z.L. and S.J.; writing—review and editing, T.G., Y.C. and S.J.; investigation, J.W. and L.J.; discussion, C.L., T.G. and Y.C. All authors have read and agreed to the published version of the manuscript.

Funding: This work was supported by Key R&D and Promotion of Special Scientific and Technological Research Projects of Henan Province: [Grant Number 182102210061].

Institutional Review Board Statement: Not applicable.

Informed Consent Statement: Not applicable.

Data Availability Statement: Some or all data, models, or codes that support the findings of this study are available from the corresponding author upon reasonable request.

Conflicts of Interest: The authors declare that Henan Transportation Research Institute Co., Ltd. and Xi'an Changda Highway Engineering Inspection Center Co., Ltd. was not involved in the study design, collection, analysis, interpretation of data, the writing of this article or the decision to submit it for publication. The authors declare no conflict of interest.

References

1. Li, P. Research on construction quality control of asphalt pavement. *Transp. Manag. World* **2022**, *24*, 10–12.
2. Wang, F. Analysis of the influence of different kinds of modifiers on the performance of matrix asphalt. *Appl. Chem. Ind.* **2021**, *50*, 2132–2135+2139. [CrossRef]
3. Chen, Q.; Li, Y.; Wang, C.; Feng, L.; Zhang, Z. Degradation of mechanical properties of polyurethane elastomer coatings under different pavement pollution conditions. *Constr. Build. Mater.* **2023**, *409*, 134181. [CrossRef]
4. Wang, Y. Application research status of nano modified asphalt materials in pavement engineering. *Aging Appl. Synth. Mater.* **2022**, *51*, 159–161. [CrossRef]
5. Yang, X. Nano-silica and its application status and development prospect. *Inn. Mong. Petrochem. Ind.* **2011**, *37*, 26–27.
6. Shafabakhsh, G.; Sadeghnejad, M.; Ebrahimnia, R. Fracture resistance of asphalt mixtures under mixed-mode I/II loading at low-temperature: Without and with nano SiO_2. *Constr. Build. Mater.* **2021**, *266*, 120954. [CrossRef]
7. Yadykova, A.Y.; Ilyin, S.O. Rheological and adhesive properties of nanocomposite bitumen binders based on hydrophilic or hydrophobic silica and modified with bio-oil. *Constr. Build. Mater.* **2022**, *342*, 127946. [CrossRef]
8. Cheraghian, G.; Wistuba, M.P. Effect of Fumed Silica Nanoparticles on Ultraviolet Aging Resistance of Bitumen. *Nanomaterials* **2021**, *11*, 454. [CrossRef] [PubMed]
9. Lu, X.; Zhang, S.; Wu, Y. Effect of Budun rock aggregate on the performance of asphalt mixture. *J. Build. Mater.* **2015**, *18*, 450–457.
10. Tang, Y.; Ling, L.; Lu, W.; Zhang, H.; Zhao, Q. Study on Performance Test and Road Use Value of BRA Modified Asphalt Mixture. *Heilongjiang Transp. Sci. Technol.* **2023**, *46*, 45–47. [CrossRef]
11. Zhang, Z. Research on Performance of BRA Modified Asphalt. *IOP Conf. Ser. Earth Environ. Sci.* **2021**, *719*, 022086. [CrossRef]
12. Zhou, Z. Study on Rheological Properties of BRA Modified Asphalt. *IOP Conf. Ser. Earth Environ. Sci.* **2019**, *330*, 042030. [CrossRef]
13. Li, R.X.; Hao, P.W.; Wang, C. Performance Evaluation of BRA Modified Asphalt Based on Analysis of Rheological Property. *Adv. Mater. Res.* **2011**, *374–377*, 1385–1390. [CrossRef]
14. Muhammad, K.; Ainalem, N.; Ahdyeh, M.; Hamid, N. Evaluation of Permanent Deformation of BRA Modified Asphalt Paving Mixtures Based on Dynamic Creep Test Analysis. *Adv. Eng. Forum* **2016**, *4416*, 69–81. [CrossRef]
15. Bo, S. Study on preparation and properties of High viscosity elastic restored asphalt. *Highw. Automob. Transp.* **2023**, *2*, 49–52+72. [CrossRef]
16. Wu, Y.; Liao, J.; Huang, W.; Feng, W.; Cao, M. High temperature performance analysis of Buton rock asphalt modified asphalt. *J. Chengdu Univ.* **2019**, *38*, 106–110.
17. Wang, M.; Lin, F.; Liu, L. Dynamic rheological properties and microscopic characteristics of Buton rock asphalt ash mortar. *J. Tongji Univ.* **2016**, *44*, 567–571.
18. Zhou, C.; Zhang, S.; Guan, Y.; Zhou, W. Research on improving the performance of matrix asphalt slurry with high ash natural rock asphalt. *Highw. Transp. Technol. (Appl. Technol. Ed.)* **2016**, *12*, 44–46.
19. Lei, M.; Fei, Y. Research on application of rock asphalt high strength mixture BRAC-16 in cold region. *Shanxi Archit.* **2017**, *43*, 112–113. [CrossRef]
20. Yang, Y.; Huang, P.; Zhou, W.; Liu, H.; Fei, Y. High ash rock asphalt modified asphalt mixture road performance and its mechanism of action. *Highw. Transp. Technol. (Appl. Technol. Ed.)* **2019**, *15*, 22–25.
21. Gholam, A.S.; Mostafa, S.; Behzad, A.; Esmaiel, T. Laboratory experiment on the effect of nano SiO_2 and TiO_2 on short and long-term aging behavior of bitumen. *Constr. Build. Mater.* **2020**, *237*, 117640. [CrossRef]
22. Sun, L.; Xin, X.; Ren, J. Inorganic Nanoparticle-Modified Asphalt with Enhanced Performance at High Temperature. *J. Mater. Civ. Eng.* **2016**, *29*, 04016227. [CrossRef]
23. Zhu, W. Effect of nano-silica content on the performance of asphalt mixture. *Contemp. Chem. Ind.* **2019**, *48*, 2553–2556. [CrossRef]
24. Sun, L.; Xin, X.; Yu, P. Pavement performance of nano-SiO_2 modified asphalt mixture. *Highw. Traffic Technol.* **2013**, *30*, 1–5.
25. Yang, Y.S.; Fan, W.Y.; Wang, Z.; Zhang, Q.Q.; Nan, G.Z. Effect of Nano SiO_2 on the Performance of Asphalt Emulsion and its Residue. *Adv. Mater. Res.* **2011**, *413*, 331–335. [CrossRef]
26. Mehmet, S.; Serdal, T.; Sebnem, K. Examination of hot mix asphalt and binder performance modified with nano silica. *Constr. Build. Mater.* **2017**, *156*, 976–984. [CrossRef]
27. He, H.; Hu, J.; Li, R.; Shen, C.; Pei, J.; Zhou, B. Study on rheological properties of silica nanofluids modified asphalt binder. *Constr. Build. Mater.* **2021**, *273*, 122046. [CrossRef]
28. Yue, C.; Gao, D.; Wang, Y.; He, W.; Fu, L.; Liu, C.; Li, Z.; Cheng, F. Preparation and properties evaluation of micro-nano SiO_2 modified asphalt. *Fine Chem. Ind.* **2023**, *40*, 2302–2311. [CrossRef]
29. Tan, Y. Study on properties of oil-wet nano-silica modified asphalt. *Transp. Sci. Technol.* **2023**, 108–114.
30. Zhang, H.; Zhu, C.; Zhang, B.; Yu, J. Effects of surface modified nano-silica on asphalt properties. *J. Build. Mater.* **2014**, *17*, 172–176.
31. Long, Z.; Zhou, S.; Jiang, S.; Ma, W.; Ding, Y.; You, L.; Tang, X. Revealing compatibility mechanism of nanosilica in asphalt through molecular dynamics simulation. *J. Mol. Model.* **2021**, *27*, 81. [CrossRef] [PubMed]
32. Long, Z.; Tang, X.; Guo, N.; Ding, Y.; Ma, W.; You, L.; Xu, F. Atomistic-scale investigation of self-healing mechanism in Nano-silica modified asphalt through molecular dynamics simulation. *J. Infrastruct. Preserv. Resil.* **2022**, *3*, 4. [CrossRef]
33. Khordehbinan, M.; Fakhrefatemi, S.-M.-R.; Ghanbari, S.; Ghanbari, M. The effect of nano-SiO_2 and the styrene butadiene styrene polymer on the high-temperature performance of hot mix asphalt. *Pet. Sci. Technol.* **2017**, *35*, 553–560. [CrossRef]

34. Abed, A.H.; Oudah, A.M. Rheological properties of modified asphalt binder with nanosilica and SBS. *IOP Conf. Ser. Mater. Sci. Eng.* **2018**, *433*, 012031. [CrossRef]
35. Mostafa, S.; Gholamali, S. Use of Nano SiO_2 and Nano TiO_2 to improve the mechanical behaviour of stone mastic asphalt mixtures. *Constr. Build. Mater.* **2017**, *157*, 965–974.
36. Shafabakhsh, G.H.; Ani, O.J. Experimental investigation of effect of Nano TiO_2/SiO_2 modified bitumen on the rutting and fatigue performance of asphalt mixtures containing steel slag aggregates. *Constr. Build. Mater.* **2015**, *98*, 692–702. [CrossRef]
37. *T/CECS G: D54-02-2020*; Technical Specification for Application of Buton Bituminous Rock in Road. People's Transportation Press: Beijing, China, 2020.
38. *JTG E20-2011*; Test Code for Asphalt and Asphalt Mixture of Highway Engineering. People's Traffic Press: Beijing, China, 2011.
39. Shao, F. *Study on Preparation Process of SBS Modified Emulsified Asphalt*; East China University of Science and Technology: Shanghai, China, 2021. [CrossRef]
40. Yin, H.; Li, K. Evaluation of low-temperature performance of asphalt based on bending beam rheological test and viscoelastic theory. *Funct. Mater.* **2021**, *52*, 10157–10165.

coatings

MDPI

Article

Thermal-Mechanical Coupling Analysis of Permeable Asphalt Pavements

Yuekun Li [1], Xulong Wang [2], Hailong Zhang [2], Zhenxia Li [2,3,4,*] and Tengteng Guo [2,3,4]

[1] College of Geosciences and Engineering, North China University of Water Resources and Electric Power, Zhengzhou 450046, China
[2] School of Civil Engineering and Transportation, North China University of Water Resources and Electric Power, Zhengzhou 450045, China
[3] Henan Province Engineering Technology Research Center of Environment Friendly and High-Performance Pavement Materials, Zhengzhou 450045, China
[4] Zhengzhou City Key Laboratory of Environmentally Friendly High Performance Road and Bridge Materials, Zhengzhou 450045, China
* Correspondence: zhenxiali2009@ncwu.edu.cn

Abstract: In order to clarify the mechanical response of permeable asphalt pavements under a temperature effect, the mechanical responses of different types of permeable asphalt pavements, which were based on a self-developed drainage SBS-modified asphalt mixture with fiber, were simulated using ANSYS finite element software (APDL 19.2). The influence of temperature and temperature change on the mechanical behavior of the permeable asphalt pavements was studied, and the mechanical responses of the pavements at different driving speeds was analyzed. The results show that the extreme values of surface deflection, compressive strain of the soil foundation top surface, and the shear stress and tensile stress of the upper-layer bottom of the three kinds of pavements under dynamic load were about 10% smaller than those under static loads, and the extreme values under different temperature conditions were 28%~50% larger than the values obtained without different temperature conditions. During the 12 h heating process, the mechanical indexes of the three types of pavements with axle loads were consistent with the change law of temperature, and the peak values of the mechanical indexes under dynamic loads were smaller than those under static loads. In addition, the mechanical indexes of the three types of pavements under dynamic loads had the same law of change with speed under the same conditions, and the values were less than the extreme values under static loads, but the degree of influence was different.

Keywords: permeable asphalt pavement; temperature effect; mechanical response; finite element simulation

1. Introduction

With the rapid development of the economy and the acceleration of urban construction, the natural ground in cities gradually becomes covered by impervious hardened surfaces. These surfaces have good bearing capacity and aesthetics but also bring some negative effects to the urban ecological environment [1–3]. Permeable Asphalt Concrete (PAC), a new type of pavement structure based on the green sponge city concept, is widely used because of its good skid resistance, noise reduction and water permeability properties [4,5].

Because porosity is the key factor affecting the permeability of a pavement, the permeability coefficient of the pavement is mainly affected by the connected pores of the material, and the connected pores are closely related to the composition of the material and the shape of the aggregate. Therefore, researchers have conducted much research on the material composition of pavements. Scholars often use the porosity and permeability of a permeable asphalt pavement as the key indicators of pavement design. Considering the relationship between the porosity of a permeable asphalt pavement and the key sieve

holes, the key sieve hole affecting the porosity of the mixture has a passing rate of 2.36 mm. Careful design to achieve passing rates of 4.75 mm and 2.36 mm allows the mixture to more easily form a skeleton structure [6–8]. The porosity of a permeable asphalt mixture affects the high-temperature stability, low-temperature deformation resistance and water damage resistance. Under the same thermal aging time, there is a positive linear relationship between dynamic stability and porosity. However, the higher the porosity of a porous asphalt mixture, the higher the tendency for flexural tensile failure and shrinkage stress at low temperature, and the worse the ability to resist water damage [9]. At the same time, researchers have found that under the same rainfall conditions, there is not only a good linear correlation between porosity and the permeability coefficient, but also a correlation between surface thickness and the permeability coefficient. In addition, the increase in porosity and pavement thickness can not only effectively improve the drainage effect of pavements, but also improve the water storage capacity of permeable roads. A greater total thickness of pavement, especially with an increase in porosity from 18% to 22%, can significantly improve the water storage capacity of permeable roads [10].

Permeable asphalt pavements are widely used in high-rainfall areas because of their high permeability. Therefore, some researchers have studied the permeability and road performance of pavement structures. The skid resistance of a drainage asphalt mixture is easily affected by rainfall conditions. From the analysis of the relationship between surface characteristics and skid resistance, it can be seen that with an increase in rainfall, the friction coefficient of a drainage asphalt mixture decreases rapidly and then tends to be stable [11]. During a rainfall event, the runoff coefficient of a permeable asphalt pavement is a single-peak dynamic change, and when the rainfall intensity is less than 50 mm/h, the permeable asphalt pavement does not produce runoff [12]. The cross slope and the longitudinal slope have significant effects on the drainage performance of the porous asphalt surface layer. The improvement in the drainage performance resulting from the cross slope is affected by the size of the longitudinal slope, and the thickness and width of the pavement. The influence of the longitudinal slope change decreases with the increase in the percentage of the cross slope and the decrease in the ratio of the thickness of the porous asphalt layer to the width of the pavement [13]. The influence of the road surface on rainwater runoff is mainly affected by the load and road slope. When the rainfall intensity is less than 98 mm/h, there will be no surface runoff [14].

More importantly, there is an inevitable relationship between the viscoelastic parameters of a permeable asphalt mixture and temperature. With decreasing temperature, the viscoelastic parameters of the mixture gradually become elastic parameters. At the same time, the bulk modulus and shear modulus in the plastic model also gradually show obvious viscoelastic properties with the increase and decrease in temperature [15]. In terms of structure design, the thickness and type of base course are the key factors affecting the mechanical properties of a permeable asphalt pavement. At the same time, the coarse-grained stress-absorbing layer can effectively absorb stress and reduce the occurrence of reflective cracks [16,17]. In addition, compared with the water-free state in the asphalt pavement structure, the stress field and displacement field inside the asphalt pavement structure widen pavement cracks under the action of water and dynamic load, causing the cracks to expand greatly, but have no obvious effect on the shear expansion of the cracks [18].

In summary, the current research on permeable asphalt pavements mainly focuses on pavement permeability, porosity, road performance and the mechanical properties of materials. The research on mechanical properties is still at the stage of single-axle loads, and there is a lack of in-depth studies on the mechanical properties of permeable asphalt pavements under multi-field coupling. According to the composition characteristics and functional objectives of porous pavement materials, the service environment is relatively complex, making it necessary to analyze multi-physical fields such as water permeability, heat transfer and stress. Therefore, it is necessary to study the temperature effect and mechanical response of permeable asphalt pavement under the coupling of temperature and structure fields. From the perspective of the coupling of heat transfer and stress, the

cooling effect and mechanical response of permeable asphalt pavement were studied, and the mechanical responses based on temperature effect and standard axle load (dynamic and static load) were analyzed.

2. Materials and Methodology

2.1. Materials

Based on its different permeable layers and permeable ranges, the pavement structure can be divided into three types [19], as shown in Figure 1: surface permeable type (Type A), base permeable type (Type B), and full permeable type (Type C). Among these, Type A is a double-sided permeable layer, and the upper layer of the three composite structures is made of self-developed drainage SBS-modified asphalt concrete (OGFC-13) mixed with fibers. The structural form of the permeable asphalt pavement and the thickness of each structural layer are as shown in Table 1.

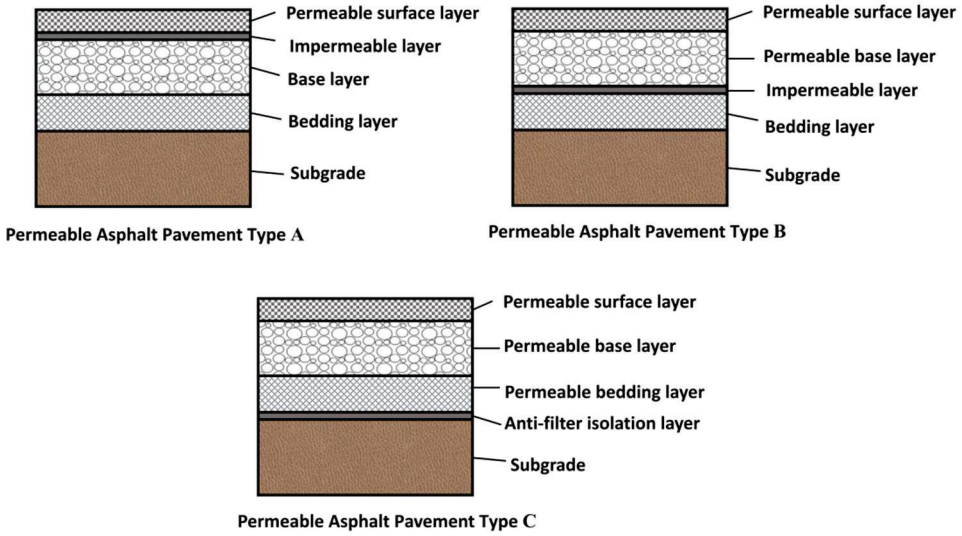

Figure 1. Permeable asphalt pavement structure types.

Table 1. Composite structure of permeable asphalt pavement.

STRUCTURAL LAYER	TYPE A	TYPE B	TYPE C	THICKNESS (CM)
TOP SURFACE COURSE	OGFC-13	OGFC-13	OGFC-13	12
THE FOLLOWING LAYER	ATPB-25	ATPB-25	ATPB-25	30
FOUNDATION COURSE	Water-stable gravel	Graded broken stone	Graded broken stone	25
BASE COURSE	Graded broken stone	Graded broken stone	Graded broken stone	20
SUBGRADE	Compacted soil	Compacted soil	Mild compacted soil	—

Note: OGFC is open graded friction course, ATPB is asphalt treated permeable base.

2.2. FEM Model

2.2.1. Basic Assumptions

Based on the theory of elastic layered systems, ANSYS (APDL19.2) was used to establish a numerical model to analyze the structural mechanics of a permeable asphalt pavement, and the actual solar radiation intensity was used as the heating condition to analyze and calculate the surface temperature of the permeable asphalt pavement. The following hypotheses were proposed.

(1) Basic assumptions of temperature field model

① Each structural layer of the permeable asphalt pavement was considered to be homogeneous and have a continuous material composition.

② The contact state, temperature and heat transfer between the structural layers were considered to be continuous, without thermal resistance, and the heat transfer interface effect between the layers was not considered.

③ The soil base surface was considered to be in a constant temperature state, and the geothermal effect on the temperature of the pavement structure was not considered.

④ The top surface of the model was the heating surface, and the other surfaces were adiabatic surfaces. The actual heat loss of the adiabatic surface and the external thermal convection process were not considered.

⑤ Only the effect of solar radiation was considered, while wind speed and other factors were not considered.

(2) Basic assumptions of mechanical model

① Each structural layer was considered to be a homogeneous and isotropic elastic material.

② The road surface was subjected to axisymmetric uniform vertical load, and the stress and strain at the infinite depth of the bottom layer and the horizontal infinite position were zero.

③ Stress, strain and displacement can be expressed by continuous functions of coordinates.

④ Structural weight was not considered.

2.2.2. Determination of Pavement Structure Parameters

In this study, ANSYS software (APDL 19.2) was used to analyze the mechanics of three kinds of permeable asphalt pavement, ignoring the instantaneous plastic deformation caused in the pavement structure during the fast-driving process of the vehicle. The size of the pavement structure model was 6000 mm × 3000 mm × 5000 mm, and SOLID 70 was selected as the temperature field analysis unit. After the analysis was completed, it was converted into the SOLID 185 unit for structural field analysis. All the units were eight-node three-dimensional hexahedral units. The grid was divided from fine to coarse, and the analysis area was encrypted.

In addition, the initial state of the pavement structure was assumed to be stress-free. The horizontal and vertical boundaries of the uppermost layer of pavement were unconstrained, and the bottom of soil foundation was completely fixed. The horizontal displacement of the left and right sides of the pavement structure model was set to 0, and the longitudinal displacement of the front and rear sides of the pavement structure model was set to 0.

2.2.3. Determination of Pavement Material Parameters

The values of material mechanical parameters and thermophysical parameters based on previous research results are shown in Tables 2 and 3. In fact, the material of permeable asphalt pavements is greatly affected by temperature, and the results analyzed without considering the influence of temperature on material parameters cannot accurately reveal the mechanical response characteristics of a permeable asphalt pavement structure [20]. Therefore, the influence of temperature change on the surface layer material parameters can be considered, and the change of other structural layer material parameters with temperature can be ignored [21].

Table 2. Mechanical parameters of pavement materials.

STRUCTURAL LAYER	MATERIAL	ELASTIC MODULUS (MPA)	POISSON RATIO (M)	DENSITY (KG/M3)
TOP SURFACE COURSE	OGFC-13	1400	0.25	2500
THE FOLLOWING LAYER	ATPB-25	800	0.35	2100
FOUNDATION COURSE	Water-stable gravel	1500	0.25	2300
BASE COURSE	Graded broken stone	500	0.35	2100
SUBGRADE	Soil	50	0.35	1850

Table 3. Values of thermal properties.

Structure Type	Heat Capacity (J/kg·°C)				Thermal Conductivity (W/m·°C)			
	Top Surface Course	The Following Layer	Foundation Course	Base Course	Top Surface Course	The Following Layer	Foundation Course	Base Course
A	800	800	600	800	0.6	0.6	1.1	0.8
B	800	800	800	800	0.6	0.6	0.8	0.8
C	800	800	800	800	0.6	0.6	0.8	0.8

(1) Elastic modulus

The functional relationship between elastic modulus and temperature load is as follows in Equation (1) [22].

$$\frac{E_T}{E_0} = 10^{0.01693(20-T)} \tag{1}$$

where T is the calculating temperature, °C, E_T is the elastic modulus at the calculated temperature, MPa, E_0 is the elastic modulus at standard temperature (20 °C), MPa.

(2) Poisson ratio

The values of the Poisson ratio of asphalt mixture at different temperatures in references are obtained [22,23]. The relationship between the Poisson ratio of an asphalt mixture and temperature is obtained by linear regression, as shown in Equation (2).

$$\mu_1(T) = 0.005 \times T + 0.15 \tag{2}$$

where $\mu_1(T)$ is the Poisson ratio of the asphalt mixture.

(3) Coefficient of linear expansion

The temperature linear expansion coefficient of an asphalt mixture can be expressed by Equation (3) [21].

$$\alpha_1(T) = 35.28e^{-\left(\frac{T+6.004}{36.07}\right)^2} \times 10^{-6} \tag{3}$$

where $\alpha_1(T)$ is the temperature linear expansion coefficient of asphalt layer at $1/°C$.

2.2.4. Determination of Load Parameters

The tire contact area needs to be determined when the pavement structure is analyzed and simulated. It is assumed that the vehicle load is evenly distributed on the contact surface between the tire and the road surface, and the area of the contact surface is calculated according to the contact pressure value. In order to facilitate the simulation, the elliptical load is transformed into a rectangular load.

(1) Static load parameters

In the pavement design, a rectangular load was used in the structural mechanics calculations [24]. The rectangular load area was 0.8712 L × 0.6 L, and the standard axle load BZZ-100 was used in the calculation and analysis. The tire grounding equivalent rectangular side length is shown in Equations (4)–(6).

$$S = \frac{F}{P} \tag{4}$$

$$L = \sqrt{\frac{S}{0.5227}} \tag{5}$$

$$D = 1.5\sqrt{\frac{4S}{\pi}} \tag{6}$$

where S is the rectangular load area, m^2; L is the rail length of the driving direction, m; and D is center distance of two wheels, m.

According to the calculation results of Equations (4)–(6), the center distance of the two wheels was 0.32 m, and the adjusted distance was 31.98 cm. The rectangular side length of the single wheel was 0.157 m × 0.227 m, and the adjusted distance was 0.167 m × 0.213 m according to the actual situation. The clearance between the two wheels was 0.106 m. The calculation parameters of the standard axle load and the specific content of the rectangular load are shown in Table 4.

Table 4. Standard axle load calculation parameters.

STANDARD AXLE LOAD	BZZ-100	STANDARD AXLE LOAD	BZZ-100
STANDARD AXLE LOAD P (KN)	100	Single wheel transmission equivalent rectangular edge length L (cm)	16.7 × 21.3
TIRE GROUND PRESSURE P (MPA)	0.70	Center distance of two wheels (cm)	31.95

(2) Dynamic load parameters

The dynamic load was in the form of half sine [25]. According to the current pavement design specifications, P_{max} = 0.7 MPa, the equivalent radius of single wheel pressure transmission was 10.65 cm. The relationship between load and time is shown in Equation (7):

$$\begin{cases} P = P_{max} \times \sin(\frac{\pi}{T}t) & 0 \le t \le T \\ P = 0 & t > \mathrm{T} \end{cases} \quad (7)$$

The relationship between loading time and vehicle speed is shown in Equation (8).

$$T = 12\frac{R}{V} \quad (8)$$

where R is the equivalent circle radius of single wheel pressure transmission, cm; and V is the vehicle speed, km/h.

When the vehicle speed was 60 km/h, the load action time was 0.0767 s. From Equations (7) and (8), the change in load period is shown in Figure 2.

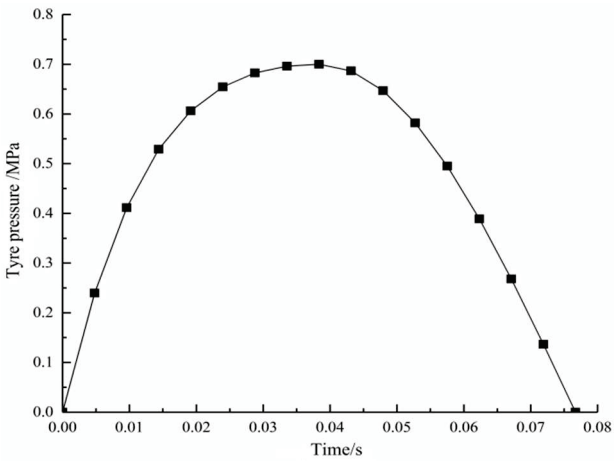

Figure 2. Diagram of load form.

(3) Temperature load parameters

The variation in daily solar radiation intensity in a certain area was taken as the daily solar radiation intensity on the road surface of the road structure. The results are shown in Figure 3. The absorption coefficient of the permeable asphalt pavement structure surface

was set as 0.87 [17]. The analysis curve of temperature change with time during the 12 h heating process for the three kinds of pavements is shown in Figure 4, which was applied as temperature load.

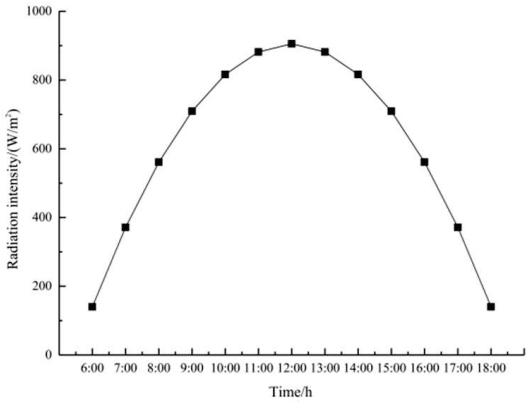

Figure 3. Diurnal variation curve of solar radiation intensity.

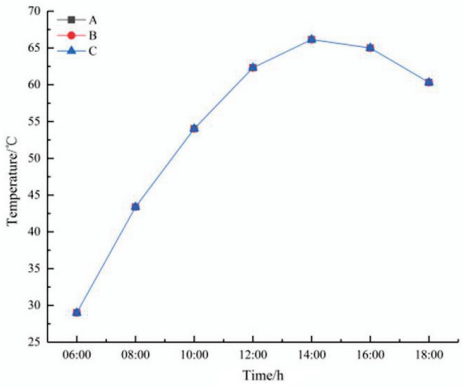

Figure 4. The 12 h heating curve of a permeable asphalt pavement.

2.3. Data Processing and Analysis

Technical specification for permeable asphalt pavement (CJJ/T 190-2012) [26] stipulates that the design of a pavement structure should take the deflection value of the pavement surface and the bending tensile stress at the bottom of structural layers as design indexes. The load mode of mechanical calculation using the theory of an elastic layered continuous system is a vertical uniform load, and the interlayer contact condition is completely continuous. According to the specification, the mechanical variation law of the permeable asphalt pavement structure was analyzed by the deflection value of the road surface, the flexural tensile stress and shear stress at the bottom of each structural layer.

2.3.1. Model Validity Analysis

When using finite element software for analysis, it is often necessary to verify the correctness of the model to ensure that the boundary conditions, mesh division and element type are reasonable. The calculation results in the relevant literature [27,28] are used as the reference to verify the correctness of the model. Due to differences in the simulation software or calculation accuracy, there will be some errors in the calculation results. Therefore, when conducting verification, if the relative error is within 10%, the model created is considered to be feasible [22]. The mechanical model verification and temperature field model verification are carried out, respectively. The modeling materials, load parameters and boundary conditions are the same as the existing research results, and the relevant parameters are shown in Tables 5 and 6.

Table 5. Material parameters of mechanical model structures.

STRUCTURAL TYPE	MATERIAL	THICKNESS (MM)	ELASTIC MODULUS (MPA)	POISSON RATIO (μ)	DENSITY (KG/M3)
TOP SURFACE COURSE	PAC-13	40	900	0.25	2100
THE FOLLOWING LAYER	PAC-16	60	850	0.25	2100
BASE LAYER	Cement stabilized macadam	200	1500	0.25	2300
PAVEMENT SUBBASE	Graded broken stone	150	500	0.35	2100
SUBGRADE	Soil	—	50	0.35	1850

Table 6. Material parameters of temperature field model structures.

STRUCTURAL TYPE	TOP SURFACE COURSE	THE FOLLOWING LAYER	BASE LAYER	PAVEMENT SUBBASE	SUBGRADE
MATERIAL	OGFC-13	ATPB	Graded broken stone	Graded broken stone	Soil
THICKNESS (MM)	100	200	200	300	500

2.3.2. Analysis of Mechanical Indexes with and without Temperature Effect

The three types of permeable asphalt pavement were analyzed with 12 h heating, and the pavement temperature calculation results at the peak time of pavement temperature were extracted as temperature conditions for the coupling field calculation. The surface deflection, compressive strain of the soil foundation top, tensile stress and shear stress of asphalt layer bottom were extracted and compared. The calculation time was 8 h, the pavement temperature was 66 °C, the static load was a standard axle load, and the dynamic load speed was 60 km/h.

2.3.3. Influence of Temperature Change on Mechanical Indexes

Firstly, the radiation intensity mentioned above was used as the temperature condition to calculate the temperature rise in the pavement structure for 12 h. Then, the temperature field calculation results were saved every 2 h from the initial time, and applied as the temperature load of the coupled field calculation. The temperature change was represented by the different time of the temperature rise calculation. The corresponding mechanical indexes were extracted and the time–mechanical index change curve was plotted to analyze the influence of temperature change. Among them, the static load was the standard axle load and the dynamic load speed was 60 km/h.

2.3.4. Influence of Vehicle Speed on Mechanical Properties of Permeable Asphalt Pavement

The finite element calculations for three kinds of permeable asphalt pavement were carried out under the same temperature condition as described in the above section, and the calculation results of each control index peak under dynamic load were extracted to analyze the influence of vehicle speed change on the main control indexes. The speed values were 40 km/h, 60 km/h, 80 km/h, 100 km/h, and 120 km/h.

3. Results and Discussion

3.1. Validity Analysis of Model

(1) Mechanical model validation analysis

The results for the deflection of the road surface and the compressive strain of the top surface of the soil foundation in the literature [24] were compared with the simulation results in this paper, as shown in Figure 5.

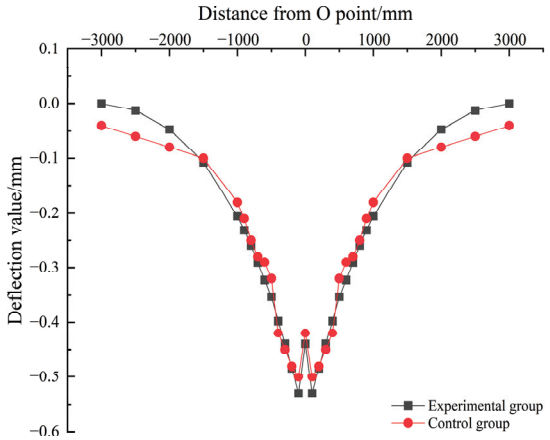

(**a**) Comparison of deflection value results

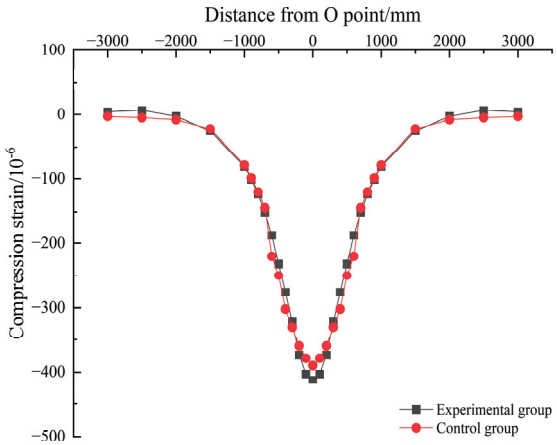

(**b**) Comparison of compressive strain results on top surface of soil foundation

Figure 5. Verification of the validity of the mechanical model.

It can be seen from Figure 5 that the calculation results of the deflection value of the finite element model and the compressive strain value of the top surface of the soil foundation in this paper are consistent with the results in the literature. In addition, the deflection value and the peak point of the compressive strain on the top surface of the soil foundation calculated in this paper are the same as those in the literature. The peak value of the surface deflection calculated in this paper is 0.53 mm, and the peak value of the compressive strain on the top surface of the soil foundation is 412 με, which are 6% and 5.6% larger, respectively, than those in the existing research results [24], which proves the rationality of the boundary conditions, mesh division and element type of the model.

(2) Temperature field model verification

The calculation results for the road surface temperature in the literature [27] were compared with the simulation results in this paper, as shown in Figure 6.

It can be seen from Figure 6 that the simulation results of this paper have the same change rule as the results of the existing research [27], and both increase with the increase in radiation intensity. However, between 6:00 and 10:00, the temperature calculation results of this paper are basically consistent with the temperature change curve in the literature results. After 10:00, the calculation results of this paper are different from those in the literature, but the difference is small. In this paper, the calculated temperature peak is 65.33 °C, which is only 1.81% larger than the existing research results, thus proving the effectiveness of the temperature field model in this paper.

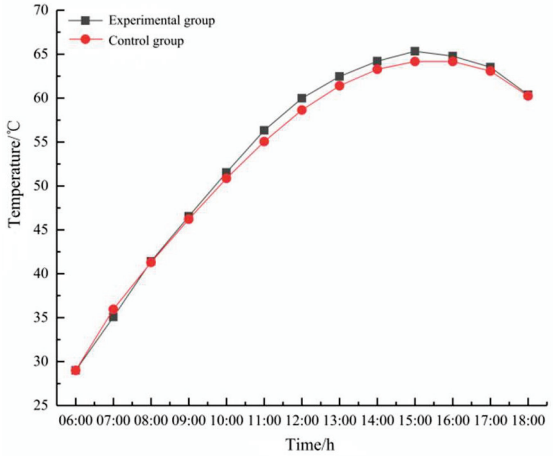

Figure 6. Verification of the validity of the temperature field model.

3.2. Analysis of Mechanical Indexes with and without Temperature Effect

3.2.1. Variation of Road Surface Deflection

It can be seen from Figure 7 that no matter whether there is temperature effect or not, the surface deflections of the three types of permeable asphalt pavements show half-sine changes under a half-sine dynamic load, while under a static load, the surface deflection value is constant. The surface deflections of the three types of pavement under a static load with a temperature effect are 0.56 mm, 0.61 mm and 0.71 mm, which are about 0.27 mm, 0.27 mm and 0.33 mm higher than the respective values under no temperature effect. The surface deflections under a dynamic load with temperature effect are 0.52 mm, 0.56 mm and 0.68 mm, which are about 0.24 mm, 0.24 mm and 0.31 mm higher than the respective values under no temperature effect. It can be seen that the peak values of the surface deflection values of the three types of pavements under dynamic load are smaller than those under static load. At the same time, due to the effect of temperature, the deflection values of the three types of pavements all increase to varying degrees, and the change in the type C structure is more prominent.

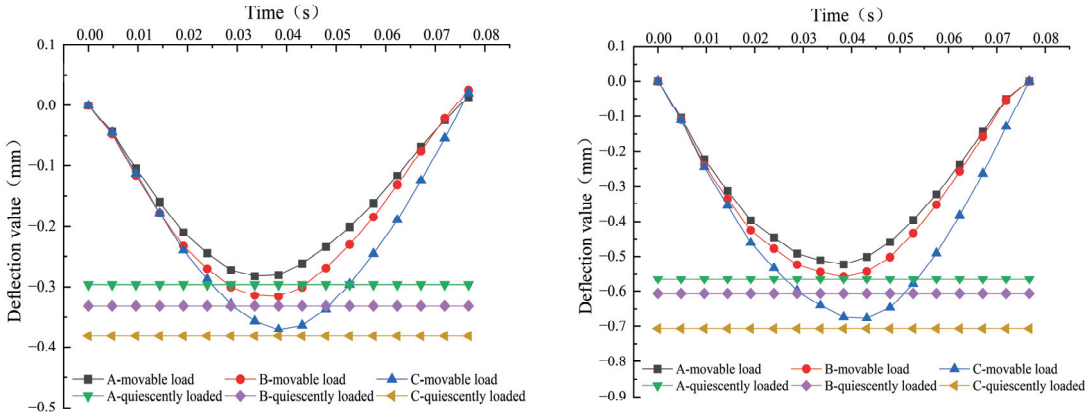

(**a**) No temperature effect (**b**) Temperature effect

Figure 7. Comparative analysis of road surface deflection.

3.2.2. Variation of Compressive Strain on Top of Soil Foundation

It can be seen from Figure 8 that whether there is temperature effect or not, the variations in the top surface compressive strain of the three kinds of permeable asphalt pavements under dynamic load are the same as those for road surface deflection, which show half-sine variation and are constant under static load. The values of peak compressive strain of the top surface of the soil foundation of the three types of pavements under static

load with temperature effect are 223 με, 246 με and 301 με, which are increased by about 30%, 28% and 38% compared with the respective values without temperature effect. The values of peak compressive strain of the top surface of the soil foundation under dynamic load with temperature effect are 208 με, 227 με and 286 με, which are increased by about 31%, 29% and 33% compared with the respective values without temperature effect. It can be seen that the peak values of the top surface compressive strain of the three types of pavements under static load are also greater than those under dynamic load. Moreover, due to the existence of the temperature effect, the compressive strain on the top surface of soil foundation has a large increase, which is similar to the road surface deflection, and the largest increase is still type C.

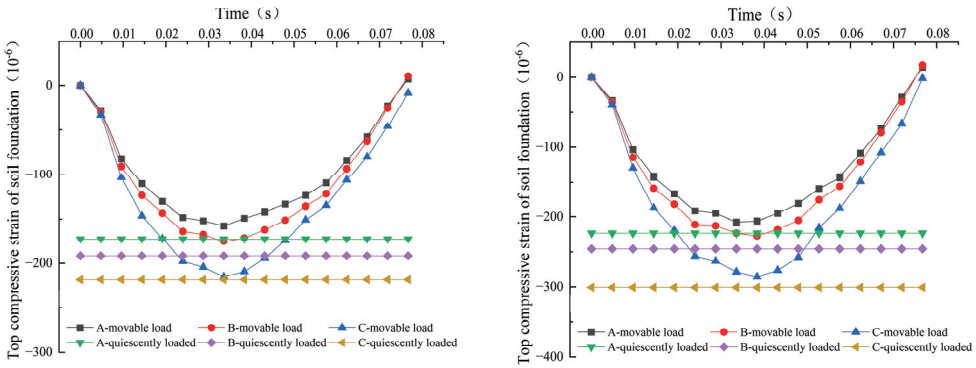

(**a**) No temperature effect (**b**) Temperature effect

Figure 8. Comparative analysis of compressive strain on top of soil foundation.

3.2.3. Shear Stress Variation of Top Surface Course

It can be seen from Figure 9 that the shear stresses at the bottom of the top surface course of the three types of permeable asphalt pavement show half-sine variation under dynamic load, and the value is fixed under static load. The peak values of the shear stress at the top surface course of the three kinds of pavements under dynamic load are less than the respective values under static load, but the differences are small. In addition, under the same conditions, the peak values of shear stress at the top layer and bottom of the three types of pavements under dynamic load and static load are about 0.10 MPa, 0.11 MPa and 0.12 MPa, respectively. However, these values increase to a certain extent under the action of temperature by about 46%, 39% and 38%, respectively. This phenomenon indicates that the existence of the temperature effect has a great influence on the shear stress of the top surface course of permeable asphalt pavements.

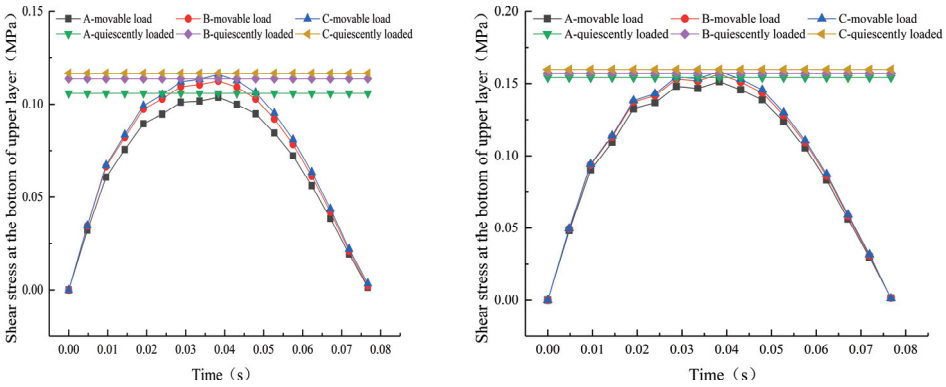

(**a**) No temperature effect (**b**) Temperature effect

Figure 9. Comparative analysis of shear stress at top surface course.

3.2.4. Variation of Tensile Stress at Bottom of Top Surface Course

It can be seen from Figure 10 that the tensile stresses at the bottom of the top surface course of the three types of permeable asphalt pavements show half-sine variation under dynamic load, and the value is fixed under static load. At the same time, as for the shear stress at the bottom of the top surface course, the peak values of the tensile stress at the bottom of the upper layer of the three types of pavements under dynamic load are smaller than those under static load, and the differences are not large. Under the same conditions, the peak values of tensile stress at bottom of the top surface course of the three types of pavements under dynamic load and static load are about 0.19 MPa, 0.19 MPa and 0.20 MPa, respectively, which are about 0.1 MPa higher than the respective values without temperature effect, which is consistent with the conclusion that the effect of high temperature on the increase in compressive stress is not significant in the existing research [28]. This also shows that the existence of the temperature effect also has a great influence on the tensile stress of the top surface course of permeable asphalt pavements.

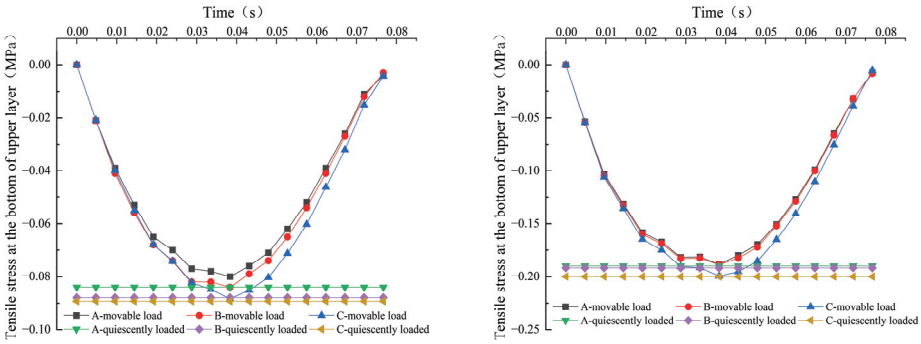

(**a**) No temperature effect (**b**) Temperature effect

Figure 10. Comparative analysis of tensile stress at bottom of top surface course.

3.3. Influence of Temperature Change on Mechanical Indexes

3.3.1. Influence on Road Surface Deflection

It can be seen in Figure 11 that under the action of dynamic load and static load, the surface deflection of the three types of permeable asphalt pavements has the same change rule with pavement temperature. The pavement temperature gradually increases from 6:00 to 14:00, and the deflection value at the surface load also continues to increase. The pavement temperature and deflection reach a peak at 14:00. Between 14:00 and 18:00, due to the decrease in pavement temperature, the deflection values of the load on the road surface begin to decrease. Comparing the road surface deflection values under static load and dynamic load, it can be found that at any time, the values for the same structure under static load are all greater than those under dynamic load, with C > B > A.

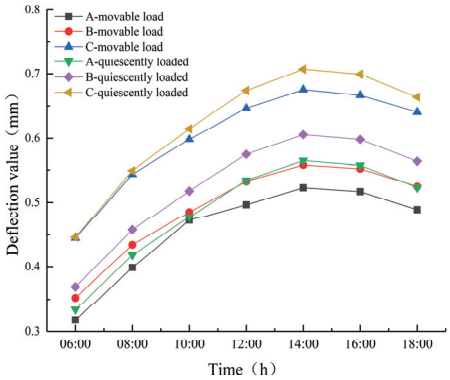

Figure 11. Influence of temperature change on road surface deflection.

3.3.2. Influence on Compressive Strain of Top Surface of Soil Foundation

It can be seen from Figure 12 that under both static and dynamic loads, the influence of temperature change on the compressive strain of soil foundation top surface of the three types of permeable asphalt pavements is different from that of road surface deflection. In the whole loading cycle, the top surface compressive strain of the three kinds of pavements increases with the increase in temperature, but the growth rate does not increase linearly with the increase in temperature, and there is no inflection point in the 12 h heating process. The top compressive strain of the three kinds of pavements can be seen as an obvious increase from 6:00 to 8:00. After 8:00, the increase is less obvious. This is because the soil foundation at the bottom of the structure is less affected by temperature, and the slight growth is mainly due to the small modulus of the soil foundation itself. This is the same as the influence of temperature on the compressive strain of the soil foundation top surface under the action of a standard axial load (static load) under the same conditions. It can also be seen from the figure that at any time, the compressive strain values of the soil foundation top surface of the three types of permeable asphalt pavements are C > B > A.

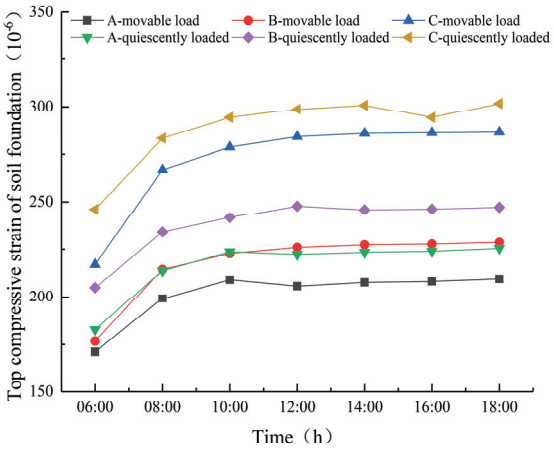

Figure 12. Influence of temperature change on the compressive strain of the top surface of the soil foundation.

3.3.3. Influence of Shear Stress on the Bottom of Top Surface Course

It can be seen from Figure 13 that during the heating process of 12 h, the shear stress at the bottom of the top surface course of the three types of permeable asphalt pavements is basically consistent with the change rule of surface deflection with temperature, and there is also an inflection point at 14:00. Between 6:00 and 14:00, the shear stress at the bottom of the top surface course of the three pavements increases gradually, and the values of shear stress reach a peak at 14:00. Then, the values of shear stress of the three pavements begin to decrease between 14: 00 and 18:00. Whether under static or dynamic load, the shear stress at the bottom of top surface course of the three pavements increases with the increase in temperature. At the same time, the shear stress values at the bottom of the type B and C pavements are basically equal in the whole cycle, while that of the type A pavement is smaller than the values for the B and C pavements. This observation is consistent with the findings of existing studies [20].

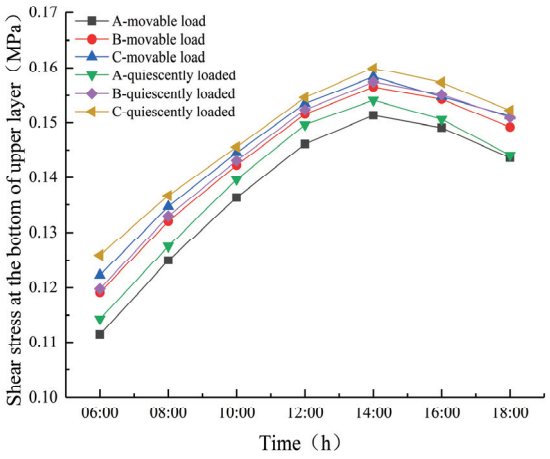

Figure 13. Influence of temperature change on shear stress on the bottom of the top surface course.

3.3.4. Influence on Tensile Stress at Bottom of the Top Surface Course

It can be seen from Figure 14 that in the 12 h heating process, the tensile stress and the shear stress at the bottom of top surface course of the three types of permeable asphalt pavements are the same, which is basically consistent with the rule of the surface deflection value changing with temperature, and the inflection point appears at 14:00. Before 14:00, the bottom tensile stress of the three pavements increases with the increase in pavement temperature. At 14:00, when the tensile stress at the bottom of the top surface course reaches a peak, the tensile stress at the bottom of the top surface course of the three pavements begins to decrease. In addition, it can be seen from Figure 14 that whether under static or dynamic load, the values of tensile stress at the bottom of the top surface course of the A and B pavements are basically equal in the whole cycle, while the tensile stress at the bottom of the top surface course of the type C pavement is greater than the respective values for A and B. In particular, the tensile stress at the bottom of the top surface course of the type C pavement under static load is significantly greater than that under other conditions.

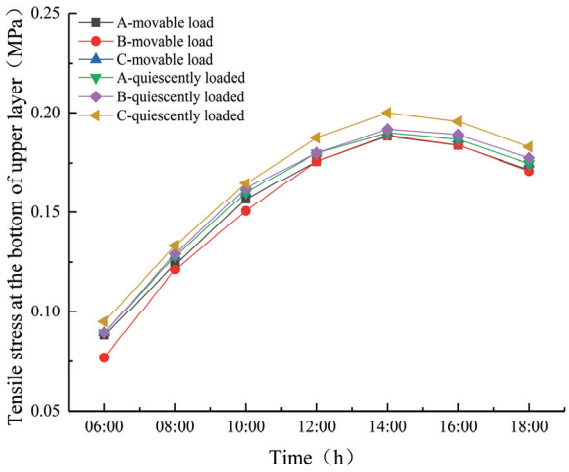

Figure 14. Influence of temperature change on tensile stress at bottom of the top surface course.

3.4. Influence of Speed Change on Mechanical Properties of Permeable Asphalt Pavement

3.4.1. Influence on Road Surface Deflection

Figure 15 shows that for the three types of pavement and under the action of dynamic load, the rule of surface deflection changes with speed is equal at the same time, regardless of the temperature effect. When the speed is 40–60 km/h, the deflection value increases with the increase in speed, reaches a peak at 60 km/h, and then decreases with further increases in speed. Comparing the road surface deflection under static load at the same

conditions, it can be seen that the peak value of road surface deflection under dynamic load is smaller than that under static load. In addition, for the three types of pavements, regardless of the temperature effect, the surface deflection values under the same load are C > B > A.

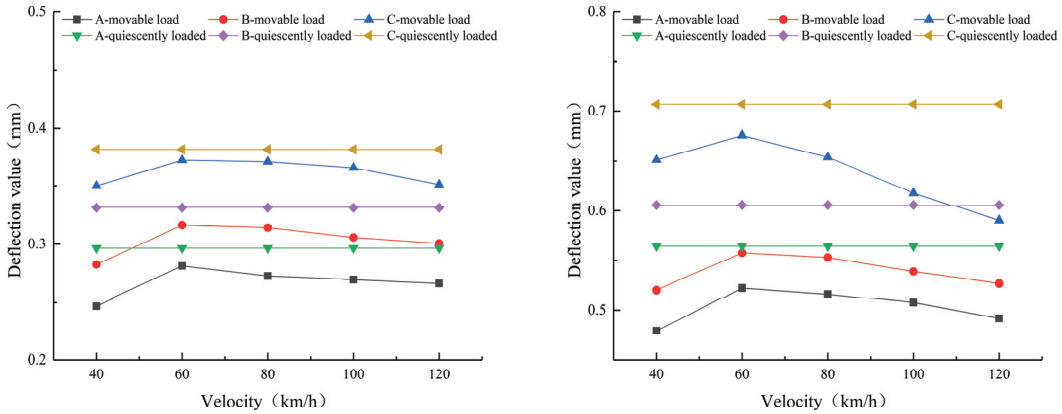

(**a**) No temperature effect (**b**) Temperature effect

Figure 15. Influence of speed change on road surface deflection.

3.4.2. Influence on Compressive Strain of Top Surface of Soil Foundation

It can be seen from Figure 16 that for the three types of pavements, the variation in compressive strain of the soil foundation top surface with speed is the same with or without temperature effect. When the load reaches a peak value (1/2T), the top compressive strain of the soil foundation increases from 40 km/h to 60 km/h without the temperature effect, but the change is not obvious. The difference between the temperature effect and the non-temperature effect condition is that there is no obvious fluctuation in the whole range of speed. When the speed is less than 60 km/h, it has a great influence on the compressive strain of the top surface of the soil foundation of the pavements without temperature effect. The degree of influence decreases with the increase in speed, and the influence of the speed change on the compressive strain of the top surface of the soil foundation of the pavement with temperature effect is small over the whole range. In addition, under the same conditions, the peak compressive strain of the soil foundation top surface under dynamic load is smaller than that under static load, which is the same pattern observed for the deflection value of the road surface.

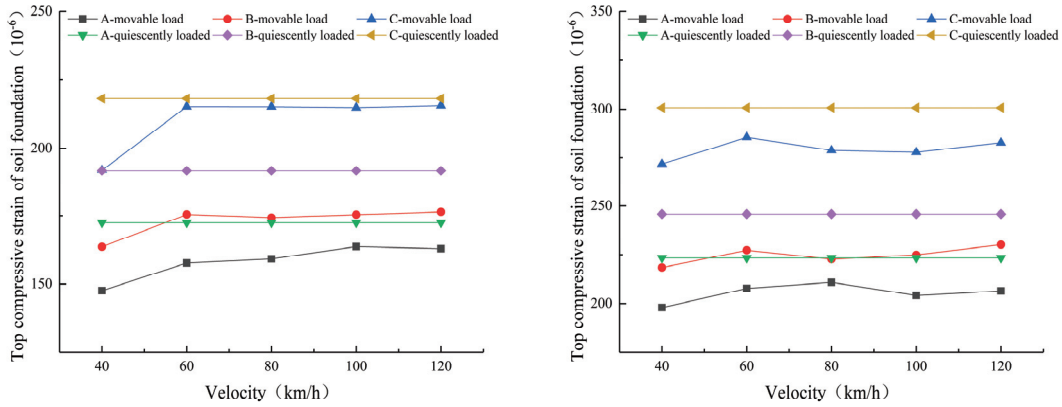

(**a**) No temperature effect (**b**) Temperature effect

Figure 16. Influence of speed change on compressive strain of the top surface of the soil foundation.

3.4.3. Influence of Shear Stress on the Bottom of the Top Surface Course

It can be seen from Figure 17 that with the increase in speed, the shear stress at the bottom of the top surface course of the three types of pavements either increases or decreases at different times. Whether the temperature effect exists or not, the changes in the shear stress at the bottom of the top surface course of these pavements are as follows: the shear stress values increase with increases in speed from 40 km/h to 60 km/h, decrease as the speed increases from 60 km/h to 80 km/h, and then increase with the speed. Therefore, whether there is temperature effect or not, the shear stress values at the bottom of the top surface course reach a maximum at the speed of 60 km/h and fluctuate between 40 km/h and 80 km/h.

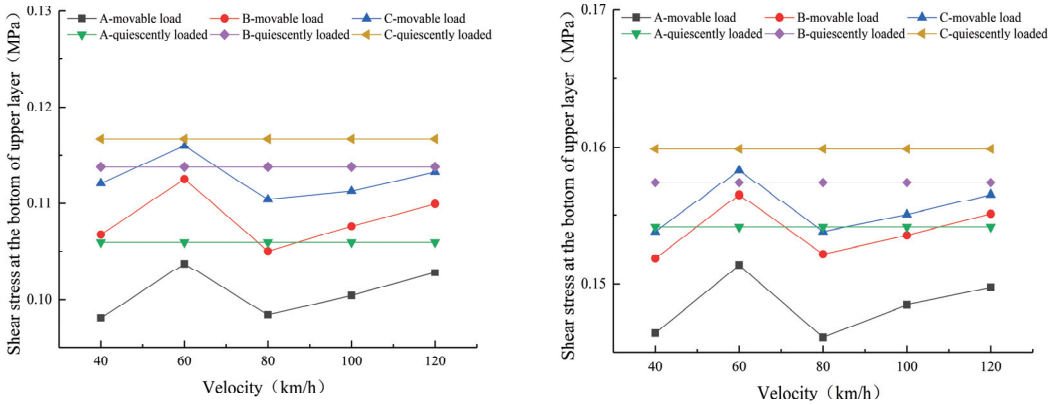

(**a**) No temperature effect (**b**) Temperature effect

Figure 17. Influence of speed change on shear stress on the bottom of the top surface course.

3.4.4. Influence on Tensile Stress at the Bottom of the Top Surface Course

It can be seen from Figure 18 that, as for the surface deflection and the compressive strain of the top surface of the soil foundation, the three pavements have the same law of tensile stress at the bottom of the upper layer, with or without the temperature effect, at the same time. Whether there is temperature effect or not, when the speed is 40–60 km/h, the tensile stress values at the bottom of the top surface course increase with increases in speed, reaching a peak at 60 km/h, and then decrease with further increases in speed. It can be seen that the speed of 60 km/h is the turning point of the tensile stress peak at the bottom of the entire top surface course at the peak load. In addition, under the same conditions, the peak tensile stress at the bottom of the top surface course under dynamic load is less than that under static load.

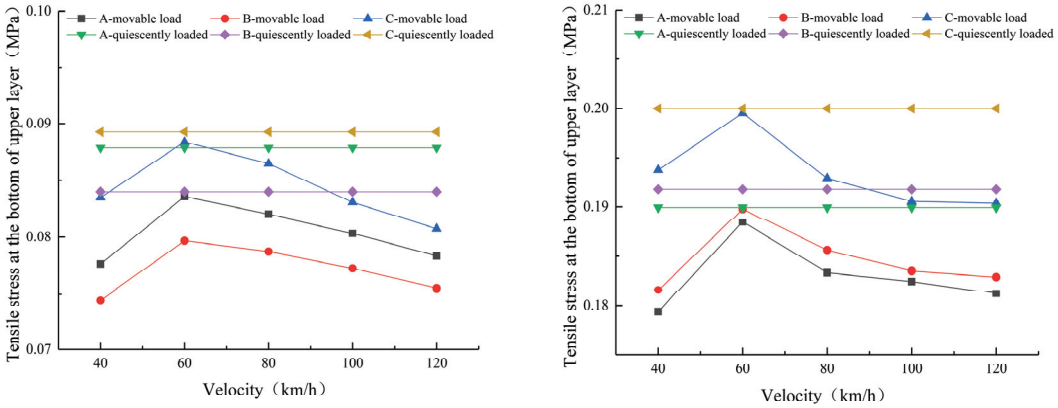

(**a**) No temperature effect (**b**) Temperature effect

Figure 18. Influence of speed change on tensile stress at the bottom of the top surface course.

4. Conclusions

(1) Regardless of whether there is a temperature effect, the peak values of the surface deflection, the compressive strain on the top surface of the soil base, the shear stress at the bottom of the upper layer, and the tensile stress at the bottom of the upper layer of the three types of permeable asphalt pavements under static load are all fixed values. Under the action of dynamic load, they all show a semi-sinusoidal change. The extreme value of each control index under dynamic load is about 10% smaller than the extreme value under static load. At the same time, the extreme values under temperature conditions are 28%–50% larger than the extreme values without temperature conditions.

(2) During the 12 h heating process of the three types of permeable asphalt pavements, regardless of the dynamic load or static load, the variation law of each control index with temperature is the same as that under static load. At the same time, the surface deflection, and the shear stress and tensile stress at the bottom of the upper layer are basically consistent with the variation law of the surface temperature. The peak value of each control index under dynamic load is smaller than that under static load.

(3) Here, we only consider the coupling analysis of standard axle load and solar radiation. The influence of the water factor should be examined in follow-up studies in water–heat–structure coupling analyses, which would allow the simulation calculation of permeable asphalt pavements to more closely approximate reality.

Author Contributions: Conceptualization, Z.L. and H.Z.; methodology, Y.L. and H.Z.; software, X.W.; validation, Y.L., X.W. and T.G.; investigation, Y.L.; data curation, Z.L.; writing—original draft preparation, Y.L. and X.W.; writing—review and editing, Y.L.; visualization, X.W. and Y.L.; supervision, Z.L.; project administration, Z.L.; funding acquisition, Z.L. All authors have read and agreed to the published version of the manuscript.

Funding: This work was supported by Key R&D and Promotion of Special Scientific and Technological Research Projects of Henan Province: [Grant Number 182102210061, 212102310089]; Key Scientific Research Projects of Colleges and Universities in Henan Province in 2021: Study on pavement performance of cotton straw cellulose modified asphalt [Grant Number 21A580004].

Institutional Review Board Statement: Not applicable.

Informed Consent Statement: Not applicable.

Data Availability Statement: Some or all data, models, or code that support the findings of this study are available from the corresponding author upon reasonable request.

Conflicts of Interest: The authors declare no conflict of interest.

References

1. Gupta, A.; Rodriguez-Hernandez, J.; Castro-Fresno, D. Incorporation of additives and fibers in porous asphalt mixtures: A review. *Materials* **2019**, *12*, 3156. [CrossRef] [PubMed]
2. Garcia, E.S.; Thives, L.P.; Ghisi, E.; Antunes, L.N. Analysis of permeability reduction in drainage asphalt mixtures due to decrease in void volume. *J. Clean. Prod.* **2020**, *248*, 119292. [CrossRef]
3. Chen, C. New solution to the dilemma, urban water culture in Henan Province and its value in the construction of sponge city. *J. North China Univ. Water Resour. Electr. Power (Soc. Sci. Ed.)* **2019**, *35*, 1–6.
4. Zhang, Y.; Xu, Y. Technical Requirements for Structures and Materials of Permeable Asphalt Pavement. *Urban Bridges Flood Control.* **2019**, *4*, 51–54+9–10. [CrossRef]
5. Wang, X.; Gu, X.; Dong, Q.; Wu, J.; Jiang, J. Evaluation of permanent deformation of multilayer porous asphalt courses using an advanced multiply-repeated load test. *Constr. Build. Mater.* **2018**, *160*, 19–29. [CrossRef]
6. Jiang, W.; Sha, A.; Xiao, J. Selection of gradation ratio of porous asphalt mixture based on discrete element method. *J. Jilin Univ. (Eng. Ed.)* **2011**, *41*, 68–72.
7. Liu, B. Study on Road Performance Improvement of Urban Road Permeable Asphalt Pavement. Ph.D. Thesis, Southeast University, Nanjing, China, 2018.
8. Kusumawardani, D.M.; Wong, Y.D. Evaluation of aggregate gradation on aggregate packing in porous asphalt mixture (PAM) by 3D numerical modelling and laboratory measurements. *Constr. Build. Mater.* **2020**, *246*, 118414. [CrossRef]
9. Li, Z.; Chen, Y.; Sun, K. Thermal aging performance of porous asphalt mixture. *J. Chang'an Univ. (Nat. Sci. Ed.)* **2014**, *34*, 41–46.

10. Jiang, Y.; Gao, B.; Yang, Y.; Wu, J.; Wang, G. Research on typical permeable pavement model based on sponge city system. *J. Chongqing Jiaotong Univ. (Nat. Sci. Ed.)* **2019**, *38*, 42–47.
11. Hu, L.; Yun, D.; Yang, Z. Research on macro-structural characteristics of open-graded asphalt wear layer and its skid resistance under rainfall conditions. *Mater. Introd.* **2017**, *31*, 113–117+134.
12. Feng, Y.; Wang, W.; Li, J.; Li, P.; Guan, P. Experimental study on runoff coefficient of permeable road. *Water Conserv. Hydropower Technol.* **2019**, *50*, 27–35.
13. Tan, S.A.; Fwa, T.F.; Chai, K.C. Drainage considerations for porous asphalt surface course design. *Transp. Res. Rec.* **2004**, *1868*, 142–149. [CrossRef]
14. Xu, X.; Qin, H.; Zhuo, W. Study on the influence of permeable concrete pavement on rainwater runoff. *Highw. Eng.* **2019**, *44*, 135–139.
15. Yi, J.; Feng, D. Viscoelastic-plastic damage model of porous asphalt mixture. *J. Harbin Inst. Technol.* **2014**, *46*, 66–71.
16. Pang, Z.; Meng, X. Structural optimization scheme of permeable asphalt pavement based on finite element analysis. *Transp. Res.* **2018**, *4*, 69–76.
17. Deng, N.; Wu, K.; Huang, W.; Deng, Q. Coarse-grained stress absorbing layer pavement structure design and finite element analysis. *Sci. Technol. Eng.* **2019**, *19*, 316–321.
18. Huang, L.; Wu, W.; Shen, Q. Hydrodynamic pressure effect analysis of crack propagation in permeable asphalt pavement. *Highw. Eng.* **2019**, *44*, 181–185.
19. Ning, F. Design and Application of Permeable Asphalt Pavement Gravel Base Mixture. Master's thesis, Changsha University of Science and Technology, Changsha, China, 2019.
20. Wang, X. Research on Dynamic Response Characteristics of Permeable Asphalt Pavement under Multi-Field Coupling. Master's thesis, Shenyang Jianzhu University, Shenyang, China, 2018.
21. Luo, S. Study on the Disease Environment and Multi-Field Coupling Effect of Asphalt Pavement in High Temperature and Rainy Area. Ph.D. Thesis, Central South University, Changsha, China, 2012.
22. He, J. Mechanical Mechanism Analysis of Rutting Formation of Urban Asphalt Pavement under Temperature Field. Master's Thesis, Central South University, Changsha, China, 2014.
23. Chen, Y. Research on Disease Prevention and Control Technology of Asphalt Pavement on Long and Large Longitudinal Slope. Ph.D. Thesis, Chang'an University, Xi'an, China, 2011.
24. Du, W. Composition Design and Application Research of Permeable Asphalt Mixture. Master's Thesis, Beijing Jiaotong University, Beijing, China, 2019.
25. Wang, L.; Shan, C.; Zheng, C. Response Characteristics of Inverted-base Asphalt Pavement Structure in Cold Area under Multi-axle Loads. *Environ. Earth Sci. Res. J.* **2020**, *7*, 141. [CrossRef]
26. *CJJ/T 190-2012*; Technical Specification for Permeable Asphalt Pavement. China Building Industry Press: Beijing, China, 2012.
27. Tian, Y. Study on Water Holding Behavior and Cooling Effect of Urban Road Permeable Asphalt Pavement. Master's Thesis, Chang'an University, Xi'an, China, 2019.
28. Yang, Z. Mechanical response analysis of asphalt pavement structure under high temperature and heavy load. *Road Traffic Technol.* **2020**, *36*, 20–26.

coatings

MDPI

Article

Influence of Construction Process on Aggregate Spalling Behavior on Ultrathin Waterborne Epoxy Resin Layer

Jiaquan Yuan [1], Yifan Zhang [2], Haoyang Huang [2], Gang Zhou [2,*], Chaoliang Fu [3,*], Wenhong Duan [1], Weihong Jiang [1], Li Xiong [1], Huimei Li [1], Xiaohua Yang [1] and Chuanqiang Li [2,4,*]

[1] Dali Danan Highway Co., Ltd., Dali 671000, China; yuanjiaquan2024@163.com (J.Y.)
[2] School of Civil Engineering, Chongqing Jiaotong University, Chongqing 400074, China; zhangyifan8691@163.com (Y.Z.); hhy@mails.cqjtu.edu.cn (H.H.)
[3] Institute of Highway Engineering, RWTH Aachen University, 52074 Aachen, North Rhine-Westphalia, Germany
[4] School of Materials Science and Engineering, Chongqing Jiaotong University, Chongqing 400074, China
* Correspondence: cjhs_2000@163.com (G.Z.); fu@isac.rwth-aachen.de (C.F.); lichuanqiang@cqjtu.edu.cn (C.L.)

Abstract: The waterborne epoxy resin (WER) colored antiskid thin layer has been widely used in asphalt pavement to improve driving safety. The tectonic depth determines the antiskid performance of aparticle antiskid type thin layer. The spalling of aggregate from a thin layer may reduce the tectonic depth, thus damaging antiskid performance. The spreading process of aggregate on the WER binder surface plays an important role in the spalling behavior of the thin layer. Herein, the influence of spreading processes on the ceramic aggregate spalling behavior on the WER thin layer was investigated based on laboratory experiments. The abrasion and British Pendulum Number (*BPN*) tests were employed to evaluate the antispalling and antiskid properties of the WER thin layers with different amounts of WER mortar, coverage rates of first-spread aggregate, and spreading orders of coarse/fine aggregates. Moreover, the tectonic depths of the layers before/after the spalling test were also investigated. The results indicated that the optimal dosage of WER mortar is 2.8 kg/m^2. The WER thin layer exhibited better anti-striping property when coarse ceramic aggregate was spread first. The first-spread coverage rate of the aggregate on the WER surface is 70%. The thin layer exhibited a superior antispalling performance according to the resulting scheme, with a spalling rate of 3.77%. The tectonic depth only decreased from 1.87 to 1.80 mm after the spalling test.

Keywords: antiskid thin layer; colored pavement; waterborne epoxy; aggregate spalling; construction process

1. Introduction

Colored pavement, owing to its bright color and obvious contrast, can play an important role in traffic guidance and warning. Because of such characteristics as improving driving safety, enhancing road aesthetics, and reducing the urban heat island effect, the use of colored pavement has received increasing attention in recent years [1,2]. At present, a variety of paving methods for colored pavement have been developed. They can be divided into two main categories: colored raw materials used for new pavement construction and colored overlays for existing pavements [3]. The color ultrathin wearing course is a form of color overlay that uses polymer resin materials, such as epoxy resin and acrylic, as the binder and appropriately adding colored ceramic particles for laying [4]. As a preventive maintenance measure, the ultrathin-wearing course can quickly repair pavement damage and enhance the antiskid performance of pavements, and it has been widely used in highway engineering construction [5–7].

Epoxy resin has been favored by many researchers, owing to its inherent mechanical and chemical stability, heat resistance, corrosion resistance, electrical insulation, and strong adhesion [8–10]. Compared with ordinary asphalt, epoxy-resin-based binder has excellent

bonding performance, good durability, good compatibility with various pavement materials, and better pavement performance, and it is widely used in road construction fields such as pavements and bridge decks [11–14]. However, because the epoxy resin is generally a solvent-based polymer, it has such defects as flammability and explosiveness, and the cross-linking of the ring epoxy resin with a curing agent to form a film releases volatile organic pollutants (VOCs), which are toxic and cause environmental pollution [15,16]. To solve these problems, researchers have developed waterborne epoxy-modified resin, which uses water as the solvent and is in a liquid state at room temperature [17]. It is convenient to operate, retains the inherent bonding performance of epoxy resin, and can be used in environmental or humid conditions. Moreover, the VOC volatility is smaller than that of traditional epoxy resin [18,19]. Therefore, the use of waterborne epoxy resins for the color ultrathin wearing course of pavement is an important trend for future development.

In a color antiskid thin-layer system, the aggregate accounts for the largest proportion by weight and is important for providing antiskid ability. When the aggregate interlocking structure is unstable, such problems as loose spalling of the aggregate and rapid attenuation of the surface function are triggered [20]. The accumulation state of the aggregate directly affects its spalling, and the accumulation state of the aggregate in the antiskid thin layer is closely related to its structural stability. Spalling is the main reason for the attenuation of the antiskid performance of the antiskid thin layer and the shortening of service life [21]. For loose spalling of aggregates, researchers have explored the occurrence mechanism using different methods. Kim [22] proposed a model that can predict and evaluate the stripping process in a mixture. Laurence [23] analyzed the interface stripping mechanism between asphalt and aggregate using physicochemical methods and argued that increasing the ratio of aromatic components and colloids in asphalt is beneficial to the adhesion of the asphalt–aggregate interface, thus reducing the water sensitivity of the mixture. For the waterborne resin-wearing layer, the antispalling property of the aggregate is particularly important. Yao's group [24] investigated the influence of water acidity and alkalinity on the spalling behavior of the aggregate–asphalt system based on the atomic force microscopy (AFM) test, boiling water method test, and theoretical calculations, which suggests that the alkaline conditions were more likely to cause water damage in bitumen mixtures. Kodur [25] investigated the fire-induced spalling behavior of geo-polymer concrete through the measurement of residual compressive and splitting tensile strength and variation in permeability; it was found that the geo-polymer concrete exhibited lower spalling risk than that of ordinary Portland cement concrete. Furthermore, deep learning methods can also be used to investigate the spalling property of concrete, thus forecasting the formation of defects in concrete structures [26].

At present, most research on the stripping mechanism is based on adhesion or stripping tests, which focuses on the stripping of asphalt aggregates by water [27], and there is a lack of research on such topics as the accumulation state of the aggregate. From a macroscopic structure point of view, the distribution state of the aggregate of the ultrathin-wearing course mainly depends on the type of construction process adopted [28].

The main methods of laying polymer color antiskid thin layers on highway pavements are surface coating, color mortar, and spreading [29]. The spreading method has a simple construction process and strong operability, and the colored thin layer has the best antiskid performance [30,31]. However, the spreading method depends more on manual operation, and the construction process flow and material indicators have not yet been standardized. Therefore, different construction processes definitely have different impacts on the spalling behavior of the color antiskid thin layer, and the main influencing factors must also be studied more deeply, especially for the particle antiskid type color ultrathin abrasion layer [32].

In this work, the influence of the construction process on the spalling behavior of the aggregate of the particle antiskid type color ultrathin abrasion layer was studied through indoor experiments. Considering the amount of resin mortar, the coverage rate of the first-spread aggregate, and the spreading sequence of coarse and fine aggregates as analysis

factors, the antispalling and antiskid properties of the waterborne composite modified resin-based colored antiskid thin layer under different construction processes were studied. The results show that, by regulating the amount of resin mortar, the spreading sequence of coarse/fine aggregates, and the spreading coverage rate, a waterborne epoxy resin pavement thin layer with stronger antispalling ability and good antiskid performance can be obtained.

2. Materials and Preparation of Specimen

The materials used were water-based compound-modified resin (with a viscosity of 1.73 Pa·s), inorganic powder filler (mainly composed of such components as carbonate and sulfate), 120-mesh sintered color sand sintered from quartz sand and pigment, and colored ceramic particles. The waterborne epoxy resin was purchased from Shenzhen Borui Technology Co., Ltd., Shenzhen, China; The colored ceramic particles were purchased from Hebei Xiaoqi New Materials Co., Ltd., Cangzhou, China. (see Table 1).

Table 1. Technical indicators of colored ceramic aggregate.

Indicator	Result	Technical Requirements [33]
Crushing value/%	2.1	$\leq$10
Abrasion value/%	16.7	$\leq$20
Mohs hardness/level	6	$\geq$6

Formwork with an inner diameter of 280 $\pm$ 1 mm was placed in the center on a flat felt disk. The adhesive, powder filler, and sand filler were mixed evenly at a ratio of 1:0.5:1 and poured into the formwork according to the amount required in the test plan. Finally, the colored ceramic particles were spread on the surface of the adhesive according to the different spreading requirements described in Section 3.1. After 24 h, a brush was used to remove the unbonded floating particles on the surface, which were then left for six days before the test was conducted.

3. Test Methods

3.1. Abrasion

A wet-wheel abrasion tester was used to conduct an abrasion test on the specimen, the mass of the specimen was measured before and after abrasion, and the spalling rate (*SR*) of the aggregate during the abrasion process was calculated according to the following formula (Equation (1)). The process is as follows.

The original mass of the specimen is weighed and recorded as m_o, and then it is placed in a tray for fixation. The instrument is started, and the specimen is abraded in a dry environment. The test is terminated after 5 min. A fine brush is used to gently brush off the floating particles on the surface of the specimen. The mass of the specimen after abrasion is measured and recorded as m_a. The spalling rate is calculated by

$$SR = \frac{m_o - m_a}{m_o} \quad (1)$$

3.2. British Pendulum Number (BPN)

The *BPN* of the thin-layer specimens was measured using a pendulum tester. The instrument is leveled, and the bolts are rotated on each base to center the level bubble of the base. The zero pointer is adjusted, the pendulum is fixed on the right cantilever so that the pendulum is in a horizontal position, and the pointer is dialed to the right cantilever close to the pendulum rod. The pendulum instrument is idled, and the tightness of the pendulum instrument nut is adjusted until the pointer points to zero. The sliding distance is adjusted, and the height of the pendulum instrument is adjusted so that the sliding distance of the rubber block of the pendulum hammer on the specimen surface is 126 mm.

After the instrument is debugged, water is sprinkled at the measuring point with a watering can to make it wet. The pendulum and pointer are fixed on the right cantilever. The release switch is pressed to make the pendulum slide over the specimen surface, and the pendulum value pointed to by the pointer is recorded. Five measurements are made at the same measuring point. If the difference between the maximum and minimum values among the five pendulum values is greater than 3, the above operation is repeated until the difference is less than 3. The average value of five sets of tests is taken. The temperature correction is performed according to equation (2) to correspond to the international standard road temperature (20 °C).

$$BPN_{20} = BPN_t + \Delta BPN \tag{2}$$

Here, BPN_{20} is the pendulum value at a standard temperature of 20 °C, BPN_t is the pendulum value measured at road temperature, and ΔBPN is the temperature correction value corrected according to Table 2.

Table 2. Temperature correction values.

Temperature (°C)	0	5	10	15	20	25	30	35	40
Temperature correction value	−6	−4	−3	−1	0	+2	+3	+5	+7

3.3. Tectonic Depth

A manual sand-laying method was used to test the depth of the thin layer. First, fine brushes are used to clean the surface of the molded color antiskid thin-layer specimen. Standard sand is loaded into the cylinder from the mouth of the cylinder to the top of the spikes. The cylinder is knocked gently three times so that the standard sand fills the cylinder, and the excess standard sand is scraped with a steel ruler at the mouth of the cylinder. The filled standard sand is poured on the surface of the antiskid thin layer, a push plate is used to perform a rotating paving movement from inside to outside in the standard sand, the standard sand is gently pushed away so that it fills the gaps in the antiskid thin layer, and an attempt is made to cause the standard sand pavement to form a circle in the process of being pushed flat. Finally, a steel ruler is used to measure the diameter of the two vertical directions of the circle, taking the average value (accurate to 1 mm). After the measurement, the standard sand is swept using the same program to repeat the above steps, and three groups of parallel tests are performed to obtain the average value. The formula for calculating the depth of the structure is

$$TD = \frac{1000V}{\pi D^2/4} = \frac{31,831}{D^2} \tag{3}$$

where TD is the pavement surface tectonic depth (mm), V is the standard sand volume (25 cm^3), and D is the average diameter of the spreading sand (mm).

3.4. Antiskid Thin-Layer Aggregate Spreading Scheme and Dosage

3.4.1. Determination of Aggregate Dosage

Aggregate is the main component of the surface micro-convex bodies of the antiskid thin layer. The amount of aggregate changes the surface structure of the thin layer and affects its structural depth and friction coefficient. The amount of resin mortar used, the coverage rate of the first spread aggregate, and the spreading sequence of coarse and fine aggregates are discussed in this section. To avoid the influence of different self-weights of the aggregate on its embedding depth, excessive spreading is used in all schemes, and the total spreading amount of the aggregate is 10 kg/m^2.

The colored ceramic particles are divided into two grades of aggregates according to the particle sizes: 2–3 and 3–5 mm. The 2–3-mm aggregate is fine aggregate, and the 3–5-mm aggregate is coarse aggregate. (See Figure 1).

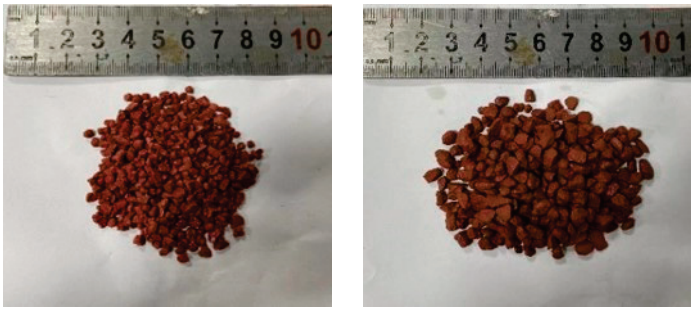

(**a**) fine aggregate (**b**) coarse aggregate

Figure 1. Colored ceramic particles.

To obtain the amounts of aggregate corresponding to different spreading coverage rates, the two grades of aggregates are laid flat in the mold so that there is only one layer of aggregate and there is no overlap, and the amount of aggregate when there is only one layer, and it is fully covered in the mold obtained. In the subsequent experiments, it is converted according to a certain proportion according to the required coverage rate. The coverage rates are listed in Table 3.

Table 3. Aggregate coverage.

Aggregate Size	**Fine Aggregate**				**Coarse Aggregate**			
Aggregate dosage (kg/m^2)	1.5	1.8	2.1	3.0	1.8	2.16	2.52	3.6
Coverage (%)	50	60	70	100	50	60	70	100

3.4.2. Aggregate Spreading Scheme

The spreading method has extremely high operability. Although, in actual construction, it is impossible to control the spreading and distribution of the lower-layer aggregate precisely, the stacking state of the aggregate can be controlled by controlling the amount of resin mortar used, coverage rate of the first spread aggregate, and spreading sequence of the coarse and fine aggregates to obtain a relatively ideal bottom-layer aggregate and improve the antispalling ability and antiskid property of the antiskid thin layer. The spreading scheme is designed, as shown in Table 4, to analyze the influence of the amount of resin mortar used, the coverage rate of the first spread aggregate, and the spreading sequence of coarse and fine aggregates on the spalling of the antiskid thin-layer aggregate. The spalling rate is directly calculated from the specimen mass loss, and the changes in the surface structure of the thin layer after abrasion are analyzed from the pendulum value and structural depth to reflect indirectly the spalling situation of the aggregate.

When the coarse and fine aggregates are spread simultaneously, the ratio of coarse to fine aggregate is 1:1. For the convenience of subsequent analysis, the schemes of each group are numbered, and the meaning of the number is "the amount of resin mortar — the coverage rate of the first spread aggregate, the particle size of the first spread aggregate, and the particle size of the later extensively spread aggregate". For example, 2-5cx means "the amount of resin mortar is 2 kg/m^2, the coarse aggregate with a 50% coverage rate is spread first, and the fine aggregate is spread in extensive amounts later."; 3.2-7xc means "the amount of resin mortar is 3.2 kg/m^2, the fine aggregate with a 70% coverage rate is spread first, and the coarse aggregate is spread in extensive amounts later."; 2-t means "the amount of resin mortar is 2 kg/m^2, and the coarse and fine aggregates are spread simultaneously." The photographs of part of the thin layer specimens are shown in Figure 2.

Table 4. Aggregate spreading program.

Program No.	Amount of Resin Mortar (kg/m^2)	Aggregate Spreading Sequence	Coverage of Spread-First Aggregate (%)
2-t	2	Coarse and fine spreading at the same time	/
2-5cx		Coarse → Fine	50
2-6cx			60
2-7cx			70
2-5xc		Fine → Coarse	50
2-6xc			60
2-7xc			70
2.4-t	2.4	Coarse and fine spreading at the same time	/
2.4-5cx		Coarse → Fine	50
2.4-6cx			60
2.4-7cx			70
2.4-5xc		Fine → Coarse	50
2.4-6xc			60
2.4-7xc			70
2.8-t	2.8	Coarse and fine spreading at the same time	/
2.8-5cx		Coarse → Fine	50
2.8-6cx			60
2.8-7cx			70
2.8-5xc		Fine → Coarse	50
2.8-6xc			60
2.8-7xc			70
3.2-t	3.2	Coarse and fine spreading at the same time	/
3.2-5cx		Coarse → Fine	50
3.2-6cx			60
3.2-7cx			70
3.2-5xc		Fine → Coarse	50
3.2-6xc			60
3.2-7xc			70

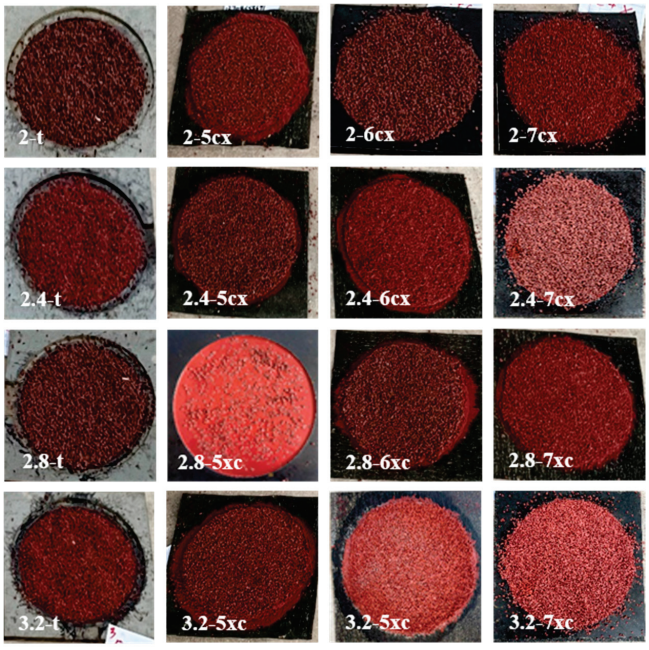

Figure 2. The photographs of WER thin layer specimens.

4. Results and Discussion

4.1. Effects of Amount of Resin Mortar on Aggregate Spalling

4.1.1. Spalling Rate

The effects of different amounts of resin mortar on the aggregate spalling rate after 5 min of abrasion are shown in Figure 3.

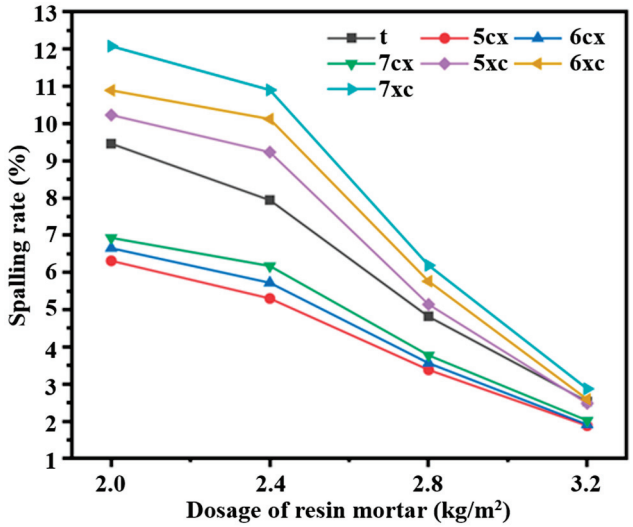

Figure 3. Spalling rate of the seven antiskid thin layer specimens after 5 min of abrasion.

As the test results reveal, as the amount of resin mortar increased, the spalling rate of the aggregate gradually decreased. When the amount of resin mortar was 2 kg/m^2, the spalling rates of the test schemes ranged from 6.31% to 12.08%. The phenomenon of large-area aggregate spalling was clearly observed during the experiment. When the amount of resin mortar was 2.8 kg/m^2, the spalling rates of the aggregates in all test schemes decreased significantly, and the spalling rates were all in the range of 3.38%–6.19%. When the amount of resin mortar was 3.2 kg/m^2, the spalling rates of the test schemes were only in the range of 1.88%–2.87%.

The greater the amount of resin mortar, the thicker the thin layer. Therefore, the deeper the embedding depth of the aggregate, the greater the contact area between the resin mortar and the aggregate, and the more obvious the bonding effect between the two. During the abrasion process, the aggregate is less likely to spall, and the smaller the amount of aggregate loss, the lower the spalling rate.

When the amount of resin mortar reached a certain value, the spalling rate of the aggregate decreased significantly, and the antispalling ability of the aggregate improved significantly. As the amount continued to increase, the effect of improving the antispalling ability gradually weakened. Therefore, considering the economy, it is not appropriate to use extensive resin mortar, and the amount should be controlled at 2.8 kg/m^2.

4.1.2. *BPN*

The greater the resin mortar dosage, the stronger the aggregate resistance to spalling; however, the resin mortar dosage not only affects the aggregate resistance to spalling but also affects the antislip resistance of the antislip thin layer. The effects of different resin mortar dosages on the pendulum values before and after abrasion of the thin layer are shown in Figure 4.

When the antiskid thin layer was not abraded, except for 3.2-5cx in each test scheme, the pendulum values were greater than 80. With the increase in the amount of resin mortar, the surface structure of the antiskid thin layer changed. The thicker the mortar layer, the deeper the embedding depth of the aggregate in the mortar, the more the parts wrapped, and the fewer the parts exposed on the surface of the thin layer. At the same time, the

mortar overflowed on the surface of the thin layer, preventing the aggregate from providing antiskid ability and wear resistance. Therefore, the greater the amount of resin mortar, the worse the antiskid property of the antiskid thin layer gradually became.

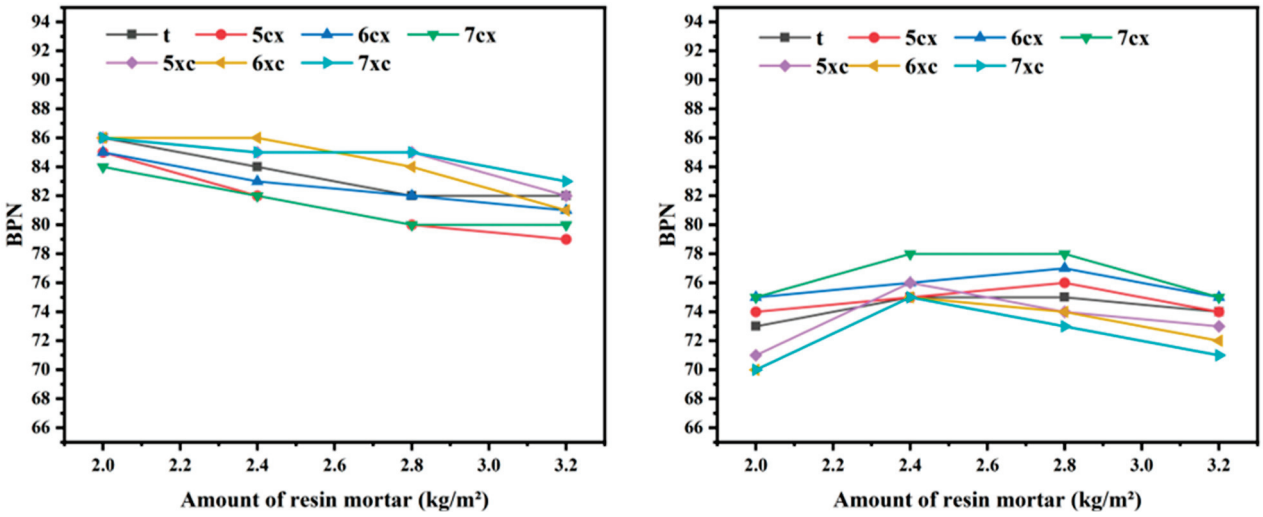

(**a**) before abrasion (**b**) after abrasion

Figure 4. Pendulum values of the antiskid thin layer specimens before (**a**) and after abrasion (**b**).

After the antiskid thin layer was abraded, the pendulum values of all test schemes decreased. When the amount of resin mortar used was 2 kg/m^2, the pendulum value after abrasion decreased most significantly. This was because an amount of 2 kg/m^2 is too small. A large area of aggregate spalling occurred during the abrasion process, and the surface structure of the antiskid thin layer was severely damaged. There was a lack of aggregate to provide microconvex bodies for the thin layer, which was relatively smooth; therefore, the pendulum value was small, and the antiskid property was poor. As the amount of resin mortar increased, the pendulum value first increased and then decreased. This was because, as the amount increased, the aggregate spalling was reduced, and the remaining aggregate on the surface of the thin layer after abrasion continued to provide an antiskid property. Compared with the test scheme with a smaller amount, the pendulum value increased. As the amount of mortar continued to increase, it was the same as the change in the pendulum value of the thin layer before abrasion. The greater the amount of mortar, the less the part of the aggregate that was exposed on the surface of the thin layer, the lower the pendulum value, and the worse the antiskid property. When the amounts were 2.4 and 2.8 kg/m^2, the thin layer had a large pendulum value both before and after abrasion.

4.1.3. Texture Depth

The greater the resin mortar dosage, the stronger the aggregate spalling resistance; however, the resin mortar dosage not only affects the spalling resistance of the aggregate but also affects the surface structure of the antislip thin layer. The effects of different resin mortar dosages on the surface structure of the thin layer are shown in Figure 5.

When the antiskid thin layer was not abraded, each test scheme had a relatively large structural depth (greater than 1.80 mm). With an increase in the amount of resin mortar, the mortar layer became thicker, the aggregate was embedded more deeply, and the exposed part was smaller. The protruding part of the surface structure of the antiskid thin layer was not evident; therefore, the structural depth began to decrease gradually.

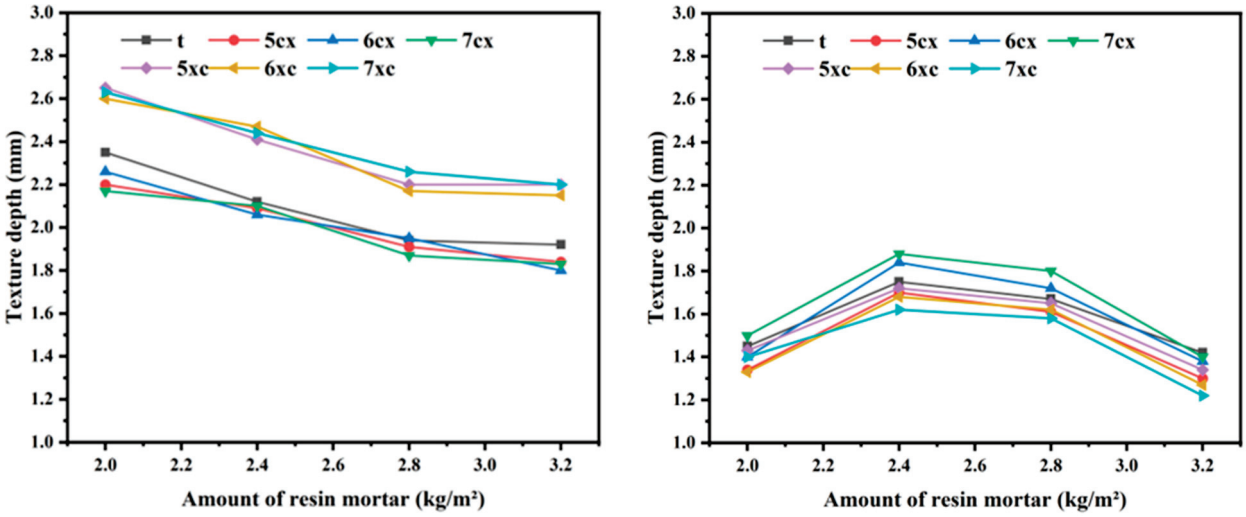

Figure 5. Texture depth of the antiskid thin layer specimens before (**a**) and after abrasion (**b**).

After the antiskid thin layer was abraded, the structural depth of each test scheme decreased to a certain extent. As the amount of resin mortar increased, the structural depth first increased and then decreased. When the amount of resin mortar used was 2 kg/m^2, the structural depth after abrasion was the smallest, and the decrease compared with that before abrasion was the most obvious. This was because the amount of mortar was too small, resulting in a large amount of aggregate spalling, and the thin-layer surface became flat owing to the lack of microconvex bodies. When the resin mortar usage reached 2.4 kg/m^2, the structural depth gradually decreased as the amount increased. This was because, after the aggregate on the surface of the thin layer was abraded, some of the remaining aggregates were embedded in the mortar layer. The greater the amount of mortar, the more the embedded part of the aggregate and the less the exposed part, so the thin layer surface gradually became flat, and the structural depth gradually decreased. When the amounts were 2.4 and 2.8 kg/m^2, the thin layer had a relatively large structural depth both before and after abrasion.

4.2. Influence of Coverage Rate of First-Spread Aggregate on Aggregate Spalling

4.2.1. Spalling Rate

The coverage of the aggregate in the thin layer was controlled to be 50%, 60%, and 70% for the aggregate spread first. The effects of the first-spread aggregates with different coverages on the aggregate spalling rate after 5 min of abrasion are shown in Figure 6.

Regardless of whether coarse or fine aggregate was spread first, the spalling rate of the antiskid thin-layer aggregate increased with the increase in the coverage rate of the first-spread aggregate. However, when the coarse aggregate was spread first, the influence of the coverage rate on the spalling rate was relatively small, and the change in the spalling rate was relatively gentle.

This was because the first-spread aggregate was first embedded into the mortar layer to ensure that it was well wrapped by the mortar. If the coverage rate is low, the aggregate spread can later fill the remaining voids in the thin layer and can also be effectively embedded in the mortar layer. As the coverage rate of the first-spread aggregate gradually increased, the remaining voids of the thin layer gradually decreased, and the later-spread aggregate could not fill the voids well, thus resulting in the aggregate not being effectively embedded in the mortar layer and the wrapping property being poor, which mainly provided antispalling ability through surface bonding with the mortar. Therefore, the spalling rate of the antiskid thin-layer aggregate increases with the increasing coverage rate of the first-spread aggregate.

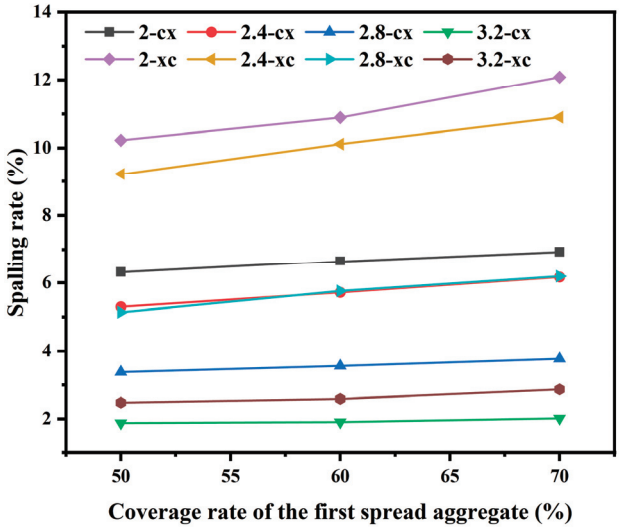

Figure 6. Spalling rate of the antiskid thin layer specimens under different coverage rate of the first-spread aggregate.

4.2.2. *BPN*

The effects of spreading aggregates with different first coverages on the pendulum values before and after thin-layer abrasion are shown in Figure 7.

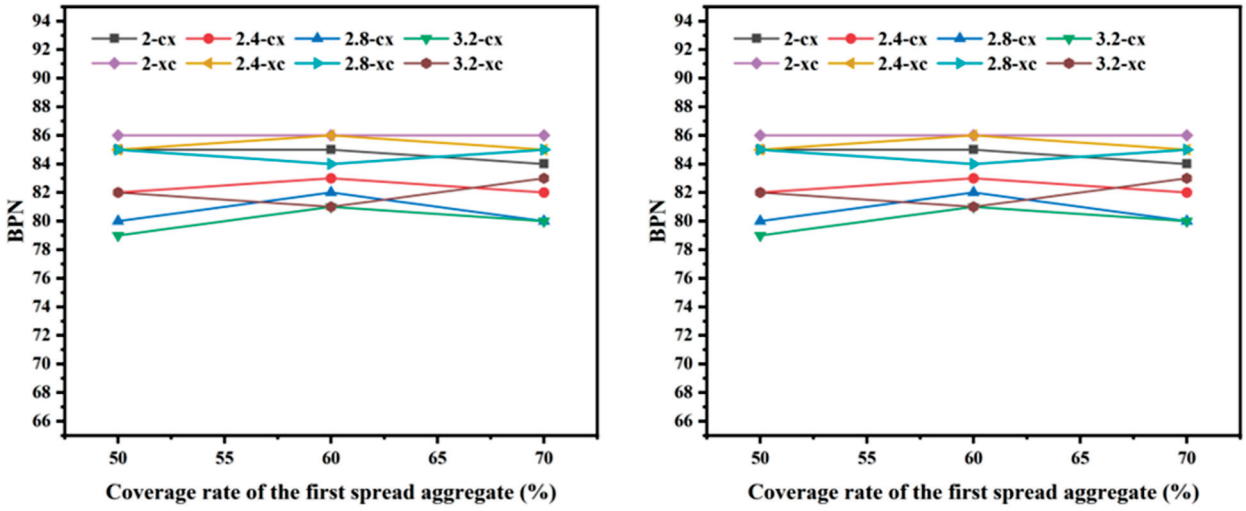

(**a**) before abrasion (**b**) after abrasion

Figure 7. Pendulum values of the antiskid thin layer specimens before (**a**) and after abrasion (**b**).

Before abrasion, the influence of the coverage rate of the first-spread aggregate on the pendulum value had no regular pattern. This was because the first-spread aggregate was mainly distributed at the bottom layer. After the extensive spreading of the second aggregate, the bottom aggregate was completely covered, and the pendulum value reflected the skid resistance of the thin-layer surface. At this time, it was mainly the aggregate on the surface of the thin layer that affected the magnitude of the pendulum value, so the influence of the coverage rate of the first-spread aggregate on the skid resistance of the thin layer before abrasion was not obvious.

After the antiskid thin layer was abraded, the magnitude of the pendulum value was affected by the coverage rate of the first-spread aggregate. If the first-spread aggregate was coarse and the later-spread aggregate was fine, the pendulum value increased with increasing coverage rate. This was because, when the thin layer was abraded, the fine aggregate was not firmly bonded to the surface and peeled off first, and the coarse aggregate

gradually spread to the bottom layer. At that time, the first-spread aggregate continuously provided skid resistance to the thin layer. The coarse aggregate had a larger particle size and more exposed parts after being embedded in the thin layer, providing a better convex structure for the thin layer. Therefore, when the first-spread aggregate was coarse aggregate, as the coverage rate of the first-spread aggregate increased, the skid resistance of the thin layer was enhanced, and the pendulum value increased. It is advisable to spread first with a coverage rate of 70%.

If fine aggregate was spread first and coarse aggregate later, the pendulum value decreased with increasing coverage rate. This was because, after abrasion, the coarse aggregate on the surface peeled off, and the fine aggregate spread first provided skid resistance. The fine aggregate had a smaller particle size and fewer exposed parts after being embedded in the thin layer. If the coverage rate of the first-spread fine aggregate is increased, when spreading for the second time, the coarse aggregate cannot fill the thin-layer voids well and is likely to peel off. There is a lack of coarse aggregates as convex bodies on the abraded thin-layer surface. Therefore, when the first-spread aggregate was a fine aggregate, as the coverage rate of the first-spread aggregate increased, the skid resistance of the thin layer weakened, and the pendulum value decreased. It is advisable to spread first with a coverage rate of 50%.

4.2.3. Texture Depth

The effects of spreading aggregates with different coverages first on the depth of construction before and after thin-layer abrasion are shown in Figure 8.

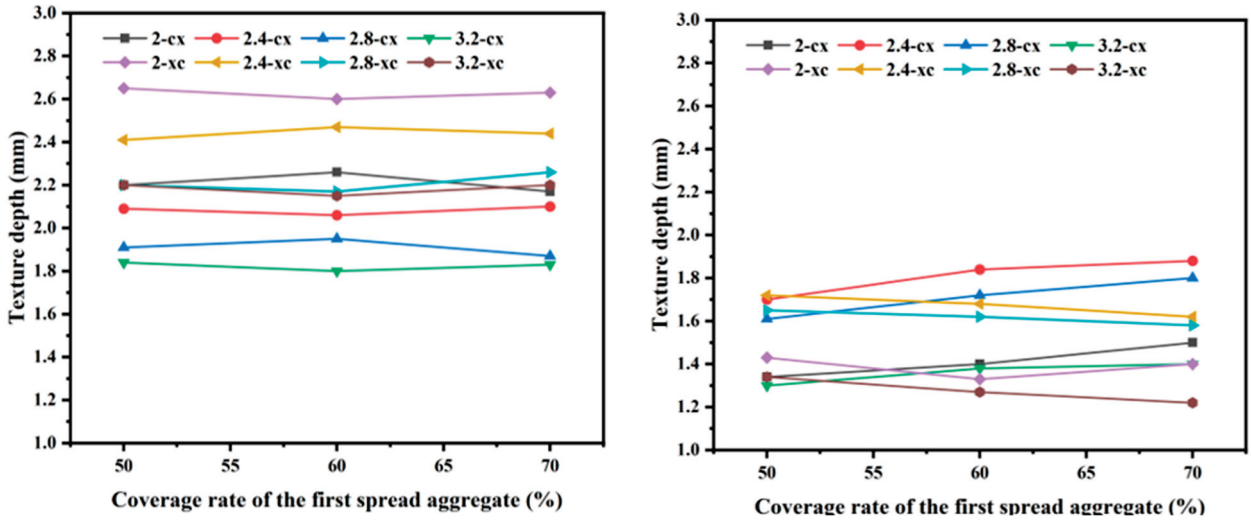

Figure 8. Texture depth of the antiskid thin layer specimens before (**a**) and after abrasion (**b**).

Before abrasion, the influence of the coverage rate of the first-spread aggregate on the texture depth of the thin layer exhibited no regular patterns. This was because the first-spread aggregate was mainly distributed at the bottom layer. After extensive spreading of the second aggregate, the bottom aggregate was completely covered. It is mainly through the aggregate on the surface of the thin layer that the magnitude of the texture depth is affected. Therefore, the influence of the coverage rate of the first-spread aggregate on the texture depth of the thin layer before abrasion was not obvious.

After the antiskid thin layer was abraded, the magnitude of the texture depth was affected by the coverage rate of the first-spread aggregate. When coarse aggregate was spread first and fine aggregate was spread later, the texture depth increased with increasing coverage rate. This was because, after the thin layer was abraded, the fine aggregate that was not firmly bonded on the surface peeled off first, and the coarse aggregate spread first at the bottom layer gradually emerged. The coarse aggregate had a larger particle size and

more exposed parts after being embedded in the thin layer. Therefore, when the coarse aggregate is spread first, as the coverage rate of the first-spread area increases, the texture depth of the thin layer increases and the coverage rate of the first-spread coarse aggregate should be 70%.

When fine aggregate was spread early and the coarse aggregate later, the texture depth decreased with increasing coverage rate. After abrasion, the coarse aggregate on the surface peeled off, and the fine aggregate spread first had a smaller particle size and fewer exposed parts after being embedded in the thin layer. When the coverage rate of the first-spread fine aggregate increased, the coarse aggregate could not effectively fill the thin-layer voids when spreading was performed for the second time, and it was likely to peel off. There was a lack of coarse aggregates as convex bodies on the abraded thin-layer surface. Therefore, when the fine aggregate is spread first, the texture depth decreases as the coverage rate of the first-spread area increases, and the coverage rate of the first-spread fine aggregate should be no more than 50%. From the point of view of a practical application, the WER should more likely be aged if the thin layer is exposed to an aggressive environment. Spreading the fine aggregate first may hinder the coating of WER binder on the surface of coarse aggregate, leading to the aggregate falling off more easily from the thin layer with the binder aged in the aggressive environment, thus reducing the texture depth of the thin layer. So, spreading the fine aggregate first may not be beneficial for the long-term performance of the WER thin layer.

4.3. Influence of Spreading Sequence of Coarse and Fine Aggregates on Aggregates Spalling

4.3.1. Spalling Rate

According to the test plan, the antiskid thin layer was divided into two spreading sequences: spreading coarse aggregate first and then fine aggregate (cx) and spreading fine aggregate first and then coarse aggregate (xc). The influences of different aggregate spreading sequences on the spalling rate of aggregates after 5 min of abrasion are shown in Figure 9.

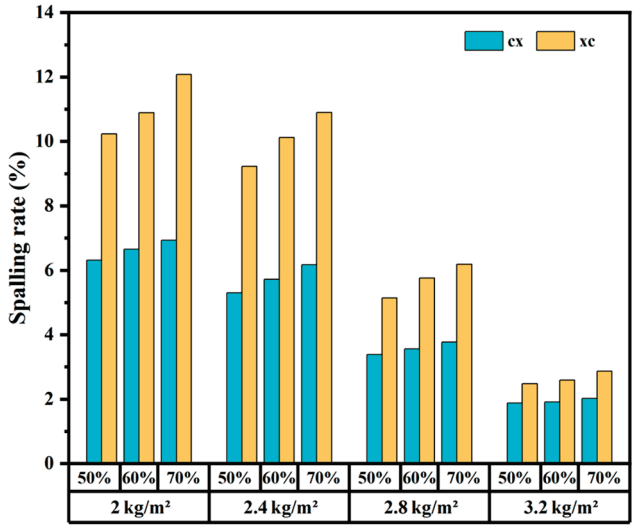

Figure 9. Spalling rate of the antiskid thin layer specimens under different order of aggregate spreading. cx: spreading coarse aggregate first and then fine aggregate; xc: spreading fine aggregate first and then coarse aggregate.

The test results show that, under the same amount of resin mortar and the same coverage rate of the first-spread aggregate, the spalling rate of spreading coarse aggregate first and then fine aggregate was smaller than that of spreading fine aggregate first and then coarse aggregate.

When the amount of resin mortar was relatively small, the influence of the spreading sequence on the spalling rate was more obvious. As the amount of resin mortar increased, the influence of the spreading sequence on the spalling rate gradually weakened.

When coarse aggregate is spread first, the coarse aggregate is well wrapped by the mortar, and there are gaps between the aggregates. When fine aggregate is spread for the second time, the fine aggregate can fill the gaps well, and there is less spalling after abrasion. If the fine aggregate is spread first, then, even though the fine aggregate is well wrapped by the mortar, the fine aggregate would occupy part of the space at the bottom of the thin layer, and the gaps between the aggregates are relatively small. This is not conducive to the filling of gaps by the coarse aggregate during the second spreading, resulting in poor wrapping of the coarse aggregate in the thin layer; thus, a large amount of spalling occurs after abrasion. When the amount of resin mortar gradually increases, the mortar layer gradually becomes thicker and effectively wraps the aggregates spread successively; thus, when the amount of resin mortar is large, the influence of the aggregate spreading sequence on the spalling rate is relatively small.

4.3.2. *BPN*

The effects of the sequential spreading order of aggregates with different particle sizes on the pendulum values before and after thin-layer abrasion are shown in Figure 10.

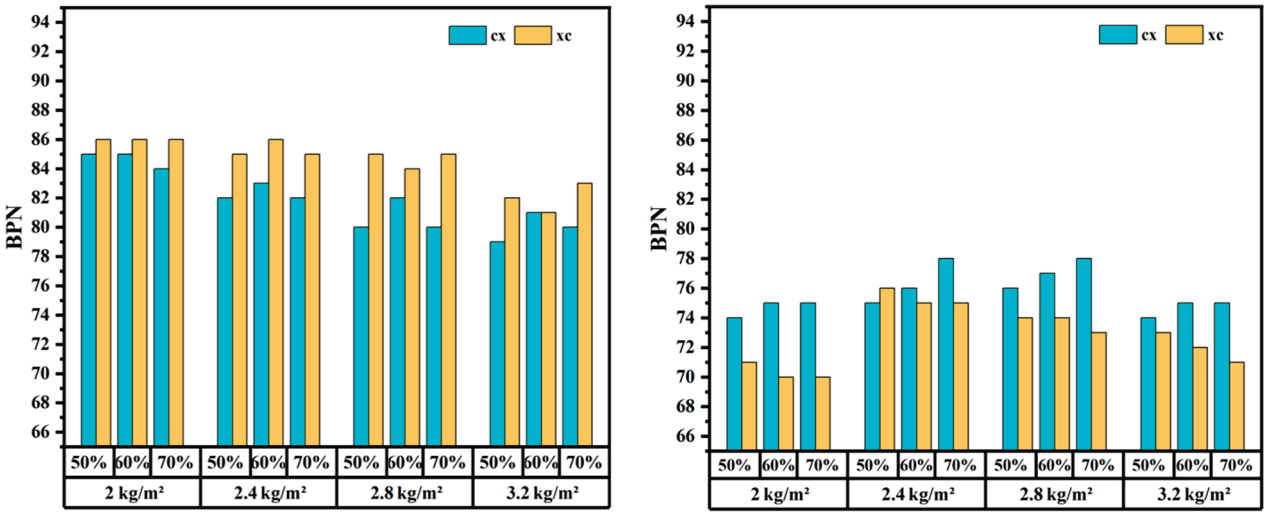

Figure 10. Pendulum values of the thin layer specimens before (**a**) and after abrasion (**b**).

Before abrasion, under different controlled aggregate spreading sequences and the same other conditions, the pendulum values of the test scheme of spreading coarse aggregate first and then fine aggregate were generally smaller than those of spreading fine aggregate first and then coarse aggregate. This was because the secondary spreading was an extensive full-coverage spreading, and the magnitude of the pendulum value mainly depended on the aggregate particle size on the surface of the thin layer. Therefore, when the surface was all fine aggregate, the magnitude of the pendulum value was smaller than that when the surface was coarse aggregate, and the antiskid performance was poorer.

After abrasion, the pendulum values of the test scheme for spreading coarse aggregate first and then fine aggregate were generally greater than those for spreading fine aggregate first and then coarse aggregate. This was because, after abrasion, the aggregate on the surface flaked off, and the first-spread aggregate was exposed and became the main component providing antiskid performance. If the coarse aggregate was spread first, the exposed area of the layer would be greater and would provide better antiskid performance. If fine aggregate was spread first, the exposed area would be smaller, and the effect of providing antiskid performance would not be obvious.

4.3.3. Texture Depth

The effect of the sequential spreading order of aggregates with different grain sizes on the depth of the structure before and after thin-layer abrasion is shown in Figure 11.

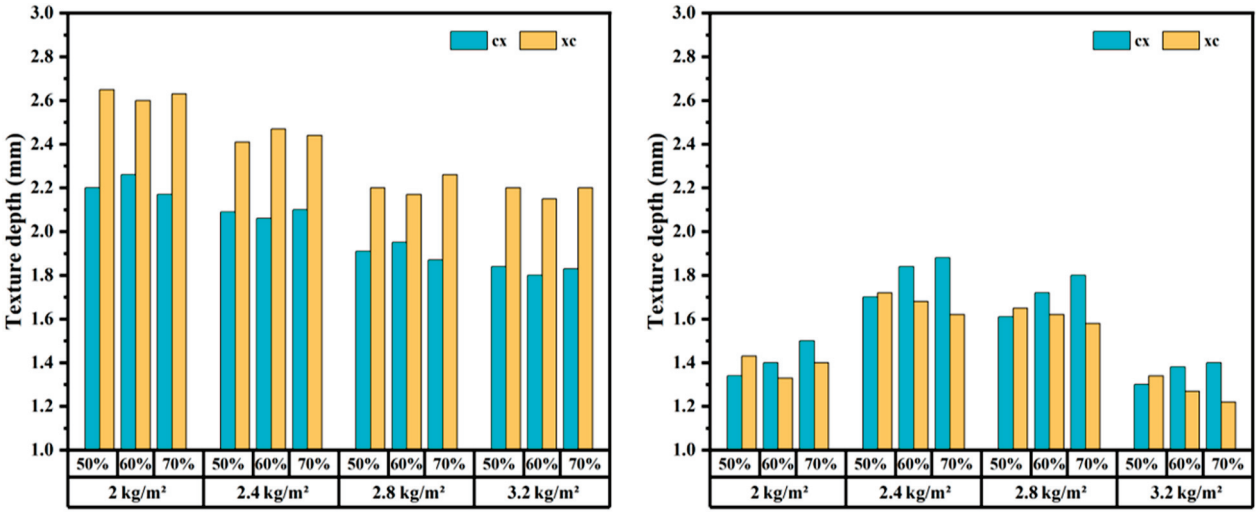

(**a**) before abrasion (**b**) after abrasion

Figure 11. Texture depth of the antiskid thin layer specimens before (**a**) and after abrasion (**b**).

Before abrasion, under different controlled aggregate spreading sequences and the same other conditions, the structural depths of the test scheme of spreading coarse aggregate first and then fine aggregate were all smaller than those of spreading fine aggregate first and then coarse aggregate because the structural depth was mainly affected by the particle size of the surface aggregate.

After abrasion, except when the coverage rate of the first-spread aggregate was 50%, the structural depths of the other test schemes were all greater than those of spreading fine aggregate first and then coarse aggregate. This was because, when the coverage rate of the first-spread aggregate was 50%, the gap between the aggregates was relatively large, and the later-spread aggregate filled the remaining 50% gap of the mortar. Therefore, when the coverage rate of the first-spread aggregate was 50%, the influence of the aggregate spreading sequence on the structural depth was relatively small. When the coverage rates of the first-spread aggregate were 60% and 70%, the structural depths of spreading coarse aggregate first were all greater than those of spreading fine aggregate first. This was because, after abrasion, the aggregates on the surface of the thin layer flaked off first. At this time, the surface structure of the thin layer was composed of first-spread aggregates, so the structural depth of spreading coarse aggregate first was greater than that of spreading fine aggregate first.

5. Conclusions

The change law of the spalling rate, *BPN*, and tectonic depths of the WER thin layer with different construction processes were investigated in the laboratory. It can be concluded from this work, which is as follows:

(1) The greater the amount of resin mortar used, the stronger the antispalling ability of the aggregates becomes. Before abrasion, the pendulum value and structural depth decrease with the increase in the amount of resin mortar; after abrasion, the pendulum value and structural depth first increase and then decrease with the increase in the amount of resin mortar. Considering the antispalling property, antiskid property, and economy, the appropriate amount of resin mortar is 2.8 kg/m^2.

(2) When coarse aggregates are spread first, the spalling rate is less affected by the coverage rate, and the pendulum value and structural depth after abrasion increase with increasing coverage rate. Therefore, the appropriate coverage rate for spreading coarse

aggregates first is 70%, and the appropriate coverage rate for spreading fine aggregates first is 50%.

(3) The spalling rate of spreading coarse aggregates first is smaller than that of spreading fine aggregates first. When the coverage rate of the first-spread aggregate is 50%, the influence of the aggregate spreading sequence on the structural depth is relatively small. For 60% and 70% coverage rates of the first-spread aggregate, the structural depth when coarse aggregates are spread first is greater than when fine aggregates are spread first.

In summary, the suggested construction process based upon this work confirms that the suitable dosage of WER binder is ~2.8 kg/m^2, which is accompanied by spreading 70% coarse aggregate first.

Author Contributions: Conceptualization, J.Y., G.Z. and C.L.; methodology, C.F., W.D. and Y.Z.; software, H.H.; validation, Y.Z., W.J. and L.X.; formal analysis, Y.Z.; investigation, H.H.; resources, G.Z.; data curation, J.Y. and H.L.; writing—original draft preparation, J.Y., H.L. and X.Y.; writing—review and editing, G.Z., W.D. and C.F.; supervision, C.F., G.Z. and C.L.; project administration, G.Z.; funding acquisition, G.Z. and C.L. All authors have read and agreed to the published version of the manuscript.

Funding: This research was funded by the Chongqing Natural Science Foundation Innovation and Development Joint Fund (CSTB2024NSCQ-LZX0076) and the Chongqing Jiaotong University Municipal Graduate United Cultivating Base (JDLHPYJD2023001).

Institutional Review Board Statement: Not applicable.

Informed Consent Statement: Not applicable.

Data Availability Statement: The research data will be made available on request.

Acknowledgments: The authors thank Chongqing Jiaoda Construction Engineering Quality Test Center Co. Ltd. for their help in sample testing.

Conflicts of Interest: Author Jiaquan Yuan, Wenhong Duan, Weihong Jiang, Li Xiong, Huimei Li, Xiaohua Yang were employed by the company Dali Danan Highway Co., Ltd. The remaining authors declare that the research was conducted in the absence of any commercial or financial relationships that could be construed as a potential conflict of interest.

References

1. Wang, K.; Gudyanga, B.; Zhang, W.; Feng, Z.; Wang, C.; Yang, B.; Yang, S. Optimization of colored pavement considering driving behavior and psychological characteristics under dynamic low-visibility conditions related to fog—A driving simulator study. *Traffic Inj. Prev.* **2024**, *25*, 518–526. [CrossRef] [PubMed]
2. McNeil, N.; Monsere, C.; Dill, J. Evaluation of driver comprehension and compliance of red color of red colored pavement markings for transit lanes in Portland, Oregon. *Transp. Res. Rec.* **2023**. [CrossRef]
3. Wang, J.; Li, Q.; Song, G.; Luo, S.; Ge, D. Investigation on the comprehensive durability and interface properties of coloured ultra-thin pavement overlay. *Case Stud. Constr. Mater.* **2022**, *17*, e01341. [CrossRef]
4. Li, X.; Ye, J.; Badjona, Y.; Chen, Y.; Luo, S.; Song, X.; Zhang, H.; Yao, H.; Yang, L.; You, L.; et al. Preparation and performance of colored Ultra-Thin overlay for preventive maintenance. *Constr. Build. Mater.* **2020**, *249*, 118619. [CrossRef]
5. Geng, L.; Ma, T.; Zhang, J.; Huang, X.; Hu, P. Research on performance of a dense graded ultra-thin wearing course mixture. *Appl. Sci.* **2017**, *7*, 800. [CrossRef]
6. Yu, J.; Feng, Z.; Chen, Y.; Yu, H.; Korolev, E.; Obukhova, S.; Zou, G.; Zhang, Y. Investigation of cracking resistance of cold asphalt mixture designed for ultra-thin asphalt layer. *Constr. Build. Mater.* **2024**, *414*, 134941. [CrossRef]
7. Jin, F.; Li, X.; Park, S. Synthesis and application of epoxy resins: A review. *J. Ind. Eng. Chem.* **2015**, *29*, 1–11. [CrossRef]
8. Mi, X.; Liang, N.; Xu, H.; Wu, J.; Jiang, Y.; Nie, B.; Zhang, D. Toughness and its mechanisms in epoxy resins. *Prog. Mater. Sci.* **2022**, *130*, 100977. [CrossRef]
9. Jiang, Y.; Liu, L.; Yan, J.; Wu, Z. Room-to-low temperature thermo-mechanical behavior and corresponding constitutive model of liquid oxygen compatible epoxy composites. *Compos. Sci. Technol.* **2024**, *245*, 110357. [CrossRef]
10. Liu, Y.; Qian, Z.; Shi, X.; Zhang, Y.; Ren, H. Developing cold-mixed epoxy resin-based ultra-thin antiskid surface layer for steel bridge deck pavement. *Constr. Build. Mater.* **2021**, *291*, 123366. [CrossRef]
11. Wang, X.; Ma, B.; Chen, S.; Wei, K.; Kang, X. Properties of epoxy-resin binders and feasibility of their application in pavement mixtures. *Constr. Build. Mater.* **2021**, *295*, 123531. [CrossRef]
12. Shi, S.; Chen, X.; Gu, L.; Ma, T. Investigated on hot mix epoxy resin used in steel bridge deck pavement affected by collaborative toughen. *Case Stud. Constr. Mater.* **2024**, *20*, e03019. [CrossRef]

13. Coni, M. Ultrathin multi-functional overlay. In *Airfield and Highway Pavement 2013: Sustainable and Efficient Pavements*; American Society of Civil Engineers (ASCE): Los Angeles, CA, USA, 2013; pp. 662–676. [CrossRef]
14. Xiang, Q.; Xiao, F. Applications of epoxy materials in pavement engineering. *Constr. Build. Mater.* **2020**, *235*, 117529. [CrossRef]
15. Liang, M.; Zhang, Y.; Xin, X.; Chen, Z.; Wang, J.; Jiao, Y.; Chen, L.; Luan, X.; Su, L. The properties of waterborne epoxy resins modified magnesium potassium phosphate cement paste: A combined experimental and molecular dynamics simulation study. *Constr. Build. Mater.* **2024**, *442*, 137494. [CrossRef]
16. Pang, B.; Zhang, Y.; Liu, G. Study on the effect of waterborne epoxy resins on the performance and microstructure of cement paste. *Constr. Build. Mater.* **2018**, *167*, 831–845. [CrossRef]
17. Yang, F.; Zhou, Q.; Yang, L.; He, L.; Chen, Q.; Tang, S. Preparation and performance evaluation of waterborne epoxy resin modified emulsified asphalt binder. *Case Stud. Constr. Mater.* **2024**, *21*, e03548. [CrossRef]
18. Kong, L.; Su, S.; Wang, Z.; Wu, P.; Zhang, Y.; Chen, Z.; Ren, D.; Ai, C. Microscale mechanism and key factors of waterborne epoxy resin emulsified asphalt enhancing interlayer bonding performance and shear resistance of bridge deck pavement. *Constr. Build. Mater.* **2024**, *419*, 135570. [CrossRef]
19. Han, S.; Yao, T.; Han, X.; Zhang, H.; Yang, X. Performance evaluation of waterborne epoxy resin modified hydrophobic emulsified asphalt micro-surfacing mixture. *Constr. Build. Mater.* **2020**, *249*, 118835. [CrossRef]
20. Zhou, Y.; Peng, Z.; Wang, J.; Wei, J.; Liu, H.; Wang, D.; Li, J.M. A review on adhesion behavior of chip seal pavement and aggregate. *J. Traffic Transp. Eng.* **2024**, *11*, 411–466. [CrossRef]
21. Xiao, Y.; van de Ven, M.; Molenaar, A.; Wu, S. Possibility of using epoxy modified bitumen to replace tar-containing binder for pavement antiskid surfaces. *Constr. Build. Mater.* **2013**, *48*, 59–66. [CrossRef]
22. Kim, Y.R.; Aragao, F.T.; Allen, D.H.; Little, D.N. Damage modeling of bituminous mixtures considering mixture microstructure, viscoelasticity, and cohesive zone fracture. *Can. J. Civ. Eng.* **2010**, *37*, 1125–1136. [CrossRef]
23. Boulangé, L.; Bonin, E.; Saubot, M. Physicochemical characterisations of the bitumen–aggregate interface to get a better understanding of stripping phenomena. *Road Mater. Pavement Des.* **2013**, *14*, 384–403. [CrossRef]
24. Zhang, Y.; Yao, K.; Zhi, P.; Dong, Y.; Feng, X.; Li, B.; Xu, Y.; Zhang, Y.; Guo, C.; Tian, J. The influence of water acidity and alkalinity on the adhesion properties of bitumen-aggregate interface. *Colloids Surf. A Physicochem. Eng. Asp.* **2024**, *695*, 134025. [CrossRef]
25. Zhang, H.; Qiu, H.; Kodur, V.; Yuan, V. Spalling behavior of metakaolin-fly ash based geopolymer concrete under elevated temperature exposure. *Cem. Concr. Compos.* **2020**, *106*, 103483. [CrossRef]
26. Mustafa, A.; Mohammed, R.; Khaled, B.; Sameh, Y.M. Application of deep learning in damage classification of reinforced concrete bridges. *Ain Shams Eng. J.* **2024**, *15*, 102297.
27. Wang, F.; Li, Y.; Yu, L.; Pang, W. Study on influencing factors of asphalt-aggregate stripping mechanism. *Adv. Mater. Sci. Eng.* **2021**, *1*, 6619118. [CrossRef]
28. Zong, Y.; Li, S.; Zhang, J.; Zhai, J.; Li, C.; Ji, K.; Feng, B.; Zhao, H.; Guan, B.; Xiong, R. Effect of aggregate type and polishing level on the long-term skid resistance of thin friction course. *Constr. Build. Mater.* **2021**, *282*, 122730. [CrossRef]
29. Liu, H.; Zhang, Z.; Guo, D.; Peng, L.; Bao, Z.; Han, W. Research progress and prospect of application technology of thin-layer antiskid colored pavement at home and abroad. In Proceedings of the 2011 International Conference on Electric Technology and Civil Engineering (ICETCE), Lushan, China, 22–24 April 2011; pp. 2557–2560.
30. Liu, F.; Qu, D.; Tan, Z.; Yang, C.; Liu, Y. Experimental investigation of the effects of four anti-slide particles on the operational performance of coated coloured pavement. *Procedia Eng.* **2016**, *161*, 589–594. [CrossRef]
31. Lee, H.; Kim, Y. Laboratory evaluation of color polymer concrete pavement with synthetic resin binder for exclusive bus lanes. *Transp. Res. Rec.* **2007**, *1991*, 124–132. [CrossRef]
32. *T/CECS G: D54-03—2021*; Standard of China Association for Engineering Construction Standardization. Technical Specifications for Colored Pavement. China Communications Press: Beijing, China, 2021.
33. *JT/T 712—2008*; Industry Standard of Transport of People' Republic of China. Pavement Antiskid Paint. Ministry of Transport of People's Republic of China: Beijing, China, 2008.

coatings

MDPI

Article

Predicting Dynamic Properties and Fatigue Performance of Aged and Regenerated Asphalt Using Time–Temperature–Aging and Time–Temperature–Regenerator Superposition Principles

Zhaoli Wang [1,*], Hongli Ding [1], Xiaoyan Ma [2,*], Wanhong Yang [1] and Xiaojun Ma [3]

[1] Gansu Road & Bridge Shan Jian Technogy Co., Ltd., Lanzhou 730030, China; 18845118635@163.com (H.D.); yangwanhoo@sina.com (W.Y.)
[2] Engineering Research Center of Transportation Materials, Ministry of Education, School of Materials Science and Engineering, Chang'an University, Xi'an 710064, China
[3] Qinghai Transportation Planning and Design Institute Co., Xining 810000, China; rock12360@163.com
* Correspondence: wangwzhaozlil@126.com (Z.W.); xiaoyanma@chd.edu.cn (X.M.)

Abstract: Reclaimed asphalt pavement (RAP) reduces energy consumption and enhances economic benefits by recycling road materials, making it an effective approach for the sustainable use of solid waste resources. The performance of reclaimed asphalt pavement is significantly affected not only by the degradation of asphalt binders due to aging but also by the dosage of the rejuvenator used. The master curve of the complex shear modulus is widely recognized as a valuable tool for characterizing the rheological properties of asphalt binders. First, a virgin asphalt binder with a grade of SK70 was subjected to varying degrees of aging, followed by the rejuvenation of the aged asphalt using different dosages of the rejuvenator. Second, frequency sweeps were conducted on the aged and rejuvenated asphalt binders at various temperatures. Complex modulus master curves were constructed, and the CAM model was applied to fit these curves. The viscoelastic properties of asphalt at different aging levels and rejuvenator dosages were then analyzed based on the CAM parameters. Next, by applying a curve-shifting technique based on the least squares method to a reference state, both the time–temperature–aging (TTA) and time–temperature–regenerator (TTR) master curves of the complex modulus were constructed. The relationships between aging shift factors and aging times, as well as between regenerator shift factors and dosages, were established to predict the complex moduli of both aged and rejuvenated asphalt. Finally, the shear stress–strain relationships and material integrity of aged and rejuvenated asphalt were evaluated to assess their fatigue performance. The results indicated that aging significantly increases the complex modulus of asphalt, with TFOT (Thin Film Oven Test) aging having a more pronounced impact than PAV (Pressurized Aging Vessel) aging, resulting in reduced viscous deformation and an increased risk of cracking. Rejuvenator dosage reduces the complex modulus, with a 6% dosage effectively restoring mechanical properties and enhancing low-temperature performance. The TTA master curve demonstrates a strong linear correlation between aging shift factors and time, allowing for accurate predictions of the complex modulus of aged asphalt. Similarly, the TTR master curve reveals a linear relationship between regenerator dosage and shift factor, offering high predictive accuracy for optimizing regenerator dosages in engineering applications. The study further explores how varying levels of aging and rejuvenator dosage affect fatigue life under different strain conditions, uncovering complex behaviors influenced by these aging and regeneration processes.

Keywords: reclaimed asphalt pavement (RAP); aged asphalt; rejuvenated asphalt; complex modulus; time–temperature–aging (TTA); time–temperature–regenerator (TTR); fatigue

1. Introduction

Asphalt pavement is commonly used on highways due to its superior performance. However, it is prone to wear and aging under high temperatures and ultraviolet radiation, leading to performance deterioration and a shortened service life [1,2]. This results in increased repair and maintenance of asphalt pavement, generating a significant amount of solid waste [3]. According to the Environmental Protection Agency (EPA), nearly 600 million tons of reclaimed asphalt pavement (RAP) are generated annually [4]. RAP consists of aged asphalt and aggregates of varying particle sizes, and its utilization helps reduce environmental pollution and costs and conserves natural resources. However, compared to original asphalt, RAP becomes more rigid and brittle when used in regenerated asphalt pavements. Additionally, according to the migration theory of components, oxidation occurs during the mixing, transportation, paving, and maintenance of asphalt pavements. This oxidation results in the loss of light components and an increase in heavy components, leading to low-temperature cracking and reduced fatigue life [5]. As a result, researchers are increasingly using regenerators to restore the performance of aged asphalt pavements [6,7].

A rejuvenator has a chemical composition similar to the lighter components of asphalt; it consists of engineered products made from various organic compounds and exhibits a specific polarity and molecular structure [8,9]. The addition of a rejuvenator can restore the performance of asphalt. Studies have shown that rejuvenators can reduce the complex modulus of aged asphalt and increase its phase angle [10]. Sharma et al. evaluated the potential use of RAP as a replacement material for asphalt binders and found that binders incorporating 40% RAP exhibited superior rheological properties [11].

Asphalt pavement aging is influenced by traffic loads and natural factors, with aging being proportional to time, temperature, and load. Since aging occurs over an extended period, real-time measurement of asphalt performance is challenging. Therefore, indoor accelerated aging tests are commonly employed to better predict the performance of aged asphalt. Anjali et al. proposed a time–temperature superposition approach to predict the complex modulus of asphalt under various dosage conditions [12]. This approach employs a consistent dose rate to construct a CA model for predicting the complex modulus of asphalt binders. Liu et al. developed a method based on a time–aging superposition approach to construct an aging master curve for the complex modulus and phase angle [13]. Rad et al. utilized the NCHRP09-54 and GAS models to predict asphalt binder properties under thermal–oxidative aging, using the viscosity index as a key metric. They found that the NCHRP09-54 model demonstrates high accuracy in predicting aging performance. Additionally, Saleh et al. used the complex modulus to predict the aging process of asphalt binders by decoupling the time–temperature and time–aging superposition effects [14]. Chen et al. employed frequency sweeps and the time–temperature superposition principle (TTSP) to construct complex modulus master curves and a black diagram, evaluating the effect of modifiers on the aging sensitivity and rheological behavior of asphalt during the aging process [15].

Over the past decades, research has verified that asphalt materials within the linear viscoelastic (LVE) domain are thermos-rheological simple, allowing their behavior in this undamaged state to be characterized using the TTSP. Building upon this theory, Chen et al. established a master curve for asphalt aging time and thoroughly examined the long-term aging performance of various modified asphalts [16]. Qin et al. explored changes in asphalt pavement performance under real aging conditions using rheological indicators, proposing a relationship between asphalt structure and these indicators to predict the rheological properties of aging asphalt binders [17]. Using the time–aging superposition principle, Wang et al. established an aging time master curve to accurately predict asphalt's dynamic modulus index under various aging conditions [18]. Wen et al. performed a series of monotonic constant shear strain-rate tests on asphalt binders at various temperatures and loading rates, subsequently constructing master curves for failure stress and failure energy [19]. Based on the above studies, adopting models to predict the performance of aging and regenerated asphalt binders is crucial for optimizing the use of reclaimed

asphalt pavement (RAP) in modern infrastructure projects. As asphalt binders age, they undergo chemical and physical changes that affect their rheological properties, including increased stiffness and a higher susceptibility to cracking. Regeneration of these aged binders with rejuvenators helps restore their flexibility and resistance to deformation. However, predicting the performance of both aged and regenerated binders requires a robust modeling approach to ensure pavement durability and longevity.

Aging not only alters the dynamic mechanical properties of asphalt but also reduces its fatigue life. Since the addition of a regenerating agent also affects the fatigue life of aged asphalt, it is essential to examine the fatigue performance of both aged and regenerated asphalt. Numerous studies have shown that the fatigue characteristics of asphalt binders decline with age [20–22]. Yang et al. evaluated the fatigue characteristics of asphalt at different aging times using the Simplified Viscoelastic Continuum Damage (S-VECD) model, finding that as aging time increased, fatigue resistance declined [23]. Researchers have also tested the fatigue characteristics of aged asphalt binders using regenerators. Jacobs et al. used the linear amplitude sweep (LAS) test to measure the fatigue characteristics of reclaimed asphalt pavement and found that the rejuvenator improved the fatigue life of regenerated asphalt binders without compromising their high-temperature performance [24]. Cao et al. studied the effects of bio-oil regenerants on the fatigue performance of asphalt binders aged for different durations and found that longer aging resulted in lower fatigue life [25]. Understanding the fatigue behavior of both aged and regenerated asphalt is crucial for ensuring the long-term durability and sustainability of pavement structures. Since aging diminishes the binder's resistance to fatigue cracking, proper evaluation helps in optimizing the dosage of rejuvenators, ensuring that the mechanical properties are restored while maintaining structural integrity. This is essential for enhancing pavement life, especially with the growing focus on recycling asphalt and reducing environmental impacts.

Existing research has investigated the aging and regeneration processes of asphalt pavements, particularly focusing on the effectiveness of rejuvenators in restoring the performance of aged asphalt. Various models and methods, such as the time–temperature superposition principle (TTSP), by shifting the complex modulus curves at different aging times, can be used to construct a time–temperature–aging (TTA) equivalent master curve for predicting asphalt performance. The previously discussed research methods, while valuable, have certain limitations that need to be addressed for a more comprehensive understanding of asphalt behavior. Specifically, these methods fail to clearly delineate the relationships between different modes of asphalt aging, the duration of aging, and the corresponding shift factor that is often used to predict material behavior under varying conditions. This gap in the methodology creates uncertainty in accurately modeling how asphalt will perform over time as it ages. Moreover, when considering the rejuvenation of aged asphalt, the connection between the shift factor and the quantity of rejuvenator used is not well defined. This lack of clarity impedes our ability to establish a reliable framework for predicting the dynamic mechanical properties of rejuvenated asphalt. Without a better understanding of these relationships, it becomes challenging to forecast how both aged and rejuvenated asphalt will behave under different loading and environmental conditions, which is critical for the effective design and maintenance of asphalt pavements. Therefore, further research is needed to elucidate these relationships and enhance the predictive accuracy of asphalt performance models. This study predicted the dynamic mechanical properties and fatigue life of aged–rejuvenated asphalt using complex modulus aging and rejuvenation master curves, along with the S-VECD model, under various aging conditions and rejuvenator admixtures. The aim of this study is to predict the dynamic properties of aged and rejuvenated asphalt binders, focusing on the effects of aging and rejuvenator dosage on the material's rheological and fatigue performance. By subjecting virgin asphalt to varying degrees of aging and rejuvenating the aged binder with different rejuvenator dosages, this research seeks to elucidate how these factors influence the complex modulus of asphalt. The study employs the master curve of the complex shear modulus, using the

CAM model and curve-shifting techniques, to construct time–temperature–aging (TTA) and time–temperature–regenerator (TTR) master curves for accurate predictions of the asphalt's performance. Additionally, the research evaluates the fatigue performance and material integrity of both aged and rejuvenated asphalt under different strain conditions, aiming to provide valuable insights for optimizing the use of reclaimed asphalt pavement (RAP) in sustainable road construction.

2. Materials

2.1. Asphalt Binders

The virgin asphalt used in this study is SK70 matrix asphalt. Its essential performance properties were tested according to the (JTG E20-2011) [26], and test results are presented in Table 1.

Table 1. Physical properties of matrix asphalt.

Property	SK70	Test Method
Penetration (25 °C, 100 g, 5 s) (0.1 mm)	57.3	T0604
Ductility (5 cm/min, 10 °C)	77.3	T0605
Softening point (°)	46.9	T0606
Viscosity (135°, Pa·s)	0.37	T0625

2.2. Rejuvenator

A generic rejuvenator was adopted in this study, and its properties are presented in Table 2.

Table 2. Essential properties of rejuvenator.

Property	Test Result	Technical Specifications	Test Method
Viscosity (60 °C, mm^2/s)	55	≥50	T0619
Flash point (°C)	234	≥220	T0611
RTFOT Viscosity ratio	1.02	≤3	T0619
RTFOT Mass Change (%)	−0.32	≤±4	T0609
Saturation content (%)	11.31	≤30	TLC-FID
Aromatic content (%)	78.8	-	TLC-FID

2.3. Specimen Preparation

As the actual aging station could be simulated in a laboratory aging process based on Kim and Saleh et al.'s study [14], this study prepared asphalt binders at three aging stages: original SK70 asphalt, short-term-aged asphalt binders at different aging times, and long-term-aged asphalt binders at different aging times. The short-term-aged asphalt binders were prepared using the Thin Film Oven Test (TFOT) at a temperature of 163 °C, with five aging durations: 5, 10, 20, 30, and 40 h, to simulate thermal–oxidative aging. The long-term-aged asphalt binders were prepared using the Pressurized Aging Vessel (PAV) at 100 °C and 2.1 MPa, with two aging durations: 20 and 40 h on TFOT-aged asphalt binders (5 h). The rejuvenation procedure was as follows: the aged asphalt (PAV: 20 h) was heated to 135 °C, and the rejuvenator was added. The mixture was then blended for 20 min at 3000 rpm in a mixer.

3. Experimental Methods

3.1. Design of Experiments

An AR2000 dynamic shear rheometer (DSR) by TA Instruments (New Castle, DE, USA) was employed to measure the rheological performance of asphalt binders. The temperature–frequency and LAS tests were conducted using plates with diameters of 8 mm and 25 mm, following AASHTO T315 standards [27]. Temperature–frequency sweep tests were performed at six temperatures: 20 °C, 30 °C, 40 °C, 50 °C, 60 °C, and 70 °C, across

frequencies ranging from 0.1 to 15.9 Hz. To ensure the test results were within the linear viscoelastic (LVE) range of the asphalt binder, a linear amplitude sweep (LAS) was applied with a strain amplitude of 1% across all test frequencies and temperatures. The LAS tests included a frequency sweep within the LVE range and an oscillatory strain amplitude sweep, following AASHTO TP 101 [28].

3.2. Christensen–Anderson–Marasteanu (CAM) Model

Based upon the time–temperature superposition principle, the master curve of the asphalt binder's dynamic shear modulus was established by multiple temperature and frequency sweep test results, and the CAM model was applied to fitting the complex modulus master curve [29,30]. Yusoff et al. demonstrated that the CAM model provides a better fit for the complex modulus master curve compared to the CA model [31]. Therefore, this study employs the CAM model to fit the complex modulus master curve of asphalt binders under different aging and regenerating conditions. The fitting of the CAM model is shown in Figure 1, and the shape parameter can be described in Equation (1).

$$|G^*| = \frac{G_g^*}{\left[1+f_c/(f)^k\right]^{m/k}} \quad (1)$$

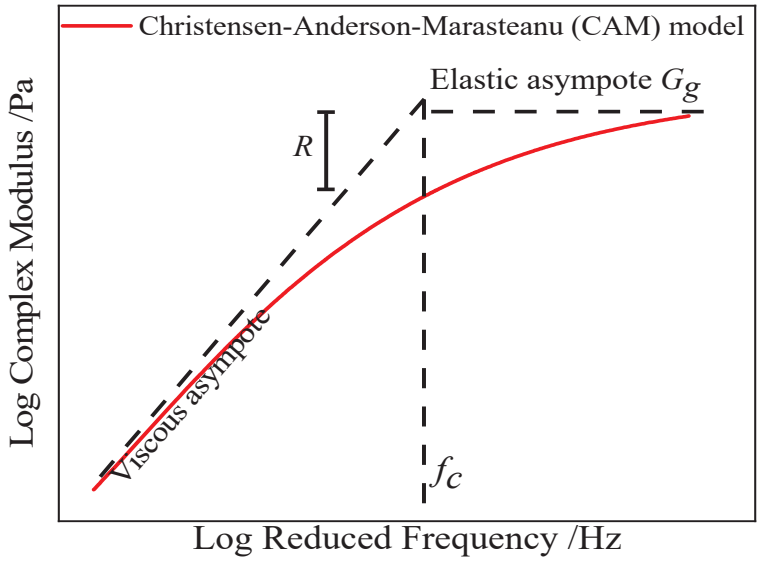

Figure 1. Fitting the complex modulus master curve for the CAM model.

Here, G_g^* is the glassy complex modulus, f is actual loading frequency, f_c is the cross frequency, and m and k are the master curve fitting parameters. The shape parameter, m, represents the slope of the third asymptote of the complex modulus's primary curve. A smaller slope of the asymptotic line indicates that the asphalt is less sensitive to frequency, suggesting better viscoelastic performance at both high and low temperatures. The parameter k determines how rapidly the complex modulus master curve converges with the two asymptotes as the frequency approaches zero or infinity.

3.3. Simplified Viscoelastic Continuum Damage Model

The viscoelastic continuum damage (VECD) model is based on Schapery's mechanical theory. It was applied to predict the fatigue life of asphalt materials of different scales. In the library, the relation of modulus and strain obtained from the LAS test was selected to calculate the fatigue life of asphalt according to the VEDC model [16]. However, the calculation process is quite complex. To reduce the calculation process, Underwood et al. simplified the VECD model to make it more effective and predict the fatigue life of asphalt

successfully. In the S-VECD model, the peak pseudostrain in any loading cycle is defined as shown in Equation (2):

$$\gamma_P^R = \frac{1}{G_R}(\gamma_P|G^*|_{LVE}) \tag{2}$$

In which γ_P is the peak pseudostrain in the loading cycle, $|G^*|_{LVE}$ is the complex modulus of the material in the linear viscoelastic range, and G_R is the reference modulus, which was set to 1.

At the beginning of the amplitude sweep process, the material exhibits linear viscoelasticity, while the pseudostrain value decreases as the material's damage level increases. Therefore, the pseudostrain value can be calculated to analyze the damage evolution characteristics of the material, referred to as the material integrity coefficient, $C^*(S)$, and the DMR is the dynamic modulus ratio, shown in Equations (3) and (4).

$$C^*(S) = \frac{\tau_P}{\gamma_P^R \times DMR} \tag{3}$$

$$DMR = \frac{|G^*|_{Fingerprint}}{|G^*|_{LVE}} \tag{4}$$

In which τ_P is effective peak shear stress, and $|G^*|_{Fingerprint}$ is the initial complex modulus measured.

To calculate the nonlinear viscoelastic properties of the material during loading, the nonlinear viscoelastic complex modulus, $|G^*|_{NLVE}$, is substituted for the linear viscoelastic complex modulus, $|G^*|_{LVE}$, during the strain sweep, and the internal damage evolution variable $S(t)$ is shown in Equations (5)–(7).

$$\gamma_P^R NLVE = \frac{1}{G_R}(\gamma_P|G^*|_{NLVE}) \tag{5}$$

$$S(t) = \sum_{i=1}^{n}\left[\frac{DMR}{2}\left(\gamma_{P,i}^R\right)^2\left(C_{i-1}^* - C_i^*\right)\right]^{\frac{\alpha}{\alpha+1}}(t_{Ri} - t_{Ri-1})^{\frac{1}{\alpha+1}} \tag{6}$$

$$t_R = \frac{t_i}{\alpha_T} \tag{7}$$

In which t_R is the reduced time, i is the cycle number, α is a non-damaged material constant, m is the fitting slope parameter of the linear viscoelastic dynamic shear modulus master curve, and n is the maximum load time. When the damage characteristic curve, $S(t)$, is independent of loading duration and temperature, the test results can predict the damage evolution in a material subjected to a given loading duration.

As fatigue damage accumulates within the asphalt material, fatigue breakdown occurs when a critical damage state is reached, which destroys material cohesion, and reduces the asphalt mixture's fatigue life. This paper evaluates the fatigue life of aged and regenerated asphalt using the pseudostrain energy release rate, G^R, and fatigue life, N_f, to predict fatigue performance more scientifically. The pseudostrain energy released, W_r^R, represents the difference between the total pseudostrain energy and the stored pseudostrain energy, and the mean pseudostrain energy release rate, G^R, is shown in Equations (8) and (9).

$$W_r^R = \frac{1}{2}(1 - C^*)(\gamma_p^R)^2 \tag{8}$$

$$G^R = \frac{\overline{W_r^R}}{N_f} = \frac{TRPSE}{{N_f}^2} \tag{9}$$

In which $TRPSE$ is the area of the curve before the point of damage and $\overline{W_r^R}$ is the mean virtual strain energy released. The relation between the mean virtual strain energy release rate, G^R, and the fatigue life constitutes the damage criterion of the material, and the relation formula is shown in Equation (10).

$$G^R = aN_f{}^b \tag{10}$$

The relation between the material's final fatigue life, N_f, and the strain, γ_p, is shown in Equation (11).

$$N_f = \left(\frac{A}{a}\gamma_p^{2+2\alpha C_2/K}\right)^{\frac{1}{b+1-C_2/K}} \tag{11}$$

In which C_1 and C_2 are optimized fitting parameters that are also the change rate parameters of the strength damage evolution associated with $C^*(S)$, A and K are calculated parameters, and a and b are material failure criterion parameters.

4. Results and Discussion

4.1. Impact of Aging on the Complex Modulus and Viscoelastic Behavior of Asphalt Binders

The complex modulus master curves of asphalt binders under different aging conditions were constructed using the least squares method, with T_{ref} taken at 40 °C. The CAM model was then applied to fit the master curve of the complex modulus, as shown in Figure 2. Compared to the original asphalt, the complex shear modulus of aged asphalt significantly increases with the extension of aging time. Comparing the effects of TFOT and PAV aging on asphalt over the same duration (Figure 2a,b) revealed that the TFOT aging has a more pronounced effect on the complex modulus of asphalt than that of PAV aging. Meanwhile, Figure 2 indicates that the differences in the complex modulus of asphalt with various aging times are more pronounced at a low frequency than that at a high frequency. According to free volume theory of polymers, asphalt binders exhibit the same time–temperature dependence as polymer materials. That means an increase in temperature causes the volume within the asphalt binders to expand, the free space between molecules to increase, and the restriction on molecular movement to decrease, resulting in a decrease in the complex modulus at high temperatures and low frequencies.

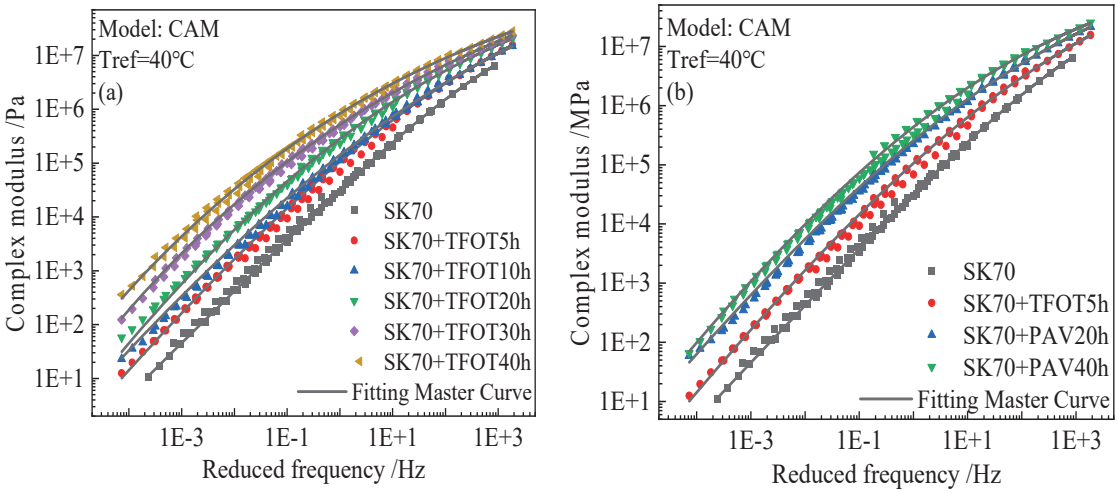

Figure 2. Evolution of complex modulus with different aging times (**a**) TFOT; (**b**) PAV.

Table 3 presents the CAM fitting parameters for both original and aged asphalt binders. The values of the fitted correlation coefficients, R^2, indicate that the CAM model can effectively fit the complex modulus master curve of the asphalt binders with varying degrees of aging. Therefore, the model parameters can be applied to analyze the impact of aging on the performance of bitumen.

Table 3. CAM model parameters for unaged and aged asphalt binders.

Aging Methods	f_c/Hz	k	m_e	R^2
SK70	4.02×10^3	0.955	0.976	0.9999
SK70 + TFOT5h	1.69×10^2	2.012	1.204	0.9990
SK70 + TFOT10h	2.46×10^1	2.365	1.278	0.9986
SK70 + TFOT20h	2.70×10^{-1}	2.943	1.598	0.9991
SK70 + TFOT30h	3.35×10^{-8}	3.556	3.182	0.9990
SK70 + TFOT40h	3.98×10^{-17}	4.451	8.848	0.9993
SK70 + PAV20h	4.90×10^1	1.924	1.162	0.9990
SK70 + PAV40h	6.55	1.987	1.353	0.9994

According to the changes observed in the frequency division parameter f_c, it is evident that as the aging time increases, the f_c value gradually decreases. This phenomenon indicates that, during the aging process of asphalt, the viscous deformation region of the material gradually diminishes, while the elastic deformation region relatively increases. This implies that aging induces more elastic behavior in the asphalt material, reducing its capacity for viscous deformation. This change may be attributed to the evaporation of light components in the asphalt, oxidative reactions, and other chemical changes during the aging process, which result in a more rigid internal structure of the asphalt. Consequently, its viscous properties decrease, and its elastic properties are enhanced. Such changes in characteristics have implications for the long-term performance of asphalt pavements, as an increase in elastic deformation may lead to a greater likelihood of cracks or other forms of damage under external loading conditions. m_e is defined as the slope of the third asymptote of the complex modulus master curve, a parameter that quantifies the material's sensitivity to variations in temperature and frequency. This parameter is crucial in characterizing the viscoelastic behavior of asphalt binders, under different thermal and loading conditions. A higher m_e value indicates that the material exhibits greater sensitivity to changes in temperature and frequency, implying that its mechanical properties, including stiffness and deformation characteristics, are more susceptible to alterations under varying environmental conditions. Table 3 shows that the m_e value tends to increase with prolonged aging of asphalt materials. This trend suggests that the aging process, which may involve oxidative hardening, loss of volatile components, and other chemical or physical changes, enhances the material's sensitivity to temperature and frequency fluctuations. As a result, aged asphalt becomes more prone to performance issues such as cracking at low temperatures, indicating a degradation in its low-temperature flexibility.

4.2. Impact of Rejuvenator on the Complex Modulus and Viscoelastic Properties of Aged Asphalt Binders

The complex modulus master curves of asphalt binders under different rejuvenator dosages were constructed using the least squares method at 40 °C, followed by the application of the CAM model to fit the master curves, as shown in Figure 3. With the increasing dosage of the rejuvenator, the complex modulus of the aged asphalt binder progressively diminishes. Notably, when the rejuvenator dosage reaches 6%, the complex modulus of the regenerated asphalt becomes comparable to that of the original asphalt. This indicates that the addition of 6% rejuvenator is sufficient to restore the mechanical properties of the aged asphalt to a level similar to that of the original material. The fitting parameters of the CAM model for the complex modulus master curve of the regenerated asphalt binder are presented in Table 4. The CAM model's fitting correlation coefficients (R^2) for the complex modulus master curves of the regenerated asphalt binders are all above 0.998, demonstrating that the CAM model is highly effective in fitting the complex modulus master curves of regenerated asphalt binders. As the rejuvenator dosage increased, the f_c value of the regenerated asphalt increased gradually, while the m_e value decreased gradually, indicating that rejuvenator can improve the low-temperature performance and temperature sensitivity of aged asphalt binders. Composed primarily of low-molecular-weight aromatic

oils, the rejuvenator exhibits a viscous flow state within the test temperature range of 20 to 70 °C, along with excellent low-temperature ductility and temperature sensitivity. These characteristics enable the rejuvenator to restore the flexibility and resilience of aged asphalt, thereby enhancing its resistance to low-temperature cracking and reducing its sensitivity to temperature fluctuations. Consequently, the addition of a rejuvenator significantly improves the low-temperature crack resistance and temperature stability of the regenerated asphalt binder, making it more durable under varying environmental conditions.

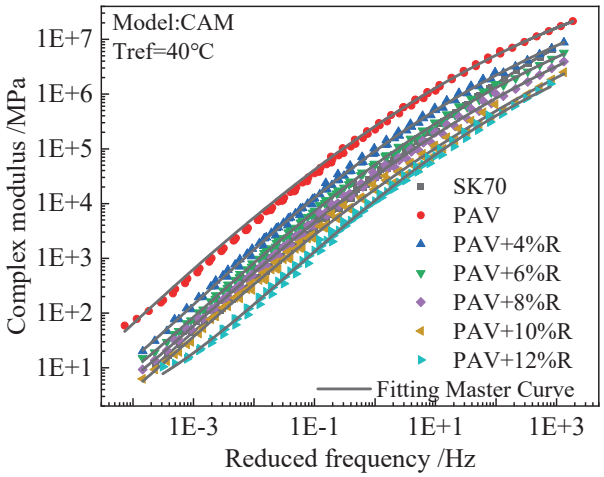

Figure 3. Temperature master curves at different regenerator dosages.

Table 4. CAM model parameters for regenerated asphalt binders.

Regeneration	f_c/Hz	k	m_e	R^2
SK70	4.02×10^3	0.955	0.976	0.9999
SK70 + PAV20h	4.90×10^1	1.924	1.162	0.9990
PAV + 4%R	4.54×10^3	1.895	0.905	0.9989
PAV + 6%R	4.95×10^4	1.803	0.849	0.9994
PAV + 8%R	2.58×10^6	1.252	0.816	0.9990
PAV + 10%R	1.62×10^7	0.061	0.737	0.9980
PAV + 12%R	1.33×10^8	0.002	0.674	0.9982

4.3. Construction and Prediction of Asphalt Complex Modulus Master Curve Based on Time–Temperature–Aging (TTA) Superposition Principle

The observation of master curves of the asphalt complex modulus at different aging times reveals that the master curves are essentially parallel. This pattern is similar to the curves obtained from frequency sweeps at different temperatures. The influence of aging time on the complex modulus of asphalt can be addressed by referencing the time–temperature superposition principle. The time–temperature superposition principle is an important method in the study of asphalt material behavior, demonstrating that within a certain range, the effects of temperature and time on the material's mechanical properties are equivalent. Therefore, the material response at different temperatures can be normalized into a single master curve through time shifting. Similarly, for the effect of aging time on the asphalt complex modulus, if the master curves at different aging times are found to be essentially parallel, the time–temperature superposition principle can be analogized. By shifting the complex modulus curves at different aging times, a time–temperature–aging (TTA) equivalent master curve can be constructed. Specifically, the steps to construct such an equivalent master curve may include the following:

(1) Determine a reference state: first, select a reference aging time and temperature as the baseline for constructing the master curve.

(2) Curve shifting: by appropriately shifting the curves (along the time or frequency axis), align the complex modulus curves at other aging times or temperatures with the master curve at the reference state.
(3) Construct the equivalent curve: after completing the curve shifts, integrate all the data points to form the time–temperature–aging equivalent complex modulus master curve.

This method treats aging as a factor similar to temperature, and by applying appropriate shifts, achieves equivalence between aging, time, and temperature. The TTA superposition principle provides an effective tool for studying the mechanical properties of asphalt materials under different aging times and temperature conditions, aiding in a better understanding of the long-term performance of asphalt [32]. In this study, the original asphalt (0 h) was applied as the reference state and the least squares method was employed to shift the complex modulus master curves at different aging times to the reference state, thereby constructing the time–temperature–aging master curve (Figure 4). During this process, the shift factors corresponding to the master curves at each aging level were also obtained. By analyzing the relationship between the shift factors and aging time, it is possible to accurately predict the complex modulus of asphalt at different aging times. The aging shift factors obtained at different aging times using the time–temperature–aging superposition method are shown in Figure 5. Aging shift factors for different aging methods (TFOT and PAV) significantly increase with aging time. A strong linear correlation is observed between the aging shift factors and aging time, with correlation coefficients greater than 0.975. Therefore, it can be concluded that the relationship between aging shift factors and aging time can be used to accurately predict the complex modulus of asphalt under different aging methods and times.

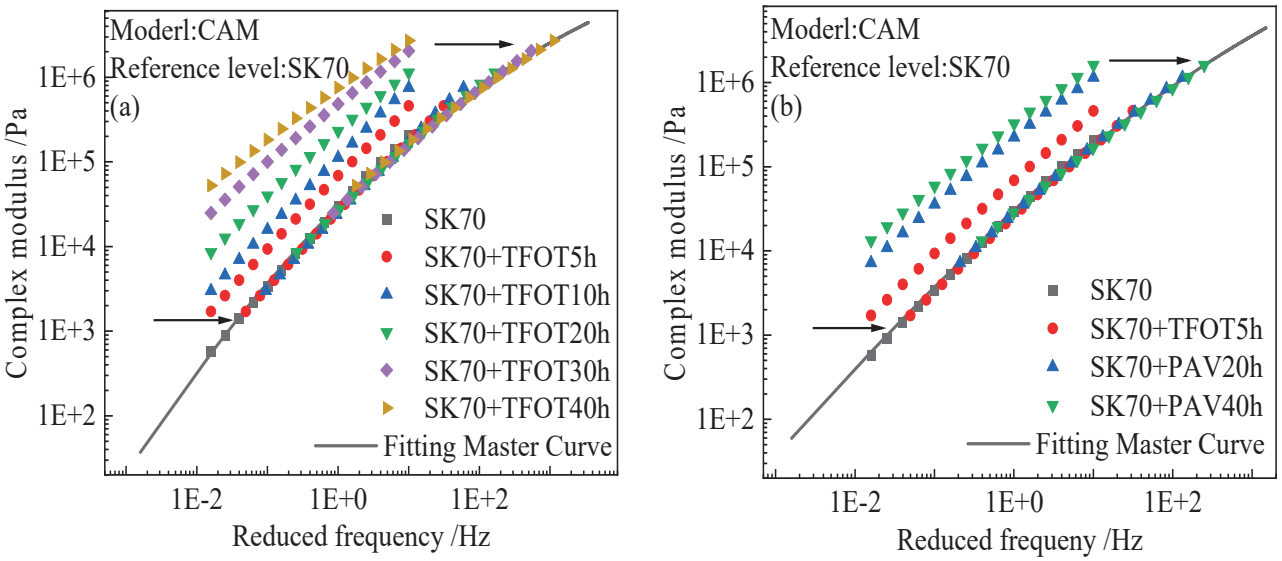

Figure 4. TTA master curves of complex modulus for asphalt binders with different aging times: (**a**) TFOT; (**b**) PAV.

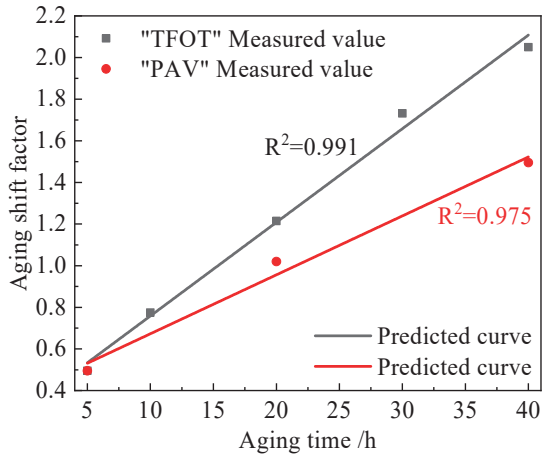

Figure 5. Relations between aging shift factors and aging time at the different aging times.

4.4. Prediction Regenerated Asphalt Complex Modulus Master Curve Based on Time–Temperature–Regenerator (TTR) Superposition Principle

Based on the parallel relationship observed between the complex modulus master curves of regenerated asphalt at different regenerator dosages and the original asphalt complex modulus master curve, this study further employs the least squares method to construct the TTR complex modulus master curve of regenerated asphalt. In this process, the complex modulus master curve of asphalt aged for 20 h was used as the reference state, and the complex modulus master curves of regenerated asphalt with varying regenerator dosages were shifted to the left to construct the time–temperature–regenerator complex modulus master curve (Figure 6). Simultaneously, shift factors associated with the regenerator dosage were extracted. Figure 7 illustrates the regenerator dosage shift factors determined using this method. The results indicate that as the regenerator dosage increases, the shift factor exhibits a decreasing trend. This phenomenon suggests a significant linear relationship between the regenerator dosage and the shift factor. Furthermore, by comparing the calculated regenerator shift factor curve with the predicted curve, it is evident that the error between the two is minimal, indicating that this method possesses a high degree of predictive accuracy. Consequently, the regenerator dosage shift factor can serve as an effective tool for predicting the complex modulus of regenerated asphalt under various regenerator dosage conditions. This method not only provides a theoretical foundation for predicting the performance of regenerated asphalt but also offers practical guidance for optimizing regenerator dosages in engineering applications.

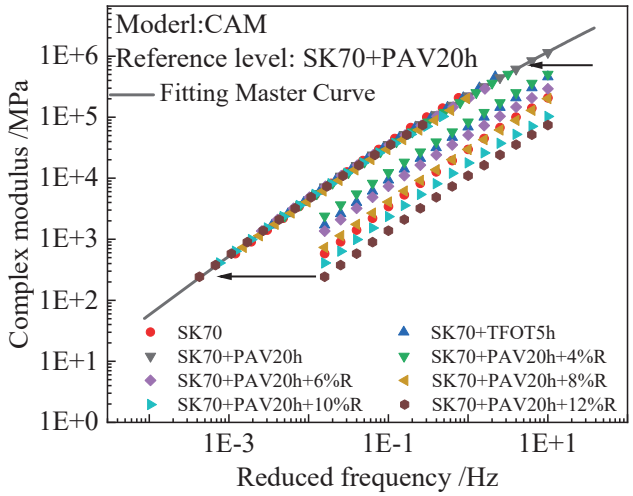

Figure 6. TTR master curve with different rejuvenator dosages.

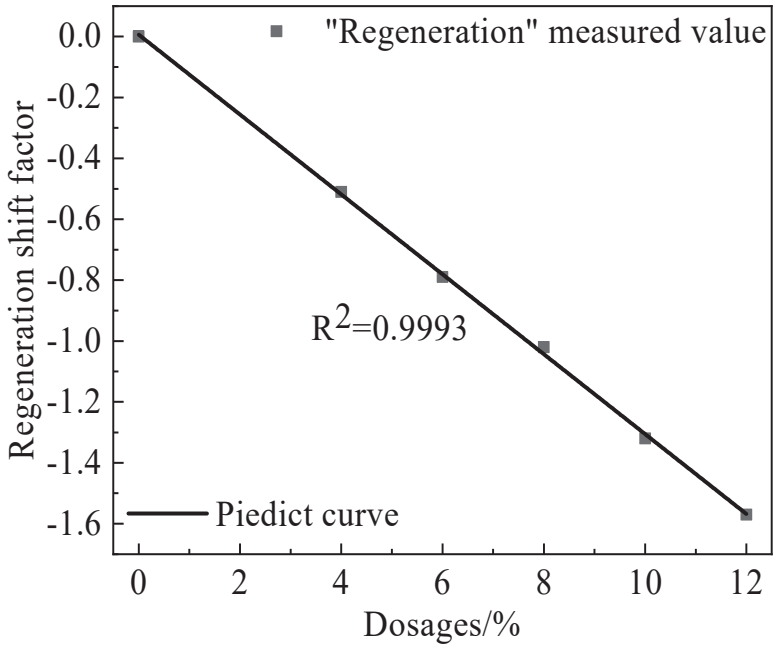

Figure 7. Relation between regeneration shift factors and rejuvenator dosages.

4.5. Material Integrity Analysis of Aged and Regenerated Asphalt Fatigue Performance

LAS test shear stress–strain curves for various levels of aged and regenerated asphalt are illustrated in Figure 8. These curves are employed to determine the breakdown strain of asphalt and to analyze the strain dependence of the material's properties. The width of the curve at its peak is indicative of the material's strain dependence. The analysis presented in Figure 8 demonstrates that aging narrows the peak width of the asphalt binder's LAS stress–strain curve, signifying an increased dependence on stress and strain as the aging level rises. Conversely, the inclusion of the regenerant causes the peak width of the stress–strain curve for the regenerated asphalt to broaden, indicating that the regenerant mitigates the stress dependence of the asphalt binder. Aging leads to an increase in the rigidity and brittleness of the asphalt binder. As the binder undergoes aging, like under TFOT and PAV conditions, its molecular structure becomes more cross-linked, and the material loses its original flexibility. This narrowing of the peak width reflects an increased strain dependence, meaning that the material becomes more sensitive to changes in stress and strain. The asphalt binder's ability to deform elastically is reduced, leading to a more pronounced stress–strain response in a narrower range of strains. The addition of a regenerant (rejuvenator), on the other hand, restores some of the flexibility and viscoelastic properties of the aged asphalt binder. Regenerants work by reintroducing light oils or maltenes that help to soften the asphalt, reducing the cross-linking that occurs during aging and improving its ability to deform under stress. The broadened peak width seen in the stress–strain curve of the regenerated asphalt indicates a reduced strain dependence, meaning that the material becomes more resilient and less sensitive to changes in stress and strain over a wider range. The regenerant helps to mitigate the material's brittleness, improving the ductility and fatigue resistance of the asphalt by increasing its ability to deform more uniformly under stress.

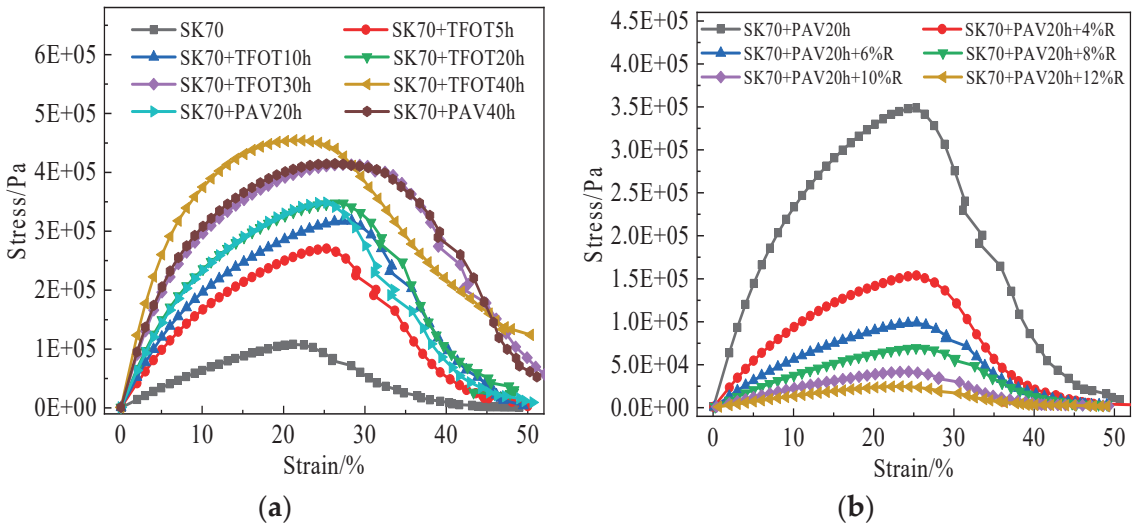

Figure 8. The LAS test strain–stress curves for aged (**a**) and regenerated asphalt binders (**b**).

Figure 9 illustrates the relationship between the material integrity factor $C^*(S)$ and the strength damage parameter $S(t)$ for various levels of aged and regenerated asphalt. As the aging time increased, the material integrity values at failure indicated a gradual decrease in the material's resistance to damage, ultimately impacting the asphalt's fatigue life. However, the addition of the regenerant resulted in a lower integrity value factor at failure, which enhanced the material's resistance to damage and subsequently improved the fatigue performance of the aged asphalt. The fitting parameters α and β were derived from the nonlinear fitting of the S-VECD model data, with the corresponding curve fitting parameters and slopes detailed in Table 5. α is a damage parameter used to characterize and model the extent of damage within the material. In this study, α was utilized to fit the energy storage modulus for various levels of aging and regeneration. As the aging time increased, α decreased due to a reduction in the material's maximum relaxation rate, which corresponds with higher levels of aging. Conversely, when different dosages of regenerant were introduced to the aged asphalt, α also decreased. This reduction occurred because the regenerant enhanced the material's maximum relaxation rate and increased the viscosity of the regenerated asphalt.

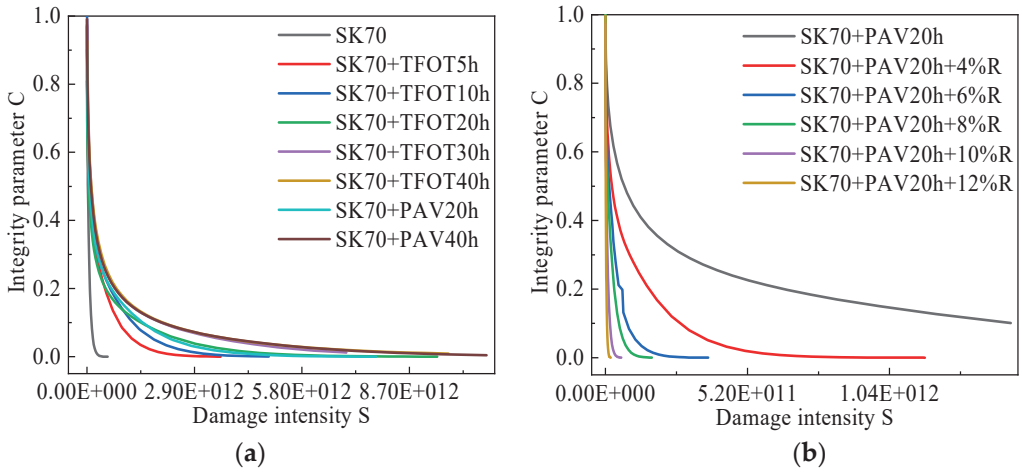

Figure 9. Damage characteristic curves of aged (**a**) and regenerated asphalt (**b**).

Table 5. Slope and damage parameters of aged and regenerated asphalt.

Asphalt	α	C_1	C_2	R^2
SK70	2.054156	0.000167	0.329662	0.9979
SK70 + TFOT5h	2.271325	0.000189	0.306717	0.9951
SK70 + TFOT10h	2.369731	0.000253	0.292416	0.9946
SK70 + TFOT20h	2.470602	0.007556	0.242607	0.9935
SK70 + TFOT30h	2.650436	0.001405	0.168638	0.991
SK70 + TFOT40h	2.892544	7.63×10^{-5}	0.223471	0.9985
SK70 + PAV20h	2.38692	0.001642	0.273924	0.9943
SK70 + PAV40h	2.584196	0.000152	0.223331	0.9967
SK70 + PAV20h + 4%R	2.283139	3.96×10^{-5}	0.286903	0.9973
SK70 + PAV20h + 6%R	2.222211	0.000431	0.349668	0.9924
SK70 + PAV20h + 8%R	2.187286	0.000143	0.350461	0.9914
SK70 + PAV20h + 10%R	2.142417	0.00021	0.390778	0.9928
SK70 + PAV20h + 12%R	2.127048	0.00015	0.441002	0.9911

The failure criterion, based on damage characterization within the S-VECD model, is employed to evaluate and predict the fatigue performance of asphalt materials. This criterion demonstrates a stronger correlation within the relationship model developed by Sabouri and Kim [33]. Figure 10 illustrates the relationship between the fatigue failure criterion and various levels of aging and regenerated asphalt, which can be utilized to estimate fatigue life under different loading conditions. The figure shows that aging caused the $G^R - N_f$ fitting curve to shift upward, with the most pronounced shift occurring after a TFOT of 5 h aging, indicating that short-term aging has a significant impact on fatigue life. Conversely, the addition of the regenerator caused the $G^R - N_f$ curve to shift downward, suggesting that the regenerator reduced the rate of damage accumulation during fatigue testing and significantly enhanced the fatigue life of the regenerated asphalt. Figure 11 presents the fatigue life under varying strain conditions for different levels of regeneration and aging. The figure illustrates that the fatigue equation, which relates N_f to strain, provides a strong fit, with the slope of the equation indicating the material's sensitivity to N_f under strain. At lower strain levels, the fatigue life of aged asphalt increased with longer aging times, and it was observed that TFOT aging had a more pronounced effect on fatigue life than PAV aging for the same duration. Conversely, under high strain conditions, the traditional view holds true: the longer the aging period, the shorter the fatigue life of the asphalt. The relationship between the fatigue life and strain of regenerated asphalt exhibited a markedly different trend compared to that of aged asphalt when varying dosages of rejuvenator were added. Under low strain conditions, the fatigue performance of regenerated asphalt gradually approached that of the original asphalt as the dosage of rejuvenator increased. In contrast, under high strain conditions, the higher the dosage of rejuvenator, the greater the fatigue life of the regenerated asphalt. The underlying reasons for this behavior remain unclear and may be linked to the complex mechanisms involved in the aging and regeneration processes, as suggested by some studies [16,20,34].

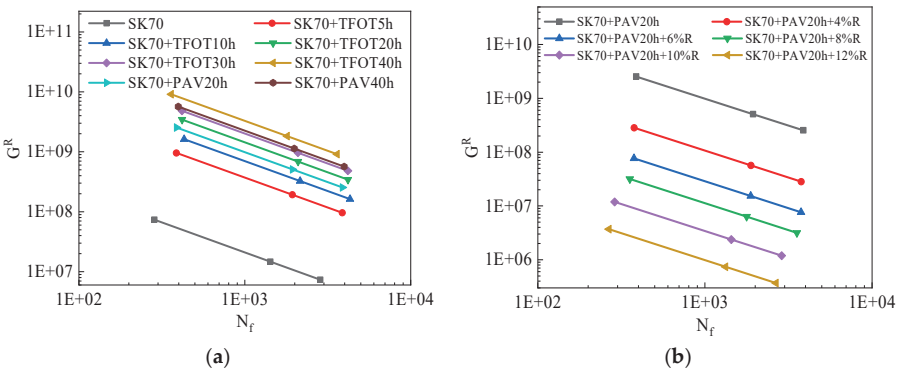

Figure 10. G^R and N_f curves of aged (**a**) and regenerated asphalt (**b**).

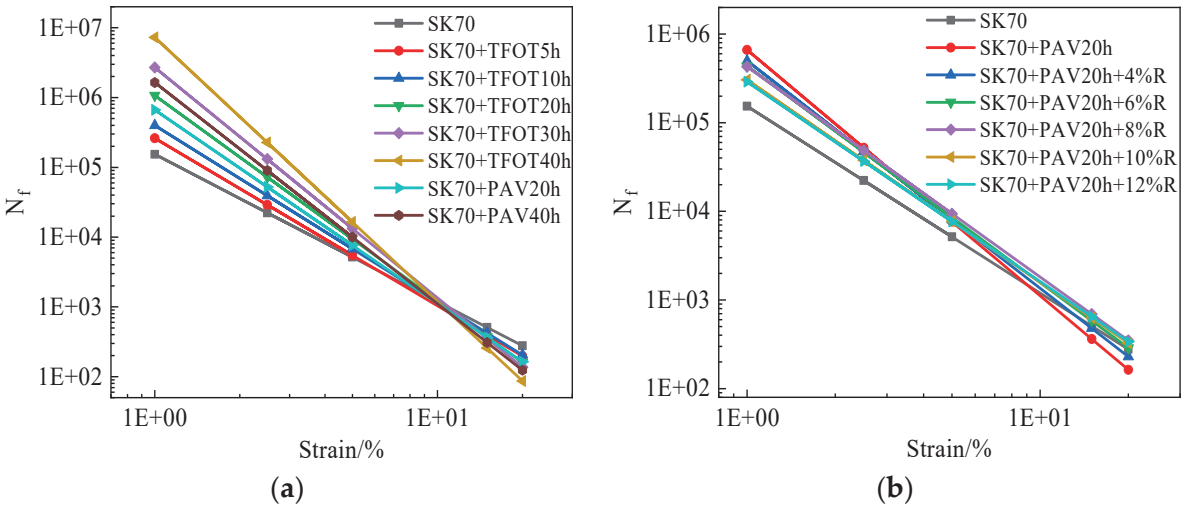

Figure 11. Aged (**a**) and regenerated (**b**) asphalt's fatigue life under various strain levels.

5. Conclusions

In this study, aging and regeneration master curves of the complex modulus for various asphalt binders were developed based on the time–temperature–aging–regeneration superposition principle. First, frequency sweep tests were conducted on aged and rejuvenated asphalt binders at various temperatures. Second, complex modulus master curves were constructed, and the CAM model was applied to fit these curves. The viscoelastic properties of asphalt at different aging levels and rejuvenator dosages were then analyzed based on the CAM parameters. Next, by applying a curve-shifting technique based on the least squares method to the reference state, both the time–temperature–aging (TTA) and time–temperature–regenerator (TTR) master curves of the complex modulus were constructed. Finally, the relationships between aging shift factors and aging times, as well as between regenerator shift factors and dosages, were established to predict the complex modulus of both aged and rejuvenated asphalt. The following conclusions can be drawn:

(1) Aging significantly increases the complex modulus, especially under TFOT aging compared to PAV aging. The CAM parameters can effectively explain the impact of aging on asphalt, revealing that aging reduces the viscous deformation and increases elastic behavior, making asphalt more prone to cracking under low-temperature conditions. Additionally, aging enhances the material's sensitivity to temperature and frequency changes.

(2) Increasing rejuvenator dosage reduces the complex modulus of aged asphalt, with 6% rejuvenator restoring its mechanical properties to near-original levels. As the rejuvenator dosage increases, the low-temperature performance and temperature sensitivity of the asphalt improve. Rejuvenators enhance flexibility, reduce temperature sensitivity, and improve resistance to low-temperature cracking, thereby enhancing the durability of regenerated asphalt under varying conditions.

(3) The master curves of the asphalt complex modulus with different aging times are essentially parallel, similar to the results observed in frequency sweeps at varying temperatures. With the original asphalt serving as the reference state and by curves shifting based on the least squares method, a time–temperature–aging equivalent master curve of the complex modulus was constructed, and aging shift factors were obtained. A strong linear correlation ($R^2 > 0.975$) between aging shift factors and aging time was observed, enabling accurate prediction of the asphalt complex modulus under different aging conditions.

(4) The time–temperature–regenerator complex modulus master curve of regenerated asphalt was constructed using the least squares method. By shifting the complex modulus master curves of regenerated asphalt with different regenerator dosages

to the reference state, shift factors were determined. Results show a significant linear relationship between regenerator dosage and shift factor, with the shift factor decreasing as dosage increases. The minimal error between calculated and predicted curves demonstrates high predictive accuracy, making this method a valuable tool for predicting the complex modulus and optimizing regenerator dosages in engineering applications.

(5) Aging narrows the stress–strain curve's peak, indicating increased stress dependence, while adding a regenerant broadens it, enhancing fatigue life. The study also explores how different levels of aging and regenerant dosage affect fatigue life under varying strain conditions, revealing complex behaviors influenced by the aging and regeneration processes.

The findings of this study provide practical guidance for improving the performance of both aged and rejuvenated asphalt in highway applications. By accurately predicting the effects of aging and rejuvenation on asphalt's dynamic properties, engineers can better design pavements that are both durable and sustainable, optimizing the use of recycled materials and enhancing the overall performance of road networks.

Author Contributions: Validation, Z.W.; Formal analysis, H.D. and W.Y.; Investigation, X.M. (Xiaoyan Ma); Data curation, X.M. (Xiaojun Ma). All authors have read and agreed to the published version of the manuscript.

Funding: This project was supported by the Natural Science Found Committee (NSFC) of China (No. 52208417), Gansu Highway Traffic Construction Group Co., Ltd. Project: Development and Application Research of Dry-Mix High Viscosity-Elastic Modifier for Ultra-Thin Wearing Course. China Postdoctoral Science Foundation Funded Project (No. 2020M683401), the Natural Science Basis Research Plan in Shaanxi Province of China (No. 2021JQ-262), the Fundamental Research Funds for the Central Universities of China (No. 300102311402), the Gansu Provincial Science and Technology Plan (23JRRA1375, 21JR7RA786) and Research project of Gansu Provincial Department of Transportation (2022–33), the Lanzhou Youth Science and Technology Talent Innovation Project (2023-QN-102), the Gansu Provincial Science and Technology Innovation Fund Project for Small and Medium-sized Technology Enterprises (22CX3GA011), the Central Leading Local Science and Technology Development Fund Project (23ZYQA314), and the Lanzhou Science and Technology Bureau Talent Innovation and Entrepreneurship Project (2022-RC-54).

Institutional Review Board Statement: Not applicable.

Informed Consent Statement: Not applicable.

Data Availability Statement: Data are contained within the article.

Acknowledgments: The authors gratefully acknowledge support from Chang'an University and Scientific Observation and Research Base of Transport Industry of Long Term Performance of Highway Infrastructure in Northwest Cold and Arid Regions.

Conflicts of Interest: Authors Zhaoli Wang, Hongli Ding and Wanhong Yang were employed by the company Gansu Road & Bridge Shan Jian Technogy Co., Ltd. Author Xiaojun Ma was employed by the company Qinghai Transportation Planning and Design Institute Co. The remaining authors declare that the research was conducted in the absence of any commercial or financial relationships that could be construed as a potential conflict of interest. The authors declare that this study received funding from Gansu Highway Traffic Construction Group Co., Ltd. The funder was not involved in the study design, collection, analysis, interpretation of data, the writing of this article or the decision to submit it for publication.

References

1. Behnood, A. Application of rejuvenators to improve the rheological and mechanical properties of asphalt binders and mixtures: A review. *J. Clean. Prod.* **2019**, *231*, 171–182. [CrossRef]
2. El-Shorbagy, A.M.; El-Badawy, S.M.; Gabr, A.R. Investigation of waste oils as rejuvenators of aged bitumen for sustainable pavement. *Constr. Build. Mater.* **2019**, *220*, 228–237. [CrossRef]
3. Xu, S.; Wu, H.; Song, W.; Zhan, Y. Investigation of the aging behaviors of reclaimed asphalt. *J. Clean. Prod.* **2022**, *356*, 131837. [CrossRef]

4. Avirneni, D.; Peddinti, P.R.T.; Saride, S. Durability and long term performance of geopolymer stabilized reclaimed asphalt pavement base courses. *Constr. Build. Mater.* **2016**, *121*, 198–209. [CrossRef]
5. Dhasmana, H.; Hossain, K.; Karakas, A.S. Effect of long-term ageing on the rheological properties of rejuvenated asphalt binder. *Road Mater. Pavement* **2021**, *22*, 1268–1286. [CrossRef]
6. Al-Saffar, Z.H.; Yaacob, H.; Katman, H.Y.; Satar, M.K.I.M.; Bilema, M.; Jaya, R.P.; Eltwati, A.S.; Radeef, H.R. A Review on the Durability of Recycled Asphalt Mixtures Embraced with Rejuvenators. *Sustainability* **2021**, *13*, 8970. [CrossRef]
7. Zaumanis, M.; Mallick, R.B.; Poulikakos, L.; Frank, R. Influence of six rejuvenators on the performance properties of Reclaimed Asphalt Pavement (RAP) binder and 100% recycled asphalt mixtures. *Constr. Build. Mater.* **2014**, *71*, 538–550. [CrossRef]
8. Borghi, A.; del Barco Carrión, A.J.; Presti, D.L.; Giustozzi, F. Effects of Laboratory Aging on Properties of Biorejuvenated Asphalt Binders. *J. Mater. Civ. Eng.* **2017**, *29*, 04017149. [CrossRef]
9. Zahoor, M.; Nizamuddin, S.; Madapusi, S.; Giustozzi, F. Sustainable asphalt rejuvenation using waste cooking oil: A comprehensive review. *J. Clean. Prod.* **2021**, *278*, 123304. [CrossRef]
10. Lv, S.; Liu, J.; Peng, X.; Liu, H.; Hu, L.; Yuan, J.; Wang, J. Rheological and microscopic characteristics of bio-oil recycled asphalt. *J. Clean. Prod.* **2021**, *295*, 126449. [CrossRef]
11. Sharma, A.; Naga, G.R.R.; Kumar, P.; Raha, S. Rheological Characterization of Recycled Asphalt Binders and Correlating the Zero Shear Viscosity to the Superpave Rutting Parameter. *J. Mater. Civ. Eng.* **2022**, *34*, 04022218. [CrossRef]
12. Anjali, B.L.; Swamy, A.K. Time-temperature-dosage superposition approach to predict the complex modulus of asphalt binders. *Constr. Build. Mater.* **2022**, *329*, 127140. [CrossRef]
13. Liu, F.; Zhou, Z.; Zhang, X. Construction of complex shear modulus and phase angle master curves for aging asphalt binders. *Int. J. Pavement Eng.* **2020**, *23*, 536–544. [CrossRef]
14. Saleh, N.F.; Mocelin, D.; Rad, F.Y.; Castorena, C.; Underwood, B.S.; Kim, Y.R. Predictive Framework for Modeling Changes in Asphalt Mixture Moduli with Oxidative Aging. *Transp. Res. Rec. J. Transp. Res. Board* **2020**, *2674*, 79–93. [CrossRef]
15. Chen, J.; Yan, K.; You, L. Rheological and Spectroscopic Properties of Ethylene Vinyl Acetate–Modified Rubberized Asphalt. *J. Mater. Civ. Eng.* **2020**, *32*, 04020142. [CrossRef]
16. Chen, M.; Geng, J.; Chen, H.; Luo, M. Effect of water aging on the fatigue performance of asphalt binders using the linear amplitude sweep. *Constr. Build. Mater.* **2021**, *304*, 124679. [CrossRef]
17. Qin, Q.; Schabron, J.F.; Boysen, R.B.; Farrar, M.J. Field aging effect on chemistry and rheology of asphalt binders and rheological predictions for field aging. *Fuel* **2014**, *121*, 86–94. [CrossRef]
18. Wang, C.; Xie, W.; Underwood, B.S. Fatigue and healing performance assessment of asphalt binder from rheological and chemical characteristics. *Mater. Struct.* **2018**, *51*, 171. [CrossRef]
19. Wen, H.; Li, X.; Bhusal, S. Modelling the effects of temperature and loading rate on fatigue properties of hot mixed asphalt. *Int. J. Pavement Eng.* **2012**, *15*, 51–57. [CrossRef]
20. Chen, H.; Bahia, H.U. Modelling effects of aging on asphalt binder fatigue using complex modulus and the LAS test. *Int. J. Fatigue* **2021**, *146*, 106150. [CrossRef]
21. Safaei, F.; Lee, J.-S.; Nascimento, L.A.H.D.; Hintz, C.; Kim, Y.R. Implications of warm-mix asphalt on long-term oxidative ageing and fatigue performance of asphalt binders and mixtures. *Road Mater. Pavement Des.* **2014**, *15*, 45–61. [CrossRef]
22. Nazari, H.; Naderi, K.; Moghadas Nejad, F. Improving aging resistance and fatigue performance of asphalt binders using inorganic nanoparticles. *Constr. Build. Mater.* **2018**, *170*, 591–602. [CrossRef]
23. Yang, K.; Li, R.; Underwood, B.S.; Castorena, C. Effect of laboratory oxidative aging on dynamic shear rheometer measures of asphalt binder fatigue cracking resistance. *Constr. Build. Mater.* **2022**, *337*, 127566. [CrossRef]
24. Jacobs, G.; Margaritis, A.; Hernando, D.; He, L.; Blom, J.; Van den bergh, W. Influence of soft binder and rejuvenator on the mechanical and chemical properties of bituminous binders. *J. Clean. Prod.* **2021**, *287*, 125596. [CrossRef]
25. Cao, W.; Wang, Y.; Wang, C. Fatigue characterization of bio-modified asphalt binders under various laboratory aging conditions. *Constr. Build. Mater.* **2019**, *208*, 686–696. [CrossRef]
26. *JTG E20-2011*; Standard Test Methods of Bitumen and Bituminous Mixtures for Highway Engineering. Research Institute of Highway Ministry of Transport: Beijing, China, 2011.
27. *AASHTO T 315: 2019*; Standard Method of Test for Determining the Rheological Properties of Asphalt Binder Using a Dynamic Shear Rheometer (DSR). American Association of State Highway and Transportation Officials: Washington, DC, USA, 2019.
28. *AASHTO TP 101-12 (2018)*; Standard Method of Test for Estimating Fatigue Resistance of Asphalt Binders Using the Linear Amplitude Sweep. Association of State Highway and Transportation Officials: Washington, DC, USA, 2012.
29. Ma, X.; Chen, H.; Gui, C.; Xing, M.; Yang, P. Influence of the properties of an asphalt binder on the rheological performance of mastic. *Constr. Build. Mater.* **2019**, *227*, 116659. [CrossRef]
30. Hou, H.; Wang, T.; Wu, S.; Xue, Y.; Tan, R.; Chen, J.; Zhou, M. Investigation on the pavement performance of asphalt mixture based on predicted dynamic modulus. *Constr. Build. Mater.* **2016**, *106*, 11–17. [CrossRef]
31. Yusoff, N.I.M.; Jakarni, F.M.; Nguyen, V.H.; Hainin, M.R.; Airey, G.D. Modelling the rheological properties of bituminous binders using mathematical equations. *Constr. Build. Mater.* **2013**, *40*, 174–188. [CrossRef]
32. Naderi, K.; Nejad, F.M.; Khodaii, A. Time-Temperature-Age Superposition Validation for Linear Viscoelastic Properties of Bituminous Materials. *J. Mater. Civ. Eng.* **2018**, *30*, 04017292. [CrossRef]

33. Sabouri, M.; Kim, Y.R. Development of a Failure Criterion for Asphalt Mixtures under Different Modes of Fatigue Loading. *Transp. Res. Rec. J. Transp. Res. Board* **2014**, *2447*, 117–125. [CrossRef]
34. Babadopulos, L.F.d.A.L.; Ferreira, J.L.S.; Soares, J.B.; Nascimento, L.A.H.d.; Castelo Branco, V.T.F. Aging-Effect Incorporation into the Fatigue-Damage Modeling of Asphalt Mixtures Using the S-VECD Model. *J. Mater. Civ. Eng.* **2016**, *28*, 04016161. [CrossRef]

coatings

Article

Characterization of Thermal and Stress Dual-Induced Nano-SiC-Modified Microcapsules

Yunlong Sun [1,2], Xiaoping Ji [2], Yueqin Hou [3,*], Siqi Wang [2,*], Ye Chen [2,4], Lu Liu [2] and Sijia Liu [1]

[1] Xinjiang Academy of Transportation Science, Co., Ltd., Urumqi 830000, China; sunyunlong6509@sina.com (Y.S.); liusijia64@gmail.com (S.L.)
[2] School of Highway, Chang'an University, Xi'an 710064, China; jixp82@163.com (X.J.); wchenye2@163.com (Y.C.); liulu_2002@163.com (L.L.)
[3] School of Human Settlements and Civil Engineering, Xi'an Jiaotong University, Xi'an 710049, China
[4] School of Transportation, Southeast University, Nanjing 211189, China
* Correspondence: houyueqin527@163.com (Y.H.); 2022021067@chd.edu.cn (S.W.); Tel.: +86-137-5997-2825 (Y.H.)

Abstract: This work reports a kind of thermal and stress dual-induced nano-SiC-modified microcapsule that is applied to asphalt pavement to improve its self-healing performance. For this purpose, the microcapsules needed to contain a regenerator and be stable in an asphalt mixture. In addition, the microcapsules needed to have good wave-absorbing and temperature-raising properties to realize the dual-mechanism-induced release of microcapsules. In the first step in this study, heat-stressed double microcapsules were prepared. Then, the properties of the microcapsules—including basic properties, stability, mechanical properties, and wave-absorbing and temperature-raising properties—were tested. Finally, the self-healing mechanism of the microcapsules was observed. The results show that the nano-SiC-modified microcapsules have a high core content (87.6%), suitable particle size (average particle size of 53.50 μm), high thermal stability (mass loss of 2.92% at 150~170 °C), high construction stability (survival rate of more than 80%), high storage stability (loss rate of 2.35% at 49 d), and high mechanical properties (Young's modulus and nano-hardness of 3.15 Gpa and 0.54 Gpa, respectively). Compared with microcapsules without nano-SiC, the thermal conductivity of the 10% nano-SiC-modified microcapsules increased by 21.6%, their specific heat capacity decreased by 10.45%, and their thermal diffusion coefficient increased by 36.96% after microwave heating for 6 min.

Keywords: microcapsules; nano-SiC; microstructure; chemical constitution; mechanical strength; stability

1. Introduction

Cracks are a significant deterioration phenomenon affecting asphalt pavement and undergo a series of processes, including emergence, expansion, and penetration. Initially, microcracks emerge and then evolve into penetration joints under the combined influence of temperature and load cycles. The timely elimination of microcracks can inhibit or delay the formation of penetration joints [1].

Microcapsules represent a novel self-healing material for pavement microcracks [2,3]. Adsorption encapsulation and sharp pore coagulation bath methods are simpler and have low raw material costs but have a low content of vesicle cores (≤40%) [4–7]. Moreover, the larger particle size of microcapsules (micron level) has a greater effect on the mechanical strength and stability of asphalt mixtures [8–10]. Microcapsules prepared by interfacial polymerization have a suitable particle size but are prone to agglomeration during the preparation process, and the shell thickness is difficult to precisely control [8–10]. Furthermore, the mechanical properties of microcapsules are poor (Young's modulus and hardness are 276.94 Mpa–408.90 Mpa and 43.38–71.08, respectively) [11,12]. In addition, microcapsules prepared by interfacial polymerization have poor thermal stability (the mass loss is 10%–15% at 160–180 °C) [12]. Compared with the previous three methods, microcapsules

prepared by in situ polymerization have a higher capsule core content (64.08%–79.33%) and higher mechanical strength (Young's modulus (MPa) and hardness (MPa) are 1000–2700 and 37.66–140, respectively) [13–15]. Moreover, the shell thickness and core content can be adjusted during the preparation process. The microcapsules prepared by this method are thermally stable (the mass loss is 3.72%–20% at 140–180 °C), which ensures the survival of the microcapsules during the construction process [16]. Therefore, this method is the most widely used preparation method for application in the self-healing of pavements [17].

Conventional microcapsules are stress-triggered by the tip of a microcrack to release their core material. This passive and uncontrollable stress-induced mode does not ensure that the vesicle core material is released promptly and in an amount that matches the microcrack at the appropriate time [18,19]. Therefore, the development of stimulus-responsive controlled-release microcapsules is essential. Controlled-release microcapsules are particles with stimuli-responsive properties that are introduced into the capsule shell. In response to internal triggers (such as pH, temperature, or enzymes) or external stimuli (such as microwaves, light, ultrasound, and electric and magnetic fields), the capsule releases its encapsulated core material [18,20]. Nano-SiC exhibits excellent wave-absorbing and temperature-raising properties. Microcapsules prepared with a nano-SiC modifier doped into the capsule shell material can achieve a microwave-induced release of capsule core material and thermodynamic dual-induced release triggered by the stress at the tips of the microcracks. This represents a desirable and innovative approach for significantly enhancing the self-healing effect of microcracks in asphalt pavement [21,22].

Therefore, this study proposes a thermal and stress dual-induced nano-SiC microcapsule for asphalt pavement applications. Nano-SiC can endow microcapsules with good basic, stable, and mechanical properties to stabilize their presence in asphalt mixtures. In addition, nano-SiC-modified microcapsules have wave-absorbing and temperature-raising properties that enable them to achieve the dual-mechanism-induced release of rejuvenating agents.

2. Materials and Methods

2.1. Materials

Thermal dual-induced microcapsules are composed of modified capsule shell material and a regeneration agent. The modified capsule shell materials are composed of a highly methylated melamine formaldehyde resin (H3M) prepolymer and nano-SiC composite. The main components of the regeneration agent are aromatic and saturated phenols. In addition, a curing agent consisting of sodium chloride, resorcinol, and ammonium chloride is added to prepare the microcapsules. The modified microcapsules were prepared by in situ polymerization with the following main steps.

(1) The SDS emulsifier was added to deionized water at a mass ratio of 100/1.71 for mixing and stirring. The resulting mixture was then placed in a constant-temperature water bath at 30 °C for one hour. Then, a regenerator was added to achieve a mass ratio of emulsifier to regenerant of 1/4.97. The mixture was stirred at the shear rate of 3500 r/min to obtain a regenerated emulsion.

(2) H3M at a mass ratio of regenerant/H3M of 1.57/1 and nano-SiC at a ratio of SiC/H3M of 3/40 were added to the beaker. After stirring to achieve a uniform mixture, a small amount of deionized water was added to form a gray prepolymer solution. Then, the prepolymer solution was dispersed for 30 min by an ultrasonic disperser.

(3) The prepolymer solution of the composite capsule shell was dropped into the emulsion regenerant solution and mechanically stirred at a speed of 600 r/min at 30 °C for 30 min. In this process, sodium chloride, resorcinol, and ammonium chloride were gradually added, and the mass ratios to H3M were set at 0.99/1, 1/20.2, and 1/20.2, respectively.

(4) A 10% acetic acid solution was added dropwise to the mixed solution of the prepolymer and regenerator at a controlled rate of 2 mL/min. The pH of the solution was adjusted to 4.5. The temperature of the mixed solution was then gradually increased

to 70 °C at a rate of 2.5 °C/min, followed by stirring at 950 rpm for 3 h to obtain the microcapsule suspension.

(5) The resulting microcapsule suspension was vacuum filtered using a Brinell funnel and washed with deionized water and petroleum ether three times to remove the uncoated regenerate. Then, the cleaned microcapsules were filtered and placed in an oven at 60 °C for 1 h to obtain the yellow-brown microcapsules.

2.2. Testing Methods

2.2.1. Basic Properties

Particle Size Distribution

The particle size of the microcapsules was determined using fluorescence microscopy (FM, Phenix, Shangrao, China). First, the microcapsule samples were added to a test tube containing a small amount of anhydrous ethanol and dispersed using an ultrasonic disperser for 1 min until a homogeneous microcapsule–ethanol suspension was formed. Next, a small volume of the suspension was drawn onto a slide using a dropper and covered with a coverslip. The particle size was then observed and recorded using FM. Finally, the particle size distribution was quantified and statistically analyzed using Image-Pro Plus 6.0 (Media Cybernetics, Rockville Maryland, MD, USA), as shown in Figure 1.

Figure 1. Particle size distribution measurement method.

Microscopic Morphology and Capsule Shell Thickness

Scanning electron microscopy (SEM, Carl Zeiss AG, Oberkoche, Germany) was used to examine the microscopic morphology of the microcapsules and measure the thickness of the capsule shell. First, the microcapsule powder was dispersed in anhydrous ethanol and uniformly applied to the sample stage. The surface of the microcapsules was then clean by air-jetting with high-pressure gas. Finally, the microcapsules were observed, and the thickness of the capsule shell was quantified using SEM at magnification ranging from 200 to 60,000, as shown in Figure 2.

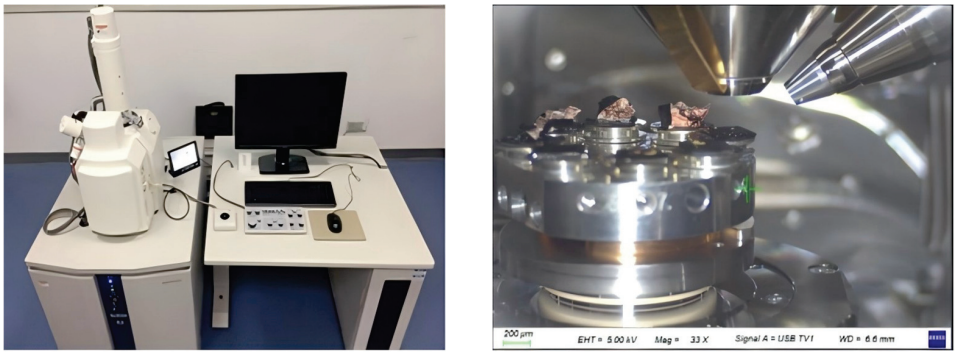

(**a**) (**b**)

Figure 2. Scanning electron microscope and specimen. (**a**) scanning electron microscope and (**b**) specimen.

Chemical Structure

The chemical structure of the microcapsules was analyzed by Fourier transform infrared spectroscopy (FTIR, Thermo Nicolet, Waltham MA, USA). The FTIR spectra of the nano-SiC composite capsule shell, microcapsule, regenerant, and nano-SiC were obtained using the potassium bromide (KBr) pellet method. The solid samples were tested in the wave numbers of 4000~400 cm^{-1}, while the liquid samples were tested in the range of 4000~600 cm^{-1}. The changes in the characteristic peaks of each absorption spectrum were analyzed to determine whether the capsule shell fully encapsulated the core materials, thereby confirming the successful preparation of microcapsule.

Core Content

The content of the microcapsule core was determined by solvent extraction. First, the microcapsules at a certain mass (m_0) were weighed and crushed to destroy the capsule shell structure, allowing the regenerator to be completely released. The remaining microcapsules were then washed, cleaned, and dried to obtain the residue of the capsule shell, which represents the mass (m_s) of the composite capsule shell. The mass of the capsule core in the tested microcapsule sample is the difference between the microcapsule sample and the mass of the composite capsule shell. Therefore, the core content of the microcapsule (R_c) can be calculated by Equation (1) [23].

$$R_c = \frac{m_c}{m_0} \times 100\% = \frac{m_0 - m_s}{m_0} \times 100\% \quad (1)$$

2.2.2. Stability

Thermal Stability

A thermogravimetric analyzer was used to assess the thermal stability of the microcapsules. The thermal stability of the capsule shell material, core material, and microcapsules was tested in the temperature range of 30~400 °C, with a heating rate of 10 K/min. High-purity nitrogen was used as the test gas, with a flow rate of 40 mL/min.

Storage Stability

The residual mass method was used to test the storage stability of the microcapsules. First, 420 g of dried microcapsules was equally divided into six sealed glass bottles, which were then placed in a cool, dry location and stored for a period protected from light. The residual mass of the microcapsules was measured at weeks 1, 2, 3, 4, 5, 6, and 7. The rate of mass loss was calculated using Equation (2) [24].

$$R_{mi} = \frac{m_0 - m_i}{m_0} \quad (2)$$

R_{mi}—Rate of mass loss of microcapsules at week I, %;
m_0—Mass of microcapsules before washing, g;
m_i—Mass of microcapsules after washing, g;
i—Number of weeks of storage, which were taken as 1, 2, 3, 4, 5, 6, and 7.

Construction Stability

The structural stability of microcapsules was tested by observation and statistics. First, an asphalt mixture containing 6% microcapsules was prepared. Once the mixture had cooled sufficiently, the asphalt and aggregate were separated using trichloroethylene (TCE) to produce the asphalt-containing microcapsules. Next, the morphology of the microcapsules in the extract was observed using FM. Finally, the survival rate of microcapsules was calculated. To quantitatively evaluate the survival rate of the microcapsules in the asphalt mixture, n_1 samples of the TCE extract from the microcapsule asphalt mixture were prepared, and n_2 monitoring points were randomly selected for FM observation. The total number of microcapsules was recorded as R_t, and the number of damaged microcapsules

was recorded as R_1. The microcapsule survival rate was then calculated using Equation (3), and the microcapsule damage rates at all monitoring sites were averaged using Equation (4). The mean value from all observation points was then calculated to characterize the survival rate of microcapsules in the mixing process.

$$R = \left(1 - \frac{R_l}{R_t}\right) \times 100\% \tag{3}$$

$$\overline{R} = \frac{\sum_{i=1}^{n_1 \cdot n_2} R_i}{n_1 \cdot n_2} \tag{4}$$

$\overline{R}$—Overall survival of microcapsules, %;
R_i—Survival of microcapsules at observation point i, %;
n_1—Number of samples of trichloroethylene extract;
n_2—Number of observation points.

2.2.3. Micromechanical Strength

The Young's modulus and nano-hardness of microcapsules were tested by a nanoindentation instrument. The load range of the nanoindentation is 0 ~ 500 mN, with a load accuracy is up to 0.05 nN and a displacement resolution of 0.01 nm. The procedure for preparing the microcapsule specimen for the nanoindentation test is as follows: ① cut the slides into squares; ② apply the pre-configured crystal adhesive to a square area of 1 cm × 1 cm and use a homogenizer to correct the thickness and flatness of the cemented layer; ③ spread the microcapsule samples on the surface of the unconsolidated crystal adhesive; ④ fix the samples for the loading stage of the nanoindentation test for subsequent experiments. The nano-hardness and Young's modulus of the microcapsules were calculated using the classic Oliver–Pharr analysis [25].

2.2.4. Thermodynamic Property

Microwave Heating Performance

The microwave heating performance of the microcapsules was tested using an infrared thermal imager and a microwave oven. First, 10 g of microcapsules was washed repeatedly with petroleum ether and then dispersed in anhydrous ethanol to remove any surface material that was not encapsulated by regenerated or unreacted H3M molecules. The cleaned microcapsules were then placed in an oven at 60 °C for 2 h to volatilize the residual water.

Next, the microcapsules were evenly distributed over an area of 1 cm^2 on the slide and covered with a coverslip to prevent them from scattering and ensure that each group received the same area of microwave radiation in the microwave oven. The slides were then placed in a microwave heating cabinet for microwave heating. Finally, the infrared thermal images of the microcapsules were obtained using infrared thermography after the microwave heating, as shown in Figure 3.

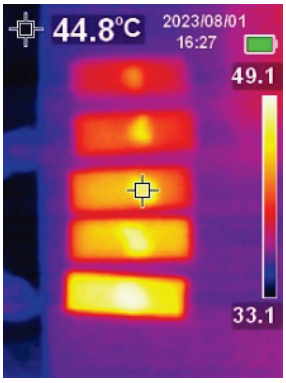

Figure 3. Infrared imaging of microcapsules.

Thermal Conductance

A thermal constant analyzer (Hot Disk, Gothenburg, Sweden) (shown in Figure 4) was used for thermal conductivity testing based on the Gustafsson transient plate heat source method [21] to accurately and rapidly evaluate the thermal conductivity of the microcapsules, including the heating coefficient, thermal conductivity, thermal diffusion coefficient, and specific heat capacity.

(**a**) (**b**)

Figure 4. Thermal conductivity test sample and Hot Disk thermal constant analyzer: (**a**) thermal conductivity test samples; (**b**) Hot Disk thermal constant analyzer.

3. Results and Discussion

3.1. Basic Performance

3.1.1. Particle Size Distribution

The results of the particle size distribution of the microcapsules are shown in Figure 5. As seen in Figure 5a, the microcapsules exhibited good dispersibility, with no obvious agglomeration. From Figure 5b, it can be observed that the particle size of the microcapsules followed a normal distribution, with a maximum particle size of 98.79 μm and a minimum particle size of 12.37 μm. The particle size of most microcapsules (86.13%) ranges from 42 to 76 μm, with an average particle size of 53.5 μm.

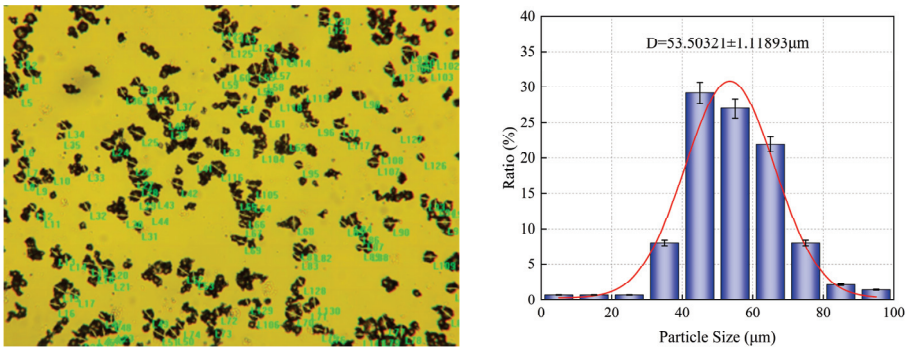

(**a**) (**b**)

Figure 5. Particle size distribution test process and results: (**a**) particle size distribution test procedure; (**b**) particle size distribution test results.

Particle size has a significant influence on the properties and viability of microcapsules [26]. The particle size of microcapsules prepared by the adsorption encapsulation and sharp pore coagulation bath methods is in the millimeter range [27]. Excessive particle size exposes the microcapsules to damage during mixing and compaction, affecting the adhesion and mechanical strength of the asphalt to the aggregate. Microcapsules produced by the interfacial polymerization method have a small particle size (5–35 μm) and are prone to an electrostatic adsorption effect, resulting in obvious agglomeration [12]. Additionally, the thickness of the microcapsule shell is difficult to control, the core content is low, and the

cost is high. Asphalt mastic film thickness is usually around 50 μm [13], and the particle size of the microcapsules prepared in this study is mainly concentrated in the range of 42–76 μm, so the microcapsules have little effect on the adhesion between the asphalt mastic and the aggregate. This also greatly reduces the likelihood of the aggregate experiencing mutual extrusion and early rupture during mixing and compaction, thus improving the survival rate of the microcapsules [28].

3.1.2. Microscopic Morphology and Shell Thickness

Figure 6 shows the SEM images of microcapsules under the optimal preparation process. It can be seen that both types of microcapsules are relatively regular in shape, though there are significant differences in their microscopic morphology. The surface of ordinary microcapsules is smooth and flat, with only a small number of resin blocks protruding. In contrast, the surface of the nano-SiC-modified microcapsules features a large number of rough and dense resin blocks, which increase the contact area between the microcapsules and the asphalt, thereby improving the adhesion performance between the two [29,30]. Additionally, the resin blocks contain nano-SiC particles, which enhance the strength of the microcapsules and improve their resistance to breakage during mixing and compaction. The shell of the microcapsules after rupture is shown in Figure 7. The thickness of the nano-SiC-modified microcapsule shell ranged from 1.5 μm to 2 μm, with an average thickness of 1.565 μm, accounting for only 3.9% of the average particle size of the microcapsule, and the shell thickness is relatively uniform.

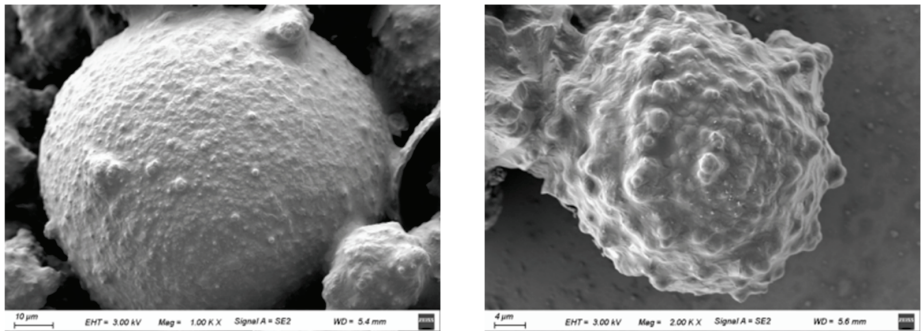

(**a**) (**b**)

Figure 6. SEM morphology of microcapsules: (**a**) SEM morphology of undoped nanogram SiC-modified microcapsules; (**b**) SEM morphology of nano-SiC-modified microcapsules.

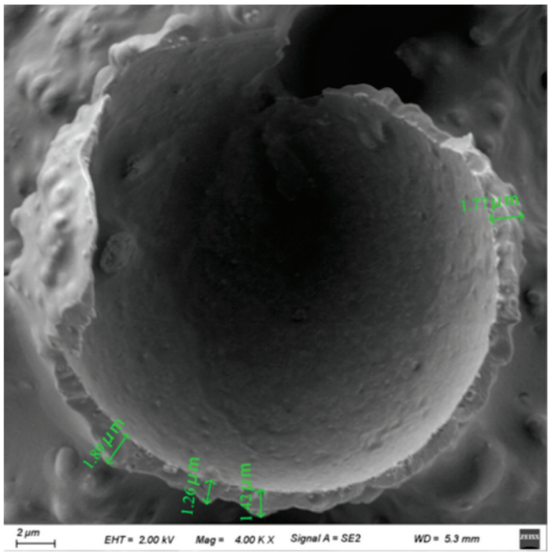

Figure 7. SEM image of microcapsule shell.

3.1.3. Chemical Structure

The changes in the characteristic peaks of each absorption curve in the infrared spectrum can be used to determine whether the microcapsules are successfully synthesized [31]. Figure 8 illustrates the infrared spectrograms of the nano-SiC-HMMM microcapsule shell, nano-SiC, microcapsules, and regenerant. The absorption peak at 843 cm^{-1} corresponds to the characteristic Si-C bond, and this peak is also observed in the microcapsule and microcapsule shell spectra. Furthermore, no new characteristic absorption peaks were detected in the microcapsules and microcapsule shell spectra, indicating that nano-SiC does not participate in the chemical reaction during the formation of the microcapsule shell. Instead, nano-SiC is likely adsorbed onto the surface of the H3M molecules through electrostatic interactions, thus remaining present in the microcapsules. Characteristic absorption peaks for the $–CH_3$ and $–CH_2$ stretching vibrations of the regenerant were observed at 1456 cm^{-1} and 2924 cm^{-1}, respectively [32].

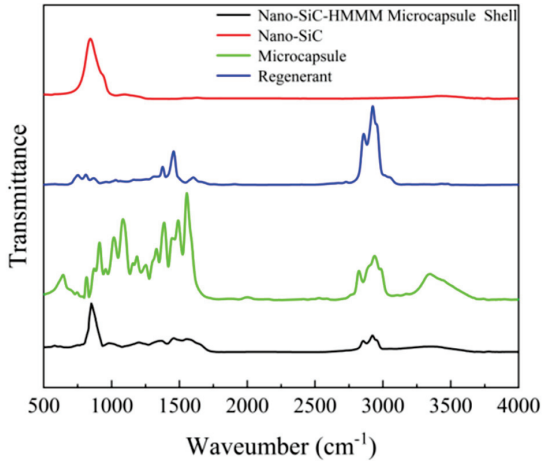

Figure 8. Infrared spectra of microcapsules.

The absorption peak at 1554 cm^{-1} corresponds to the characteristic bending deformation of the –N=C=N– in melamine molecules, which is present in both microcapsules and microcapsule shell materials, confirming that the shell of microcapsules is formed by the dehydration and polymerization of H3M molecules under acidic conditions. As shown in Figure 8, the microcapsules exhibit all the characteristic peaks corresponding to the nano-SiC-HMMM microcapsule shell, nano-SiC, microcapsules, and regenerant, indicating that the thermal and stress dual-induced nano-SiC-modified microcapsules have been successfully prepared.

3.1.4. Core Content

The core contents of four groups of microcapsules were randomly detected, as shown in Table 1. The average core content of the dual-induced microcapsules was 87.6%, which increased the core content of the thermal dual-induced microcapsules by about 2–16 times compared to the existing calcium alginate microcapsules and porous sand microcapsules [6,7,33]. This is because calcium alginate microcapsules have multi-chamber structures, porous sand microcapsules have multi-core structures, and these complex shell structures significantly reduce the core content. However, thermal stress induced the inner shell of the microcapsules to become smooth, with the microcapsule shell containing only the regenerant. The core content of the double-induced microcapsules increased by 8.29%~23.54% compared to the in situ polymerization microcapsules and by 15.34%~17.22% compared to the interfacial polymerization microcapsules [5,14,34]. This is because the microcapsule shell prepared in this paper is 2~3 μm thick, which provides more space for storing the regenerant. The reason is due to the combination of modified materials and resin molecules, which improves the mechanical properties of the microcapsule shell materials,

thereby increasing the core content. A higher core content indicates better self-healing performance [27,35,36].

Table 1. The core content of microcapsules.

Specimens	1	2	3	4	Average
Core content /%	84.01	89.76	88.52	88.19	87.62

3.2. Stability

3.2.1. Thermal Stability

Figure 9 shows the TGA curves of the microcapsules, shell material, and core material. As the temperature increases, the mass loss of microcapsules gradually increases. The mass loss process can be divided into three main stages. The first stage occurs between 30 and 200 °C, where the mass loss of the microcapsule is small, accounting for only 5.642% of the total microcapsule. During this stage, the mass loss is primarily due to the evaporation of water within the microcapsules, as well as the degradation of small molecules from the polymer that are not fully cross-linked or cured [37]. The second stage occurs between 200 and 420 °C, where the mass of the microcapsules decreases rapidly. The DTG curves of the shell material show that the surface layer of the shell undergoes violent decomposition, leading to a gradual thinning of the capsule shell, and eventually, the microcapsules rupture. At this point, the core material is directly exposed to the high-temperature environment, experiencing extremely rapid thermal decomposition, which significantly damages the quality of the microcapsules [38]. From the curve in this stage, it can be seen that the thermal stability of the microcapsules is significantly higher than that of the shell material, indicating that the addition of nano-SiC effectively improves the thermal stability of the microcapsules. In the third stage (>700 °C), the residual mass of the microcapsules is significantly higher than that of both the shell and core material. This is due to the excellent thermal stability of nano-SiC, which hardly decomposes at 700 °C. Compared with the existing microcapsules, the thermal stress dual-induced nano-SiC microcapsules prepared in this study exhibit better thermal stability, with a mass loss rate of only 2.919% in the temperature range used for construction mixing (150–170 °C), which is much smaller than that of interfacial polymerization microcapsules, calcium alginate microcapsules, and porous sand microcapsules. Meanwhile, the addition of suitable modifiers of the capsule shell materials (such as nano-SiC, nano-SiO_2 carbide, etc.) can significantly improve the high-temperature resistance of microcapsules [2]. This is because the addition of inorganic modified materials makes the shell of the microcapsules denser and improves their resistance to high-temperature deformation, while the rough shell surface also provides more space for high-temperature deformation. Compared with other microcapsules, the mass loss of the nano-SiC-modified microcapsules is reduced by 5%~15% at the same temperature [24].

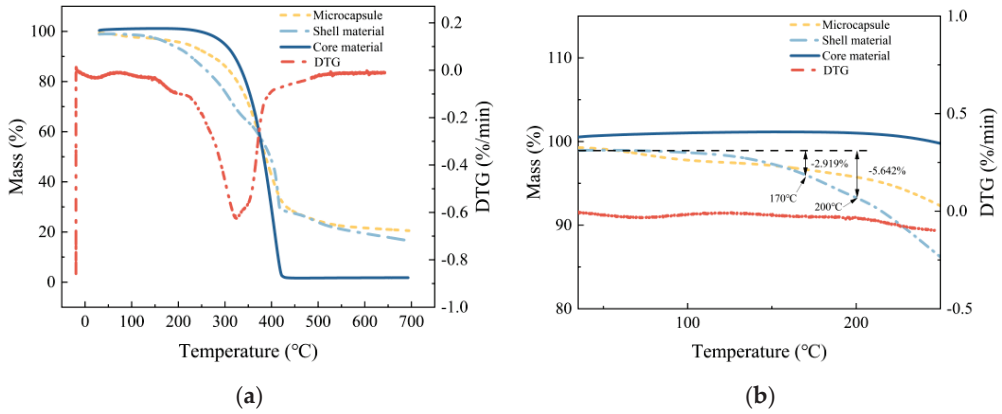

Figure 9. Mass loss of microcapsules. (**a**) is mass loss of microcapsules at room temperature to 700 °C; (**b**) is enlarged view of mass loss of microcapsules at room temperature to 300 °C.

3.2.2. Storage Stability

Figure 10 demonstrates the variation in the mass loss of microcapsules over different storage periods (7 d, 14 d, 21 d, 28 d, 35 d, 42 d, and 49 d). The fastest mass loss of microcapsules was observed during the first 7 days, due to the small amount of uncondensed H3M molecules and water on the surface of the microcapsules, which volatilized rapidly into the air [39]. The mass loss of the microcapsules gradually increased with the extension of the storage time. This may be due to the prolonged storage resulting in exposure of the shell material to air oxidation [24]. In addition, the regenerant may also be exposed to air infiltration through weak portions of the shell and slowly volatilize, further contributing to the mass loss of the microcapsules. As the storage time continued to increase, the mass loss rate of the microcapsules decreased and gradually stabilized (with a 2.25% mass loss after 49 d), indicating that the microcapsules have good storage stability [40].

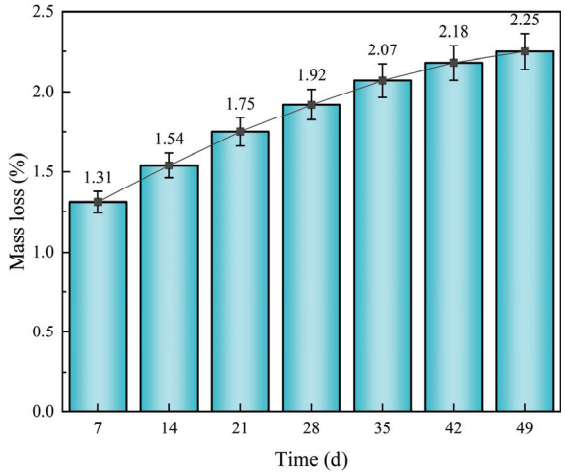

Figure 10. Rate of mass loss of microcapsules at different storage days.

3.2.3. Construction Stability

To investigate the construction stability of the microcapsules, FM was used to observe their morphology in asphalt mixture extracts. Asphalt mixtures were prepared at 130 °C and 160 °C with 6% microcapsules. The results are shown in Figure 11. It was found that most of the microcapsules maintained an intact structure with no leakage of the core material after mixing and compression at 130 °C and 160 °C. In addition, a few microcapsules retained their intact circular morphology, although the internal core material was prone to leakage, causing the fluorescence of the microcapsules to be significantly reduced under FM.

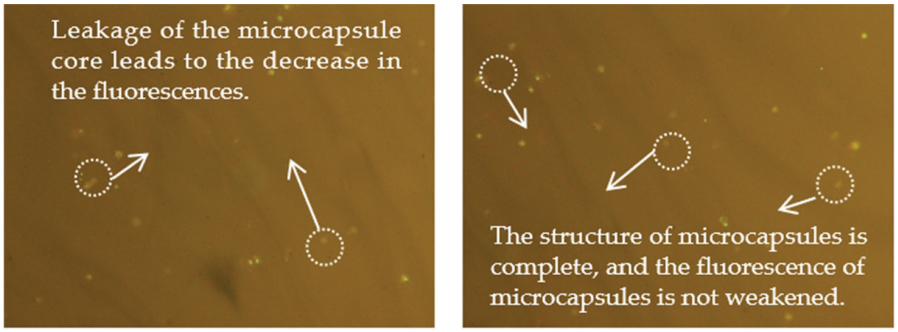

Figure 11. Fluorescence microscopy images of surviving microcapsules in asphalt mixes.

Based on the survival state of microcapsules observed under FM, mathematical and statistical methods were used to roughly estimate their survival rate after construction mixing [41]. The results are shown in Figure 12. The microcapsules remained highly viable

under high-temperature mixing, with survival rates of 82.66% at 130 °C and 79.12% at 160 °C. As the temperature increased, the survival rate of microcapsules produced a certain decrease. This was because the higher temperature softened the resin components in the microcapsule shell, reducing its strength, while the thermal expansion of the core material caused the microcapsule shell to expand, further increasing the likelihood of damage to the microcapsule shell. During the statistical process, it was found that microcapsules with a particle size larger than 60 μm were more likely to rupture. This is because microcapsules with larger particle sizes cannot be protected by the asphalt film on the aggregate surface and are more likely to be crushed directly by the aggregate [27].

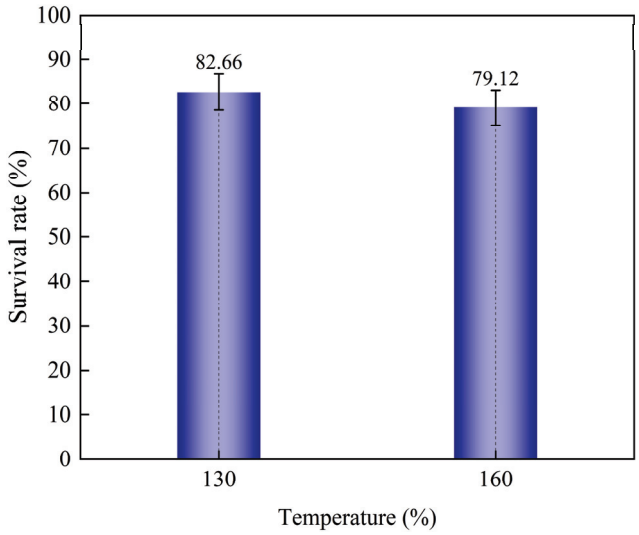

Figure 12. Survival of microcapsules at 130 °C and 160 °C mixing temperatures.

3.3. Mechanical Strength

Figure 13 shows the nanoindentation force–displacement curves of the modified microcapsules with different nano-SiC contents. The testing results of Young's modulus and nano-hardness are shown in Table 2. The mechanical strength of the microcapsules increased gradually with the increase in nano-SiC content. When the nano-SiC content increased from 0% to 10%, the nano-hardness increased from 0.26 Gpa to 0.54 Gpa, and the Young's modulus increased from 2.45 Gpa to 3.15 Gpa. This is because the nano-SiC combines with resin molecules to form a three-dimensional structure with alternating rigid parts (nano-SiC) and flexible parts (H3M), which improves the mechanical strength of the shell material. This ensures the survival of the microcapsules during the construction of asphalt mixtures. Compared with the existing microcapsules, the Young's modulus and nano-hardness of the dual-induced nano-SiC-modified microcapsules prepared in this paper were increased by about 20%–290% and 63.6%– 760%, respectively. This indicates that the hardness and content of the modified materials have an important effect on the mechanical strength of the microcapsule shell, proving that the modification of the microcapsule shell with high-strength nanomaterials is an effective way to improve the mechanical strength of the microcapsules. Compared with other microcapsules, the Young's modulus and nano-hardness of the nano-SiC-modified microcapsules increased by 1.5 times and 3.0 times, respectively [6,7,12,14–16].

Table 2. Results of Young's modulus and nano-hardness test of microcapsules.

Mechanical Parameter	Nano-SiC Doping (%)				
	0	**2.5**	**5**	**7.5**	**10**
Nano-hardness (Gpa)	0.26	0.31	0.39	0.50	0.54
Young's modulus (Gpa)	2.45	2.62	2.91	3.07	3.15

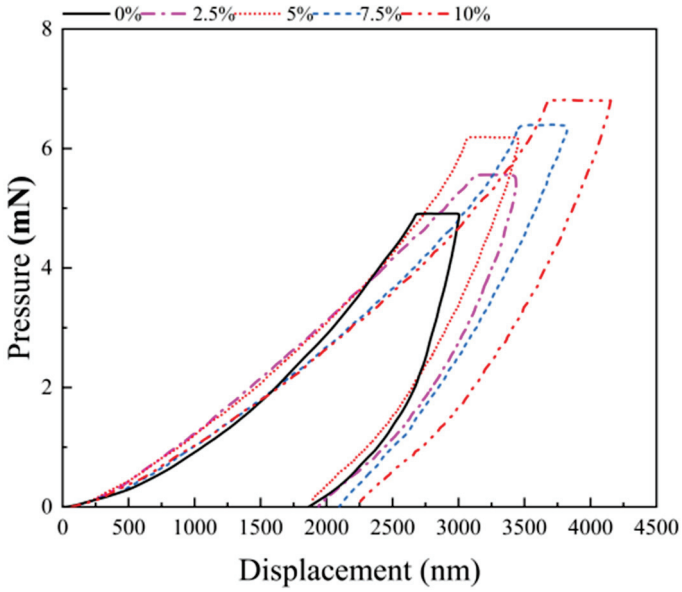

Figure 13. Nanoindentation force–displacement curve.

3.4. Thermodynamic Property

3.4.1. Microwave Heating Performance

To investigate the effect of nano-SiC content on the microwave heating performance of microcapsules, infrared thermography was used to monitor the temperature changes of microcapsules with different nano-SiC contents (0%, 2.5%, 5%, 7.5%, and 10%) in real time at different heating times (1.5 min, 3 min, 4.5 min, and 6 min). The results are shown in Table 3.

Table 3. Results of microwave heating characteristics of different kinds of microcapsules (°C).

Nano-SiC Doping (%)	Microwave Heating Time (min)			
	1.5	**3.0**	**4.5**	**6.0**
0	36.2	37.1	38.7	39.4
2.5	38.1	40.7	45.6	48.6
5.0	44	44.8	48.2	54.7
7.5	45.5	47.9	50.9	57.0
10	46.1	49.1	52.5	58.6

The microwave heating effect of the microcapsules gradually increased with the increase in nano-SiC content. The temperature of the microcapsules with 10% nano-SiC was 48.73% higher than that of the microcapsules without nano-SiC after the same heating time (6 min). When the nano-SiC content was 0%, the temperature difference between the microcapsules after heating for 1.5 min and 6 min was only 3.2 °C. This is due to heat accumulation caused by prolonged heating. When the nano-SiC content was 10%, the temperature of the microcapsules reached 58.6 °C after 6 min of heating, and the heating effect was significant. It was enhanced by 48.73% compared to heating for 1.5 min. However, for the same heating time (6 min), the temperature of the microcapsules with 7.5% nano-SiC increased by only 4.2% compared with that of the microcapsules with 5% nano-SiC, indicating that the enhancement of the microwave heating characteristics of the microcapsules was gradually weakened by a nano-SiC content higher than 5%. In addition, the heating rate of the microcapsules increased with the prolongation of microwave heating time. When the microwave heating time was 3 min, the warming rate was 2 °C/min, and when the microwave heating time was 6 min, the warming rate was 4.07 °C/min. This is because the coupling of nanosized SiC with microwave radiation

has a more significant warming effect on enhancing absorption after arriving at a certain temperature [42]. Combining the economic factors, the extended microwave heating time required to increase the temperature of the microcapsules is preferred.

3.4.2. Thermal Conductivity

To investigate the effect of different nano-SiC contents on the thermal conductivity of microcapsules, microcapsules with different nano-SiC contents (0%, 2.5%, 5%, 7.5%, and 10%) were tested using a hot plate thermal constant meter. The results are shown in Figure 14.

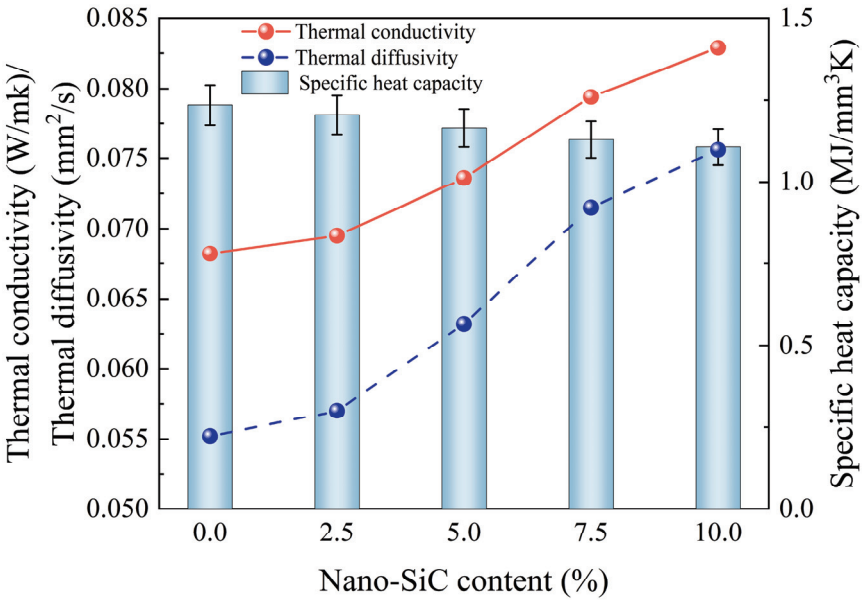

Figure 14. Thermal conductivity of microcapsules with different contents of nano-SiC.

The thermal conductivity of the microcapsules increased gradually with the increase in nano-SiC content. When the nano-SiC content was 10%, the thermal conductivity of the microcapsules increased by 21.6% compared to that of the microcapsules without nano-SiC. In addition, the specific heat capacity of the microcapsules decreased significantly, indicating that the microcapsules warmed up faster after thermal radiation. The accelerated warming rate of the microcapsules would reduce the time required for the core material to fill the microcracks, thus improving the self-healing efficiency of microcapsules. It can be observed that the thermal diffusion coefficient of the microcapsules gradually increases with the increase in nano-SiC content. This property helps transfer heat, which contributes to the rapid warming of the asphalt material around the microcapsules, and thus positively promotes the diffusion and penetration of the repair agent as well as the diffusion of asphalt molecules [43].

3.5. Self-Healing Mechanism

To investigate the self-healing behavior of the stress dual-induced nano-SiC-modified microcapsules, fluorescence microscopy was used to observe the state of microcracks in asphalt with a 6% microcapsule content. Under the fluorescence microscope, the asphalt and regenerant agents emit deep orange and yellow-green fluorescence, respectively, allowing observation of the distribution of the regenerant agents around the cracks.

As seen from Figure 15, a certain amount of the microcapsules in the asphalt show yellow fluorescence. As the microcrack passes over the location of the microcapsule, the microcapsule is punctured and releases a yellow-green regenerant. It can be observed that the microcapsules darkened, and the fluorescence significantly decreased. The regenerant flowed and diffused around the microcracks by capillary action. Under the action of microwave heating, the temperature of the microcapsules gradually increased, and this flow–diffusion phenomenon was accelerated, further promoting the healing of microcracks. At this time, both sides of the microcrack emitted yellow-green fluorescence, and the width of the microcrack was reduced, indicating that the regenerant had successfully repaired the microcrack.

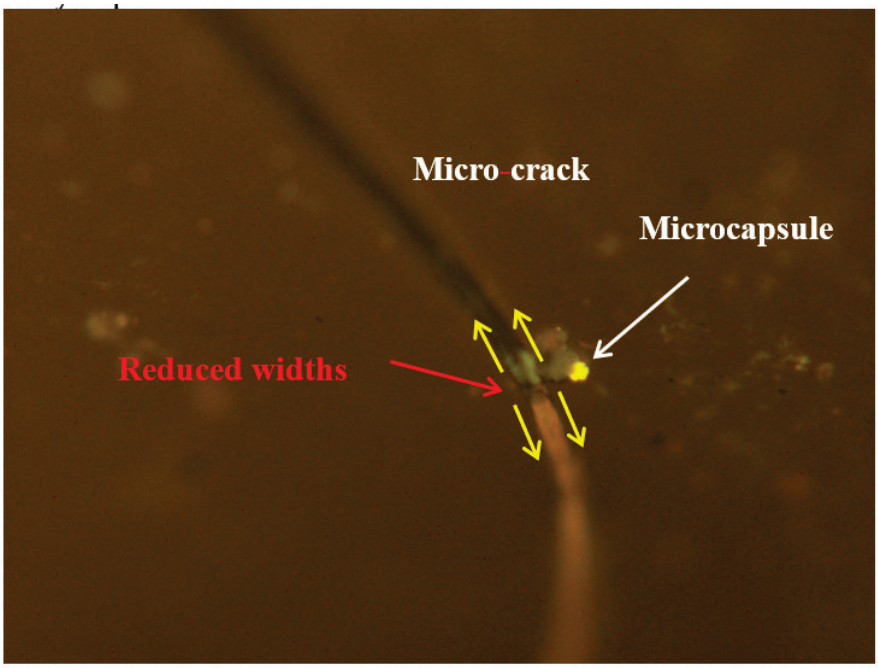

Figure 15. Self-healing process of microcapsule.

3.6. Comparison of the Prepared Nano-Sic-Modified Microcapsules with Other Microcapsules

The results of the comparative analysis of the technical performance of the nano-SiC-modified microcapsules and other microcapsules are shown in Table 4. The results show that the average particle size of the nano-SiC-modified microcapsules was 53.50 μm, and the core content reached 87.6%, which was an increase of 2~23% compared to other road microcapsules. Meanwhile, through process optimization and improvement, the mass loss of microcapsules in the temperature range of 150–170 °C was only 2.92%, which was 5%~15% lower than that of other microcapsules. The Young's modulus and nano-hardness of the 10% SiC-modified microcapsules reached 3.15 Gpa and 0.54 Gpa, respectively. Compared to other microcapsules, the Young's modulus and nano-hardness of the nano-SiC-modified microcapsules are increased by 1.5 times and 3.0 times, respectively [6,7,12,14–16]. After microwave heating for 6 min, the thermal conductivity of the 10% nano-SiC-modified microcapsules increased by 21.6%, the specific heat capacity decreased by 10.45%, and the heat diffusion coefficient increased by 36.96%, compared to that of microcapsules without nano-SiC.

Table 4. Comparison of the prepared nano-SiC-modified microcapsules with other microcapsules.

Microcapsule Type	Particle Size/μm	Core Content/%	Mechanical Strength	Thermal Stability (Temperature °C/Mass Loss Ratio %)
Adsorption encapsulation [6]	1–10 mm	20	Ultimate resistance (N)/deformation (μm) 17.61/106.92	180/3
Piercing solidification method [7,33]	1–6.8 mm	40	Uniaxial compression 130 °C/12N	200/4
Interfacial polymerization [12,34]	5–35	70.40–72.28	Young's Modulus (MPa)/ hardness (MPa) 276.94–408.90 43.38–71.08	160–180/10–15
In situ polymerization [14–16,35]	2–230	64.08–79.33	Young's Modulus (MPa)/ hardness (MPa) 1000–2700 37.66–140	140–180/3.72–20
Nano-SiC-modified microcapsules	40–100	87.62	Young's Modulus (MPa)/ hardness (MPa) 2620–3150 310–540	140–200/4.257

4. Conclusions

The study of thermal and stress dual-induced nano-SiC microcapsules is highly significant to the field of microcapsule self-repair. In this paper, the core content, stability, and mechanical properties of the microcapsules were significantly improved by doping nano-SiC into the microcapsule shell. In addition, doping nano-SiC simultaneously significantly improved both the microwave warming performance and thermal conductivity of the microcapsules. Compared to other microcapsules, the core content of these microcapsules was increased by 8.29–23.54%, the thermal mass loss was reduced by 5%–15% at the same temperature, and the mechanical strength was enhanced by 1.5 times and 3.0 times. Additionally, compared to microcapsules without nano-SiC, the thermal conductivity and microwave heating performance of the microcapsules with 10% nano-SiC increased by 21.6% and 48.73%, respectively, enabling the thermal induction and core release in the modified microcapsules. Further research is needed to explore the trade-offs between the performance and benefits of microcapsules in practical engineering. Despite these challenges, this study provides valuable insights into the in-depth exploration of microcapsules in the field of asphalt self-repair and suggests directions for the study of novel microcapsules. The authors anticipate future research that builds upon, scrutinizes, and refines the findings of this study, further contributing to this critical area of study.

Author Contributions: Investigation, Y.S. and Y.C.; writing—original draft, S.W. and Y.C.; funding acquisition, Y.S., X.J. and Y.H.; supervision, X.J. and Y.H.; formal analysis, S.W. and Y.C.; writing—review and editing, L.L. and S.L. All authors have read and agreed to the published version of the manuscript.

Funding: This research was funded by the Natural Science Foundation of Xinjiang Uygur Autonomous Region under Grant No. 2023D01A88, the Natural Science Basic Research Program of Shaanxi Province under Grant No. 2024JC-YBMS-435, and the Fundamental Research Funds for the Central Universities of CHD under Grant No. 300102214909.

Institutional Review Board Statement: Not applicable.

Informed Consent Statement: Not applicable.

Data Availability Statement: The data presented in this study are available upon request from the corresponding author.

Conflicts of Interest: Author Yunlong Sun and Sijia Liu was employed by the company Xinjiang Academy of Transportation Science, Co., Ltd. The remaining authors declare that the research was conducted in the absence of any commercial or financial relationships that could be construed as a potential conflict of interest.

References

1. Ji, X.; Yang, Z.; Zhou, Z.; Zhang, Y.; Lei, Y. Evaluation method for self-healing performance of densely graded asphalt mixture. *J. Chin. Highw.* **2018**, *31*, 51–57. (In Chinese) [CrossRef]
2. Lu, T.; Li, B.; Sun, D.; Hu, M.; Ma, J.; Sun, G. Advances in controlled release of microcapsules and promising applications in self-healing of asphalt materials. *J. Clean. Prod.* **2021**, *294*. [CrossRef]
3. He, L.; Huang, H.; Wim, V.; Tóth, C.; Gao, J.; Kowalski, K.; Jan, V. A state-of-the-art on microcapsules for asphalt self-healing. *Cailiao Daobao* **2020**, *34*, 15092–15101. (In Chinese) [CrossRef]
4. He, L.; Zhao, L.; Ling, T. Research on the induced thermal self-healing performance of cracks in dense asphalt mixtures. *J. Chin. Highw.* **2017**, *30*, 17–24. (In Chinese)
5. García, Á.; Schlangen, E.; van de Ven, M.; Sierra-Beltrán, G. Preparation of capsules containing rejuvenators for their use in asphalt concrete. *J. Hazard. Mater.* **2010**, *184*, 603–611. [CrossRef]
6. Liu, L.; Wu, F.; Ju, X.; Xie, R.; Wang, W.; Niu, C.; Chu, L. Preparation of monodisperse calcium alginate microcapsules via internal gelation in microfluidic-generated double emulsions. *J. Colloid Interface Sci.* **2013**, *404*, 85–90. [CrossRef]
7. Micaelo, R.; Al-Mansoori, T.; Garcia, A. Study of the mechanical properties and self-healing ability of asphalt mixture containing calcium-alginate capsules. *Constr. Build. Mater.* **2016**, *123*, 734–744. [CrossRef]
8. Garcia, A.; Jelfs, J.; Austin, C.J. Internal asphalt mixture rejuvenation using capsules. *Constr. Build. Mater.* **2015**, *101*, 309–316. [CrossRef]
9. Xu, S.; Tabaković, A.; Liu, X.; Palin, D.; Schlangen, E. Optimization of the calcium alginate capsules for self-healing asphalt. *Appl. Sci.* **2019**, *9*, 468. [CrossRef]
10. Zhang, L.; Liu, Q.; Li, H.; Norambuena-Contreras, J.; Wu, S.; Bao, S.; Shu, B. Synthesis and characterization of multi-cavity Ca-alginate capsules used for self-healing in asphalt mixtures. *Constr. Build. Mater.* **2019**, *211*, 298–307. [CrossRef]
11. Liu, X.; Zhang, H.; Wang, J.; Wang, Z.; Wang, S. Preparation of epoxy microcapsule based self-healing coatings and their behavior. *Surf. Coat. Technol.* **2012**, *206*, 4976–4980. [CrossRef]
12. Ji, X.; Li, J.; Hua, W.; Hu, Y.; Si, B.; Chen, B. Preparation and performance of microcapsules for asphalt pavements using interfacial polymerization. *Constr. Build. Mater.* **2021**, *289*, 123179. [CrossRef]
13. Li, J.; Ji, X.; Tang, Z.; Hu, Y.; Hua, W. Preparation and evaluation of self-healing microcapsules for asphalt based on response surface optimization. *J. Appl. Polym. Sci.* **2021**, *139*. [CrossRef]
14. Zhang, H.; Bai, Y.; Cheng, F. Rheological and self-healing properties of asphalt binder containing microcapsules. *Constr. Build. Mater.* **2018**, *187*, 138–148. [CrossRef]
15. Sun, D.; Hu, J.; Zhu, X. Size optimization and self-healing evaluation of microcapsules in asphalt binder. *Colloid Polym. Sci.* **2015**, *293*, 3505–3516. [CrossRef]
16. Wang, Y.-Y.; Tan, Y.-Q. Preparation, with graphene, of novel biomimetic self-healing microcapsules with high thermal stability and conductivity. *Front. Struct. Civ. Eng.* **2023**, *17*, 1–11. [CrossRef]
17. Su, J.-F.; Schlangen, E.; Qiu, J. Design and construction of microcapsules containing rejuvenator for asphalt. *Powder Technol.* **2013**, *235*, 563–571. [CrossRef]
18. Bao, C.; Xu, Y.; Zheng, C.; Nie, L.; Yang, X. Rejuvenation effect evaluation and mechanism analysis of rejuvenators on aged asphalt using molecular simulation. *Mater. Struct.* **2022**, *55*, 1–16. [CrossRef]
19. Wan, P.; Liu, Q.; Wu, S.; Zhao, Z.; Chen, S.; Zou, Y.; Rao, W.; Yu, X. A novel microwave induced oil release pattern of calcium alginate/ nano-Fe_3O_4 composite capsules for asphalt self-healing. *J. Clean. Prod.* **2021**, *297*, 126721. [CrossRef]
20. Wang, X.; Guo, Y.; Su, J.; Zhang, X.; Wang, Y.; Tan, Y. Fabrication and Characterization of Novel Electrothermal Self-Healing Microcapsules with Graphene/Polymer Hybrid Shells for Bitumenious Material. *Nanomaterials* **2018**, *8*, 419. [CrossRef]
21. Wang, Y.-Y.; Su, J.-F.; Schlangen, E.; Han, N.-X.; Han, S.; Li, W. Fabrication and characterization of self-healing microcapsules containing bituminous rejuvenator by a nano-inorganic/organic hybrid method. *Constr. Build. Mater.* **2016**, *121*, 471–482. [CrossRef]
22. Liang, Y.; Wang, T.; He, Z.; Sun, Y.; Song, S.; Cui, X.; Cao, Y. High thermal storage capacity phase change microcapsules for heat transfer enhancement through hydroxylated-silanized nano-silicon carbide. *Energy* **2023**, *285*, 129502. [CrossRef]
23. Li, B.; Sun, G.; Sun, D.; Lu, T.; Ma, J.; Deng, Y. Survival and activation behavior of microcapsules in self-healing asphalt mixture. *Constr. Build. Mater.* **2020**, *260*, 119719. [CrossRef]
24. Ji, X.; Wang, S.; Yao, B.; Si, W.; Wang, C.; Wu, T.; Zhang, X. Preparation and properties of nano-SiO_2 modified microcapsules for asphalt pavement. *Mater. Des.* **2023**, *229*, 111871. [CrossRef]

25. Oliver, W.; Pharr, G. An improved technique for determining hardness and elastic modulus using load and displacement sensing indentation experiments. *J. Mater. Res.* **1992**, *7*, 1564–1583. [CrossRef]
26. Norambuena-Contreras, J.; Concha, J.; Valdes-Vidal, G.; Wood, C. Optimised biopolymer-based capsules for enhancing the mechanical and self-healing proper-ties of asphalt mixtures. *Mater. Struct.* **2024**, *57*, 236. [CrossRef]
27. Al-Mansoori, T.; Micaelo, R.; Artamendi, I.; Norambuena-Contreras, J.; Garcia, A. Microcapsules for self-healing of asphalt mixture without compromising mechanical performance. *Constr. Build. Mater.* **2017**, *155*, 1091–1100. [CrossRef]
28. Liang, B.; Lan, F.; Shi, K.; Qian, G.; Liu, Z.; Zheng, J. Review on the self-healing of asphalt materials: Mechanism, affecting factors, assessments and improvements. *Constr. Build. Mater.* **2020**, *266*, 120453. [CrossRef]
29. He, L.; Cai, Z.; Feng, C.; Garcia, A.; Ma, Y. Review of research on microcapsule self-healing technology of asphalt mixtures. *J. Chang. Univ. (Nat. Sci. Ed.)* **2018**, *38*, 9–18, 77. [CrossRef]
30. Zhang, H.; Yao, T.; Li, C. Study on the mechanical behavior of microcapsules during the mixing process of asphalt mixture. *Constr. Build. Mater.* **2024**, *441*, 137531. [CrossRef]
31. Sun, D.; Pang, Q.; Zhu, X.; Tian, Y.; Lu, T.; Yang, Y. Enhanced Self-Healing Process of Sustainable Asphalt Materials Containing Microcapsules. *ACS Sustain. Chem. Eng.* **2017**, *5*, 9881–9893. [CrossRef]
32. Sun, D.; Sun, G.; Zhu, X.; Guarin, A.; Li, B.; Dai, Z.; Ling, J. A comprehensive review on self-healing of asphalt materials: Mechanism, model, characterization and enhancement. *Adv. Colloid Interface Sci.* **2018**, *256*, 65–93. [CrossRef] [PubMed]
33. Norambuena-Contreras, J.; Liu, Q.; Zhang, L.; Wu, S.; Yalcin, E.; Garcia, A. Influence of encapsulated sunflower oil on the mechanical and self-healing properties of dense-graded asphalt mixtures. *Mater. Struct.* **2019**, *52*, 1–13. [CrossRef]
34. Chung, K.; Lee, S.; Park, M.; Yoo, P.; Hong, Y. Preparation and characterization of microcapsule-containing self-healing asphalt. *J. Ind. Eng. Chem.* **2015**, *29*, 330–337. [CrossRef]
35. Tan, X.; Zhang, J.; Guo, D.; Sun, G.; Zhou, Y.; Zhang, W. Preparation and Repeated Repairability Evaluation of Sunflower Oil-Type Microencapsulated Filling Materials. *J. Nanosci. Nanotechnol.* **2020**, *20*, 1554–1566. [CrossRef]
36. Su, J.-F.; Wang, L.-Q.; Xie, X.-M.; Gao, X. Understanding the final surface state of self-healing microcapsules containing rejuvenator in bituminous binder of asphalt. *Colloids Surfaces A Physicochem. Eng. Asp.* **2021**, *615*. [CrossRef]
37. Zhang, H.; Wang, R.; Cheng, F. Study on the properties and self-healing ability of asphalt and asphalt mixture containing methanol-modified melamine-formaldehyde microcapsules. *Mater. Today Commun.* **2024**, *41*. [CrossRef]
38. Khorasani, S.N.; Ataei, S.; Neisiany, R.E. Microencapsulation of a coconut oil-based alkyd resin into poly(melamine–urea–formaldehyde) as shell for self-healing purposes. *Prog. Org. Coatings* **2017**, *111*, 99–106. [CrossRef]
39. Yang, P.; Han, S.; Su, J.; Wang, Y.; Zhang, X.; Han, N.; Li, W. Design of self-healing microcapsules containing bituminous rejuvenator with nano-$CaCO_3$/organic composite shell: Mechanical properties, thermal stability, and compactability. *Polym. Compos.* **2017**, *39*, E1441–E1451. [CrossRef]
40. Shirzad, S.; Hassan, M.; Aguirre, M.; Mohammad, L.; Cooper, S.; Negulescu, I. Microencapsulated Sunflower Oil for Rejuvenation and Healing of Asphalt Mixtures. *J. Mater. Civ. Eng.* **2017**, *29*, 04017147. [CrossRef]
41. Ji, X.; Yao, Z.; Si, W.; Wang, C.; Yi, K.; He, S.; Zhang, X. Self-healing behavior and microscopic mechanism of microencapsulated asphalt. *J. Traffic Transp. Eng. Engl. Ed.* **2023**, *23*, 67–77. [CrossRef]
42. Wang, X.; Li, C.; Zhao, T. Fabrication and characterization of poly(melamine-formaldehyde)/silicon carbide hybrid microencapsulated phase change materials with enhanced thermal conductivity and light-heat performance. *Sol. Energy Mater. Sol. Cells* **2018**, *183*, 82–91. [CrossRef]
43. Zhang, B.; Li, S.; Fei, X.; Zhao, H.; Lou, X. Enhanced mechanical properties and thermal conductivity of paraffin microcapsules shelled by hydrophobic-silicon carbide modified melamine-formaldehyde resin. *Colloids Surf. A Physicochem. Eng. Asp.* **2020**, *603*, 125219. [CrossRef]

coatings

MDPI

Article

Non-Linear Support Vector Machine Prediction of the Mechanical Properties of Asphalt Binders Subjected to Varying Temperatures and Frequencies Based on SARA

Shanglin Song [1,2], Yiqian Ma [3], Xiaoqiang Jiang [4], Dengzhou Li [4,*], Xiaoyan Ma [2,5,*] and Shidong Qiu [5]

[1] Gansu Provincial Highway Development Group Co., Ltd., Lanzhou 730070, China; 18193106299@163.com
[2] Scientific Observation and Research Base of Transport Industry of Long Term Performance of Highway Infrastructure in Northwest Cold and Arid Regions, Lanzhou 736200, China
[3] The School of Surveying and Geoinformatics, Lanzhou Jiaotong University, Lanzhou 730070, China; 15506151339@163.com
[4] Gansu Hengtong Road and Bridge Engineering Co., Ltd., Lanzhou 730030, China; 13909380007@163.com
[5] Xi'an Key Laboratory of Modern Transportation Function Materials, Chang'an University, Xi'an 710064, China; 2021903592@chd.edu.cn
* Correspondence: lidengzhouyx@126.com (D.L.); xiaoyanma@chd.edu.cn (X.M.); Tel.: +86-15389401508 (X.M.)

Abstract: This study investigates the effects of chemical fractions on the mechanical properties of asphalt binders and predicts the mechanical properties of asphalt binders based on the chemical fractions. Initially, four fractions—saturate, aromatic, resin, and asphaltene (SARA)—were isolated from 36 asphalt binders using a thin-layer chromatography with flame ionization detection (TLC-FID) analyzer. Subsequently, the complex modulus and phase angle of the asphalt binders were determined for a range of frequencies and temperatures. The relationships between SARA content, heavy components, colloidal instability index, and the complex modulus and phase angle were analyzed. Advanced models, including quadratic polynomial and non-linear support vector machine (SVM) with sigmoid and RBF (Gaussian) kernels, were employed to predict the complex modulus and phase angle of asphalt binders based on the SARA data, and the reliability of these prediction models was critically assessed. The findings indicate that the contents of asphaltenes, resins, aromatics, and saturates significantly influence the rheological properties at different frequencies, though a clear correlation between SARA contents and both the complex modulus and phase angle was not established. Alternative methods should be considered for studying the mechanical properties of asphalt derived from SARA. The RBF kernel demonstrated superior performance compared to the quadratic polynomial and non-linear SVM with the Sigmoid kernel. While the non-linear SVM with the RBF kernel accurately predicts the complex modulus, it fails to predict the phase angle at low frequencies. The validation of this model confirmed its efficacy in capturing the relationship between input (SARA) and output (complex modulus and phase angle) vectors for each asphalt binder. The predicted complex modulus master curves closely match the experimental results, yet the model only approximates the trend of phase angle variation with frequency.

Keywords: mechanical properties of asphalt binders; SARA; non-linear SVM; prediction of complex modulus and phase angle master curves

1. Introduction

As a by-product of the oil industry, bitumen is primarily used in building waterproofing, road pavement, and water resource dams. The performance and durability of these

structures are significantly influenced by the properties of bitumen, particularly in road paving. The characteristics of bitumen depend on the source of the crude oil and the manufacturing process, both of which contribute to variations in bitumen components. The saturates, aromatics resins, and asphaltenes (SARA) have a substantial impact on the rheological properties, stiffness, viscosity, aging, deformation, temperature sensitivity, and the degree of adhesion of bitumen to aggregates in the asphalt mixture [1]. The composition of bituminous components largely determines its performance, and any changes in composition directly result in changes to bitumen performance.

As the rheological indices of complex modulus and phase angle at various frequencies and temperatures determine the performance of bitumen, researchers have separated bitumen into saturates, aromatics, resins, and asphaltenes to study their mechanical properties. This separation helps further understand how composition influences the properties of asphalt. Regarding their specific properties, saturates and aromatics are oily liquids at room temperature, while resins are semi-solid, and asphaltenes are solid materials, resulting in distinct viscoelastic properties for these components. For saturates, the complex shear modulus exhibits an almost linear relationship with frequency reduction, while the phase angle remains constant at about 20°; for aromatics, the complex shear modulus master curve resembles that of asphalt binders, and the phase angle curve levels off at 80° around 10 Hz. Resins display similar trends and glassy moduli as aromatics but reach the structure transition point at a lower frequency [2,3]. Xie's study reveals that saturates and aromatics show typical viscoelastic characteristics, contributing significantly to the flexibility of bitumen, with saturates displaying the lowest modulus at each frequency, although their phase angle varies widely. In contrast, resins exhibit the lowest phase angle but the highest modulus [4]. By segregating asphalt into four fractions and doping resins and asphaltenes into aromatics at varying contents to fabricate asphalt binders, researchers observed that increasing the content of resins or asphaltenes raises the complex shear modulus while lowering the phase angle value. Saturates maintain a constant phase angle regardless of temperature and frequency. Aromatics and resins share a similar Black diagram and master curve shape, characterized by a plateau in phase angle values [5]. The dynamic modulus shows a decreasing trend with increases in asphaltene or resin content and an increasing trend with increases in saturate or aromatic content [6–8]. By adding asphaltenes as a modifier, the stiffness, elasticity, and viscosity of bitumen increase, with every 6% addition of asphaltenes resulting in a one-interval rise in the high Performance Grade temperature grade [9].

Increasing asphaltene content also leads to a rise in the creep stiffness modulus and a decrease in the m-value at low temperatures, indicating that asphaltene content is a crucial determinant of the low-temperature flexibility of asphalt bitumen. Interestingly, however, the glass transition temperature (T_g) of asphalt binders is primarily influenced by the saturate and aromatic fractions, though it also increases with rising asphaltene content [10]. Kristina Hofer's research further confirmed that asphaltene content is inversely proportional to lower temperature performance [11]. Leite's studies on the lower temperature performance of asphalt binders revealed that hydrogen and carbon in the aromatic compounds are closely linked to binder stiffness; lower aromatic hydrogen content and higher saturated carbon content appear desirable for achieving lower stiffness at low temperatures [7]. Beyond macro-rheological properties, the micro-rheological properties of asphalt binders, characterized by the Derjaguin–Müller–Toporov (DMT) modulus, also increase with higher asphaltene and resin contents and decrease with higher saturate and aromatic contents. These micro-rheological results show good agreement with the macro-rheological properties [12]. Zhao's study indicated that changes in chemical properties leading to an increase in log dynamic viscosity depend on the type of binder and its age [13]. Studies

using molecular dynamics simulations to explore the initiation and cracking process of asphalt binders have shown that SARA influence the cracking process, with cracks appearing in areas with lower concentrations of asphaltenes and heteroatoms [14].

Salehfard examined 11 different asphalt binders, characterized by varying SARA compositions, to assess the impact of colloidal instability on rheological properties. The results indicated a notable increase in the viscosity of the asphalt binder corresponding to an increase in the Ic value. Additionally, there was a gradual shift of the Black curves towards higher complex moduli and lower phase angles, particularly at low frequencies, where the changes were significantly more pronounced than at high frequencies [15]. Further studies suggested that changes in the SARA analysis of bitumen serve as indicators of colloidal stability, with asphaltenes having a substantial impact. A higher asphaltene content resulted in less stability, leading to the asphalt binders being more gel-like [16].

Other research has focused on the internal colloidal structure of asphalt by examining the interactions among asphaltenes, resins, aromatics, and saturates. These studies revealed that resins and asphaltenes contain many unsaturated aromatic compounds and polar functional groups, making them more susceptible to aging than other fractions [17]. It was also found that the long-chain alkenes of saturates do not always reside on the outermost region of the colloidal structure; some penetrate the gaps within asphaltene molecules and adhere to the aliphatic areas [18]. Reconfiguring the internal colloidal structure of asphalt further demonstrated that as the distance from the center of the asphaltene micelle increases, polarity decreases. Oxidation predominantly occurs on the surface of the micelle mantles, with the highly polar aromatics and resins prone to oxidation, rendering the micelle mantles susceptible to aging [19].

Additionally, some researchers have focused on exploring the relationship between asphalt components and their safety in use, specifically the thermal properties of asphalt binders. By separating the SARA from the asphalt binder, their studies suggest that thermal stability increases progressively from saturates to asphaltenes [20]. When the heating rate is increased, the release of small molecular volatiles from saturates, aromatics, and asphaltenes increases, whereas the pattern is reversed for resins [21]. The thermal–oxidative aging of asphalt binder is characterized by endothermic reactions occurring in saturates and aromatics; both endothermic and exothermic reactions are roughly equivalent in resins, while exothermic reactions dominate in asphaltenes. During this process, the mass losses of saturates and resins are 2.1% and 0.7%, respectively, but the masses of aromatics and asphaltenes increase by 2.0% and 5.2%, respectively [22,23].

The relationship between SARA and the performance of asphalt is crucial because it defines the rheological (flow) properties, durability, and overall performance of asphalt binders under various environmental and loading conditions. Asphalt must provide structural strength while maintaining enough flexibility to resist cracking under stress. A proper balance between SARA ensures that the asphalt binder performs well under heavy loads, temperature variations, and aging processes. By understanding and optimizing the SARA balance, manufacturers can produce binders tailored to specific performance needs (e.g., heavy traffic, extreme weather) and better control over asphalt chemistry improves durability and reduces cracking, rutting, and aging, ultimately extending road service life. Also, optimized binders minimize maintenance and rehabilitation costs, reducing long-term expenditures for governments and construction companies. The studies mentioned above highlight the significant impact of SARA on the rheological properties of asphalt binders. However, most existing research primarily provides a qualitative description of the relationship between asphalt SARA and factors such as ductility, modulus, and aging, with little quantitative data on the relationship between asphalt components and mechanical properties. Furthermore, research on predicting asphalt performance based

on SARA components is sparse, indicating that the composition–structure–mechanics relationships of asphalt binders are not well understood. Currently, a major challenge for many researchers is accurately describing the relationship between asphalt components and performance, and reliably predicting performance based on SARA. In this study, SARA were obtained from 36 asphalt binders using a thin-layer chromatography with flame ionization detection (TLC-FID) analyzer, and their temperature- and frequency-dependent properties were measured by conducting frequency sweeps at different temperatures. The relationship between SARA, heavy components, colloidal instability index, complex modulus, and phase angle were analyzed. To quantitatively describe the relationship between asphalt components and mechanical properties, quadratic polynomial models and non-linear SVMs with sigmoid and RBF (Gaussian) kernels were employed to predict the complex modulus and phase angle master curve of asphalt binders based on SARA, and then reliability of these prediction models was evaluated.

2. Non-Linear Support Vector Machine

The theory of the support vector machine (SVM) originated from the field of data classification. When neural networks address linearly separable problems, the process typically involves generating a hyperplane randomly and adjusting it until the points of different categories in the training set are on opposite sides. However, this method does not ensure that the hyperplane is centrally located between the categories, which is crucial for the fault tolerance of data classification. Vapnik [24] ingeniously solved this issue with the introduction of the SVM. The core principle of the SVM is to identify the optimal linear hyperplane in the feature space that maximizes the separation of the two target classes. For both linearly separable and non-separable data, this is converted into quadratic programming (QP) to achieve a unique solution point (Figure 1). This method is effective only for linear sample sets. However, many sample sets are not linearly separable, and the use of the SVM in such cases may lead to significant risks due to its limitations. To address this, the SVM employs a linear function in a high-dimensional feature space by mapping the input vector to this space through non-linear functions, and then constructing an optimal hyperplane in this high-dimensional feature space (Non-Linear SVM, Figure 2). With the correct mapping function, most non-linearly separable problems in the input space can be transformed into linear classifications in high-dimensional feature space [25].

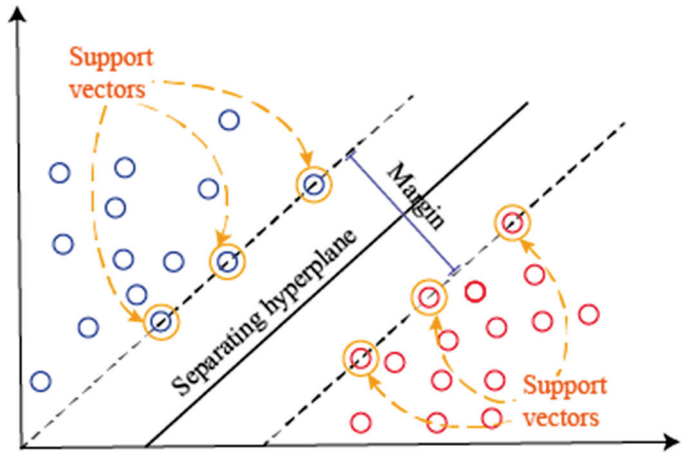

Figure 1. The optimal linear hyperplane.

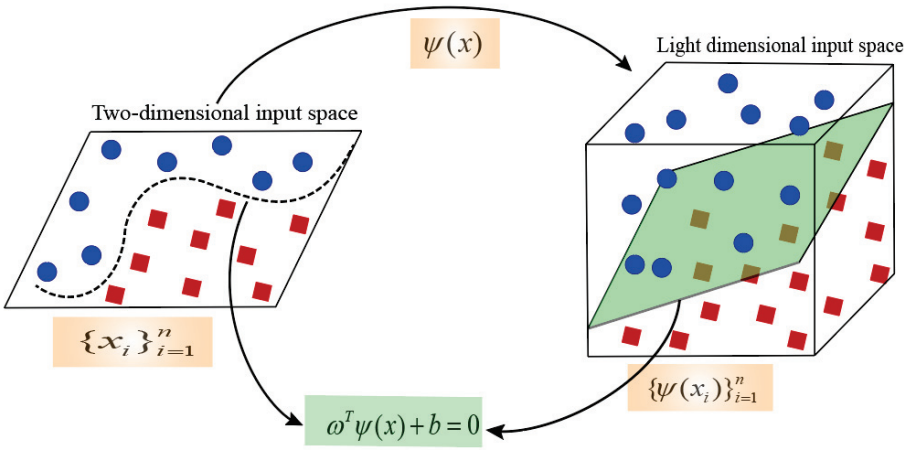

Figure 2. The non-linearly separable problem.

Recently, the SVM and non-linear SVM have been employed extensively across various scientific fields, including predicting the compressive strength and properties of fresh high-volume fly ash self-compacting concrete [26], petroleum reservoir properties [27], classification of nailfold capillary images in patients [28], soil total nitrogen, organic carbon, and moisture content [29]. One of the notable advantages of the SVM method is that, unlike neural networks which often settle at local optima, this technique is governed by a convex optimization problem. Additionally, unlike many other machine learning models that require large datasets to generalize well, SVMs are particularly effective with small to medium-sized datasets due to their reliance on support vectors. Support vectors are the critical data points that define the decision boundary, rather than using all data points, which allows SVMs to avoid overfitting when there are limited data. This achieves accurate and reliable predictions, provided the data are representative and well pre-processed. These benefits render the SVM superior to other artificial intelligence methods.

The non-linear SVM utilizes a specifically defined kernel function to address non-linear regression challenges. Commonly used kernels include the d-order polynomial kernel and the RBF (Gaussian) kernel, among others.

The d-order polynomial kernel is referred to as Function 1, while the support vector machine, functioning as a d-order polynomial classifier, is termed Function 2. Here, d is a parameter determined by the user, making the d-order polynomial kernel a global kernel [25].

$$K(x_i \cdot x) = [(x \cdot x_i) + \gamma]^d \tag{1}$$

$$f(x) = \operatorname{sgn}\left\{\sum_{i=1}^{l} y_i a_i [(x \cdot x_i) + \gamma]^d + b\right\} \tag{2}$$

The RBF (Gaussian) kernel is referred to as Function 3, and the support vector machine employing this kernel is classified as Function 4 [25].

$$K(x_i \cdot x) = \exp(-\gamma \|x - x_i\|^2) \tag{3}$$

$$f(x) = \operatorname{sgn}\left\{\sum_{i=1}^{l} y_i a_i \exp(-\gamma \|x - x_i\|^2) + b\right\} \tag{4}$$

The sigmoid kernel is defined as Function 5, and the corresponding support vector machine operates as a perceptron with hidden layers, where the number of nodes in each hidden layer is automatically determined by the algorithm [25].

$$K(x_i \cdot x) = \tanh[\gamma(x - x_i) + c] \tag{5}$$

In this paper, the d-order polynomial kernel, the RBF (Gaussian) kernel, and the sigmoid kernel have been utilized to predict the complex modulus of various asphalt binders. The performance of the proposed models is evaluated using the root-mean squared error (RMSE) [25].

$$RMSE = \sqrt{\frac{1}{n}\sum_{i=1}^{n}(t_i - o_i)^2} \tag{6}$$

3. Material and Experiment

3.1. Obtaining Asphalt SARA Properties

To predict the complex modulus and phase angle of asphalt binder using SARA analysis, 36 distinct types of asphalt binders were selected. The SARA properties of these binders were determined through thin-layer chromatography with flame ionization detection (TLC-FID), a technique commonly employed for analyzing components in crude oil, heavy oil, residual oil, wax, and lubricating oil asphalt. The detailed testing steps and analysis methods are described in reference [30]. The process is carried out through the following specific steps:

(1) Separation of Saturates, Aromatics, Resins, and Asphaltenes: A 0.3 g sample of asphalt is dissolved in 30 mL of n-heptane, with gentle swirling until complete dissolution. A 1 mL aliquot of the solution is then added to a packed column and allowed to soak naturally. Successive rinsing with four different solvents is performed to elute the individual components from the column, yielding solutions of saturates, aromatics, resins, and asphaltenes in sequence.

(2) Spotting: A 0.6 mL aliquot of each of the saturates, aromatics, resins, and asphaltenes solutions is applied to the appropriate positions on a chromatographic rod. Each solution is spotted 15 times, after which the rod is dried for 5 min.

(3) Chromatographic Analysis: The dried chromatographic rod is placed in the TLC-FID system, where it is subjected to a hydrogen flame at a constant rate. The combustion produces electrons, which are converted into electrical signals and subsequently recorded on the display.

(4) Spectral Analysis: The mass fraction of each component—saturates, aromatics, resins, and asphaltenes—is determined by integrating the corresponding peak areas from the resulting spectra.

The SARA data for the 36 asphalt binders are presented in Table 1.

The colloidal index (Ic) of asphalt is an important parameter that reflects the stability of the colloidal system in asphalt. The Ic provides insight into the balance between SARA, especially the relationship between the dispersed phase (asphaltenes and saturate), and the stabilizing components (resins and aromatics). The Ic helps evaluate the stability of the asphalt binder. Ic represents the ratio of the sum of asphaltenes and saturate to the sum of resins and aromatics. The proportion of heavy component (HC) in asphalt refers to the relative content of its weight components, primarily asphaltenes and resins. These heavy fractions significantly influence the physical and mechanical properties of asphalt, such as stiffness, viscosity, and aging resistance. A high proportion of heavy component increases stiffness but reduces flexibility. A low proportion improves flexibility but may reduce the binder's ability to resist permanent deformation and rutting. Therefore, this

study uses the test results of the four asphalt components to calculate the colloidal index and the proportion of heavy fractions, analyzing the effect of the colloidal index and heavy fraction ratio on the dynamic mechanical properties of asphalt.

Table 1. The SARA of 36 asphalt binders obtained by TLC-FID.

Asphalt Binder	Asphaltenes	Resins	Aromatics	Saturates
1	5.82	37.60	34.11	22.48
2	7.60	39.96	33.26	19.19
3	11.34	50.39	26.20	12.06
4	8.06	40.83	36.10	15.01
5	11.82	43.30	30.92	14.96
6	14.00	47.08	24.96	13.96
7	11.82	43.30	34.92	9.96
8	12.73	43.87	26.40	17.01
9	17.14	43.50	26.30	13.06
10	3.80	37.88	13.33	44.99
11	3.30	52.88	12.73	31.09
12	2.37	55.31	11.49	30.83
13	3.75	42.95	22.71	30.59
14	3.99	43.60	23.95	28.46
15	2.98	56.21	13.77	27.04
16	4.55	46.72	20.91	27.59
17	4.92	50.60	18.95	25.46
18	5.30	59.31	15.77	20.04
19	3.33	50.14	23.75	22.78
20	3.44	54.41	18.81	23.34
21	4.34	57.89	16.88	20.88
22	8.32	30.76	46.66	14.26
23	19.05	34.21	35.88	10.86
24	11.51	36.03	36.96	15.50
25	4.14	39.89	25.46	30.60
26	4.57	46.87	17.24	31.32
27	4.83	49.39	13.41	32.37
28	4.74	20.67	54.26	20.36
29	7.31	27.05	47.98	17.56
30	6.59	42.31	39.36	11.80
31	7.07	41.10	39.02	12.82
32	10.79	39.70	37.53	11.98
33	14.51	45.61	27.51	12.38
34	6.21	31.97	46.65	15.16
35	9.06	39.83	36.10	15.01
36	11.18	48.49	26.64	13.69

3.2. The Complex Modulus and Phase Angle of Asphalt

The complex modulus and phase angle of asphalt binders were measured using an AR2000 dynamic shear rheometer (DSR) manufactured by TA Corporation (Singapore). Initially, linear amplitude sweep (LAS) tests were conducted on the asphalt binders to ensure the applied shear strain remained within the linear viscoelastic interval. Subsequently, a temperature–frequency sweep was performed to determine the complex modulus and phase angle of various asphalt binders at temperatures ranging from 20 °C to 70 °C and frequencies from 0.1 to 100 Hz. Each asphalt binder was tested in three replicates. The construction of the complex modulus and phase angle master curve was based on the least squares function of Microsoft Excel. The complex modulus and phase angle of 36 asphalt binders at three different frequencies are displayed in Table 2.

Table 2. The complex modulus and phase angle of 36 asphalt binders at three different frequencies.

Asphalt Binder	High Frequency 1000 Hz		Medium Frequency 10 Hz		Low Frequency 0.001 Hz	
	G*/MPa	δ/°	G*/Pa	δ/°	G*/Pa	δ/°
1	12,153,900	52.59	136,842	77.56	68.9116	83.66
2	22,132,700	44.40	277,622	70.47	244.471	83.05
3	35,882,600	36.76	1,292,990	57.96	853.304	84.42
4	14,140,100	49.72	202,373	75.84	113.283	86.38
5	29,654,100	42.36	432,385	68.53	244.471	83.05
6	42,821,600	36.17	1,055,650	61.04	956.679	83.62
7	25,577,100	44.45	423,659	72.91	198.272	86.31
8	45,880,000	39.31	584,782	67.19	332.298	87.11
9	50,137,900	32.15	1,450,670	56.77	198.272	86.31
10	7,140,780	59.22	75,939.9	75.86	68.0887	83.41
11	8,243,620	56.20	133,607	71.04	147.93	83.54
12	13,505,900	49.11	262,270	63.91	68.0887	83.41
13	11,211,000	55.56	137,179	74.15	118.895	83.10
14	13,439,600	52.11	182,702	69.11	219.238	84.88
15	21,567,800	49.63	365,054	54.93	439.621	82.17
16	10,230,400	53.27	179,856	73.62	174.351	85.61
17	19,541,600	46.35	278,463	69.83	237.870	83.55
18	30,234,800	42.69	432,670	61.37	539.773	83.59
19	9,635,470	52.23	123,226	75.66	76.5012	86.37
20	16,329,100	46.63	279,415	70.11	187.791	84.46
21	28,826,400	38.43	609,089	60.59	716.599	83.57
22	7,790,010	53.99	107,880	76.06	73.4251	84.16
23	12,362,200	48.46	235,566	70.37	157.201	84.89
24	32,252,100	38.60	597,492	60.76	693.457	83.32
25	2,981,530	47.10	90,249.4	59.67	111.437	76.88
26	4,859,010	45.10	224,960	50.34	151.374	75.21
27	10,297,600	32.28	1,029,875	46.27	1241.64	70.88
28	13,650,500	55.09	147,156	77.74	77.9307	80.41
29	14,262,400	49.10	203,440	72.11	166.515	86.55
30	28,648,000	43.43	747,156	77.74	453.370	84.93
31	21,946,300	46.23	186,655	74.64	146.431	84.48
32	34,475,700	41.08	283,855	70.85	225.771	86.60
33	42,657,900	36.32	944,482	59.38	1106.84	83.96
34	9,370,620	47.86	95,010.3	75.28	73.5107	79.66
35	20,055,600	49.63	225,000	69.17	160.541	83.71
36	25,130,600	38.64	693,841	56.39	1228.19	81.14

4. Result and Discussion

4.1. Relation Between the Single Component, Complex Modulus, and Phase Angel of Asphalt

4.1.1. Relation Between the Single Component, Complex Modulus, and Phase Angel of Asphalt at Low Frequency

To fully comprehend the impact of SARS on the rheological properties of asphalt binders—specifically complex modulus and phase angle at varying temperatures—we selected three different reduced frequencies from the complex modulus and phase angle master curves: 0.001 Hz, 10 Hz, and 1000 Hz. Low frequency (0.001 Hz) is representative of very slow loading or long-term conditions, which are relevant for simulating the behavior of asphalt binders under low-stress, long-term loading situations, such as those encountered in pavement design and analysis of aging or fatigue-related issues. Intermediate frequency (10 Hz) corresponds to typical traffic loading frequencies, which are commonly observed in real-world conditions where traffic loads are applied at moderate speeds. It is often used

in studies to simulate the dynamic response of asphalt under normal service conditions. High frequency (1000 Hz) is used to simulate fast loading conditions that may occur during high-speed traffic or in laboratory settings where short-term, high-rate stresses are applied. It is also relevant for assessing the viscoelastic behavior of asphalt binders under rapidly changing conditions. These frequencies were selected to cover a broad range of practical loading scenarios, thus enhancing the relevance and applicability of our findings to real-world conditions in asphalt pavement performance analysis.

It was observed that the SARA contents exhibit non-linear influence patterns on the complex modulus and phase angle of asphalt at low frequencies (0.001 Hz), as shown in Figure 3. The presence of asphaltenes, resins, aromatics, and saturates significantly affects the rheological properties at low frequencies, with no clear correlation between the SARA contents and either complex modulus or phase angle. These complex interactions are challenging to describe precisely with mathematical formulas and are difficult to determine using traditional mathematical methods such as linear equations. However, a notable relationship exists between the ratio of heavy components and both the complex modulus and phase angle; specifically, an increase in the ratio of heavy components leads to a significant increase in complex modulus and a decrease in phase angle. Similarly, like the relationship between SARA components and rheological properties, the colloidal instability index also shows no specific correlation with the rheological properties of asphalt binders.

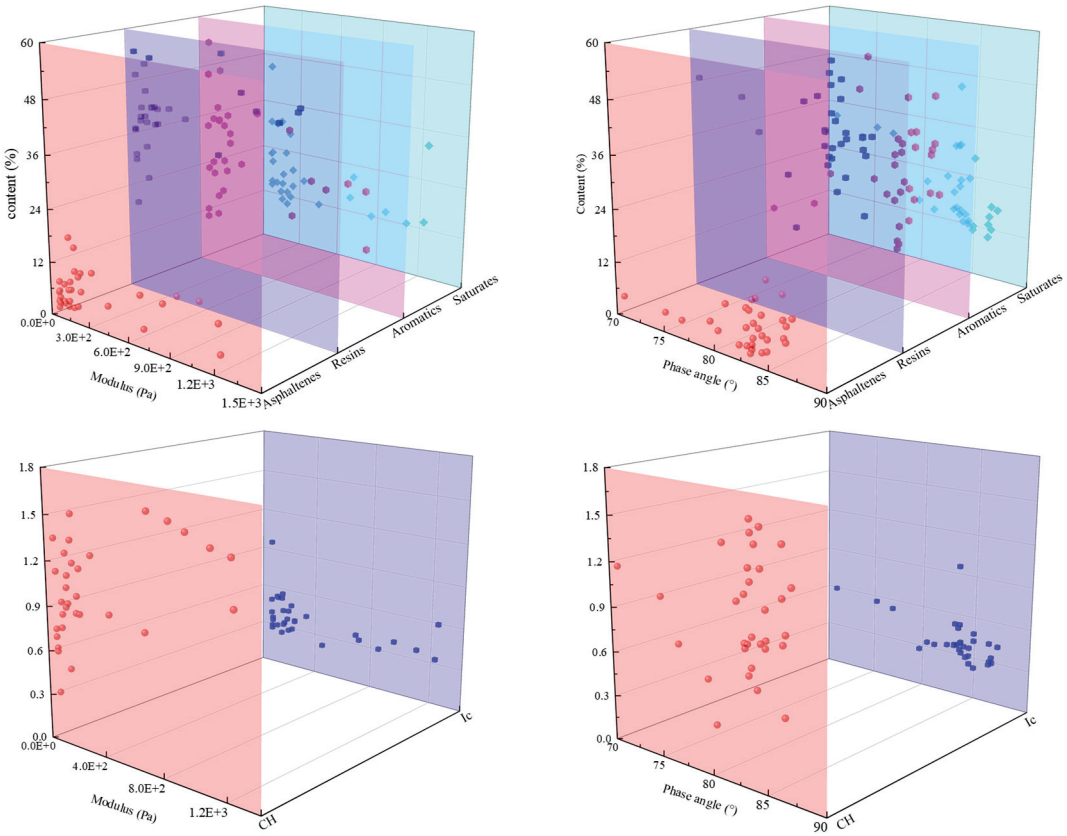

Figure 3. Relationship between the SARA, HC, Ic, and the complex modulus and phase angle of asphalt binder at low frequency.

4.1.2. Relation Between the Single Component and Complex Modulus and Phase Angel of Asphalt at Medium Frequency

The relationships between the SARA, HC, Ic, and the complex modulus, together with the phase angle of asphalt at medium frequency (10 Hz), are illustrated in Figure 4. Although there appears to be no distinct correlation between the content of asphaltenes, resins,

and aromatics and the complex modulus of asphalt at medium frequency, the complex modulus decreases as the saturates increase. Furthermore, the relationship between the SARA components of asphalt and its phase angle is complex, with no evident correlation between them. Regarding the comprehensive indicators of asphalt such as HC and Ic, it is evident that the complex modulus increases and the phase angle decreases with an increase in HC. However, the relationships between Ic, the complex modulus, and the phase angle remain ambiguous.

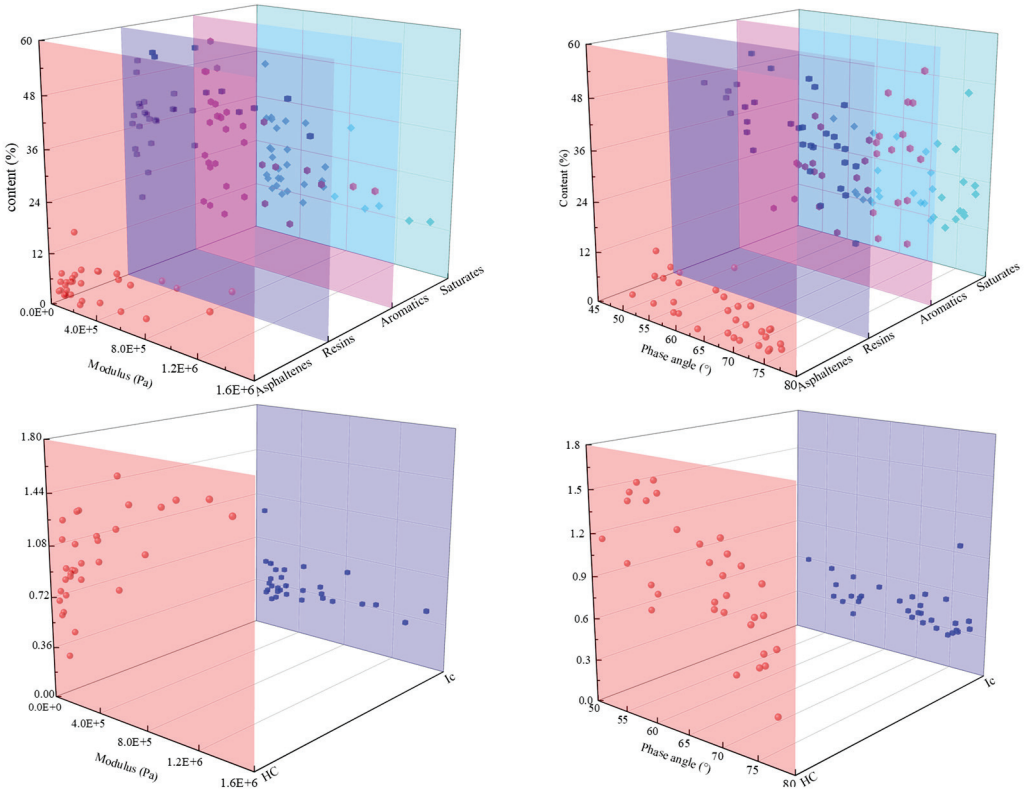

Figure 4. Relation between the SARA, HC, Ic, and the complex modulus and phase angle at medium frequency of asphalt binder.

4.1.3. Relation Between the Single Component and Complex Modulus and Phase Angel of Asphalt at High Frequency

The relationships between SARA, HC, Ic, and the complex modulus, together with the phase angle of asphalt at high frequency (1000 Hz), are depicted in Figure 5. It appears there is no clear relationship between the contents of asphaltenes, resins, and aromatics; however, the complex modulus decreases with an increase in saturates. The relationship between the SARA components of asphalt and its phase angle is complex, and SARA shows no obvious correlation with the phase angle at high frequency, similar to its behavior at low and medium frequencies. For the comprehensive indicators of asphalt such as HC and Ic, it is evident that the complex modulus increases and the phase angle decreases with HC, but the relationships between Ic, the complex modulus, and the phase angle remain unclear.

To summarize, despite the significant influence of SARA components on the rheological properties of asphalt, the complex interactions between these components, as well as the influence of external factors such as temperature and frequency, complicate the establishment of clear linear correlations. The SARA fractions—saturates, aromatics, resins, and asphaltenes—interact in non-linear and sometimes synergistic ways, which can obscure direct relationships with the complex modulus and phase angle. Additionally, the rheological behavior of asphalt binders is highly sensitive to temperature and frequency,

with these factors modulating the viscoelastic properties in ways that cannot always be captured by simple linear models. Consequently, while the individual SARA components play a crucial role in determining the overall mechanical performance, their effects are often overshadowed by these dynamic and multi-factorial interactions. Therefore, regarding the research subjects in this study—the SARA of the 36 types of asphalt binders, which cover nearly all main types of asphalt binders in asphalt pavement construction—the most significant indicators of asphalt binders show no specific relationship with the content of asphaltenes, resins, or aromatics, or the colloidal index Ic. It is only confirmed that the complex modulus increases as saturates decrease and heavy components increase. The remaining three components are interrelated and jointly influence the complex modulus and phase angle of asphalt binders by forming a colloidal structure. This suggests that the impact of SARA components on the complex modulus and phase angle is intricate and cannot be simplified into simple mathematical expressions. Alternative methods should be explored to study the rheology of asphalt from the perspective of SARA components.

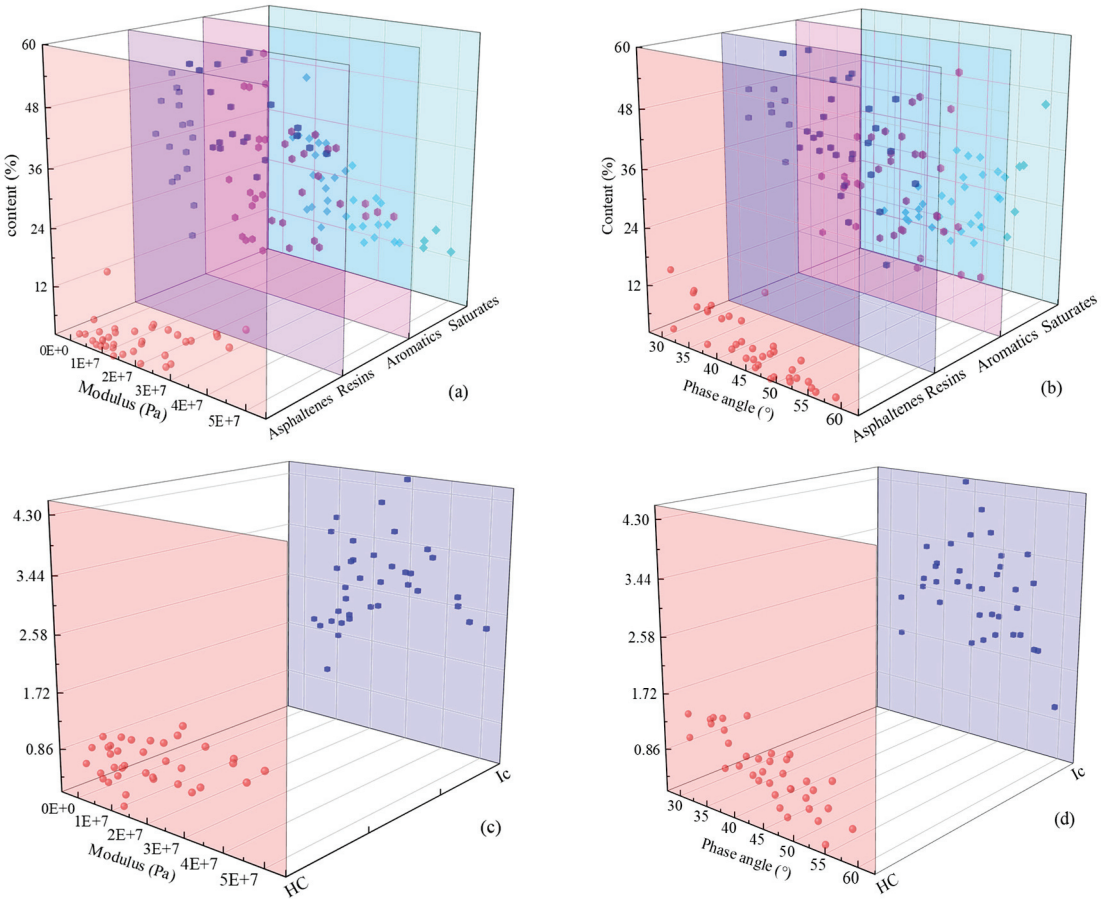

Figure 5. Relationship between the SARA contents, HC, Ic, and the complex modulus and phase angle of asphalt binder at high frequency. Relationship at high frequency: (**a**) the SARA contents and the complex modulus; (**b**) the SARA contents and phase angle of asphalt binder; (**c**) the HC and the complex modulus; (**d**) the HC and phase angle of asphalt binder.

4.2. Predicting the Complex Modulus and Phase Angle and Building the Master Curve

4.2.1. Predicting the Complex Modulus and Phase Angle Using the Quadratic Polynomial and Non-Linear SVM

The quadratic polynomial and non-linear SVM with both the sigmoid kernel and the RBF (Gaussian) kernel were utilized to predict the complex modulus and phase angle of asphalt binders based on SARA data, HC, and Ic. Components of asphalt, such as

asphaltenes, resins, aromatics, saturates, heavy components, and the colloidal index, were used as input vectors, and output vectors were derived from experimental results. The performance of the three models in predicting the complex modulus and phase angle is illustrated in Figures 6–8. The accuracy of these predictions was assessed using the correlation coefficient (R^2) and the root-mean squared error (RMSE) in Table 3. The prediction results varied significantly among the models, with RMSE values for the RBF (Gaussian) kernel at 2.6725, 3.5721, and 2.396 for the complex modulus, and 12.1947, 8.2980, and 4.3571 for the phase angle at low, medium, and high frequencies, respectively. For the quadratic polynomial, the RMSE values were 27.9251, 12.3741, and 5.7612 for the complex modulus, and 100.5855, 89.1380, and 7.6577 for the phase angle at the same frequencies. The RMSE values for the sigmoid kernel were 6.8162, 25.7219, and 8.1068 for the complex modulus, and 15.9452, 25.7219, and 19.6127 for the phase angle, respectively. The results demonstrate that the RBF kernel outperforms the quadratic polynomial and non-linear SVM with the sigmoid kernel, indicating its efficacy in predicting the complex modulus of asphalt binders subjected to different frequencies. Additionally, the prediction accuracy for all three models improved with decreasing frequency. The higher accuracy of the RBF kernel in the SVM models can be attributed to its high effectiveness in capturing non-linear relationships in data by mapping the input features into a higher dimensional space. This allows it to model complex patterns that are often present in real-world data, such as the rheological properties of asphalt binders. Also, RBF kernel-based models generally exhibit better generalization compared to other kernels. Its ability to create complex decision boundaries without overfitting makes it more robust and capable of handling noisy or high-dimensional data.

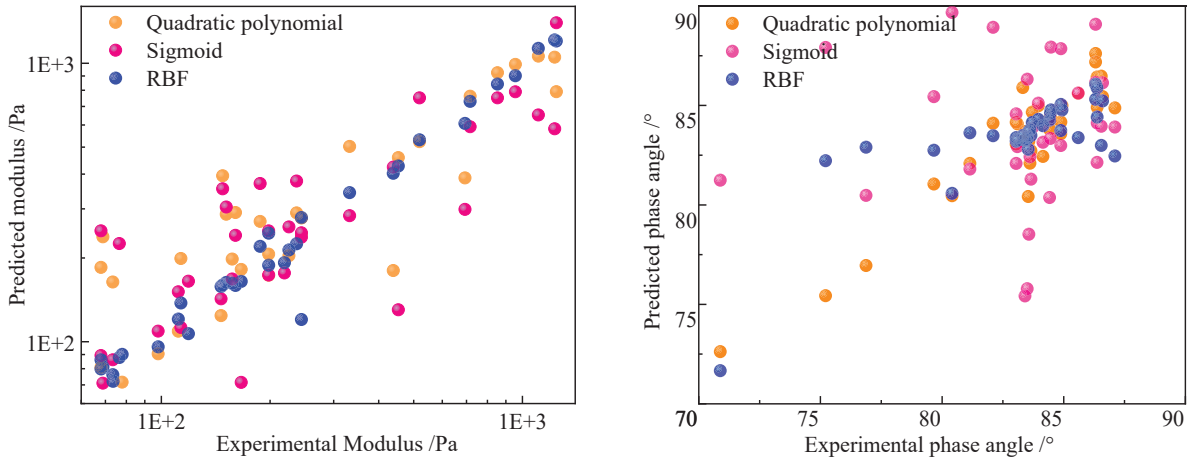

Figure 6. Prediction of the complex modulus and phase angle of asphalt at low frequency using the quadratic polynomial and the SVM with different kernel functions.

However, the RMSE values for predicting phase angle remained relatively high at low frequencies, suggesting that while the non-linear SVM with the RBF kernel is effective for predicting the complex modulus, it is less suitable for predicting the phase angle at low frequencies. Furthermore, the correlation coefficient, R^2, also confirms that the non-linear SVM with the RBF kernel performs better than the quadratic polynomial and the non-linear SVM with the sigmoid kernel.

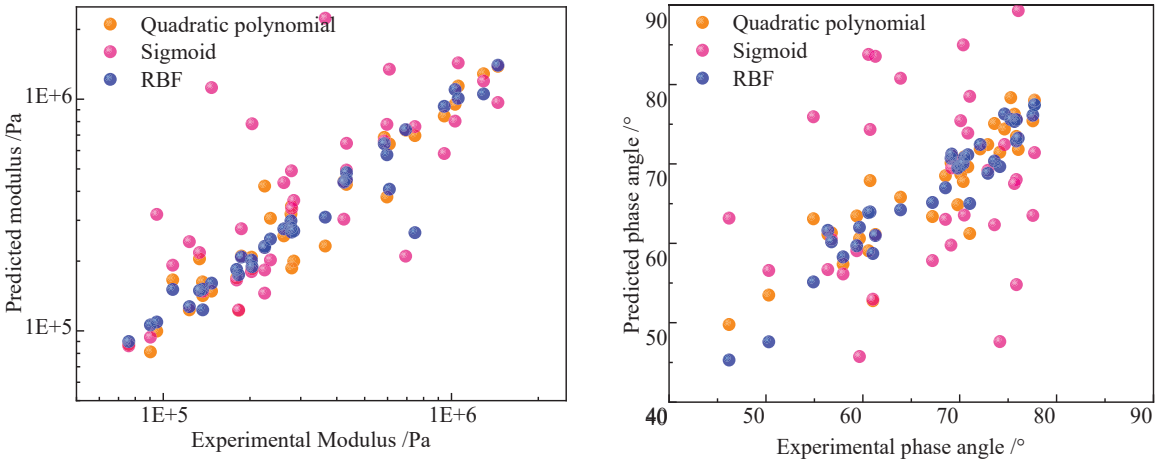

Figure 7. Prediction of the complex modulus and phase angle of asphalt at medium frequency by quadratic polynomial and the SVM with different kernel functions.

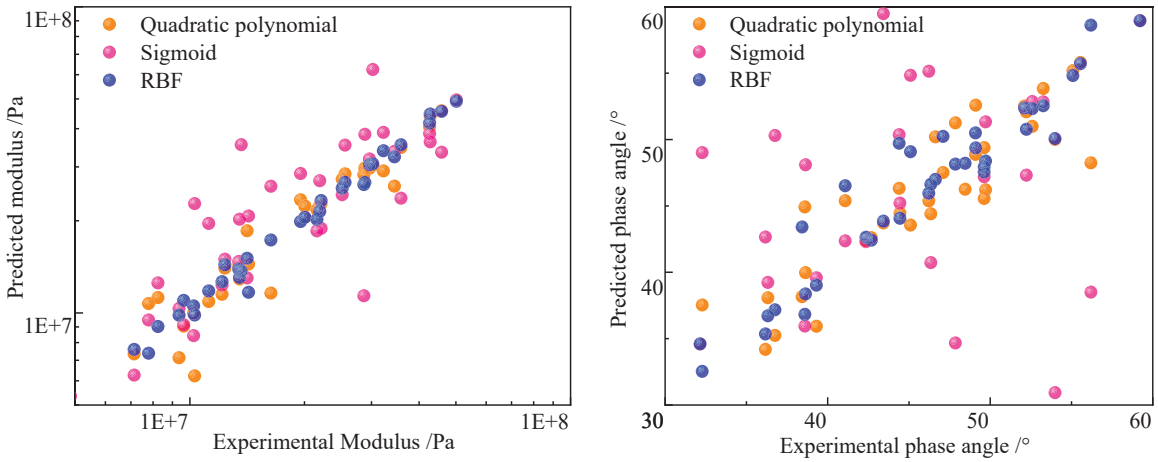

Figure 8. Prediction of the complex modulus and phase angle of asphalt at high frequency by quadratic polynomial and the SVM with different kernel functions.

Table 3. Statistical results of the quadratic polynomial and SVM models trained on collected data.

Frequency /Hz	Experimental Test	Prediction Methods	Statistical Parameters Results R^2	RMSE
0.001	Complex modulus	Polynomial	0.4651	27.9251
		Sigmoid	0.3567	6.8162
		RBF	0.9661	2.6725
	Phase angle	Polynomial	0.2019	100.5855
		Sigmoid	0.2523	15.9452
		RBF	0.8772	12.1947
10	Complex modulus	Polynomial	0.8260	12.3741
		Sigmoid	0.3821	25.7219
		RBF	0.9458	3.5721
	Phase angle	Polynomial	0.5050	89.1380
		Sigmoid	0.2886	11.6129
		RBF	0.8236	8.2980
1000	Complex modulus	Polynomial	0.7461	5.7612
		Sigmoid	0.5273	8.1068
		RBF	0.9785	2.3961
	Phase angle	Polynomial	0.2371	7.6577
		Sigmoid	0.2112	19.6127
		RBF	0.8569	4.3571

4.2.2. Validation of the Non-Linear SVM of the RBF (Gaussian) Kernel

To validate the non-linear SVM with the RBF kernel for predicting the complex modulus and phase angle of asphalt binders at various frequencies, an experimental program was established, and the non-linear SVM of the RBF kernel was tested. Three types of asphalt binders, characterized by their SARA, HC, and Ic values, as shown in Table 4, were selected. The complex modulus and phase angle of the asphalt binders were determined through temperature–frequency sweeps, and the master curves for both were constructed using the least squares method in Microsoft Excel. To assess the accuracy of the non-linear SVM with the RBF kernel, the complex modulus and phase angle at frequencies of 0.001 Hz, 10 Hz, and 1000 Hz were calculated from the SARA, HC, and Ic of the asphalt binders. These points were then plotted and compared with the tested master curves of complex modulus and phase angle to evaluate the reliability of the non-linear SVM with the RBF kernel in predicting the complex modulus and phase angle of asphalt binders. The effectiveness of the non-linear SVM with the RBF kernel in predicting the master curves for complex modulus and phase angle of the asphalt binders can be seen in Figure 9. The results showed that the trained SVM with the RBF kernel successfully learned the relationship between input (SARA component) and output (complex modulus) vectors for different asphalt binders. The predicted complex modulus master curves closely matched the tested results, indicating that using an appropriate input vector for prediction models and finding optimum values of the kernel function using a suitable method can lead to an accurate model capable of predicting the complex modulus of asphalt binders.

Table 4. SARA, HC, and Ic of selected asphalt binders.

Asphalt Binder	Asphaltenes	Resins	Aromatics	Saturates
Sample 1	8.06	40.83	36.10	15.01
Sample 2	17.14	43.50	26.30	13.06
Sample 3	4.34	57.89	16.88	20.88

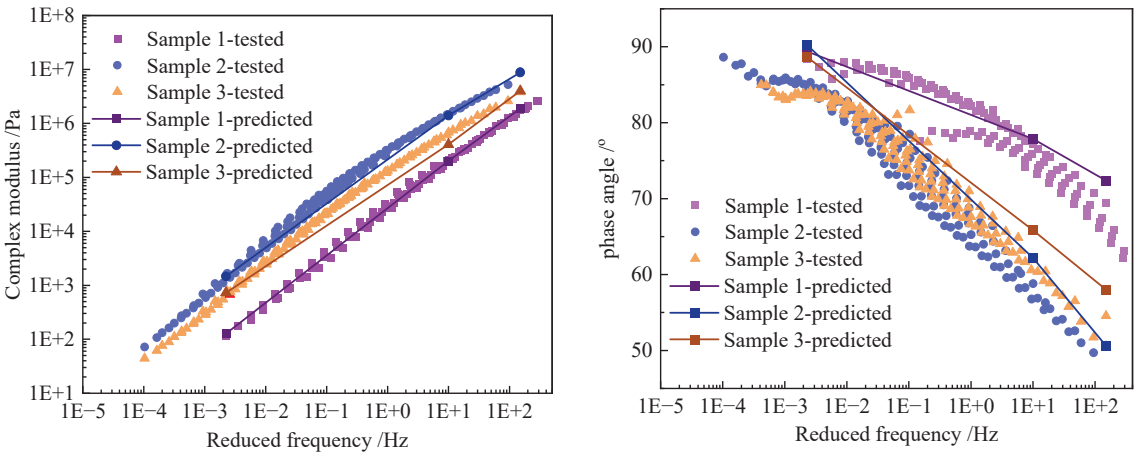

Figure 9. Validation of the SVM for prediction of the complex modulus and phase angle of asphalt binders.

However, the predicted master curves for phase angle significantly deviated from the tested results, especially at low frequencies. This suggests that the SVM with the RBF kernel is unable to accurately predict the phase angle of asphalt binders from SARA, and instead, it only approximates the trend of phase angle changes with frequency.

5. Conclusions

The aim of this research was to explore the relationships between the SARA fraction and the varying mechanical properties of asphalt binders at different temperatures and frequencies. SARA data were collected from 36 asphalt binders to examine their impact on the complex modulus and phase angle at various frequencies. Additionally, the quadratic polynomial and non-linear SVM with the sigmoid kernel and the RBF (Gaussian) kernel were employed to predict the complex modulus and phase angle of asphalt binders based on SARA, and the reliability of these prediction models was evaluated. The following conclusions can be drawn.

1. The content of asphaltenes, resins, aromatics, and saturates demonstrated the most complex effects on the rheological properties at different frequencies, with no clear correlation between SARA components and the complex modulus or phase angle. An increase in the ratio of heavy components led to a significant increase in complex modulus and a decrease in phase angle at each frequency. The colloidal instability index showed no specific relationship with the complex modulus and phase angle of asphalt binders at low, medium, or high frequency.
2. The impact of SARA on the complex modulus and phase angle is intricate and cannot be simplified through straightforward mathematical formulations. Alternative methods should be employed to study the mechanical properties of asphalt based on SARA.
3. The quadratic polynomial and non-linear SVM with both the sigmoid kernel and the RBF (Gaussian) kernel were applied to predict the complex modulus and phase angle of asphalt binders using SARA, the ratio of heavy components, and the colloidal instability index. The results indicate that the RBF kernel performs better than the quadratic polynomial and the non-linear SVM with the sigmoid kernel. Additionally, the accuracy of all three models improved as the frequency decreased. However, despite the high accuracy of the non-linear SVM with the RBF kernel in predicting complex modulus, it was not suitable for predicting the phase angle at low frequencies.
4. The validation of the non-linear SVM with the RBF kernel for predicting the complex modulus and phase angle of asphalt binders demonstrated that the trained SVM effectively learned the relationship between input (SARA component) and output (complex modulus) vectors for different asphalt binders. The predicted complex modulus master curves closely matched the tested results. However, the predicted master curves for the phase angle deviated significantly from the tested results, particularly at low frequencies. The SVM with the RBF kernel was unable to predict the phase angle of asphalt binders from SARA accurately and merely approximated the trend of phase angle changes with frequency.

Author Contributions: Conceptualization, S.S. and Y.M.; methodology, X.J.; software, D.L.; validation, X.M. and S.Q.; formal analysis, X.M.; funding acquisition, S.S. All authors have read and agreed to the published version of the manuscript.

Funding: This project was supported by Gansu Provincial Science and Technology Plan (23JRRA1375, 21JR7RA786) and Research project of Gansu Provincial Department of Transportation (2022-22, 2022-33), Lanzhou Youth Science and Technology Talent Innovation Project (2023-QN-102), China Postdoctoral Science Foundation Funded Project (Project No. 2020M683401), the Natural Science Basis Research Plan in Shaanxi Province of China (No. 2021JQ-262), the Fundamental Research Funds for the Central Universities of China (No. 300102311105).

Institutional Review Board Statement: Not applicable.

Informed Consent Statement: Not applicable.

Data Availability Statement: The data supporting the findings of this study are contained within the article.

Acknowledgments: The authors gratefully acknowledge support from Chang'an University and Scientific Observation and Research Base of Transport Industry of Long Term Performance of Highway Infrastructure in Northwest Cold and Arid Regions.

Conflicts of Interest: Author Shanglin Song was employed by the company Gansu Provincial Highway Development Group Co., Ltd. Author Xiaoqiang Jiang and Dengzhou were employed by the company Gansu Hengtong Road and Bridge Engineering Co., Ltd. The remaining authors declare that the research was conducted in the absence of any commercial or financial relationships that could be construed as a potential conflict of interest.

References

1. Weigel, S.; Stephan, D. Relationships between the chemistry and the physical properties of bitumen. *Road Mater. Pavement Des.* **2017**, *19*, 1636–1650. [CrossRef]
2. Wang, J.; Wang, T.; Hou, X.; Xiao, F. Modelling of rheological and chemical properties of asphalt binder considering SARA fraction. *Fuel* **2019**, *238*, 320–330. [CrossRef]
3. Mirwald, J.; Werkovits, S.; Camargo, I.; Maschauer, D.; Hofko, B.; Grothe, H. Understanding bitumen ageing by investigation of its polarity fractions. *Constr. Build. Mater.* **2020**, *250*, 118809. [CrossRef]
4. Yang, C.; Xie, J.; Wu, S.; Amirkhanian, S.; Zhou, X.; Ye, Q.; Yang, D.; Hu, R. Investigation of physicochemical and rheological properties of SARA components separated from bitumen. *Constr. Build. Mater.* **2020**, *235*, 117437. [CrossRef]
5. Wang, J.; Xiao, F. Rheological Properties of Derivative Fractions Composed of Aromatics, Resins, and Asphaltenes. *J. Test. Eval.* **2022**, *50*, 1572–1586. [CrossRef]
6. Xu, Y.; Zhang, E.; Shan, L. Effect of SARA on Rheological Properties of Asphalt Binders. *J. Mater. Civ. Eng.* **2019**, *31*, 04019086. [CrossRef]
7. Leite, L.F.M.; Osmari, P.H.; Aragão, F.T.S. Rheological indexes for asphalt binders considering different aging conditions: Evaluation and correlations with performance. *Constr. Build. Mater.* **2022**, *338*, 127549. [CrossRef]
8. Xiao, M.M.; Fan, L. Ultraviolet aging mechanism of asphalt molecular based on microscopic simulation. *Constr. Build. Mater.* **2022**, *319*, 126157. [CrossRef]
9. Ghasemirad, A.; Bala, N.; Hashemian, L. High-Temperature Performance Evaluation of Asphaltenes-Modified Asphalt Binders. *Molecules* **2020**, *25*, 3326. [CrossRef]
10. Wang, T.; Wang, J.; Hou, X.; Xiao, F. Effects of SARA fractions on low temperature properties of asphalt binders. *Road Mater. Pavement Des.* **2019**, *22*, 539–556. [CrossRef]
11. Hofer, K.; Mirwald, J.; Bhasin, A.; Hofko, B. Low-temperature characterization of bitumen and correlation to chemical properties. *Constr. Build. Mater.* **2023**, *366*, 130202.
12. Zhang, E.; Shan, L.; Qi, X.; Wang, X.; Fan, Y. Investigating the relationship between chemical composition and mechanical properties of asphalt binders using atomic force microscopy (AFM). *Constr. Build. Mater.* **2022**, *343*, 128001. [CrossRef]
13. Zhao, K.; Wang, Y.; Li, F. Influence of ageing conditions on the chemical property changes of asphalt binders. *Road Mater. Pavement Des.* **2019**, *22*, 653–681. [CrossRef]
14. Sun, W.; Wang, H. Molecular dynamics simulation of nano-crack formation in asphalt binder with different SARA fractions. *Mol. Simul.* **2022**, *48*, 789–800. [CrossRef]
15. Salehfard, R.; Behbahani, H.; Dalmazzo, D.; Santagata, E. Effect of colloidal instability on the rheological and fatigue properties of asphalt binders. *Constr. Build. Mater.* **2021**, *281*, 122563. [CrossRef]
16. Li, J.; Huang, X.; Zhang, Y.; Xu, M. Bitumen Colloidal and Structural Stability Characterization. *Road Mater. Pavement Des.* **2011**, *10*, 45–59. [CrossRef]
17. Guo, M.; Liang, M.; Fu, Y.; Sreeram, A.; Bhasin, A. Average molecular structure models of unaged asphalt binder fractions. *Mater. Struct.* **2021**, *54*, 173. [CrossRef]
18. Wang, P.; Dong, Z.-J.; Tan, Y.-Q.; Liu, Z.-Y. Investigating the Interactions of the Saturate, Aromatic, Resin, and Asphaltene Four Fractions in Asphalt Binders by Molecular Simulations. *Energy Fuels* **2015**, *29*, 112–121. [CrossRef]
19. Eberhardsteiner, L.; Füssl, J.; Hofko, B.; Handle, F.; Hospodka, M.; Blab, R.; Grothe, H. Micromechanical Description of Bitumen Aging Behavior. In *8th RILEM International Symposium on Testing and Characterization of Sustainable and Innovative Bituminous Materials*; Springer: Dordrecht, The Netherlands, 2016; pp. 411–421.
20. Zhang, C.; Xu, T.; Shi, H.; Wang, L. Physicochemical and pyrolysis properties of SARA fractions separated from asphalt binder. *J. Therm. Anal. Calorim.* **2015**, *122*, 241–249. [CrossRef]

21. Xia, W.; Xu, T. Thermal Characteristics, Kinetic Models, and Volatile Constituents during the Energy Conversion of Bituminous SARA Fractions in Air. *ACS Omega* **2020**, *5*, 20831–20841. [CrossRef] [PubMed]
22. Hu, Z.; Zhang, H.; Wang, S.; Xu, T. Thermal-oxidative aging mechanism of asphalt binder based on isothermal thermal analysis at the SARA level. *Constr. Build. Mater.* **2020**, *255*, 119349. [CrossRef]
23. Xia, W.; Wang, S.; Wang, H.; Xu, T. Thermal effects of asphalt SARA fractions, kinetic parameter calculation using isoconversional method and distribution models. *J. Therm. Anal. Calorim.* **2020**, *146*, 1577–1592. [CrossRef]
24. Do, T.-N. Non-linear Classification of Massive Datasets with a Parallel Algorithm of Local Support Vector Machines. In *Advanced Computational Methods for Knowledge Engineering: Proceedings of 3rd International Conference on Computer Science, Applied Mathematics and Applications-ICCSAMA 2015, Metz, France, 11–13 May 2015*; Springer: Cham, Switzerland, 2015; pp. 231–241.
25. Zhao, H.; Yao, Y.; Liu, Z. A Classification Method Based on Non-linear SVM Decision Tree. In Proceedings of the Fourth International Conference on Fuzzy Systems and Knowledge Discovery (FSKD 2007), Haikou, China, 24–27 August 2007; IEEE: Piscataway, NJ, USA, 2007; pp. 635–638.
26. Azimi-Pour, M.; Eskandari-Naddaf, H.; Pakzad, A. Linear and non-linear SVM prediction for fresh properties and compressive strength of high volume fly ash self-compacting concrete. *Constr. Build. Mater.* **2020**, *230*, 117021. [CrossRef]
27. Otchere, D.A.; Ganat, T.O.A.; Gholami, R.; Ridha, S. Application of supervised machine learning paradigms in the prediction of petroleum reservoir properties: Comparative analysis of ANN and SVM models. *J. Pet. Sci. Eng.* **2021**, *200*, 108182. [CrossRef]
28. Nivedha, R.; Brinda, M.; Suma, K. Classification of Nailfold Capillary Images in Patients with Hypertension Using Non-linear SVM. In Proceedings of the 2016 International Conference on Circuits, Controls, Communications and Computing (I4C), Bangalore, India, 4–6 October 2016; IEEE: Piscataway, NJ, USA, 2016; pp. 1–5.
29. Morellos, A.; Pantazi, X.-E.; Moshou, D.; Alexandridis, T.; Whetton, R.; Tziotzios, G.; Wiebensohn, J.; Bill, R.; Mouazen, A.M. Machine learning based prediction of soil total nitrogen, organic carbon and moisture content by using VIS-NIR spectroscopy. *Biosyst. Eng.* **2016**, *152*, 104–116. [CrossRef]
30. Ma, X.; Ma, X.; Wang, Z.; Song, S.; Sheng, Y. Investigation of changing SARA and fatigue properties of asphalt bitumen under ageing and analysis of their relation based upon the BP neural network. *Constr. Build. Mater.* **2023**, *394*, 132163. [CrossRef]

coatings

MDPI

Article

Assessment of the Wettability and Mechanical Properties of Stearic-Acid-Modified Hydrophobic Cementitious Materials

Xuhao Wang [1], Wenxiao Zhang [1], Yuan Wang [1], Hongke Wu [2,*], Dunzhu Danzeng [3] and Yahong Meng [4,*]

[1] School of Highway, Chang'an University, Xi'an 710064, China; wangxh@chd.edu.cn (X.W.); zhangwx023@163.com (W.Z.); wangyuan@chd.edu.cn (Y.W.)
[2] Longxi County Highway Management Station, Dingxi 748100, China
[3] Xizang Gaozheng Building Materials Company, Lhasa 851400, China; 13582838001@163.com
[4] Gansu Yuanlong Road and Bridge Mechanized Highway Engineering Co., Ltd., Lanzhou 730030, China
* Correspondence: wangyize1111@gmail.com (H.W.); 13919118937@163.com (Y.M.); Tel.: +86-18793100077 (H.W.); +86-13919118937 (Y.M.)

Abstract: Moisture is a critical factor leading to the deterioration of concrete structures. Hydrophobic cement-based materials, with their excellent waterproof performance, hold significant application value in humid, coastal, and cold environments. This study employed stearic acid (STA, $CH_3(CH_2)_{16}COOH$) as a hydrophobic agent dissolved in anhydrous ethanol using ultrasonication to create an STA–ethanol solution. In addition, the ball-milling method was used to mix STA with tuff powder (TP) to prepare hydrophobic modified tuff powder (MTP). This study investigated the effects of the STA content, water–cement (w/c) ratio, cement–sand (c/s) ratio, the replacement rate, and addition method of TP and MTP on the wettability (contact angle and sorptivity) and compressive strength of the mortar. The effects of the STA on the cement hydration were explored by microanalysis techniques, such as SEM, XRD, and FTIR, and the modification method with the best effect was recommended based on a gray correlation degree analysis. The results indicate that the STA could be successfully grafted into the mortar without affecting the types of cement hydration products. When using the STA–ethanol solution for hydrophobic modification, adding 0.9% STA by weight increased the mortar contact angle to 69.5° and reduced the sorptivity by 22%, while the 28-day compressive strength was decreased. When the w/c ratio was 0.5, the contact angle rose with the increase in the replacement rate of MTP, while the sorptivity and compressive strength decreased. The grey relational analysis showed that at a w/c ratio of 0.4, the STA–ethanol solution was a more effective modification method in terms of reducing the mortar sorptivity.

Keywords: cementitious materials; stearic acid; tuff powder; wettability; mechanical properties

1. Introduction

Concrete, as one of the most common materials in the construction field, is prone to damage when exposed to natural environments for a long time due to the corrosive effects of water, CO_2, chlorides, and sulfates [1–3]. To prevent salt solutions and moisture from penetrating into the concrete structure and causing damage, a common method is to reduce the water–cement ratio or add additional cementitious materials to the cement-based materials, thereby improving the density and reducing the porosity [4]. However, these approaches offer limited success in improving the durability and can heighten the risk of cracking post-hardening [5]. The hydrophobic modification of cement-based materials

has also been explored to enhance concrete durability. This technique fundamentally operates by coating the surface particles of concrete with hydrophobic substances that form a water-repellent barrier, significantly diminishing the potential for water, salt, and chemical ingress, thereby extending the service life of the concrete [6–8]. Nonetheless, surface treatments are prone to failure due to cracking in the concrete or the aging and peeling of the coating caused by environmental factors, indicating their relatively poor mechanical stability [9]. In contrast, integral hydrophobic modification presents higher mechanical stability, typically achieved through the direct incorporation of hydrophobic agents or the addition of pre-treated hydrophobic materials [10,11]. Despite some existing studies on integral hydrophobic modification materials, the research still faces various challenges, such as limited preparation methods, complex preparation processes, and a restricted variety of hydrophobic materials.

With the gradual depletion of natural sand and gravel resources, the adoption of manufactured sand in lieu of river sand for concrete casting has become an inevitable trend for the future development of concrete applications [12,13]. In our country, tuff is extensively distributed and serves as one of the primary raw materials for the production of manufactured sand. However, the production process generates a considerable amount of tuff powder (TP) with particle sizes smaller than 0.075 mm. This TP is classified as solid waste, which is predominantly managed through on-site piling and landfilling, thereby occupying land resources and severely polluting the water and air [14,15]. Numerous scholars explored the reutilization of TP, and studies indicate that TP exhibits certain pozzolanic activity, making it suitable as an admixture in concrete [16,17]. Additionally, research revealed that STA can be co-ground with paper sludge ash and ground granulated blast furnace slag to produce hydrophobic powders [18,19]. Thus, co-grinding STA with TP to create hydrophobic powder and incorporating it into cement-based materials not only conserves cementitious materials but also enhances the concrete durability. This method holds significant importance for improving the utilization of solid waste, reducing carbon emissions, and extending the service life of concrete.

The literature indicates that hydrophobic modification may influence the mechanical properties of cement-based materials. Surface hydrophobic modifications primarily adhere to the surface or penetrate the superficial layer of cement-based materials, thereby exerting a minimal impact on the internal structure of the material and consequently having a negligible effect on its strength [20]. In contrast, when hydrophobic agents are incorporated throughout the material, they typically interact with the cement matrix to form hydrophobic groups, subsequently affecting the hydration process, and thereby imparting a more pronounced effect on the mechanical strength of the cement-based materials [21,22]. However, the addition of certain micro-nano particles or pozzolanic particles to hydrophobic agents can mitigate the strength reduction or even enhance the strength, achieving an optimal balance of hydrophobicity and mechanical performance. Wong et al. [18] found that by using STA dry-milled modified paper sludge ash to partially replace cement in the preparation of hydrophobic mortar, the addition of an appropriate amount of hydrophobic PSA could enhance both the 3d and 28d strengths of the mortar. In terms of mechanical properties, directly adding hydrophobic agents tends to adversely affect the strength of cement-based materials. In contrast, employing surface modification or integral modification with pretreated hydrophobic materials results in less pronounced negative impacts on strength. Therefore, based on the current state of research, integral hydrophobic modification is considered an ideal approach to enhancing the durability of cement-based materials. However, the development and application of superhydrophobic materials capable of imparting superhydrophobic performance throughout the entire thickness of the material remain largely unexplored. Additionally, the mechanisms by which hydrophobic modifiers

influence the setting and hardening processes of cement-based materials are still unclear and require further investigation.

In terms of selecting hydrophobic materials, it was observed that silicone-based substances and fluorinated chemicals are widely utilized. However, silane- and siloxane-based hydrophobic agents, due to their relatively high cost, cannot be extensively adopted, while fluorinated chemicals are now recognized as toxic pollutants with severe environmental repercussions. In contrast, stearic acid presents numerous advantages. First, as a naturally occurring compound found in various foods, it is characterized by low toxicity, making it a safe and environmentally friendly option for many applications. Second, its affordability renders it an appealing choice for cost-sensitive uses.

Therefore, this study selected tuff manufactured sand as the fine aggregate and employed STA for the hydrophobic modification. Hydrophobic cement-based materials were prepared using two methods: an STA–ethanol solution and the co-grinding of STA with TP. First, the wettability of the two modified cement-based materials was evaluated through contact angle and sorptivity tests. Subsequently, the impact of the two hydrophobic modification methods on the compressive strength of the cement-based materials was investigated. The mechanisms of interaction between the STA and cement-based materials, the resultant products, and their effects on the microstructure of the cement-based materials were explored using scanning electron microscopy (SEM), X-ray diffraction (XRD), and Fourier transform infrared spectroscopy (FTIR). Furthermore, the differences in the performance of the cement-based materials with varying w/c and c/s ratios influenced by the STA were also examined. Finally, the degree of influence of the two modification methods on the performance of the cement-based materials was compared through grey relational analysis.

2. Materials and Methods

2.1. Materials

The cement used was P.O 42.5 supported by a company in Shaanxi Province, China with specific indices detailed in Table 1. The fine aggregate was manufactured sand from tuff, supportd by a company in Gansu Province, China, possessing a fineness modulus of 2.86, with its technical specifications listed in Table 2 and its gradation curve illustrated in Figure 1. TP was obtained by sieving the manufactured sand through a 0.075 mm mesh, which resulted in a content of 2.97%. The chemical composition of the cement and TP can be found in Table 3. The density of anhydrous ethanol at 20 °C ranges from 0.789 to 0.791 g/mL, with the mass fraction of evaporation residue being less than 0.001%.

Table 1. Technical indexes of cement.

Density (g/cm^3)	Cement Standard Consistency (%)	Soundness	Initial Setting Time (min)	Final Setting Time (min)	Flexural Strength (MPa)	Compressive Strength (MPa)
3.06	28.4	Qualified	206	284	5.4	22.3

Table 2. Technical indexes of fine aggregate.

Type	Apparent Density (g/cm^3)	Angularity (s)	Crushing Value (%)	MB Value (g/kg)	Sand Equivalent (%)	Saturated Surface Dry Water Absorption (%)
Tuff manufactured sand	2.82	26.92	6.4	1.4	71	2.06

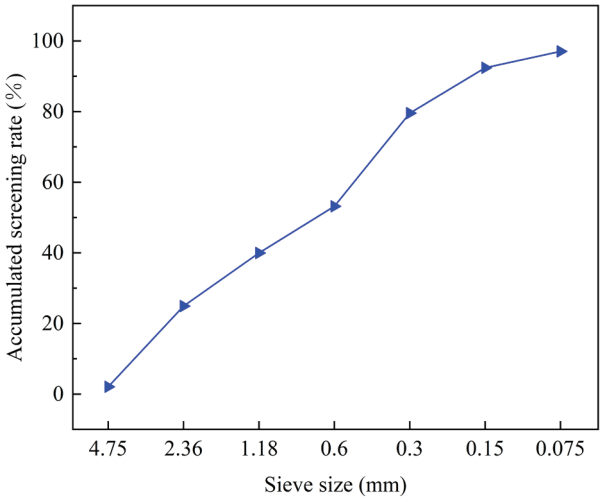

Figure 1. Grading curve of tuff manufactured sand.

Table 3. Chemical composition of cement and TP.

Chemical Composition	Cement (%)	TP (%)
SiO_2	21.20	39.71
TiO_2	1.28	0.86
Al_2O_3	4.85	14.24
Fe_2O_3	2.57	9.78
MnO	0.05	0.18
MgO	3.00	6.95
CaO	54.92	11.39
Na_2O	0.11	1.55
K_2O	0.42	1.64
P_2O_5	0.05	0.23
LOI	3.94	13.64
Total	92.39	100.17

2.2. Experimental Design and Mix Proportions

STA, due to its substantial hydrocarbon chain, is insoluble in water at room temperature, leading to clumping in aqueous solutions and thereby resulting in an uneven distribution within cement-based materials. Ethanol, owing to its dual polar and non-polar characteristics, is capable of interacting with both the polar and non-polar segments of STA, thereby facilitating the effective dispersion of STA within the ethanol. At room temperature, approximately 1 g of STA dissolves in 16.6 g of anhydrous ethanol. Consequently, this study employed ultrasonic waves to dissolve STA in anhydrous ethanol, and thus, prepared an STA–ethanol solution to enhance the dispersion of STA in mortar. Additionally, hydrophobic solid substances can be ground and coated onto powders to form a hydrophobic layer. Based on this principle, a planetary ball mill was used to co-grind the STA with TP to produce modified TP. The ball mill utilized for this purpose was equipped with four 500 mL grinding jars, where each contained 20 mL aluminum balls as the grinding medium.

2.2.1. STA–Ethanol-Modified Mortar

In order to investigate the effects of the STA–ethanol mixed solution, water–cement ratio, and sand–cement ratio on the wettability and mechanical properties of cementitious materials, STA was used to replace cement by equal mass, and tuff manufactured sand was used as the fine aggregate. Standard mortar specimens were prepared for comparative analysis, with the mix proportions shown in Table 4. The specific experimental groups were as follows: S-0 indicates the mortar without STA, while S-0.3, S-0.6, S-0.9, S-1.2, and S-1.5 denote the mortars with various STA contents (as a percentage of cement mass). W0.35-0.9 and W0.45-0.9 denote the mortars with a water–cement ratio of 0.35 and 0.45, respectively,

when the stearic acid content was 0.9% of the cement mass. W-0.35 and W-0.45, on the other hand, represent the mortars with a water–cement ratio of 0.35 and 0.45, respectively, without any stearic acid. C11-0.9 and C12-0.9 represent mortars with an STA content of 0.9% of the cement mass and sand–cement ratios of 1:1 and 1:2, respectively, while C-11 and C-12 denote the mortars without STA and sand–cement ratios of 1:1 and 1:2, respectively.

Table 4. Mix proportions (kg/m^3) of STA–ethanol-modified mortar.

Serial Number	Sample	w/c Ratio	c/s Ratio	Water	Cement	Tuff Manufactured Sand	Anhydrous Ethanol	STA
1	S-0	0.40	1:3	263.6	658.9	1976.7	0	0
2	S-0.3						32.8	1.98
3	S-0.6						65.6	3.95
4	S-0.9	0.40	1:3	263.6	658.9	1976.7	98.4	5.93
5	S-1.2						131.3	7.91
6	S-1.5						164.1	9.88
7	W0.35-0.9	0.35	1:3	233.2	666.5	1999.5	99.6	6.00
8	W-0.35						0	0
9	W0.45-0.9	0.45	1:3	293.2	651.5	1954.5	97.3	5.86
10	W-0.45						0	0
11	C11-0.9	0.40	1:1	483.2	1208.0	1208.0	141.7	8.54
12	C-11						0	0
13	C12-0.9	0.40	1:2	341.0	852.7	1705.5	127.4	7.67
14	C-12						0	0

To mitigate the impact of tuff manufactured sand on the XRD test results, pure paste specimens were prepared for the XRD testing, as detailed in Table 5. Specifically, P-0 represents the control group of cement paste; P-0.3, P-0.9, and P-1.5 denote the paste specimens with STA additions of 0.3%, 0.9%, and 1.5% by mass of cement, respectively. PW-0.35 indicates the paste specimen with a w/c ratio of 0.35 and an STA addition of 0.9% by mass of cement.

Table 5. Mix proportions (%) of STA–ethanol-modified cement paste.

Sample	w/c Ratio	Cement	STA
P-0	0.40	100	0
P-0.3	0.40	100	0.3
P-0.9	0.40	100	0.9
P-1.5	0.40	100	1.5
P-W0.35	0.35	100	0.9

2.2.2. STA–Tuff-Powder-Modified Mortar

In pursuit of achieving the most hydrophobic modified TP, this study examined the impact of STA addition and grinding duration on the contact angle. As illustrated in Figure 2, it was evident that at a rotational speed of 600 rpm, after grinding for 60 min with the incorporation of 3 wt% STA, the prepared hydrophobic modified TP exhibited the largest contact angle. Consequently, this modified TP demonstrated the most superior hydrophobic properties, which designated it as the optimal modified tuff powder (MTP).

The particle size distributions of the TP, MTP, and cement were analyzed using a Beckman Coulter LS 13 320 laser particle size analyzer (Backman Coulter: Brea, CA, USA). The resulting particle size distributions are depicted in Figure 3, with the relevant particle size parameters presented in Table 6. The results reveal that the TP exhibited the largest particle size, with the majority falling within the 50–150 μm range. The cement particles were smaller, predominantly within the 0–50 μm range, and generally less than 100 nm overall. The MTP displayed the smallest particle size, with 90% of the particles under 20 μm. When comparing the average particle size, median particle size, and particle size mode of the three materials, the size hierarchy was observed to be TP > cement > MTP.

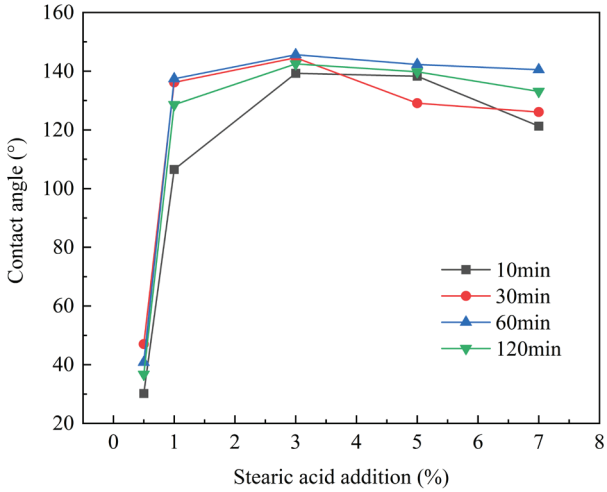

Figure 2. Effects of the ball-milling time and STA content on the contact angle of the modified tuff powder.

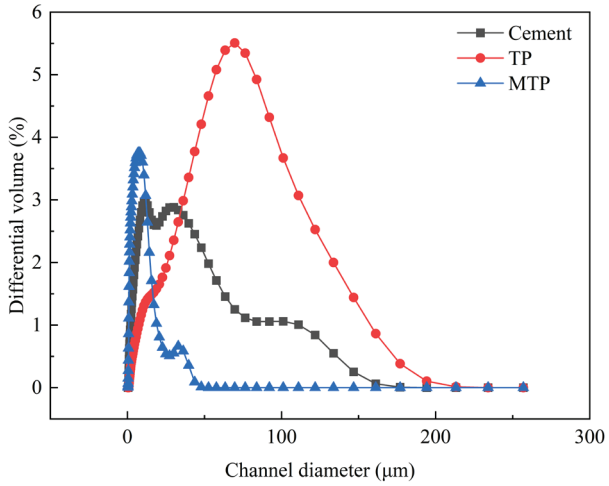

Figure 3. Particle size distribution of cement, TP, and MTP.

Table 6. Particle size parameter (μm).

	Cement	TP	MTP
Average	25.63	56.40	7.15
Median	14.73	51.84	5.06
Mode	12.40	72.94	7.78
D < 10%	2.81	7.91	1.36
D < 25%	6.28	22.00	2.41
D < 50%	14.73	51.84	5.06
D < 75%	34.50	81.53	9.51
D < 90%	62.47	112.40	14.88

The experimental mix proportions are shown in Table 7. The specific experimental groups were as follows: MS-0 denotes specimens without added TP; M-10, M-20, and M-30 represent mortars where 10%, 20%, and 30% of the mass of the cement was replaced with MTP, respectively, which served as supplementary cementitious materials; U-10, U-20, and U-30 indicate mortars where 10%, 20%, and 30% of the mass of the cement was replaced with TP, respectively, which served as supplementary cementitious materials. Furthermore, AM-10, AM-20, and AM-30 represent mortars with the direct addition of 10%, 20%, and 30% (based on the mass percentage of cement, hereinafter the same) of MTP, whereas

AU-10, AU-20, and AU-30 denote mortars with the direct addition of 10%, 20%, and 30% of TP, respectively.

Table 7. Mix proportions (kg/m^3) of STA–tuff-powder-modified mortar.

Serial Number	Sample	w/c Ratio	c/s Ratio	Water	Cement	TP	MTP	MS
1	MS-0	0.4	1:3	263.6	659.1	0	0	1977.2
2	M-10	0.4	1:3	263.6	593.2	0	65.9	1977.2
3	M-20				527.2	0	131.9	
4	M-30				461.4	0	197.7	
5	U-10				593.2	65.9	0	
6	U-20				527.2	131.9	0	
7	U-30				461.4	197.7	0	
8	MS-0	0.5	1:3	322.1	644.3	0	0	1932.8
9	M-10	0.5	1:3	322.1	579.9	0	64.4	1932.8
10	M-20				515.4	0	128.9	
11	M-30				451.0	0	193.3	
12	U-10				579.9	64.4	0	
13	U-20				515.4	128.9	0	
14	U-30				451.0	193.3	0	
15	AM-10	0.5	1:3	322.1	644.3	0	64.4	1932.8
16	AM-20					0	128.9	
17	AM-30					0	193.3	
18	AU-10					64.4	0	
19	AU-20					128.9	0	
20	AU-30					193.3	0	

2.3. Contact Angle

An optical contact angle goniometer was employed to measure the contact angle. The test specimen, a cylindrical piece with dimensions of Φ 100 × 10 mm, was cured in a standard curing chamber for 28 days. Subsequently, it was removed and dried in an oven at 80 °C for one day, followed by an additional day of drying under ambient conditions. During the measurement, a syringe was used to carefully place a 5 μL drop of water onto the surface of the specimen at room temperature. The contact angle was then measured using the angle measurement method. Five different positions on each specimen were selected for the measurement, and the average value was recorded. A single measurement was considered valid if the difference between the individual measurement and the average did not exceed 5°.

2.4. Sorptivity

The sorptivity test was conducted in accordance with ASTM C1585-04. After curing for 28 days, the specimens were placed in an 80 °C oven for 12 h of drying, followed by 12 h of drying in natural conditions. To ensure unidirectional water penetration into the mortar, all surfaces except the water-absorbing one were sealed with epoxy resin and cured at room temperature for 24 h. The initial mass of the specimens, M_0, was then measured and recorded. The exposed surface of the specimens was submerged in water, ensuring the water level was 1–3 mm above the surface. The mass of the specimens was measured and recorded at intervals of 1, 5, 10, 20, and 30 min, and at 1, 2, 3, 4, 5, and 6 h. Excess water on the surface was wiped off with a cloth, and the specimens were flipped to prevent the wet surface from contacting the balance.

The sorptivity ($mm/s^{1/2}$) is defined as the slope of the best-fit line plotted using all the data points from 1 min to 6 h (excluding points where the slope of the curve significantly changes) against the square root of time ($s^{1/2}$). Due to the small magnitude of this value, the unit is expressed as $\mu m/s^{1/2}$. Using the least squares method, linear regression analysis of the I versus the square root of time ($s^{1/2}$) curve provides this slope. In this experiment, the regression coefficients were all greater than 0.98.

2.5. Compressive Strength

In accordance with JTG 3420-2020, specifically T0506-2005, the compressive strengths of mortar specimens at 3 and 28 days of curing were tested. The dimensions of the specimens were 40 × 40 × 40 mm, where each group comprised six specimens, and the results were averaged.

2.6. Microscopic Experiment

The samples needed to be ground into powder in advance for the XRD and FTIR testing, and the SEM samples needed to be gold-coated. For the XRD test, to determine the mineral composition of the hydration products after the addition of the STA–ethanol solution, we prepared 40 × 40 × 40 mm cubic paste specimens to eliminate the interference from sand on the diffraction peaks. To assess the impact of co-grinding STA and TP on the phase composition of the TP, we directly tested the powder after mixing the two. The XRD instrument model used was D8 ADVANCE, with a diffraction angle range of 10° to 80°, a scanning step size of 0.02626, and post-test phase analysis conducted using Jade 6.5 software. The FTIR testing was carried out using a Bruker ALPHA II infrared spectrometer (Bruker: Billerica, MA, USA), with a beam range of 400–4000 cm^{-1}, 32 scans, and a resolution of 2 cm^{-1}. The microstructure of the samples was examined using a Nova Nano SEM 450 field emission scanning electron microscope, with magnifications of 20,000× and 10,000×, an electron beam current that ranged from 0.6 pA to 200 nA, and stepless adjustment.

3. Results and Discussions

3.1. Wettability of STA–Ethanol-Modified Mortars

3.1.1. Contact Angle

The contact angle is one of the crucial indicators for evaluating the hydrophobic modification effect of cement-based materials; the greater the contact angle, the more pronounced the hydrophobic effect. Figure 4a reveals that the contact angle of the cement mortar initially increased and then decreased with the increase in the STA content. When the STA content reached 0.9% of the cement mass, the contact angle peaked at 69.5°. Figure 4b illustrates that when the STA content was 0.9% of the cement mass, the contact angle value of the mortar increased as the w/c ratio decreased. When the w/c was lower, the mortar became denser, with a lower porosity, which resulted in a higher contact angle. Figure 4c demonstrates that when the STA content in the mortar was 0.9% of the cement mass, the contact angle increased as the c/s decreased. As the c/s decreased, the mortar structure became more compact and uniform with more sand filling, which reduced the porosity. Although a lower c/s ratio resulted in relatively less cement and STA content, the contact angle value still increased, indicating that the compactness of the mortar structure significantly influenced the contact angle [23].

3.1.2. Sorptivity

From Figure 5, it can be observed that the sorptivity coefficient of the mortar initially decreased and then increased with the increase in the STA content, yet remained lower than that of the unmodified mortar. This phenomenon could be attributed to the capillary forces that draw water into the pores of porous materials, such as concrete, when they come into contact with water. These capillary forces are determined by factors such as the surface tension of the liquid, the contact angle between the liquid and the pore walls, and the radius of the pores, as described by Equation (1) [24]:

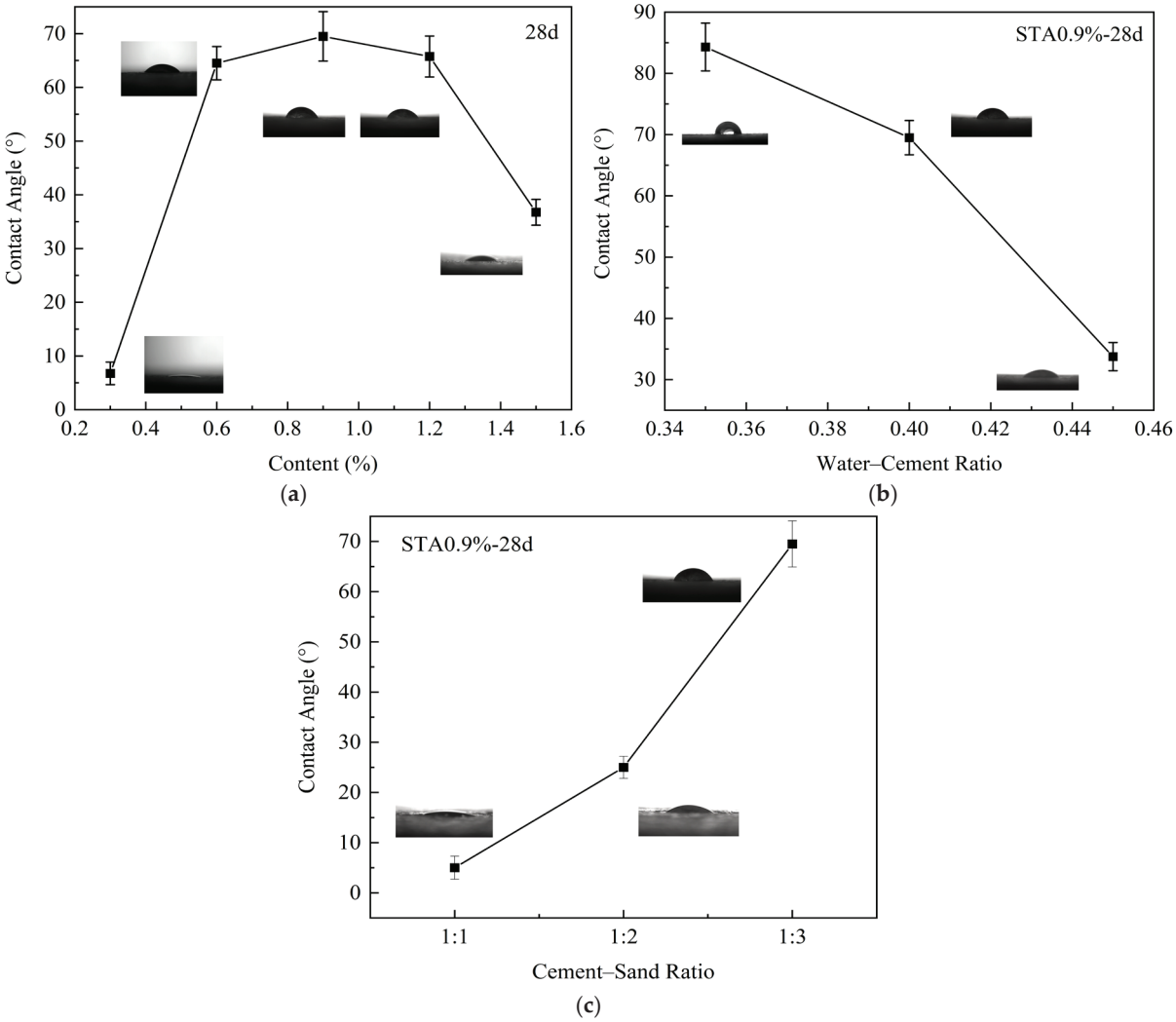

Figure 4. Effects of different factors on contact angle of STA–ethanol-modified mortar: (**a**) STA content, (**b**) w/c ratio, and (**c**) c/s ratio.

$$P = \frac{2\sigma\cos\theta}{r} \times 100\% \quad (1)$$

where P represents the capillary force of water on the material's surface; σ denotes the surface tension of water; θ is the contact angle between the water and the pore walls; and r is the radius of the pores in the mortar. When the contact angle is less than 90°, molecular attraction between the water and the concrete causes a capillary rise, resulting in a concave meniscus. The addition of STA forms a hydrophobic lining on the pore walls, increasing the contact angle and thereby reducing the capillary action [25]. When the contact angle exceeds 90°, a reverse pressure differential arises, necessitating additional pressure for water to infiltrate the pores [26]. In this experiment, the measured contact angles of the modified mortar were all less than 90°, thus the reduction in sorptivity was relatively minimal.

As illustrated in Figure 5a, with the increase in the STA content, the sorptivity of the mortar exhibited a decreasing trend. When the STA addition reached 1.2% of the cement mass, the sorptivity coefficient of the mortar at 28d of age decreased by 27.8% compared with the control group without STA (S-0). However, when the STA content was further increased, the product formed from the reaction between the hydroxyl groups in the mortar and the STA contained water, which increased the free water in the mortar, which

consequently led to a higher porosity. Therefore, although the addition of STA improved the water resistance, excessive porosity could facilitate water penetration, which increased the sorptivity. Hence, the STA content should not be overly high [19,27]. Moreover, as deduced from Equation (1), the capillary force is directly proportional to the cosine of the contact angle and inversely proportional to the contact angle. The experimental results demonstrate a consistent relationship between the sorptivity and contact angle.

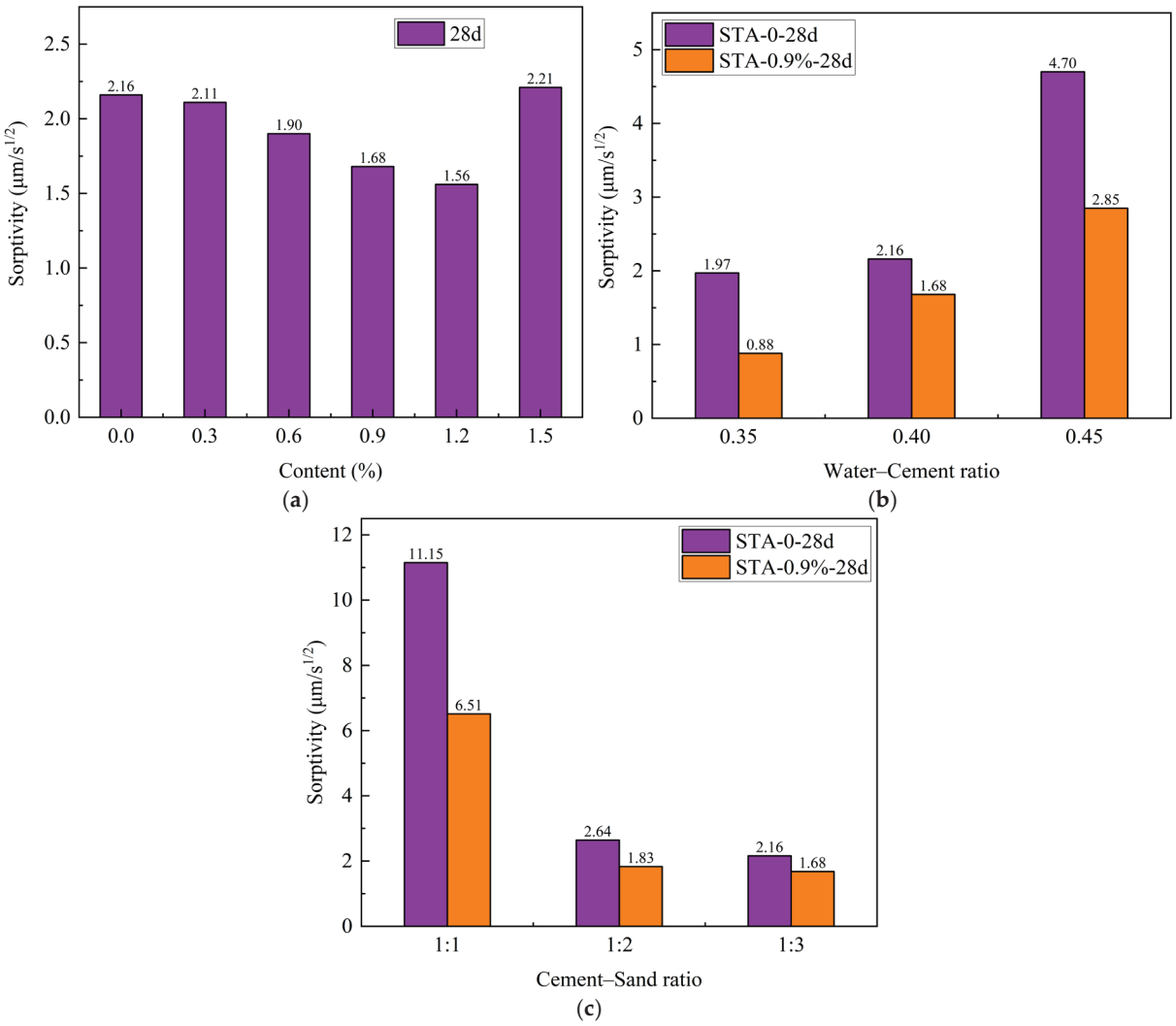

Figure 5. Effects of different factors on sorptivity of STA–ethanol-modified mortar: (**a**) STA content, (**b**) w/c ratio, and (**c**) c/s ratio.

From Figure 5b, it can be discerned that the sorptivity of mortar at 28d of age generally diminished as the w/c ratio decreased. The higher w/c ratio resulted in an increased content of free water within the mortar, thereby elevating its porosity and facilitating easier water permeation. When the STA addition was 0.9% of the cement mass, the sorptivity coefficients of the mortars with w/c ratios of 0.35, 0.40, and 0.45 decreased by 55.3%, 22.2%, and 39.4%, respectively, compared with the mortar without STA. This reduction was because the STA formed a waterproof lining on the mortar pore walls, which increased the contact angle and reduced the capillary action, which lowered the sorptivity across all the w/c ratios [25]. When the w/c ratio was low, the addition of STA generated extra water, which enhanced the mortar's fluidity and promoted a uniform distribution, which made the sorptivity reduction effect more pronounced at lower w/c ratios [27]. Furthermore, it could be observed that reducing the w/c ratio from 0.45 to 0.40 resulted in a 54.0% decrease

in the sorptivity, while the addition of 0.9wt% STA achieved an improvement equivalent to about 70% of the effect of reducing the w/c ratio by 0.05.

From Figure 5c, it can be discerned that the sorptivity of the mortar at 28d decreased with the reduction in the c/s ratio. This variation in the sorptivity reflected changes in the porosity; as the c/s ratio diminished, the compactness of the mortar increased, which led to a reduction in the porosity and, consequently, a decrease in the sorptivity. The addition of the STA could further reduce the sorptivity of the mortar. When the c/s ratios were 1:1, 1:2, and 1:3, the sorptivity coefficients decreased by approximately 41.6%, 30.7%, and 22.2%, respectively, compared with the mortar without the STA. It can be observed that the larger the c/s ratio, the more significant the improvement effect of the STA on the mortar's sorptivity. This was attributable to the hydrophilic nature of sand; increasing the c/s ratio reduced the sand content in the mortar, which enlarged the surface and internal areas affected by the STA coating, which rendered the mortar more waterproof. Additionally, when the c/s ratio was reduced from 1:2 to 1:3, the sorptivity coefficient of the mortar decreased by 18.2%. When comparing this with the reduction in the sorptivity of the mortar modified with 0.9 wt% STA, it was observed that at a c/s ratio of 1:2, the improvement in the sorptivity due to the addition of 0.9 wt% STA was superior to that achieved by reducing the c/s ratio. However, when the c/s ratio was reduced from 1:1 to 1:2, the sorptivity coefficient of the mortar decreased by approximately 76.3%, indicating that the improvement in the sorptivity through reducing the c/s ratio surpassed that achieved by adding 0.9 wt% STA.

3.2. Mechanical Properties of STA–Ethanol-Modified Mortars

Figure 6a illustrates the impact of the STA content on the compressive strength of the cement mortar at 28d of age. It can be observed that as the amount of STA increased, the compressive strength of the mortar significantly decreased. Specifically, with the STA additions of 0.3 wt%, 0.6 wt%, 0.9 wt%, 1.2 wt%, and 1.5 wt%, the compressive strengths decreased by 31.2%, 47.3%, 61.4%, 82.4%, and 88.2%, respectively, compared with the control group. This phenomenon was primarily attributed to the reaction between the STA and the cement hydration product calcium hydroxide, which resulted in the formation of insoluble calcium stearate and water. The calcium stearate impeded further cement hydration, and the generation of water led to an increased the actual w/c ratio. Under the combined influence of these factors, the compressive strength of the mortar experienced a substantial reduction [27,28].

The influence of the w/c ratio on the compressive strength of mortar is illustrated in Figure 6b. Generally, as the w/c ratio increased, the amount of free water in the mortar also rose. Upon hardening, the evaporation of free water resulted in a greater porosity, which led to a decrease in the compressive strength. However, it was observed that the compressive strength of the unmodified mortar at a w/c ratio of 0.35 was lower than that at a ratio of 0.40. This anomaly could be attributed to the irregular shape of the tuff manufactured sand, which caused insufficient fluidity and decreased the density of the mortar at a lower w/c ratio, which resulted in a reduced compressive strength. When the STA was added, the increased amount of free water enhanced the fluidity and density of the mortar. Consequently, with the addition of a consistent amount of STA, the compressive strength increased as the w/c ratio decreased. Specifically, with the addition of 0.9 wt% STA, the strength of the mortar decreased by approximately 56.7% at a w/c ratio of 0.35, by about 61.4% at a ratio of 0.40, and by roughly 67.3% at a w/c ratio of 0.45. Thus, it was evident that the negative impact of the STA–ethanol solution on the compressive strength was relatively smaller at lower w/c ratios.

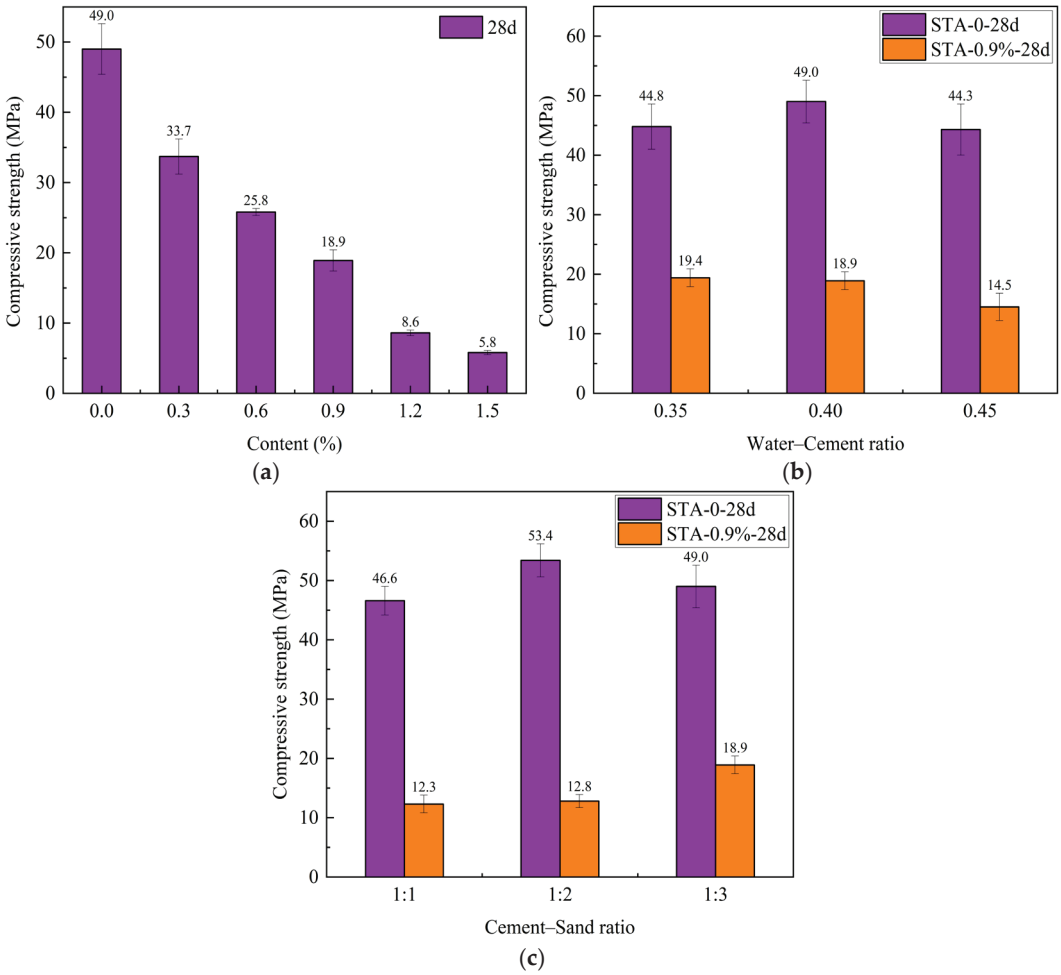

Figure 6. Effects of different factors on the compressive strength of STA–ethanol-modified mortar: (**a**) STA content, (**b**) w/c ratio, and (**c**) c/s ratio.

The influence of the c/s ratio on the compressive strength of the mortar, as depicted in Figure 6c, revealed that the compressive strength was lower at ratios of 1:1 and 1:3 compared with a ratio of 1:2. This phenomenon occurred because a higher c/s ratio resulted in a relatively lower sand content, which was insufficient to adequately fill the voids between the cement particles. Consequently, the skeletal structure provided by the sand was inadequate, which led to a diminished density and strength of the mortar. When the sand content was sufficient to meet the skeletal requirements, the compressive strength of the mortar was primarily determined by the cement paste. As the c/s ratio decreased, the volume fraction of the cement paste declined, which reduced the average thickness of the paste between the sand particles, and thus, diminished the bonding force and resulted in a decrease in the compressive strength [29]. Upon the addition of 0.9 wt% STA to the mortar, the compressive strength exhibited an increasing trend as the c/s ratio decreased.

3.3. Wettability of STA–Tuff-Powder-Modified Mortars

3.3.1. Contact Angle

Figure 7 indicates that when the w/c ratio was 0.4, the contact angle of the mortar gradually decreased with the increase in the replacement rate of MTP. This phenomenon was related to the increase in porosity, as the increase in MTP led to a higher porosity in the mortar, which enlarged the contact surface area between the water and mortar. Conversely, when the w/c ratio was 0.5, the contact angle of the mortar increased with the replacement

rate of MTP. This was attributed to the heightened content of STA and the reduction in porosity. When additional MTP was incorporated into the mortar at the same proportion, the contact angle of the mortar further increased. This was primarily because, compared with the 0.5-M group specimens, directly adding MTP resulted in a lower porosity in the mortar, which caused a greater contact angle in the 0.5-AM group.

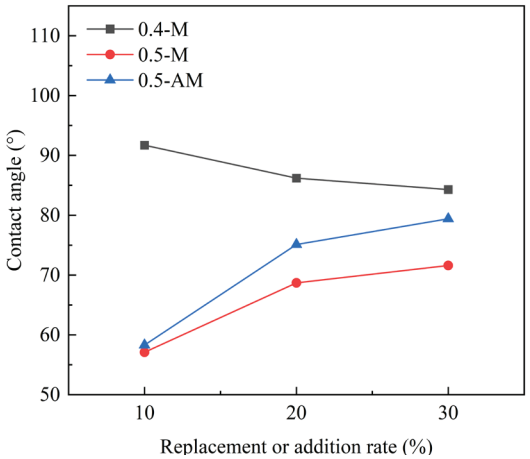

Figure 7. Effect of the MTP replacement or addition rate on the contact angle of mortar.

3.3.2. Sorptivity

From Figure 8a, it can be observed that with an increase in the replacement rate of TP, the sorptivity coefficient of the mortar shows a progressive rise compared with the control group (0.5-MS-0). Specifically, the sorptivity coefficients increased by 17.0%, 42.5%, and 52.8% for the replacement rates of 10%, 20%, and 30% respectively. This phenomenon was mainly attributed to the higher w/c ratio, which reduced the cement content and consequently formed numerous pores in the hardened mortar. The particle size analysis revealed that the TP particles were larger than those of cement; hence, when the TP replaced the cement by mass, it occupied more space, which reduced the space for water, and thereby increased the porosity. Research indicates that excessive TP acts as an inert filler between aggregates in concrete, forming channels around it, which deteriorates the impermeability of concrete as the TP content increases [30,31]. However, the incorporation of MTP significantly reduced the sorptivity of mortar, with coefficients lower than the 0.5-MS-0 group at all replacement levels. Specifically, at the replacement rates of 10%, 20%, and 30%, the sorptivity coefficients of the mortar decreased by 16.4%, 22.6%, and 26.5%, respectively, compared with the 0.5-MS-0 group, and by 33.4%, 65.1%, and 79.3%, respectively, compared with the use of TP. This improvement could be attributed to the reaction between the carboxyl groups in STA and hydroxyl groups in the mortar, which grafts hydrophobic long-chain alkyl groups onto the mortar, thereby reducing surface energy and increasing the contact angle, which is consistent with the results of the contact angle tests [25,32]. According to Equation (1), an increase in the contact angle diminishes the capillary suction, thereby reducing the capillary action and lowering the sorptivity in mortar with MTP, thus enhancing the impermeability. As the replacement rate of MTP increased, the content of STA also increased, which dispersed more uniformly with MTP, which further decreased the sorptivity of the mortar.

Figure 8b illustrates the impact of varying the replacement rates of TP and MTP on the sorptivity of mortar with a w/c ratio of 0.4. It can be observed that when the TP was used, the sorptivity of the mortar followed a similar pattern to that with a w/c ratio of 0.5. As the replacement rate of TP increased, the sorptivity of the mortar gradually rose. Specifically, when the replacement rates are 10%, 20%, and 30%, the mortar's sorptivity coefficients

increased by 50.1%, 136.1%, and 121.8%, respectively, compared with the control group (0.4-MS-0). This indicates that with a lower w/c ratio, the cement content in the mortar was higher, which resulted in a lower porosity and better overall impermeability. The 0.5-MS-0 group exhibited a higher sorptivity than the 0.4-MS-0 group, which confirmed that a lower w/c ratio enhanced the impermeability of the mortar. However, due to the higher cement content at a lower w/c ratio, the corresponding TP content increased when it was substituted for the cement, and the TP had a greater adsorption of water [33], so the rise in sorptivity was more pronounced compared with the w/c ratio of 0.5. Upon using the MTP, although the sorptivity coefficients of the mortar with all the replacement rates remained higher than the 0.4-MS-0 group, they were lower compared with the mortar using the TP. Specifically, with the MTP replacement rates of 10%, 20%, and 30%, the sorptivity coefficients increased by 19.9%, 24.1%, and 26.4%, respectively, compared with the 0.4-MS-0 group, while they decreased by 23.5%, 101.9%, and 104.2%, respectively, compared with the mortar with TP. This suggests that the STA improved the impermeability of the mortar. The STA formed a hydrophobic film on the surface of the mortar particles, which impeded water ingress. As the replacement rate of MTP increased, the STA content also increased. Hence, the decline in sorptivity was more significant in comparison with the test groups using TP with the same replacement rate. Overall, considering the detrimental impact of TP on the sorptivity and the beneficial effect of the STA, the M-10 group exhibited the lowest sorptivity coefficient. However, it still exceeded that of the 0.4-MS-0 group, as the lower w/c ratio inherently enhanced the mortar's impermeability, while the adverse impact of the TP on the impermeability was substantial.

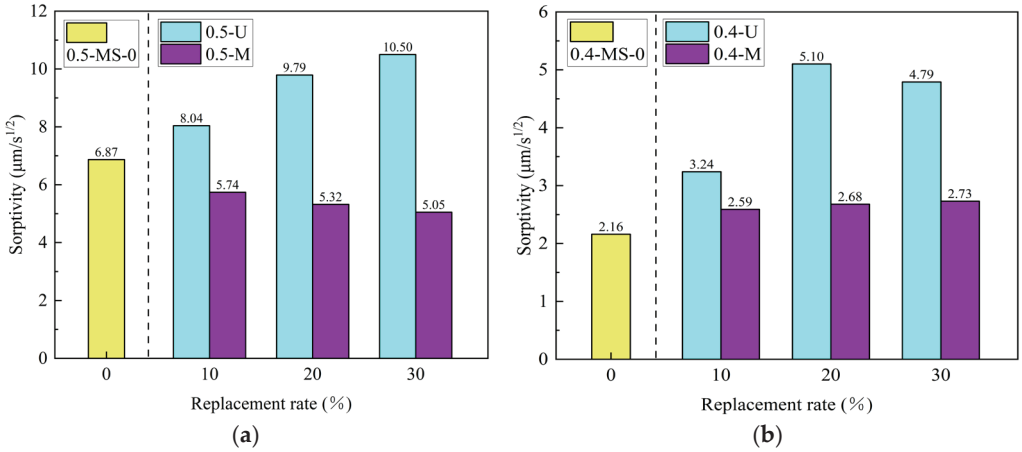

Figure 8. Effects of the TP and MTP replacement rates on the sorptivity of mortar: (**a**) w/c ratio of 0.5 and (**b**) w/c ratio of 0.4.

Figure 9 illustrates the effects of the TP and MTP addition rates on the sorptivity of the mortar with a w/c ratio of 0.5. It can be observed that at this w/c ratio, the cementitious material content in the mortar was relatively low, which led to larger voids between the aggregates. Due to the particle size of TP being less than 0.075 mm, its additional incorporation could enhance the pore structure of the concrete, optimize the particle gradation, and increase the density, and thus, reduce the sorptivity of the mortar [34]. Specifically, in this experiment, the sorptivity coefficients of AU-10, AU-20, and AU-30 groups decreased by approximately 4.9%, 12.1%, and 17.0%, respectively, compared with the control group (0.5-MS-0). With the addition of MTP, the sorptivity coefficients further decreased, where the AM-10, AM-20, and AM-30 groups showed reductions of 18.5%, 33.5%, and 42.8%, respectively, compared with the 0.5-MS-0 group. These results indicate that the higher the addition rate of MTP, the more significant the improvement in the impermeability of the mortar, which was primarily attributed to the action of the STA.

Research suggests that the air-entraining effect of STA can form numerous microbubbles within the mortar, which exist in a closed form beneath larger bubbles, thereby preventing the extension of surface pores inward and enhancing impermeability [35].

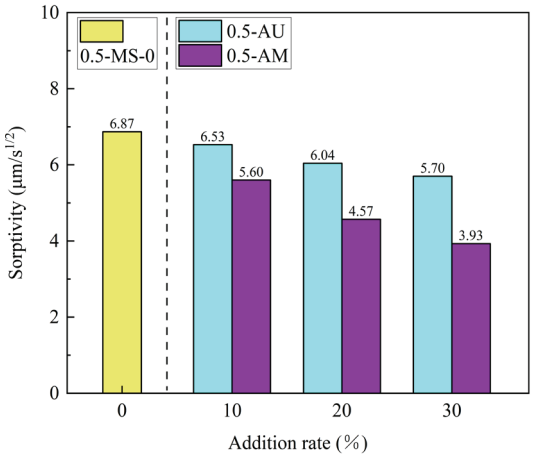

Figure 9. Effects of the TP and MTP addition rates on the sorptivity of mortar at a w/c ratio of 0.5.

3.4. Mechanical Properties of STA–Tuff-Powder-Modified Mortars

When the w/c ratio was 0.5, the influences of the TP and MTP replacement rates on the compressive strength of mortar are shown in Figure 10a. It can be observed that at the 3d and 28d ages, the compressive strength difference between the specimens using the TP and MTP was minimal when the replacement rate was identical, with the strength of the specimens using the TP slightly higher than those using the MTP. Additionally, with an increase in the replacement rate of TP, the compressive strength of the mortar showed a downward trend. At 3d of age, the compressive strengths of the U-10, U-20, and U-30 groups decreased by 33.3%, 42.4%, and 70.4%, respectively, compared with the control group (MS-0). At 28d of age, the decline pattern of compressive strength was similar to that at 3d, but the extent of the reduction in compressive strength at 28d was generally smaller than at 3d. This could be attributed to the pozzolanic activity of the tuff powder, whose main components were SiO_2 and Al_2O_3, accounting for 53.4%. These active components can react with calcium hydroxide to produce C-S-H, C-A-H, and C-A-S-H, thereby providing the mortar with certain strength [16,36].

When the w/c ratio was 0.4, the influence of the TP and MTP replacement rates on the compressive strength of mortar is depicted in Figure 10b. The results indicate that at 3d of age, as the replacement rate of TP increased, the compressive strength of the mortar gradually decreased. Specifically, the compressive strengths of groups U-10, U-20, and U-30 decreased by approximately 9.3%, 27.5%, and 46.2% respectively, compared with the control group (MS-0). This decline was less pronounced than that observed with a w/c ratio of 0.5, primarily since the lower w/c ratio reduced the water content and enhanced the density of the mortar. Consequently, the partial replacement of cement with TP had a lesser impact on the mortar density. When the MTP was used, the 3d compressive strengths of the mortar for each replacement rate exhibited different degrees of increase compared with using the TP, which differed from the results with a w/c ratio of 0.5. This was attributed to the addition of the STA to the surface of the MTP, which generated additional free water, increased the workability of the mortar, and thus, improved its density and compressive strength. At 28d of age, the compressive strengths of the mortars with cement replaced by the TP followed a pattern similar to that at 3d. The compressive strengths of groups U-10, U-20, and U-30 decreased by 6.5%, 22.7%, and 54.1%, respectively, compared with the MS-0 group. However, when the MTP replaced the cement, the compressive strength

of the mortar significantly increased with the replacement rate. This was because the higher replacement rate of the MTP introduced more STA, which led to more free water generation over time as the STA reacted with the calcium hydroxide, which exhibited a superplasticizer-like effect that enhanced the compressive strength of the mortar. The lower strength of the M-30 group compared with the control group could be attributed to the excessive reduction of the cementitious materials. However, its compressive strength decreased by only approximately 12.9% relative to the control group, which was not a particularly significant decline.

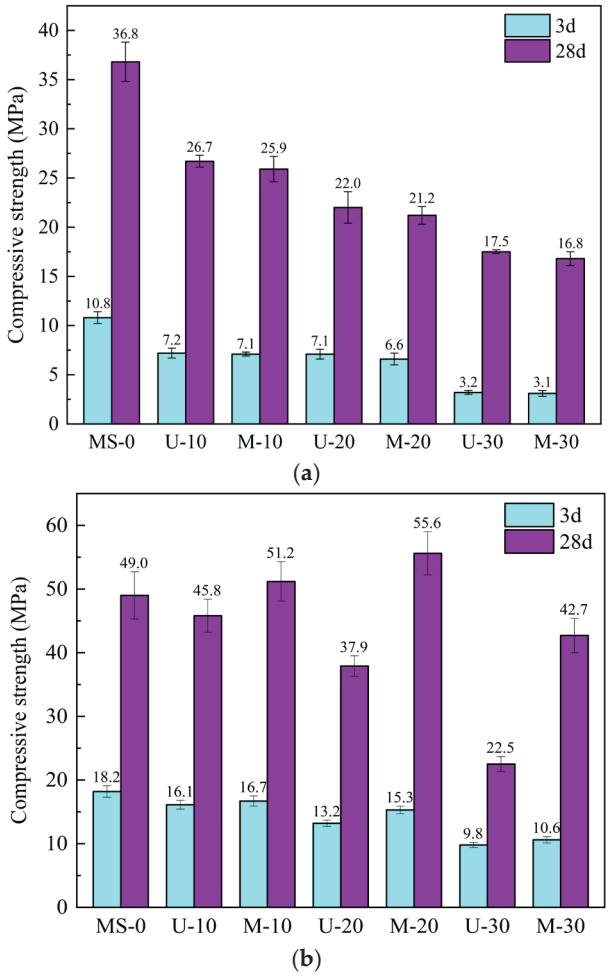

Figure 10. Effects of TP and MTP replacement rates on compressive strength of mortar: (**a**) w/c ratio of 0.5 and (**b**) w/c ratio of 0.4.

As illustrated in Figure 11, the influences of the TP and MTP addition rates on the compressive strength of mortar at a w/c ratio of 0.5 is evident. At 3d of age, a certain amount of TP enhanced the early compressive strength of the mortar, but with the increased TP content, the compressive strength decreased. This improvement was primarily attributed to the unique particle shape and size distribution of the tuff powder, which optimized the particle packing, making the mortar denser and stronger. At 28d of age, the compressive strength of the mortar initially increased and then decreased with the increasing content of TP. Specifically, the compressive strengths of the AU-10, AU-20, and AU-30 groups increased by approximately 4.9%, 15.5%, and 9.0%, respectively, compared with the MS-0 group. This was mainly due to the micro-aggregate effect and pozzolanic activity of the tuff powder. Tuff powder exhibits pozzolanic reactivity, reacting with calcium hydroxide and C-S-H in cement to form a low-alkalinity, high-strength C-S-H gel. It can also react

with free CaO to form more binding materials, enhancing the compressive strength of the mortar. However, excessive tuff powder content disrupts the optimal packing structure of the mortar or deviates the c/s ratio from the optimal value, thus affecting the strength of the mortar [30]. In this experiment, a 10% TP content caused an increase in the 3d compressive strength, while the 20% and 30% contents resulted in a reduced compressive strength. At 28d of age, mortar with a 20% TP content achieved the highest strength, while a 30% content increased the negative effects. When the MTP was added, the compressive strength of the mortar decreased compared with the addition of TP due to factors such as the STA affecting the cement hydration; introducing air bubbles that increase porosity; and generating more water, thereby increasing the w/c ratio [37,38].

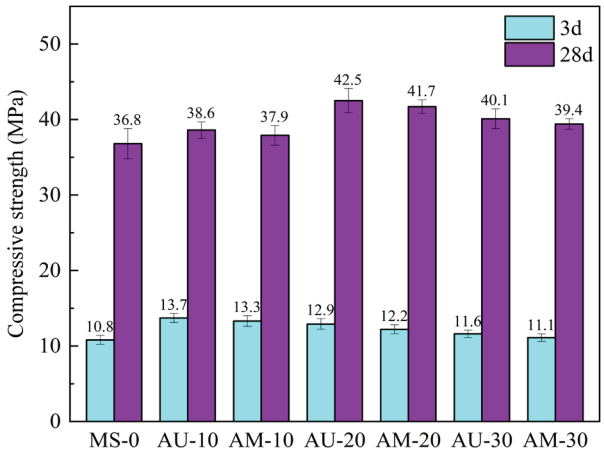

Figure 11. Effects of the TP and MTP addition rates on the compressive strength of the mortar at a w/c ratio of 0.5.

3.5. SEM

As seen in Figure 12a, the surface of the mortar without the STA primarily consisted of hydration products, such as C-S-H gel and AFt, with localized aggregation of C-S-H gel, that exhibited poor integration with other hydration products and a high porosity. Figure 12b–d illustrate that as the STA content increased, the production of hydration products, like $Ca(OH)_2$ and C-S-H gel, gradually decreased. The integration between the hydration products deteriorated, which resulted in a looser structure and increased porosity. Concurrently, the aggregates could be clearly observed, indicating a reduced density of hydration products. In Figure 12d, with a 1.5 wt% addition of STA, distinct rhizome-like products were observed stacked on the surface of the hydration products. The carboxyl group in STA reacts with the hydroxyl groups in the mortar, linking the long hydrophobic tails of STA to the mortar, impeding the contact between cement and water [23].

When comparing Figure 12c,e, the influences of different w/c ratios on the microstructures of the mortar when the STA addition was 0.9 wt% can be observed. When the water–cement ratio was 0.4, the primary products formed were C-S-H gel and ettringite, with less hydrophobic formation. Additionally, the aggregates could be clearly observed. In contrast, when the w/c ratio was reduced to 0.35, root-like hydrophobic substances could be observed covering the surface of the hydration products. As the w/c ratio decreased, the content of cementitious materials in the mortar increased, which accordingly led to a higher concentration of STA. This resulted in the more pronounced formation of hydrophobic materials, which could be more easily observed on the surface of the hydration products.

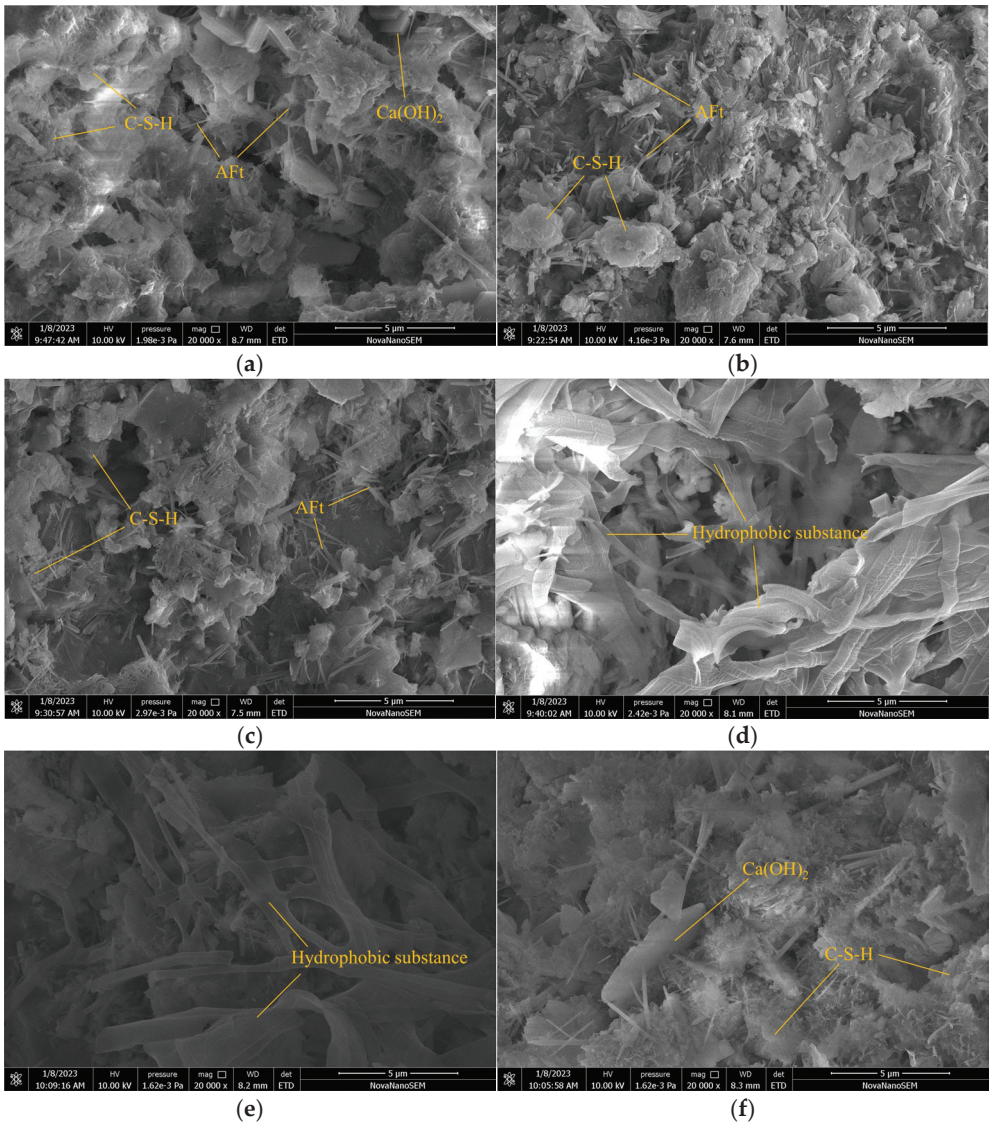

Figure 12. SEM microstructure of STA–ethanol-modified mortar at 28d of age: (**a**) S-0; (**b**) S-0.3; (**c**) S-0.9; (**d**) S-1.5; (**e**) W0.35-0.9; (**f**) C12-0.9.

Figure 12c,f illustrate the microstructure of mortar with an STA content of 0.9 wt% at different c/s ratios. When the c/s ratio was 1:2, a significantly greater abundance of hydration products, such as $Ca(OH)_2$, C-S-H gel, and AFt, could be observed. These products interlocked with each other and formed a denser structure. This was attributed to the higher c/s ratio, which resulted in a lower sand content in the mortar, which increased the average thickness of the cement paste and subsequently generated more hydration products, which made them more readily observable.

The SEM microstructure of the STA–tuff-powder-modified mortar is depicted in Figure 13. When the w/c ratio was 0.5, the primary hydration products were $Ca(OH)_2$, C-S-H gel, and needle-like AFt. The overall structure was relatively loose, with notable large pores and microcracks. Figure 13b shows a reduced content of C-S-H gel, which appeared to have locally aggregated and grown. The structure remained rather loose, albeit with smaller microcracks. Additionally, cubic C_3AH_{13} was observed, likely due to the reduced cement content leading to fewer hydration products. With the use of MTP, Figure 13c illustrates the presence of C-S-H gel within the pores, a clear increase in cubic C_3AH_{13}, and a reduction in AFt formation, with no significant microcracks observed.

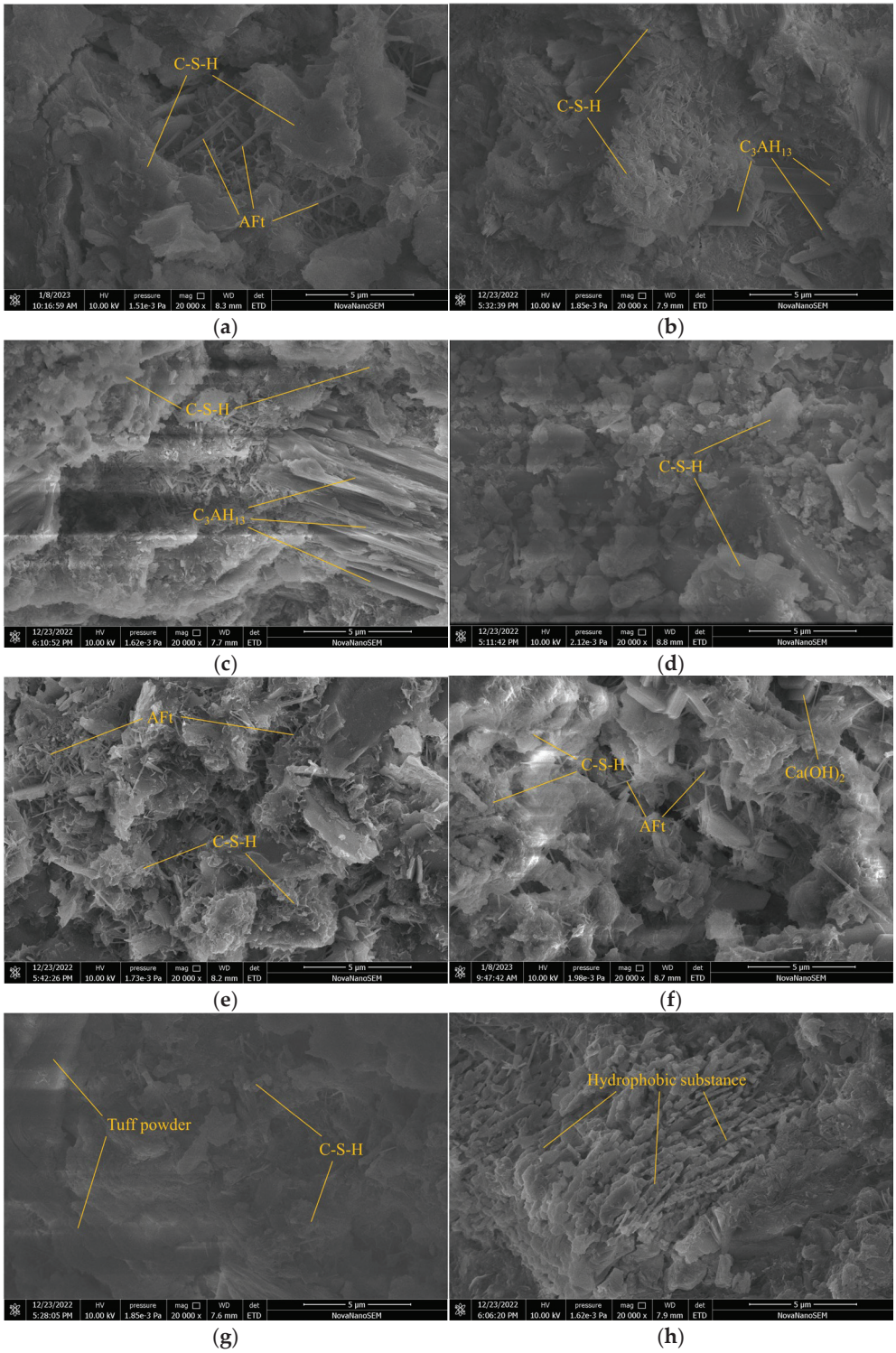

Figure 13. SEM microstructure of STA–tuff-powder-modified mortar at 28d of age: (**a**) 0.5-MS-0; (**b**) 0.5-U-20; (**c**) 0.5-M-20; (**d**) 0.5-AU-20; (**e**) 0.5-AM-20; (**f**) 0.4-MS-0; (**g**) 0.4-U-20; (**h**) 0.4-M-20.

Figure 13d reveals that with the direct addition of 20% TP, there was a noticeable reduction in the presence of AFt and fibrous C-S-H within the hydration products, which predominantly displayed as massive C-S-H gel. This resulted in a poorer interconnection of the hydration products, although, unlike the 0.5-MS-0 group, no significant microcracks were observed. Conversely, when 20% MTP was added, there was a substantial presence of fibrous C-S-H gel on the surface of the hydration products, along with an increased content of AFt.

Observing Figure 13f, it is evident that with a lower w/c ratio, the hydration products intertwined and overlapped, and thus, displayed a more pronounced microstructure compared with the mortar with a w/c ratio of 0.5 shown in Figure 13a. When the TP replacement rate was 20%, there were numerous fibrous and flaky C-S-H gels, indicating a denser structure. It is clear that at a 20% MTP replacement rate, calcium stearate was directionally aligned on the surface of the cement particles, which hindered the hydration of the cement.

3.6. XRD

From Figure 14, it can be observed that the primary constituents of the paste samples remained consistent before and after the modification, which encompassed CH, SiO_2, C_3S, and C_2S, where the C-S-H gel presented an amorphous phase depicted as a diffuse peak and treated as background. No significant diffraction peaks for AFt and AFm were detected in the diffraction patterns. A comparative analysis revealed that the positions of the effective diffraction peaks largely coincided, indicating that the STA did not influence the types of hydration products of cement. Additionally, by comparing the intensities of the various diffraction peaks, it can be observed that with an increase in the STA content, the intensity of the CH diffraction peaks diminished, while the intensities of the C_3S and C_2S peaks gradually increased, suggesting that the STA impeded the hydration of the cement. This observation was consistent with the results from the SEM analysis. When comparing the spectra of W0.35-0.9 and S-0.9, it could be observed that when the w/c ratio was 0.35, the CH diffraction peak intensity was higher, whereas the intensities of the C_3S and C_2S peaks were lower. This indicates that under the same mass fraction of the STA, the mortar with a lower w/c ratio exhibited a higher degree of hydration.

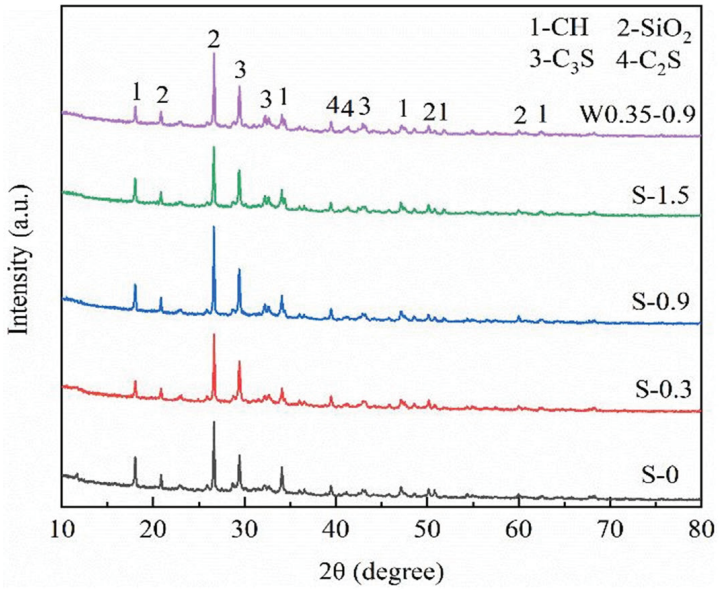

Figure 14. XRD patterns of STA–ethanol-modified cement paste at 28d of age.

It can be observed that the diffraction patterns of MTP were essentially similar to those of the TP from Figure 15. However, the co-grinding of the STA with the tuff powder led to a reduction or disappearance of certain peak intensities in the MTP. This could be attributed to the STA molecules that covered the crystal surface, which inhibited X-ray penetration through the lattice and resulted in the reduction or disappearance of some diffraction peaks. Notably, no new diffraction peaks appeared in the pattern of the MTP, indicating that the co-grinding of the tuff powder with the STA did not alter the crystal

structure of the tuff powder. This was because the co-grinding process was a physical one, where STA primarily acted as a surfactant [19].

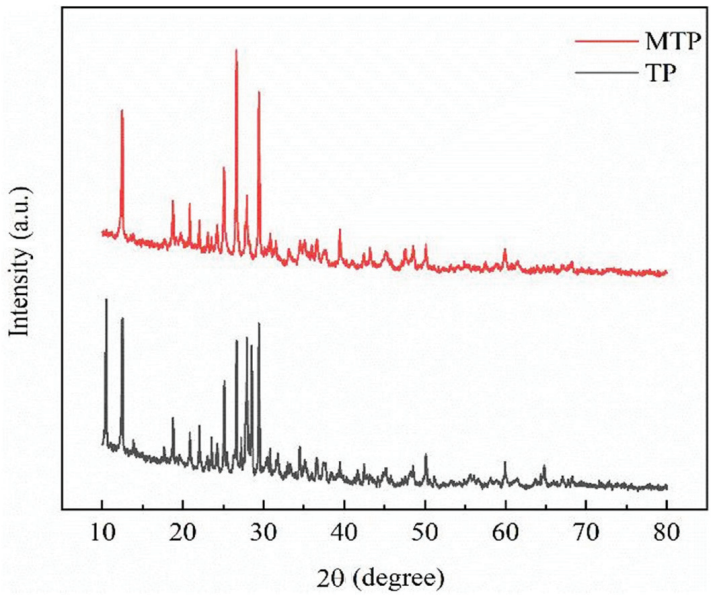

Figure 15. XRD patterns of TP and MTP.

3.7. FTIR

From Figure 16, we can know that the addition of the STA to the samples resulted in the appearance of two additional absorption peaks at 2918 cm^{-1} and 2847 cm^{-1}, which corresponded to the asymmetric and symmetric stretching vibrations of CH_2 groups [39]. As the concentration of STA increased, the intensities of these peaks were also amplified, indicating the successful grafting of the STA onto the mortar. Furthermore, the literature indicates that at higher concentrations of STA or stearates, distinctive absorption peaks emerge at 1540 cm^{-1} and 1578 cm^{-1}, which are attributable to the asymmetric stretching vibrations of carboxylate groups (COO–) [40–42]. Peaks at 3742 cm^{-1} and 980 cm^{-1} correspond to C-S-H gel [37]. Characteristic peaks at 1510 cm^{-1}, 1430 cm^{-1}, and 870 cm^{-1} correspond to the asymmetric stretching and out-of-plane bending vibrations of CO_3^{2-} [43]. A comparative analysis revealed that with an increase in the STA content, there was a reduction in the amount of carbonation products within the samples, suggesting that the incorporation of the STA enhanced the mortar's resistance to carbonation.

The FTIR analysis results of the TP and the MTP are depicted in Figure 17. In the spectrum of the TP, the peak at 891 cm^{-1} corresponded to the vibration of Si-O, while the band around 1439 cm^{-1} was primarily caused by the vibrations of CO_3^{2-}. In the spectrum of the MTP, the newly emerged characteristic peaks at 2920 cm^{-1} and 2850 cm^{-1} corresponded to the asymmetric and symmetric stretching vibrations of CH_2 groups, respectively. The asymmetric stretching vibration of the C-H bond in CH_3 groups typically appeared at 2957 cm^{-1}, indicating that through physical grinding, the STA was successfully coated onto the surface of the tuff powder [21].

3.8. Role Efficiency Analysis Based on Gray Correlation

Using the grey relational analysis method, the influence of the STA content and MTP replacement rate on the mortar sorptivity and compressive strength at a w/c ratio of 0.4 and the influence of the MTP replacement rate and addition rate at a w/c ratio of 0.5 were studied separately.

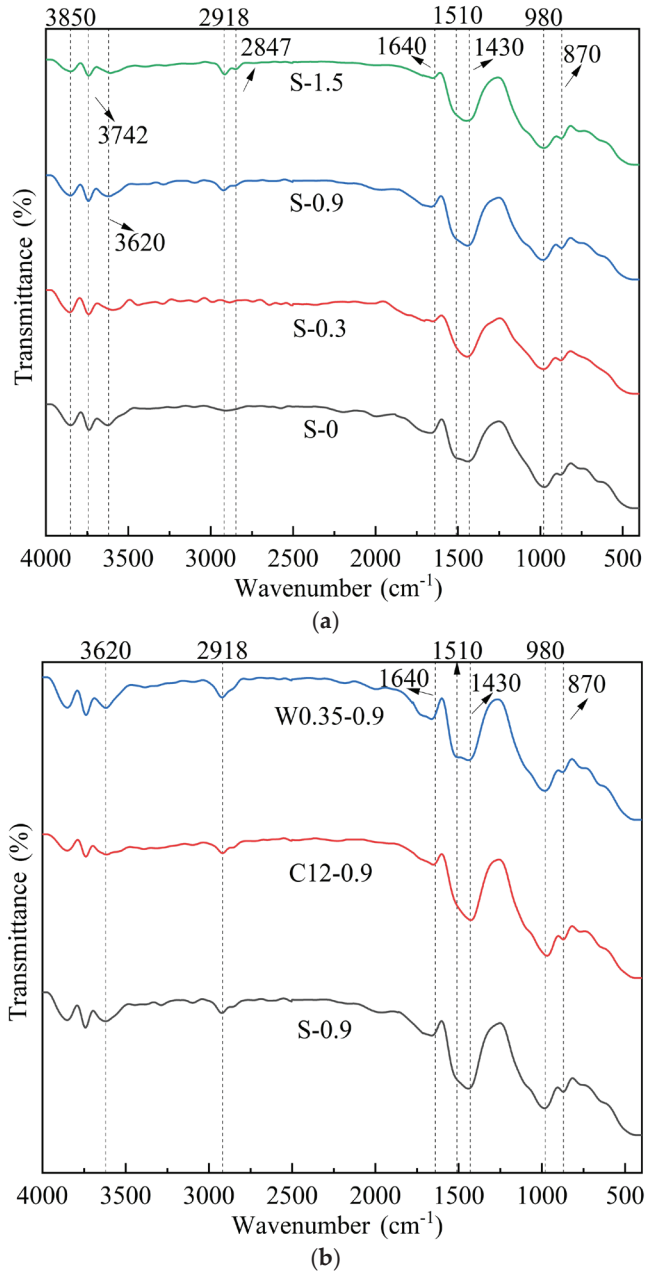

Figure 16. Influences of different factors on the infrared spectra of the STA–ethanol-modified mortar at 28d of age: (**a**) STA content and (**b**) w/c ratio and c/s ratio.

Under the conditions of co-grinding the STA with tuff powder, the optimal content of STA was 3% of the powder's mass. When the MTP replaced the cement at rates of 10%, 20%, and 30% of the cement's mass, the corresponding additions of STA were 0.3%, 0.6%, and 0.9% of the cement's mass, respectively. These values aligned with the STA addition values in the STA–ethanol solutions, and both had a w/c ratio of 0.4. Therefore, these three addition levels were used for comparative analysis. Table 8 illustrates the effects of the STA-ethanol solution and the MTP on the performance of cement mortar at a w/c ratio of 0.4. When the w/c ratio was 0.5, the proportions of MTP used to replace the cement and directly added to the mortar were the same at 10%, 20%, and 30%. Thus, an analysis was performed on the correlation between the content of MTP and the sorptivity and compressive strength of the mortar. Table 9 depicts the effects of the replacement rate and addition rate of MTP on the performance of cement mortar at a w/c ratio of 0.5.

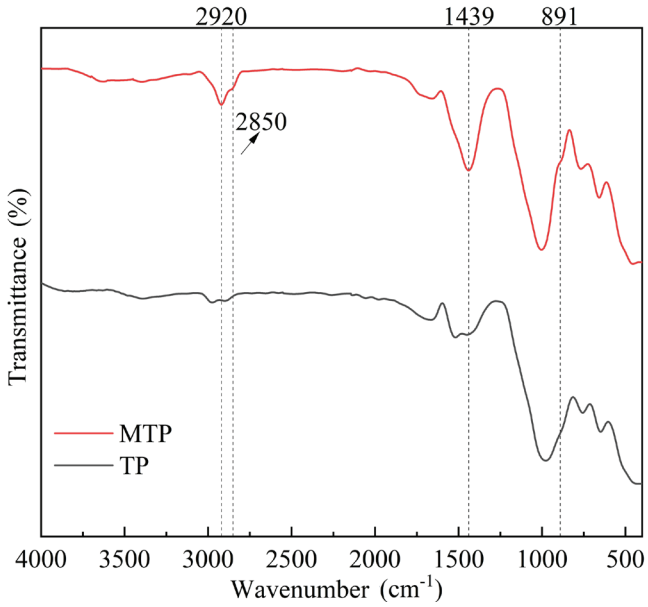

Figure 17. Infrared spectra of TP and MTP.

Table 8. Effects of the STA–ethanol solution and MTP on the performance of the cement mortar at a 0.4 w/c ratio.

STA Content (%)	0.4-STA–Ethanol		0.4-MTP Replacement	
	Sorptivity ($\mu m/s^{1/2}$)	Compressive Strength (MPa)	Sorptivity ($\mu m/s^{1/2}$)	Compressive Strength (MPa)
0	2.16	49.0	2.16	49.0
0.3	2.11	33.7	2.59	51.2
0.6	1.90	25.8	2.68	55.6
0.9	1.68	18.9	2.73	42.7

Table 9. Effects of the replacement rate and addition rate of the MTP on the performance of the cement mortar at a 0.5 w/c ratio.

MTP Replacement Rate (%)	Sorptivity ($\mu m/s^{1/2}$)	Compressive Strength (MPa)	MTP Addition Rate (%)	Sorptivity ($\mu m/s^{1/2}$)	Compressive Strength (MPa)
0	6.87	36.8	0	6.87	36.8
10	5.74	25.9	10	5.60	37.9
20	5.32	21.2	20	4.57	41.7
30	5.05	16.8	30	3.93	39.4

From Table 10, it can be observed that when the w/c ratio was 0.4, the addition of the STA–ethanol solution and the replacement of cement with MTP both significantly affected the sorptivity of the mortar. However, using MTP to partially replace the cement resulted in an increased sorptivity. Therefore, from the perspective of reducing the sorptivity and enhancing the impermeability of the mortar, the addition of the STA–ethanol solution was more appropriate. When the w/c ratio was 0.5, the impact on the sorptivity was similar between using the MTP to replace the cement and directly adding MTP.

Table 10. Gray correlation calculation results.

Sample	Sorptivity	Compressive Strength
0.4-STA–ethanol	0.999	0.938
0.4-MTP replacement	0.999	0.911
0.5-MTP replacement	0.985	0.983
0.5-MTP addition	0.985	0.976

When the w/c ratio was 0.5, replacing the cement with MTP had the greatest impact on the compressive strength of the mortar, but it led to a reduction in the compressive strength. Comparatively, directly adding MTP to the mortar had a lesser impact on the compressive strength and resulted in a certain degree of improvement.

4. Conclusions

(1) The XRD analysis results indicate that the incorporation of STA into cementitious materials did not affect the types of hydration products formed. The FTIR analysis confirmed that the STA could successfully graft onto the mortar, and physical grinding was able to coat the tuff powder with STA. The SEM test results demonstrated that the STA influenced the cement hydration process to a certain extent.

(2) The STA formed a hydrophobic film on the surface of the cement paste, which reduced the surface energy of the mortar, increased the contact angle, and enhanced the impermeability of the mortar. In the STA–ethanol-modified mortar, the contact angle initially increased and then decreased with the rise in the STA content. For a constant STA content, the contact angle increased as the w/c ratio decreased while it decreased with an increased c/s ratio. In the condition of a w/c ratio of 0.4, the STA addition of 0.9% by cement weight, and the c/s ratio of 1:1, the sorptivity of the mortar decreased by approximately 41.6% compared with the control group, which represented the highest value in this method's experimental group. This indicates that the c/s ratio had a significant impact on the efficiency of STA's effect.

(3) Replacing cement with TP, due to the low pozzolanic activity of TP, resulted in a reduction of the cementitious material, which failed to fully encapsulate the TP, which caused an increase in the sorptivity. Directly adding TP, however, reduced the porosity of the mortar due to its micro-aggregate effect, which led to a decrease in the sorptivity. With a w/c ratio of 0.4, the lowest sorptivity achieved with MTP still exceeded that of the control group. At a w/c ratio of 0.5, directly adding MTP at 30% of the cement mass resulted in the greatest reduction in sorptivity, where it reached 42.8%, a consequence of the combined effects of the STA and TP, both of which exerted positive influences.

(4) The STA adversely affected the compressive strength of the mortar. When using the STA–ethanol solution, each 0.3 wt% increase in the STA resulted in a 10–30% reduction in the compressive strength of the mortar. However, when the MTP was used to replace the cement, the micro-aggregate effect and mild pozzolanic activity of the TP partially mitigated the negative impact of the STA on the strength. When the MTP was directly added to the mortar, its compressive strength increased compared with the control group.

(5) Based on the grey relational analysis, the STA–ethanol solution could better enhance the impermeability of the mortar. When the w/c ratio was set to 0.5, the negative impact on the compressive strength of the mortar was the greatest when the MTP was used to replace the cement.

(6) Due to limitations in my knowledge and other objective conditions, this paper still contains numerous areas that require further exploration: Durability tests, such as those examining frost resistance and resistance to chloride ion penetration, can be conducted to deepen the study of the effects of STA on the durability of cement-based materials. This would aid in summarizing the patterns and mechanisms by which STA influences the durability of such materials. Additionally, the impact of STA–ethanol solutions and MTP on cement hydration can be further analyzed through techniques such as heat of hydration analysis.

Author Contributions: Conceptualization, X.W. and H.W.; data curation, X.W. and Y.M.; formal analysis, W.Z. and Y.W.; investigation, D.D. and Y.W.; methodology, X.W. and W.Z.; resources, X.W. and Y.M.; supervision, X.W., H.W. and Y.M.; writing—original draft preparation, W.Z. and D.D.; writing—review and editing, X.W., Y.W., H.W. and Y.M. All authors have read and agreed to the published version of the manuscript.

Funding: This study was funded by the National Natural Science Foundation Project (NSFC 52178185, U2333216), Key Technology Projects in the Transportation Industry (2022-MS1-079), and Xizang Autonomous Region Science and Technology Department Base and Talent Plan Project (XZ202402JD0002).

Institutional Review Board Statement: Not applicable.

Informed Consent Statement: Not applicable.

Data Availability Statement: Data are contained within this article.

Conflicts of Interest: Author Hongke Wu was employed by the company Longxi County Highway Management Station. Author Dunzhu Danzeng was employed by the company Xizang Gaozheng Building Materials Company. Author Yahong Meng was employed by the company Gansu Yuanlong Road and Bridge Mechanized Highway Engineering Co., Ltd. The remaining authors declare that the research was conducted in the absence of any commercial or financial relationships that could be construed as a potential conflict of interest.

References

1. Xiao, T.; Niankun, Z. Durability Prediction Method of Concrete Soil Based on Deep Belief Network. *Adv. Civ. Eng.* **2022**, *2022*, 4338306.
2. Zhang, F.; Hu, Z.; Wei, F.; Wen, X.; Li, X.; Dai, L.; Liu, L. Study on concrete deterioration in different NaCl-Na_2SO_4 solutions and the mechanism of Cl^- diffusion. *Materials* **2021**, *14*, 50–54. [CrossRef] [PubMed]
3. Crespi, P.; Zucca, M.; Valente, M.; Longarini, N. Influence of corrosion effects on the seismic capacity of existing RC bridges. *Eng. Fail. Anal.* **2022**, *140*, 106546. [CrossRef]
4. Al-Zu'bi, M.; Fan, M.; Al Rjoub, Y.; Ashteyat, A.; Al-Kheetan, M.J.; Anguilano, L. The effect of length and inclination of carbon fiber reinforced polymer laminates on shear capacity of near-surface mounted retrofitted reinforced concrete beams. *Struct. Concr.* **2021**, *22*, 3677–3691. [CrossRef]
5. Papadakis, G.V. Effect of supplementary cementing materials on concrete resistance against carbonation and chloride ingress. *Cem. Concr. Res.* **2000**, *30*, 291–299. [CrossRef]
6. Muzenski, S.; Flores-Vivian, I.; Sobolev, K. Hydrophobic engineered cementitious composites for highway applications. *Cem. Concr. Compos.* **2015**, *57*, 68–74. [CrossRef]
7. Gao, Y.; Qu, L.; He, B.; Dai, K.; Fang, Z.; Zhu, R. Study on effectiveness of anti-icing and deicing performance of super-hydrophobic asphalt concrete. *Constr. Build. Mater.* **2018**, *191*, 270–280. [CrossRef]
8. Husni, H.; Nazari, M.R.; Yee, H.M.; Rohim, R.; Yusuff, A.; Ariff, M.A.M.; Ahmad, N.N.R.; Leo, C.P.; Junaidi, M.U.M. Superhydrophobic rice husk ash coating on concrete. *Constr. Build. Mater.* **2017**, *144*, 385–391. [CrossRef]
9. Li, G.; Yang, B.; Guo, C.; Du, J.; Wu, X. Time dependence and service life prediction of chloride resistance of concrete coatings. *Constr. Build. Mater.* **2015**, *83*, 19–25. [CrossRef]
10. Mora, E.; González, G.; Romero, P.; Castellón, E. Control of water absorption in concrete materials by modification with hybrid hydrophobic silica particles. *Constr. Build. Mater.* **2019**, *221*, 210–218. [CrossRef]
11. Li, K.; Wang, Y.; Zhang, X.; Wu, J.; Wang, X.; Zhang, A. Intrinsically hydrophobic magnesium oxychloride cement foam for thermal insulation material. *Constr. Build. Mater.* **2021**, *288*, 123–129. [CrossRef]
12. Kumar, S.; Kumar, R.; Bandopadhyay, A. Innovative methodologies for the utilization of wastes from metallurgical and allied industries. *Resour. Conserv. Recycl.* **2006**, *48*, 301–314. [CrossRef]
13. Wang, Z.; Han, Z.L.; Li, H.J.; Huang, F.L.; Yi, Z.L. Study on Performance of Manufactured Sand Concrete for Prestressed Structures in Railway Engineering. *Railw. Eng.* **2019**, *59*, 11–16.
14. He, H.; Wang, Y.; Wang, J. Compactness and hardened properties of machine-made sand mortar with aggregate micro fines. *Constr. Build. Mater.* **2020**, *250*, 118828. [CrossRef]

15. Hao, T.; Tian, W.Q.; Cao, L.Q. Large amount of waste granite stone powder on the mechanical properties of mortar. *Concrete* **2021**, *3*, 103–106+111.
16. Zerbo, L.; Sawadogo, M.; Sawadogo, Y.; Salogo, S.; Ouedrago, M.; Seynou, M.; Lecomte-Nana, G.; Blanchart, P. Usability of a Natural Tuff as Admixture in Clinker and Its Influence on the Physico-Chemical and Mechanical Properties of Mortar. *J. Miner. Mater. Charact. Eng.* **2021**, *9*, 480–498.
17. Liu, S.; Fang, P.; Wang, H.; Kong, Y.; Ouyang, L. Effect of tuff powder on the hydration properties of composite cementitious materials. *Powder Technol.* **2021**, *380*, 59–66. [CrossRef]
18. Wong, H.S.; Barakat, R.; Alhilali, A.; Saleh, M.; Cheeseman, C.R. Hydrophobic concrete using waste paper sludge ash. *Cem. Concr. Res.* **2015**, *70*, 9–20. [CrossRef]
19. Qu, Z.; Yu, Q. Synthesizing super-hydrophobic ground granulated blast furnace slag to enhance the transport property of lightweight aggregate concrete. *Constr. Build. Mater.* **2018**, *191*, 176–186. [CrossRef]
20. Karthick, S.; Park, D.J.; Lee, Y.S.; Saraswathy, V.; Lee, H.S.; Jang, H.O.; Choi, H.J. Development of water-repellent cement mortar using silane enriched with nanomaterials. *Prog. Org. Coat.* **2018**, *125*, 48–60. [CrossRef]
21. Tittarelli, F.; Moriconi, G. Comparison between surface and bulk hydrophobic treatment against corrosion of galvanized reinforcing steel in concrete. *Cem. Concr. Res.* **2011**, *41*, 609–614. [CrossRef]
22. Albayrak, A.T.; Yasar, M.; Gurkaynak, M.A.; Gurgey, I. Investigation of the effects of fatty acids on the compressive strength of the concrete and the grindability of the cement. *Cem. Concr. Res.* **2005**, *35*, 400–404. [CrossRef]
23. Kobayashi, K.; Kojima, Y. Effect of fine crack width and water cement ratio of SHCC on chloride ingress and rebar corrosion. *Cem. Concr. Compos.* **2017**, *80*, 235–244. [CrossRef]
24. Pane, I.; Hansen, W. Investigation of blended cement hydration by isothermal calorimetry and thermal analysis. *Cem. Concr. Res.* **2005**, *35*, 1155–1164. [CrossRef]
25. Lei, L.; Wang, Q.; Xu, S.; Wang, N.; Zheng, X. Fabrication of superhydrophobic concrete used in marine environment with anti-corrosion and stable mechanical properties. *Constr. Build. Mater.* **2020**, *251*, 118946. [CrossRef]
26. Huhtamäki, T.; Tian, X.; Korhonen, J.T.; Ras, R.H. Surface-wetting characterization using contact-angle measurements. *Nat. Protoc.* **2018**, *13*, 1521–1538. [CrossRef]
27. Feng, Z.; Wang, F.; Xie, T.; Ou, J.; Xue, M.; Li, W. Integral hydrophobic concrete without using silane. *Constr. Build. Mater.* **2019**, *227*, 116678. [CrossRef]
28. Wang, F.; Zhang, M.; Lei, S.; Ou, J.; Li, W. Rapid preparation of superhydrophobic surface on cement stone. *Appl. Phys. A* **2019**, *125*, 386. [CrossRef]
29. Chen, Y.; Li, Z.; Wu, K. Influence of binder-sand ratio on fiber-reinforced cementitious composites performance. *Concrete* **2018**, *2020*, 68–70+74.
30. Li, P.P.; Xiong, J.B.; Fan, Z.H. Influence of Stone Dust Content in Manufactured Sand on Properties of Concrete with Volcanic Ash Incorpoated. *J. Mater. Sci. Eng.* **2019**, *37*, 828–832.
31. Chen, B.; Wang, J.L.; Yang, Y.H.; Zhou, M.K. Effects of Stone-dust on Resistance to Chlorine Ion Permeating and Volume Stability of C80 Manufactured-sand Concrete. *J. Wuhan Univ. Technol.* **2007**, *8*, 41–43.
32. Wang, N.; Wang, Q.; Xu, S.; Zheng, X.; Zhang, M. Facile fabrication of amphiphobic surfaces on copper substrates with a mixed modified solution. *RSC Adv.* **2019**, *9*, 17366–17372. [CrossRef] [PubMed]
33. Tian, H.; Qiao, H.; Feng, Q.; Han, W. Effect of Stone Powder Substitution Rate on the Performance and Microstructure of Mechanism Sand Polymer-bonded Mortar. *Mater. Rep.* **2024**, *38*, 138–144.
34. Aissa, H.Y.; Goual, I.; Benabed, B. Mix-design and properties of self-compacting concrete made with calcareous tuff. *J. Build. Eng.* **2020**, *27*, 100997. [CrossRef]
35. Lagazzo, A.; Vicini, S.; Cattaneo, C.; Botter, R. Effect of fatty acid soap on microstructure of lime-cement mortar. *Constr. Build. Mater.* **2016**, *116*, 384–390. [CrossRef]
36. Wang, X.; Hou, X.; Gan, L.; Wang, Y.; Bian, Q.; Zhang, J. Pozzolanic Reactivity and Hydration Properties Assessment of Tuff Powder in Composite Cementitious Materials. *Mater. Rep.* **2022**, *36*, 147–154.
37. Falchi, L.; Müller, U.; Fontana, P.; Izzo, F.C.; Zendri, E. Influence and effectiveness of water-repellent admixtures on pozzolana–lime mortars for restoration application. *Constr. Build. Mater.* **2013**, *49*, 272–280. [CrossRef]
38. Falchi, L.; Zendri, E.; Müller, U.; Fontana, P. The influence of water-repellent admixtures on the behaviour and the effectiveness of Portland limestone cement mortars. *Cem. Concr. Compos.* **2015**, *59*, 107–118. [CrossRef]
39. Lu, Y.; Miller, J.D. Carboxyl stretching vibrations of spontaneously adsorbed and LB-transferred calcium carboxylates as determined by FTIR internal reflection spectroscopy. *J. Colloid Interface Sci.* **2002**, *256*, 41–52. [CrossRef]
40. Spathi, C.; Young, N.; Heng, J.Y.; Vandeperre, L.J.; Cheeseman, C.R. A simple method for preparing super-hydrophobic powder from paper sludge ash. *Mater. Lett.* **2015**, *142*, 80–83. [CrossRef]
41. Qu, Z.Y.; Alam, Q.; Gauvin, F.; Dezaire, T.; Brouwers, H.J.H.; Wang, F.Z. Development of water-resisting mortar by incorporation of functionalized waste incineration ashes. *J. Clean. Prod.* **2020**, *249*, 119341. [CrossRef]

42. Li, Q.; Yang, K.; Yang, C. An alternative admixture to reduce sorptivity of alkali-activated slag cement by optimising pore structure and introducing hydrophobic film. *Cem. Concr. Compos.* **2019**, *95*, 183–192. [CrossRef]
43. Lu, B.; Shi, C.; Zhang, J.; Wang, J. Effects of carbonated hardened cement paste powder on hydration and microstructure of Portland cement. *Constr. Build. Mater.* **2018**, *186*, 699–708. [CrossRef]

coatings

MDPI

Article

Performance Evaluation of Waterborne Epoxy Resin-Reinforced SBS, Waterborne Acrylate or SBR Emulsion for Road

Hao Fu [1] and Chaohui Wang [2,*]

[1] Institute of Future Civil Engineering Sciences and Technology, Chongqing Jiaotong University, Chongqing 400074, China; 990202400014@cqjtu.edu.cn
[2] School of Highway, Chang'an University, Xi'an 710064, China
* Correspondence: wchh0205@chd.edu.cn; Tel.: +86-13379278369

Abstract: To obtain waterborne polymer-modified emulsified asphalt materials with better comprehensive performance, waterborne polymer modifiers including waterborne epoxy resin (WER)-reinforced styrene–butadiene–styrene block copolymer (SBS), waterborne acrylate (WA) or styrene butadiene rubber (SBR) emulsion were prepared. The mechanical strength, toughness, adhesion and impact resistance of these waterborne polymers were evaluated. Furthermore, the correlation between the performance indicators of the waterborne polymers was analyzed. Based on Fourier transform infrared (FTIR) spectroscopy and thermogravimetric (TG) analysis, the mechanism of WER-modified SBS and WA was characterized. The results show that adding 10%–15% WER can significantly improve the mechanical properties of the waterborne polymer. The performances of modified SBS and WA are better than that of modified SBR. When the content of WER is 10%, the tensile strength, elongation at break and pull-off strength of WER-modified SBS and WA are 4.80–6.38 MPa, 476.3%–579.6% and 1.62–1.70 MPa, respectively. The mechanical strength and breaking energy of the waterborne polymers show a significant linear correlation with their application properties such as adhesion, bonding and impact resistance. FTIR and TG analyses indicate that WER-modified SBS or WA prepared via emulsion blending undergo primarily physical modifications, enhancing thermal stability while promoting crosslinking and curing.

Keywords: road materials; waterborne epoxy resin; SBS; waterborne acrylate; SBR

1. Introduction

The modified emulsified asphalt material can be sprayed and mixed at room temperature, which can reduce energy consumption and pollutant emission. It has the advantages of environmental protection, energy conservation, safety and convenient construction. It has been widely used in bridge deck waterproof bonding layers, pavement tack coats, micro-surfacing, fog seals and cold mix binder mixtures. Compared with the preparation of modified emulsified asphalt by emulsifying polymer-modified asphalt, the preparation method of combining waterborne polymer and emulsified asphalt cannot only effectively avoid the problem of the high viscosity and difficult emulsification of modified asphalt, but also avoid the destructive effect of high temperature and high speed shear on the polymer modifier in the emulsification process of modified asphalt. In recent years, waterborne polymer-modified emulsified asphalt has been widely studied and applied.

At present, commonly used waterborne polymer emulsified asphalt modifiers include styrene butadiene rubber (SBR), styrene–butadiene–styrene block copolymer (SBS), waterborne acrylate (WA) emulsion, etc. [1–4]. Hu et al. [5] prepared modified emulsified

asphalt with SBR and SBS emulsion, and comprehensively evaluated its basic properties such as penetration, softening point and ductility of evaporation residue. At the same time, some researchers [6], based on dynamic shear rheological and bending beam rheological tests, used complex modulus (G*), rutting resistance factor (G*/sinδ), creep stiffness (s), creep rate (m) and other indicators to evaluate the high-temperature and low-temperature rheological properties of the evaporation residue of modified emulsified asphalt. The road performance of modified emulsified asphalt applied in different application scenarios such as bridge deck waterproof bonding layers, pavement tack coats, micro-surfacing [7,8], fog seals [9–11] and cold mix binder mixtures has been systematically evaluated. Relevant research and application showed that SBR, SBS, WA and other waterborne polymer modifiers can improve the bonding performance, temperature sensitivity and aging resistance of emulsified asphalt to a certain extent. At the same time, Xu et al. [1] pointed out that the high temperature and bonding properties of SBR-modified emulsified asphalt need to be improved, the storage stability of SBS-modified emulsified asphalt is poor and the water stability needs to be improved.

In the WER-modified emulsified asphalt, the WER and curing agent form a three-dimensional network structure through physical–chemical crosslinking, so that it retains the thermal stability, bonding strength and waterproof performance of the epoxy resin, and has the construction advantages of emulsified asphalt at the same time [12–14]. In recent years, to meet the comprehensive effect of complex climatic conditions, increasing traffic volume and heavy-duty vehicles, etc., higher requirements for road construction and maintenance quality have been put forward. Many studies have been carried out on WER-modified emulsified asphalt and WER composite SBR- or SBS-modified emulsified asphalt [15–17]. Yao et al. [18] studied the effects of WER/SBR composite modification on the rheological properties, low temperature crack resistance, thermal stability and micro-morphology of evaporation residues of emulsified asphalt. Zhang et al. [19] studied the bonding and waterproof properties of WER/SBR-modified emulsified asphalt when applied to the waterproof bonding layer of a bridge deck. Liu et al. [20] used WER/SBR composite-modified emulsified asphalt as a binder to overcome the problems of insufficient wear resistance, rutting resistance and water stability of ordinary micro-surfacing. Zhang et al. [21] prepared the cold mix binder mixture of WER/SBR composite-modified emulsified asphalt. Li et al. [22] used WER/SBS composite-modified emulsified asphalt as binder to prepare a color ultra-thin wearing course. Yao et al. [23] used WER/SBR composite-modified emulsified asphalt to prepare a cold recycled mixture, and studied its fusion mechanism with aging asphalt. The above studies show that WER can further improve the application effect of SBR-, SBS- and WA-modified emulsified asphalt in the field of road engineering. However, the current studies on waterborne polymer-modified emulsified asphalt mainly focuses on its basic performance evaluation, modification mechanism analysis and road performance evaluation under different application scenarios. Existing studies have basically directly added SBR, SBS, WER emulsion, etc., to emulsified asphalt, and few studies have optimized waterborne polymer modifiers based on their own mechanical strength, deformation ability, adhesion and other properties. In addition, there are many types of waterborne polymer modifiers on the market with different properties. It is necessary to further ensure the performance of polymer-modified emulsified asphalt by controlling the properties of waterborne polymer modifiers.

Based on this, WER-modified SBS, WA and SBR emulsions were prepared. The mechanical strength, toughness, adhesion and impact resistance of these waterborne polymers were evaluated. The performance differences between various waterborne polymers and the performance improvement effect of WER were clarified. The correlation between the performance indicators of the waterborne polymers was analyzed. Furthermore, the mech-

anism of WER strengthening SBS and WA was characterized. This is expected to lay a foundation for the performance evaluation of waterborne polymer emulsified asphalt modifiers and the preparation of higher performance modified emulsified asphalt materials.

2. Materials and Methods

2.1. Raw Materials

The physical blending method has the advantages of being a simple and controllable preparation process, adjustable mixing proportions and performance, and the stable performance of different batches of composite emulsion. Therefore, this study used the physical blending method to prepare WER-modified SBS, WA and SBR emulsions. Cationic SBS emulsion, non-ionic WA emulsion and cationic SBR emulsion commonly used in the road engineering field produced by Jinan Shanhai Chemical Co., Ltd. (Jinan, China), were selected. Bisphenol A type E-51 epoxy resin, which is liquid at room temperature, was selected, and it was emulsified by the phase inversion method. A non-ionic modified alicyclic amine WER curing agent that can be cured at room temperature was selected. The main technical indicators of each material are shown in Table 1.

Table 1. The main technical indexes of each material.

No.	Materials	Basic Performance Indices
1	SBS	Milky white viscous liquid; solid content, 48%–52%; density, ≥1.10 g/cm^3; viscosity, 10–40 mPa.s; pH, 6–7
2	WA	Milky translucent liquid; solid content, 46%–48%; density, ≥1.05 g/cm^3; viscosity, 350–500 mPa.s; pH, 7–8
3	SBR	Milky white viscous liquid; solid content, 49%–51%; density, ≥1.10 g/cm^3; viscosity, 50–350 mPa.s; pH, 7–9
4	E-51 epoxy resin	Transparent liquid; molecular weight, 350–400; epoxy value, 0.48–0.54 (mol/100 g)
5	WER curing agent	Non-ionic yellowish transparent liquid; solid content, 48%–52%; density, 1.05–1.10 g/cm^3; active hydrogen equivalent (solids), 291; viscosity, 10 Pa·s; pH, 11–13

2.2. Preparation of WER-Modified SBS, WA or SBR Emulsions

The preparation process of WER-modified SBS, WA or SBR emulsions is as follows:

1. Preparation of WER emulsion: First, the epoxy resin was emulsified by the phase inversion method [24]. A certain weight of emulsified epoxy resin, WER curing agent and defoaming leveling agent were weighed, which were stirred at the rate of 200–300 r/min for 30 s to mix evenly, and then stirred at the rate of 400–500 r/min for 3 min. Finally, WER emulsion was obtained after defoaming treatment.
2. Modification of SBS, WA or SBR emulsions: A certain weight of WER emulsion was weighed and added to SBS, WA or SBR emulsions. First, they were sheared and stirred at low speed (100–300 r/min) for 3 min by using a high-speed mixing shear apparatus, and then sheared and stirred at high speed (500–800 r/min) for 2 min. During the mixing process, the shearing speed can be adjusted appropriately. After defoaming, the WER-modified SBS, WA or SBR emulsions were obtained.

The content (mass fraction) of WER was preliminarily set at 6 levels: 0%, 5%, 10%, 15%, 20% and 30%. First, observe whether there will be demulsification, agglomeration, flocculent matter or thickening in the mixing process of WER emulsion with SBS, WA or

SBR emulsion. If so, it will be determined as an infeasible scheme, and only the feasible scheme will be further studied. When the WER content reaches 30%, flocculent matter forms during the preparation of the modified SBR lotion; therefore, this formulation is excluded from further study.

2.3. Performance Test Method

Mechanical property tests including tensile, low-temperature impact and pull-off, as well as FTIR and TG tests, were carried out in this study. In each group, five specimens were tested, and the average of three valid measurements was reported.

2.3.1. Tensile Test

Referring to the tensile test method in Water quality asphalt waterproof coating for highway (JT/T 535-2015), China [25], the tensile strength, elongation at break and breaking energy were used to evaluate the mechanical strength, deformation capacity and toughness of the waterborne polymers, respectively. First, the prepared waterborne polymer was poured into the mold coated with release agent and cured at 25 °C. To improve the uniformity of the film formation, the film formation was carried out two times with an interval of 24 h to form a polymer film with a thickness of 2 ± 0.2 mm. After the polymer film was formed, it was cured at 35–40 °C for 7 days, and then the dumbbell-shaped test specimen was cut. Finally, the tensile test was carried out at 25 °C, and the tensile rate was 100 mm/min. The process of specimen fabrication and the performance test is shown in Figure 1.

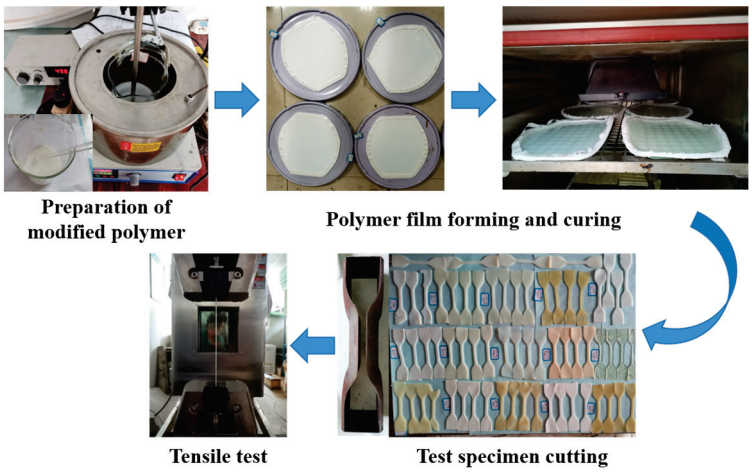

Figure 1. The process of specimen fabrication and tensile performance test.

Breaking energy represents the work per unit volume required to stretch a specimen to fracture, determined by integrating the area under the tensile stress–strain curve [26]. In this study, breaking energy served as a measure of waterborne polymer toughness and was calculated using Equation (1):

$$W_t = \int_0^{\varepsilon_b} \sigma_{t(\varepsilon)} \mathrm{d}\varepsilon \quad (1)$$

where W_t is the tensile breaking energy, J/m^3; σ_t is the tensile stress, MPa; ε is the tensile strain; and ε_b is the maximum tensile strain.

2.3.2. Adhesion Test of Waterborne Polymer and Aggregate

Referring to the water boiling method in the Standard Test Methods of Bitumen and Bituminous Mixtures for Highway Engineering (JTG E20-2011), China [27], an ultrasonic wave was used to simulate the action of dynamic water pressure to accelerate the shedding

of the waterborne polymers from the aggregate surface [13]. The adhesion between the waterborne polymer and aggregate was evaluated using the shedding rate of polymer after ultrasonic treatment for 30 min at 100 °C.

2.3.3. Low-Temperature Impact Test

The −20 °C impact strength was used to evaluate the low impact resistance and toughness of the waterborne polymers according to the test methods for the properties of a resin casting body (GB/T 2567-2021), China [28]. Films (2.0 ± 0.2 mm thickness) were formed, cured and cut into 80 mm × 10 mm strips. Specimens were conditioned at −20 °C for 4 h before immediate testing using a simple beam impact instrument. Impact strength was then calculated.

2.3.4. Pull-Off Strength Test

According to the relevant requirements in Water quality asphalt waterproof coating for highway (JT/T 535-2015), China [25], the pull-off strength was used to evaluate the bonding performance of the waterborne polymers. The waterborne polymer (1.0 kg/m^2) was uniformly applied to C30-grade cement concrete specimens and cured at 25 °C for 3 days. A steel puller was bonded to the cured surface using rapid-cure AB adhesive, and the pull-off strength was tested with a drawing tester at a loading rate of 10 mm/min.

2.3.5. Attenuated Total Reflection FTIR Test

Attenuated total reflection Fourier transform infrared spectroscopy (ATR-FTIR) was used to identify specific functional groups and characterize chemical changes during the modification of the waterborne polymers. Spectra were acquired using a Thermo Scientific Nicolet iS20 FTIR spectrometer with a wavenumber range of 4000–600 cm^{-1} and a resolution of ≤4 cm^{-1}.

2.3.6. TG Test

The thermogravimetric (TG) analysis was carried out using a Netzsch STA449 F5 TG analyzer produced by Germany's Naichi Instrument Manufacturing Co., Ltd. (Krefeld, Germany). Testing parameters included a temperature range of 30 °C to 600 °C, a heating rate of 10 °C/min and a nitrogen atmosphere.

3. Results and Discussion

3.1. Composition Optimization and Performance Evaluation of WER-Modified SBS, WA or SBR

The mechanical strength, deformation ability, toughness, adhesion, impact resistance and bonding properties of WER-modified SBS, WA or SBR were evaluated. The performance differences between various waterborne polymers and the performance improvement effect of WER were clarified.

3.1.1. Tensile Properties

Based on the tensile test, the tensile strength, elongation at break and breaking energy were used to evaluate the mechanical strength, deformation capacity and toughness of each waterborne polymer, respectively. The results are shown in Figures 2–5.

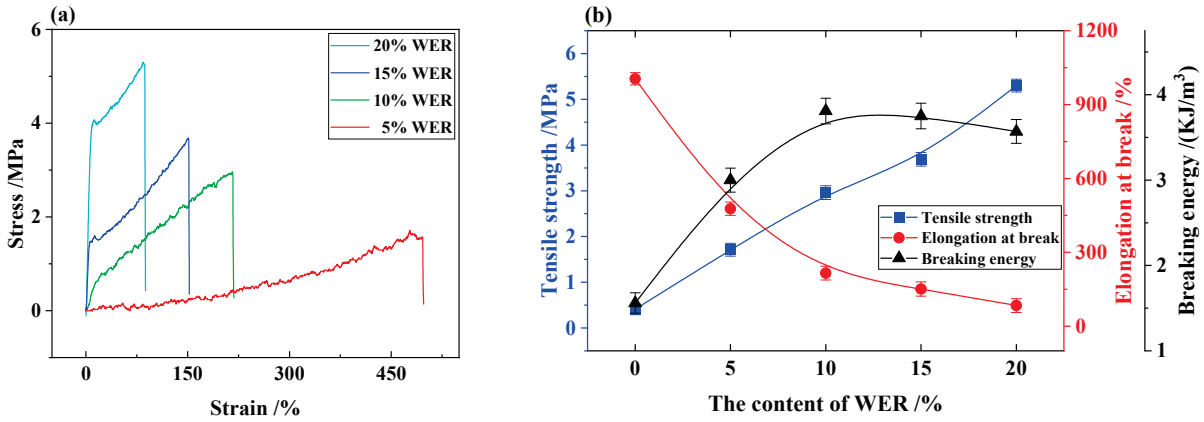

Figure 2. Tensile properties of WER-modified SBR: (**a**) stress–strain curve; (**b**) tensile strength, elongation at break and breaking energy.

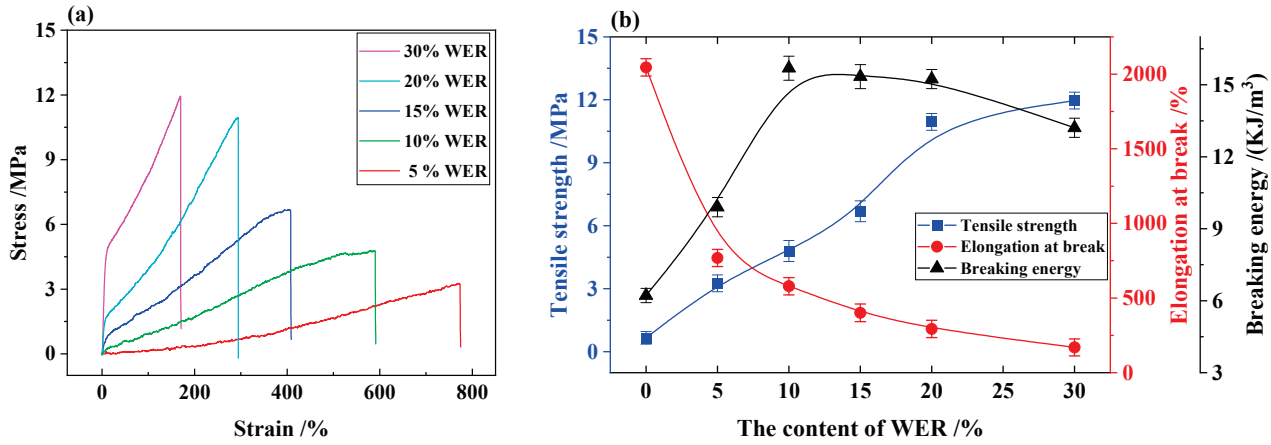

Figure 3. Tensile properties of WER-modified SBS: (**a**) stress–strain curve; (**b**) tensile strength, elongation at break and breaking energy.

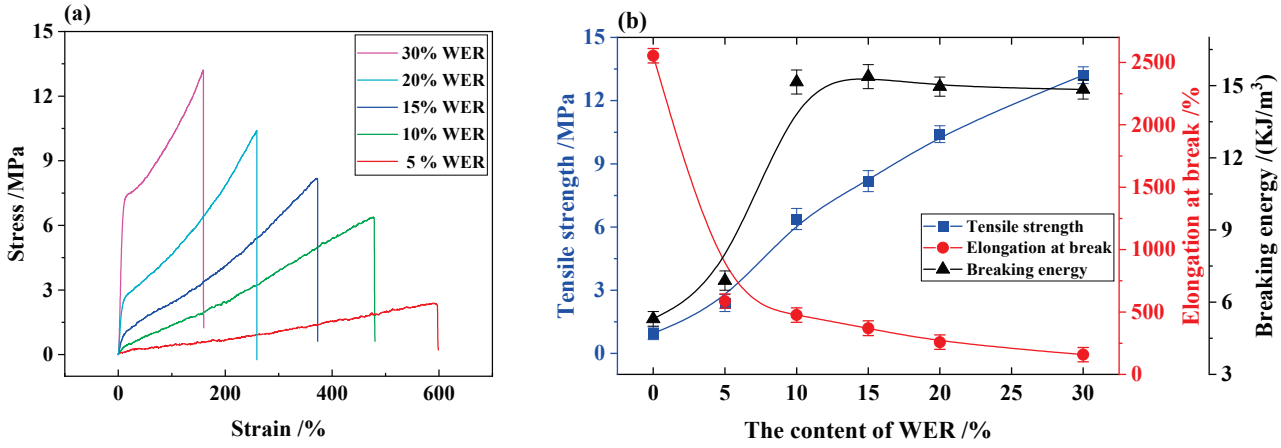

Figure 4. Tensile properties of WER-modified WA: (**a**) stress–strain curve; (**b**) tensile strength, elongation at break and breaking energy.

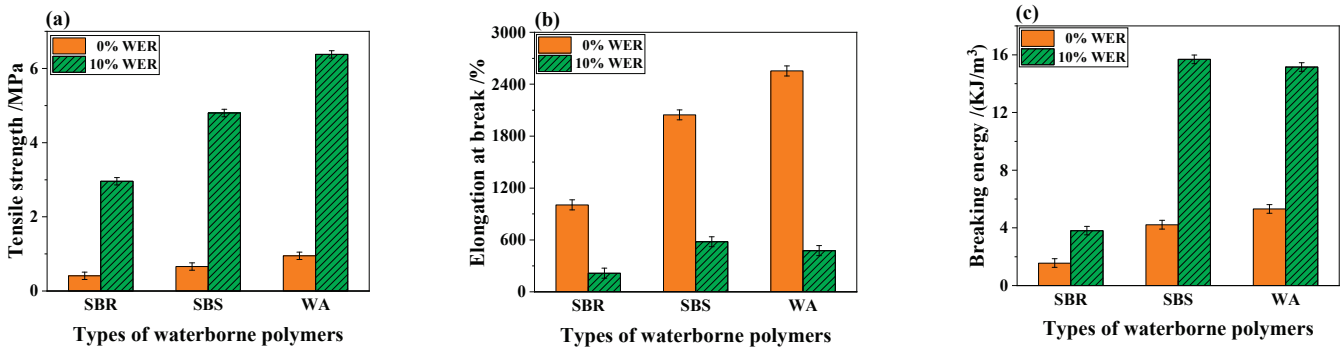

Figure 5. Comparison of tensile properties of different types of waterborne polymers: (**a**) tensile strength; (**b**) elongation at break and (**c**) breaking energy.

Figures 2–5 show that with the increase in the content of WER, the tensile strength and tensile modulus of these waterborne polymers continue to increase, the elongation at break gradually decreases, and the breaking energy first increases and then decreases. When the content of WER increases from 0% to 10%, the tensile strength and breaking energy increase by about 600% and 200% respectively, and the mechanical strength and toughness of the waterborne polymers are significantly improved. When the content of WER is 10%–15%, the breaking energy of the modified polymers reaches the maximum value. With the continuous increase in the content of WER, the growth rate of the tensile strength of the waterborne polymers is obviously decreased. The modified waterborne polymers show the brittleness of epoxy resin, and the breaking energy shows a decreasing trend. It shows that adding an appropriate content of WER can improve the mechanical strength, tensile modulus and toughness of waterborne polymer to a certain extent, and increase its ability to resist deformation and damage. The content of WER is suggested to be 10%–15%.

Under the same content of WER, the tensile strength, elongation at break and breaking energy of WER-modified SBS or WA are significantly better than that of modified SBR, and the difference between the tensile properties of modified SBS and modified WA is small. When the content of WER is 10%, the tensile strength, elongation at break and breaking energy of WER-modified SBS are 4.80 MPa, 579.60% and 15.69 KJ/m^3, respectively.

3.1.2. Adhesion Performance

The waterborne polymer shall have sufficient adhesion performance to ensure the adhesion performance of modified emulsified asphalt. The adhesion and thermal stability of the waterborne polymers to the aggregate were evaluated by using the shedding rate of polymer after ultrasonic treatment for 30 min at 100 °C. The test results are shown in Figure 6.

It can be seen from Figure 6 that with the increase in the content of WER, the shedding rate of the polymers gradually decreases, and the adhesion performance of the waterborne polymers continues to grow. Under the same content of WER, the shedding rate of WER-modified WA is the lowest, followed by modified SBS, and the shedding rate of modified SBR is the highest. When the content of WER is increased from 0% to 10%, the shedding rate of modified WA or SBS is reduced from 2.5%–4.5% to less than 1%. The modified polymers would hardly fall off the surface of the aggregate after ultrasonic treatment for 30 min at 100 °C, showing excellent thermal stability and adhesion properties. It shows that WER can effectively enhance the adhesion, water stability and heat resistance of SBS lotion, waterborne acrylate and styrene butadiene latex.

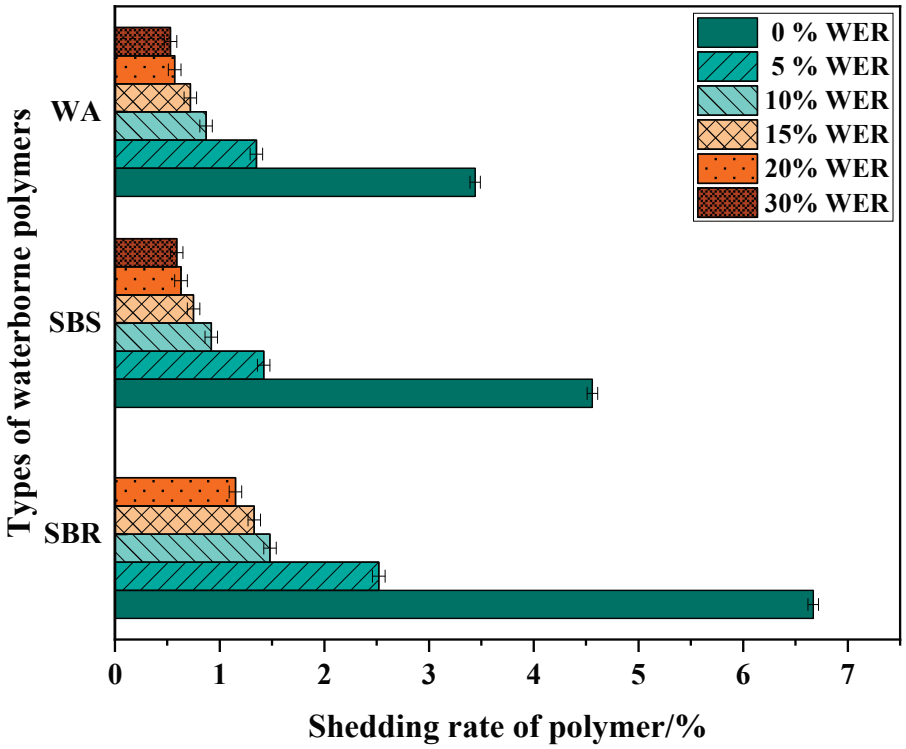

Figure 6. Shedding rate of modified SBS, WA or SBR under different WER contents.

3.1.3. Impact Resistance

The −20 °C impact strength was used to evaluate the low-temperature toughness of the waterborne polymers. The test results are shown in Figure 7.

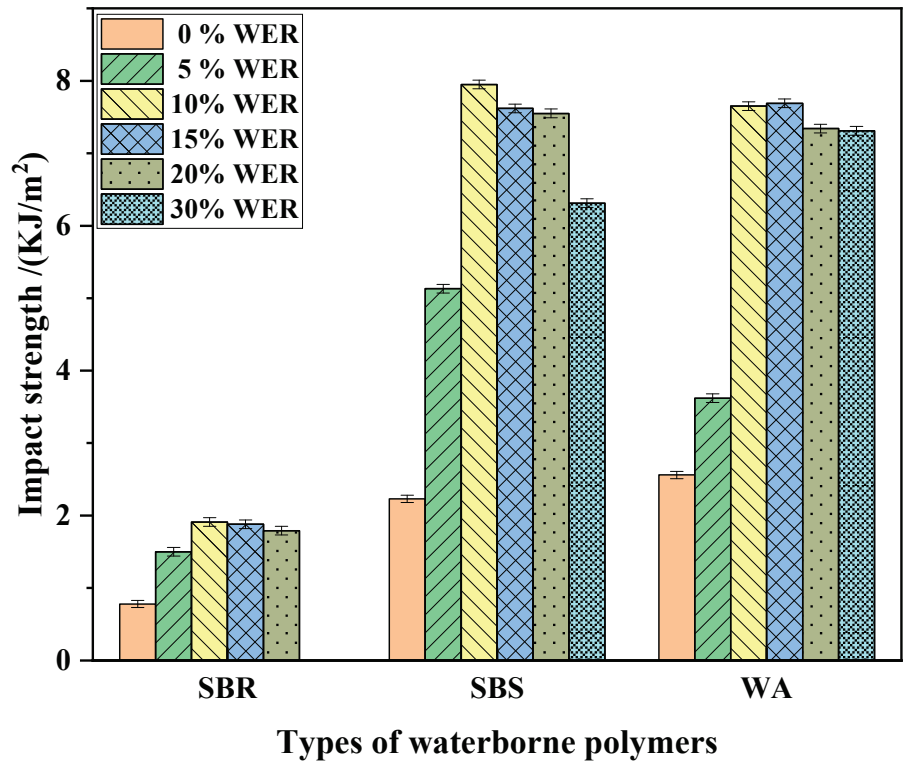

Figure 7. The −20 °C impact strength of modified SBS, WA or SBR under different WER contents.

Figure 7 shows that with the increase in the content of WER, the crosslinking degree of the waterborne polymers continues to improve, and the impact strength increases to

varying degrees. When the content of WER is 10%–15%, the −20 °C impact strength of these modified waterborne polymers reaches the maximum value, showing better low-temperature toughness. With the continuous increase in the content of WER, the modified waterborne polymer shows the brittleness of epoxy resin, the impact strength showed a decreasing trend and the content of WER was further determined to be 10%–15%.

3.1.4. Bonding Performance

Based on the pull-off test, the pull-out strength was used to evaluate the influence of the content of WER on the bonding performance of various waterborne polymers. The test results are shown in Figure 8.

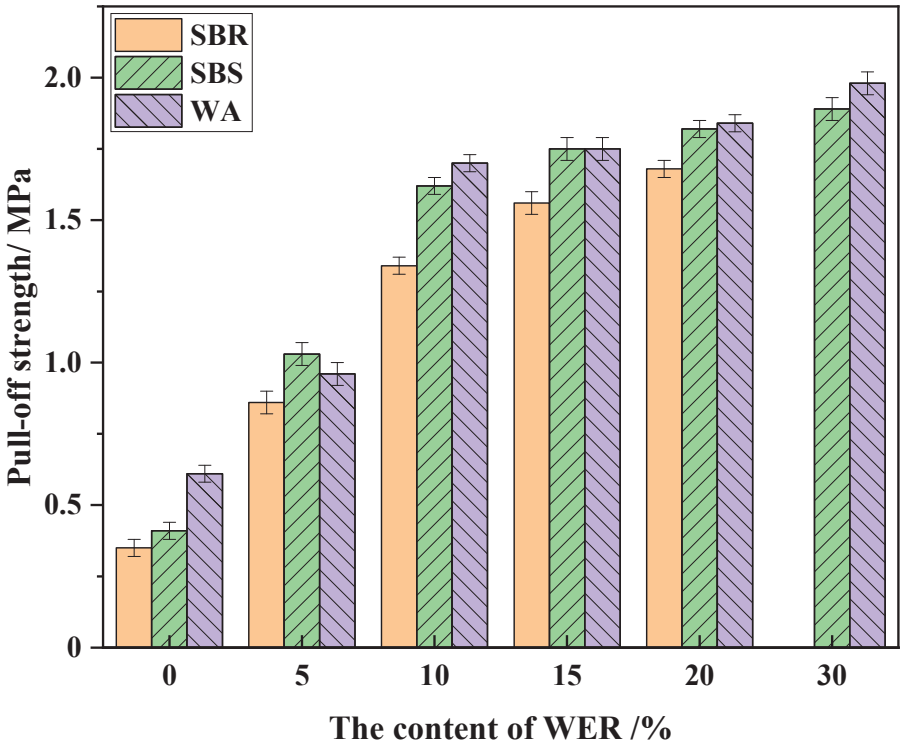

Figure 8. Pull-out strength of modified SBS, WA or SBR under different WER contents.

Figure 8 shows that when the content of WER increases from 0% to 5% and 5% to 10%, the pull-off strength of the waterborne polymers increase by 60%–150% and 55%–80%, respectively. When the WER content is 10%, the tensile strength of modified SBS and WA exceeds 1.6 MPa. With the continuous increase in the content of WER, the growth rate of pull-off strength decreases significantly. When the content of WER increases from 10% to 20%, the pull-off strength of the waterborne polymers increases by 12%–15%. After adding WER reinforcement modification, the adhesion performance and mechanical strength of the waterborne polymers have been improved to a certain extent, so that its ability to resist external force damage has been enhanced and the pull-off strength has been improved.

3.2. Correlation Analysis Between Various Performances

Based on Pearson correlation analysis, the "*p*-value" (Saliency test) and "R^2" (Correlation coefficient) are used to evaluate the correlation between the tensile, adhesion, low-temperature impact resistance and bonding performance of the waterborne polymers. The scatter diagram between the performance indicators is shown in Figure 9, and the Pearson correlation coefficient is shown in Table 2.

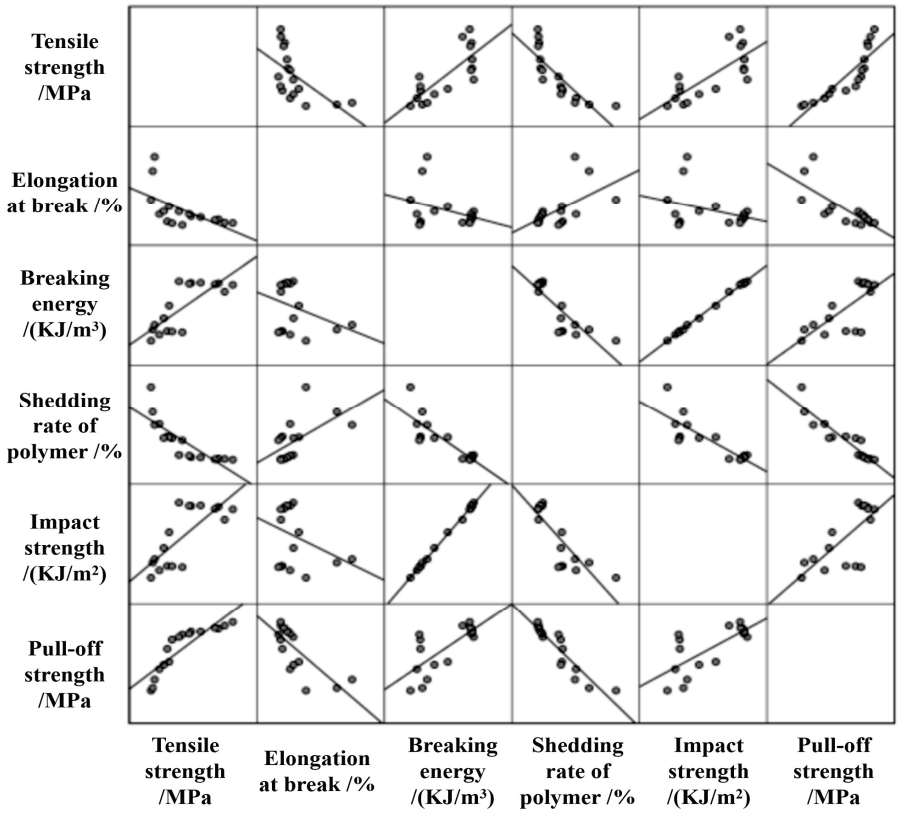

Figure 9. The scatter diagram between the performance indicators of the waterborne polymers.

Table 2. Pearson correlation coefficient R^2 ("*" represents a significance level *p*-value of 5%, and "**" represents a *p*-value of 1%).

Pearson Correlation Coefficient R^2	Tensile Strength /MPa	Elongation at Break /%	Breaking Energy /(KJ/m^3)	Shedding Rate of Polymer /%	Impact Strength /(KJ/m^2)	Pull-Off Strength /MPa
Tensile strength /MPa	-	-	-	-	-	-
Elongation at break /%	−0.586 *	-	-	-	-	-
Breaking energy /(KJ/m^3)	0.781 **	−0.348	-	-	-	-
Shedding rate of polymer /%	−0.815 **	0.573 *	−0.843 **	-	-	-
Impact strength /(KJ/m^2)	0.762 **	−0.343	0.959 **	−0.837 **	-	-
Pull-off strength /MPa	0.870 **	−0.760 **	0.739 **	−0.924 **	0.727 **	-

It can be seen from Figure 9 and Table 2 that the linear correlation coefficients, R^2, between the shedding rate of the polymers, pull-off strength and tensile strength are −0.815 and 0.870, respectively. The linear correlation coefficient R^2 between the −20 °C impact strength and breaking energy of the waterborne polymers is 0.959, and the pull-off strength of the waterborne polymers is negatively correlated with the shedding rate of the polymers, and the correlation coefficient R^2 is −0.924. It shows that there is a certain correlation between the adhesion, bonding performance and mechanical strength of the waterborne polymers, and the impact resistance of the waterborne polymers is related to their breaking energy. When the mechanical strength and breaking energy of the waterborne polymers are at a high level, their application performance such as adhesion, bonding and impact resistance shows a higher level. To effectively ensure the application quality of modified emulsified asphalt in the field of road engineering, it is necessary to

strengthen the optimization and performance improvement of basic materials such as the waterborne polymer modifiers.

3.3. FTIR and TG Analysis of WER-Modified SBS or WA

Based on FTIR and TG analysis, the physical and chemical changes in the process of WER modifying SBS or WA emulsion were characterized, and the mechanism of WER enhancing the properties of SBS or WA was revealed. Under the same WER content, the mechanical properties of modified SBR are significantly lower than those of modified SBS or WA. Considering that SBR and SBS have similar physicochemical properties, modified SBR will not be further studied.

3.3.1. FTIR Analysis

The FTIR of SBS, WA, WER, WER-modified SBS or WA were tested, and the changes in functional groups of waterborne polymers before and after the modification of WER were compared and analyzed. The results are shown in Figures 10 and 11.

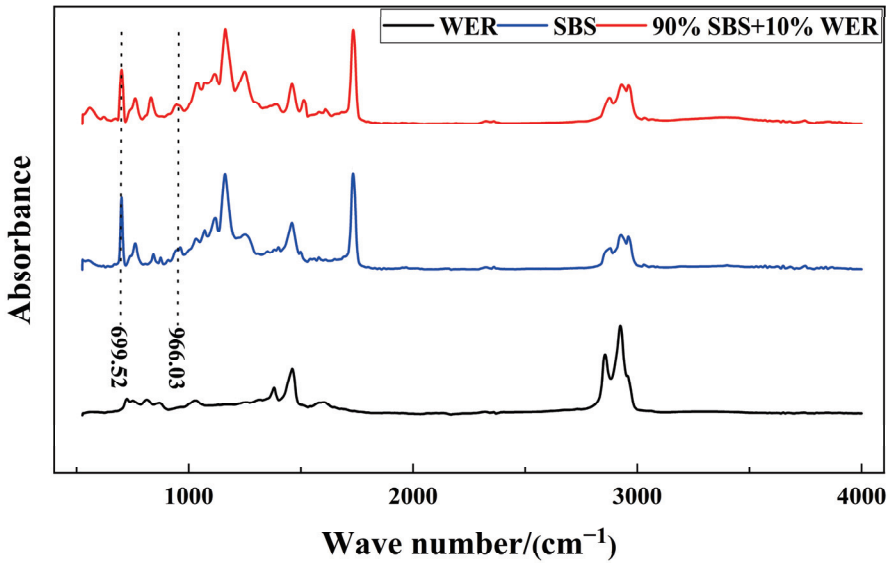

Figure 10. FTIR of WER, SBS and WER-modified SBS.

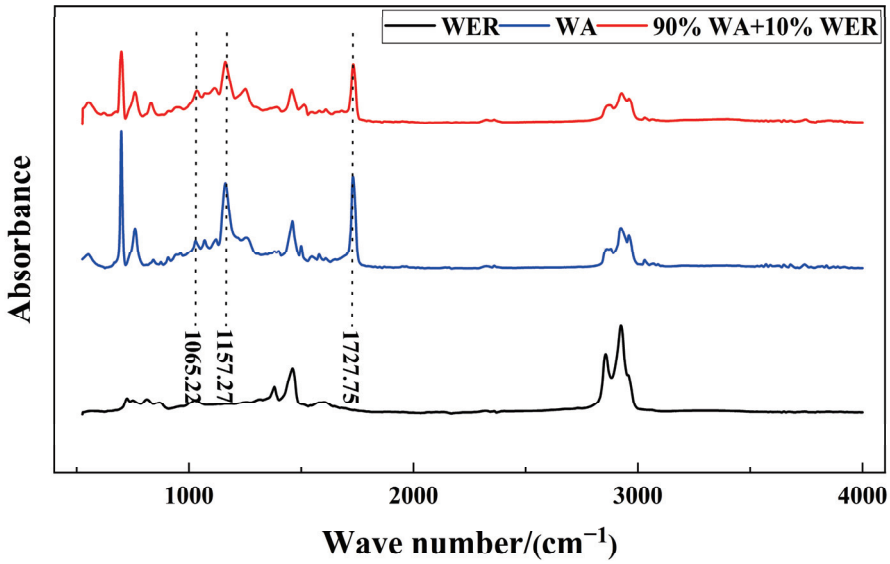

Figure 11. FTIR of WER, WA and WER-modified WA.

It can be seen from Figures 10 and 11 that the absorption peaks near 966 cm^{-1} and 699 cm^{-1} are the C-H out of plane bending vibration bands of trans-configuration and cis-configuration of olefins in segment B of the SBS molecular chain, which are the characteristic absorption peaks of SBS. There is no significant difference in the positions of infrared absorption peaks between SBS and WER-modified SBS, and the intensities of characteristic peaks are slightly different. The absorption peak near 1730 cm^{-1} is the ester carbonyl C=O stretching vibration peak of acrylate, the absorption peak near 1160 cm^{-1} is the symmetric stretching vibration peak of ether bond C-O-C in acrylate and the absorption peak near 1065 cm^{-1} is the antisymmetric stretching vibration peak of ether bond C-O-C, which can be used as the characteristic absorption peak of acrylate polymer. By comparing the FTIR of WER-modified WA with that of WA and WER, it can be seen that their respective characteristic absorption peaks are still mainly retained in the modification process. The above analysis shows that the modification process of WER-modified SBS or WA prepared by the lotion blending method in this study is mainly through physical changes.

3.3.2. TG Analysis

The compatibility, thermal stability and thermal decomposition of WER-modified SBS or WA were analyzed through TG curves and derivative thermogravimetric (DTG) curves. The results are shown in Figures 12 and 13.

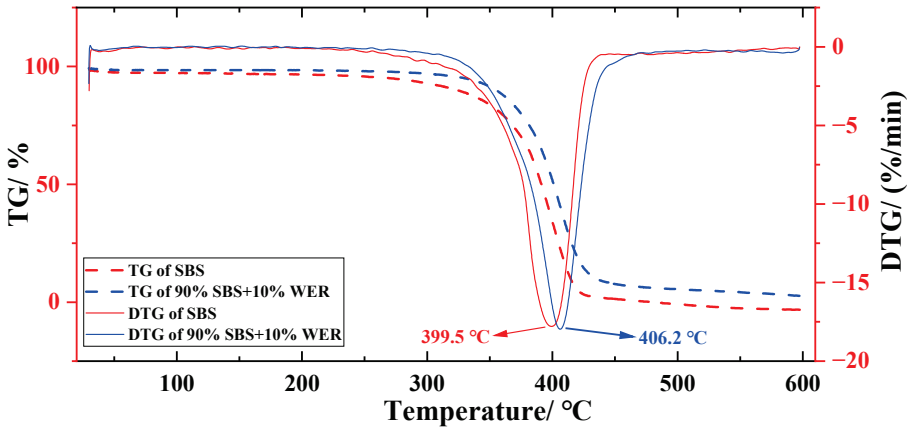

Figure 12. TG and DTG of WER, SBS and WER-modified SBS.

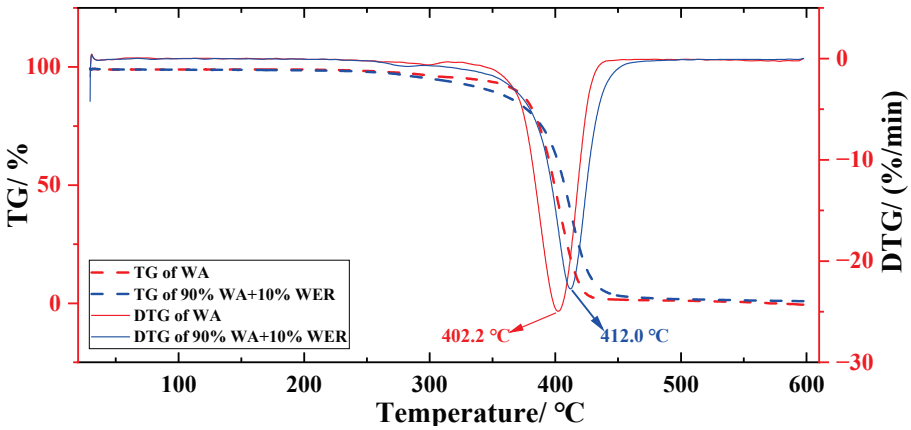

Figure 13. TG and DTG of WER, WA and WER-modified WA.

It can be seen from Figures 12 and 13 that the TG curves of SBS and WA modified by adding WER do not show obvious steps, and their DTG curves have only one peak, which indicates that WER has improved compatibility and crosslinking with SBS and WA to a

certain extent. The main weight loss temperature range of SBS, WA and WER-modified polymers is 350–450 °C. Under the same heating rate, the TG curves and DTG curves of SBS and WA modified by adding WER generally shift to the right. At the same weight loss rate, the decomposition temperature increases. The initial decomposition temperature and the end decomposition temperature increase. After adding WER for modification, the temperature at which SBS reaches the maximum thermal decomposition rate increases from 399.5 °C to 406.2 °C, and the temperature at which waterborne acrylate reaches the maximum thermal decomposition rate increases from 399.5 °C to 406.2 °C. It shows that WER can improve the thermal stability of SBS and WA, and enhance the crosslinking and curing degree of SBS and WA.

4. Conclusions

1. Adding an appropriate content of WER can significantly improve the mechanical strength, tensile modulus and toughness of SBS, WA and SBR, and increase its ability to resist deformation and damage. The content of WER is suggested to be 10%–15%.
2. There is a certain correlation between the adhesion, bonding and mechanical strength of the waterborne polymers, and the impact resistance is related to their breaking energy. The application properties of adhesion, bonding and impact resistance can be further improved by improving the mechanical strength and breaking energy of the waterborne polymers.
3. FTIR and TG analyses indicate that the modification process involving WER-modified SBS or WA prepared via emulsion blending primarily involves physical changes. WER enhances the thermal stability of SBS and WA while promoting crosslinking and curing. This study compares the performance differences among WER-reinforced SBS, WA, and SBR. Further investigation into the performance variations of these modified emulsified asphalts is warranted.

Author Contributions: Conceptualization, H.F. and C.W.; methodology, H.F. and C.W.; software, H.F.; validation, C.W.; formal analysis, H.F.; investigation, H.F.; resources, H.F.; data curation, C.W.; writing—original draft preparation, H.F.; writing—review and editing, C.W.; visualization, H.F.; supervision, C.W.; project administration, C.W.; funding acquisition, C.W. All authors have read and agreed to the published version of the manuscript.

Funding: This research was funded by the National Natural Science Foundation of China, grant number 52378429, and the Innovation Capability Support Program of Shaanxi, grant number 2022TD-07.

Institutional Review Board Statement: Not applicable.

Informed Consent Statement: Not applicable.

Data Availability Statement: The original contributions presented in this study are included in the article. Further inquiries can be directed to the corresponding author.

Conflicts of Interest: The authors declare that they have no conflicts of interest regarding the publication of this paper.

References

1. Xu, L.; Li, X.R.; Zong, Q.D.; Xiao, F.P. Chemical, morphological and rheological investigations of SBR/SBS modified asphalt emulsions with waterborne acrylate and polyurethane. *Constr. Build. Mater.* **2021**, *272*, 121972. [CrossRef]
2. Yang, F.; Zhou, Q.; Yang, L.M.; He, L.H.; Chen, Q.; Tang, S.G. Preparation and performance evaluation of waterborne epoxy resin modified emulsified asphalt binder. *Case Stud. Constr. Mater.* **2024**, *21*, e03548. [CrossRef]
3. Xu, L.; Zhao, Z.F.; Li, X.R.; Yuan, J.; Zhou, Q.Y.; Xiao, F.P. Cracking investigation on fog seal technology with waterborne acrylate and polyurethane as a clean modification approach. *J. Clean. Prod.* **2021**, *329*, 129751. [CrossRef]

4. Wang, H.Z.; Li, C.X.; Xu, G.; Zhou, Y.X.; Wang, R. Study of high-temperature rheological properties of emulsified asphalt residues. *Coatings* **2024**, *14*, 522. [CrossRef]
5. Hu, F.G.; Tian, X.G.; Hu, H.L.; Li, G.Y.; Guo, C.H. Effect of SBR latex content on performance of modified emulsified asphalt. *J. Build. Mater.* **2021**, *24*, 895–900. (In Chinese) [CrossRef]
6. Song, W.M.; Chen, D.W.; Wu, H.; Wu, Z.Z.; Wada, S.A.; Yuan, H. Preparation and performance characterization of waterborne epoxy resin modified asphalt emulsion for tack coat. *J. Clean. Prod.* **2024**, *475*, 143715. [CrossRef]
7. Huang, S.L.; Jin, F.; Chen, D.D.; Xiao, Q.; Ding, Q.J. Study on modification mechanism and performance of waterborne epoxy resin Micro-surfacing. *Coatings* **2023**, *13*, 504. [CrossRef]
8. Lu, C.; Zheng, M.L.; Gao, Y.; Ding, X.Y.; Zhang, W.W.; Chen, W. Study of long-term skid and wear resistance of waterborne epoxy resin-SBR compound modified emulsified asphalt microsurfacing. *J. Appl. Polym. Sci.* **2024**, *141*, 54937. [CrossRef]
9. Zeng, Q.W.; Yang, S.X.; Cui, Q.X.; Luan, D.X.; Xiao, F.; Xu, C. Prediction of moisture content ratio of emulsified asphalt chip seal based on machine learning and electrical parameters. *Constr. Build. Mater.* **2024**, *450*, 138633. [CrossRef]
10. Zhang, Z.Q.; Yang, J.H.; Fang, Y.; Luo, Y.F. Design and performance of waterborne epoxy-SBR asphalt emulsion (WESE) slurry seal as under-seal coat in rigid pavement. *Constr. Build. Mater.* **2020**, *270*, 121467. [CrossRef]
11. Chen, Q.; Lan, X.; Li, A.Q.; Sun, X.L.; Wang, C.H. The novel rapid curing pavement maintenance seal with a low environmental impact: Preparation and performance evaluation. *Wear* **2025**, *566–567*, 205919. [CrossRef]
12. Yan, K.Z.; Shi, J.Y.; Shi, K.X.; Wang, M.; Li, G.K.; Hong, Z. Effects of the chemical structure of curing agents on rheological properties and microstructure of WER emulsified asphalt. *Constr. Build. Mater.* **2022**, *347*, 128531.
13. Fu, H.; Wang, C.H.; Niu, L.L.; Yang, G.L.; Liu, L.Q. Composition optimisation and performance evaluation of waterborne epoxy resin emulsified asphalt tack coat binder for pavement. *Int. J. Pavement Eng.* **2022**, *23*, 4034–4048. [CrossRef]
14. Gu, Y.; Tang, B.M.; He, L.H.; Yang, F.; Wang, H.; Ling, J.M. Compatibility of cured phase-inversion waterborne epoxy resin emulsified asphalt. *Constr. Build. Mater.* **2019**, *229*, 116942. [CrossRef]
15. Li, R.; Leng, Z.; Zhang, Y.; Ma, X. Preparation and characterization of waterborne epoxy modified bitumen emulsion as a potential high-performance cold binder. *J. Clean. Prod.* **2019**, *235*, 1265–1275. [CrossRef]
16. Li, R.; Leng, Z.; Partl, M.N.; Raab, C. Characterization and modelling of creep and recovery behaviour of waterborne epoxy resin modified bitumen emulsion. *Mater. Struct.* **2021**, *54*, 8. [CrossRef]
17. Ji, J.; Yao, H.; Zheng, W.H.; Suo, Z.; Xu, Y.; Han, S.; Xu, S.F.; You, Z.P. Preparation and properties of waterborne epoxy–modified emulsified asphalt binder (WEMEAB). *J. Test. Eval.* **2018**, *48*, 3172–3187. [CrossRef]
18. Yao, X.G.; Tan, L.Z.; Xu, T. Preparation, properties and compound modification mechanism of waterborne epoxy resin/styrene butadiene rubber latex modified emulsified asphalt. *Constr. Build. Mater.* **2022**, *318*, 126178. [CrossRef]
19. Zhang, Q.; Xu, Y.H.; Wen, Z.G. Influence of water-borne epoxy resin content on performance of waterborne epoxy resin compound SBR modified emulsified asphalt for tack coat. *Constr. Build. Mater.* **2017**, *153*, 774–782. [CrossRef]
20. Liu, F.Q.; Zheng, M.L.; Liu, X.; Ding, X.Y.; Wang, F.; Wang, Q.Q. Performance evaluation of waterborne epoxy resin-SBR composite modified emulsified asphalt fog seal. *Constr. Build. Mater.* **2021**, *301*, 124106. [CrossRef]
21. Zhang, W.; Zhang, Z.Q.; Zhao, Q.S. Laboratory performance evaluation of a waterborne epoxy-modified asphalt mixture with styrene-butadiene rubber for cold patching applications. *J. Mater. Civ. Eng.* **2022**, *34*, 04022111. [CrossRef]
22. Li, X.L.; Yang, L.; Luo, S.; Song, X.J.; Fan, L.; Chen, J.J.; Diab, A.; Ye, J.H.; Ning, Z.F. Aging characteristics of a colored ultrathin overlay. *J. Transp. Eng. Part B Pavements* **2022**, *148*, 04022009. [CrossRef]
23. Yao, X.G.; Xu, H.Y.; Xu, T. Syncretization mechanism between emulsified asphalt and aged asphalt in cold recycled asphalt mixture using developed demulsification-dehydration method. *Constr. Build. Mater.* **2022**, *326*, 126860. [CrossRef]
24. Wang, F.; Fu, H.; Liu, G.X.; Wang, C.H.; Yu, S.X. Preparation optimization and performance evaluation of waterborne epoxy resin for roads. *Adv. Civ. Eng.* **2021**, *2021*, 8977674. [CrossRef]
25. *JT/T 535-2015*; Water Quality Asphalt Waterproof Coating for Highway. Ministry of Transport of the People's Republic of China: Beijing, China, 2015. (In Chinese)
26. Wang, Y.L.; Hou, L.J.; Liu, Z.Y.; Li, S.Y.; Li, Z.H. Study on coating properties of waterborne polyurethane modified epoxy resin latex. *Mater. Rep.* **2019**, *33*, 2456–2460. (In Chinese)
27. *JTG E20-2011*; Standard Test Methods of Bitumen and Bituminous Mixtures for Highway Engineering. Ministry of Transport of the People's Republic of China: Beijing, China, 2011. (In Chinese)
28. *GB/T 2567-2021*; Test Methods for Properties of Resin Casting Body. Standardization Administration of China: Beijing, China, 2021. (In Chinese)

MDPI AG
Grosspeteranlage 5
4052 Basel
Switzerland
Tel.: +41 61 683 77 34

Coatings Editorial Office
E-mail: coatings@mdpi.com
www.mdpi.com/journal/coatings

MDPI

Academic Open
Access Publishing

mdpi.com

ISBN 978-3-7258-7527-6